THE UNIVERSITY OF HULL

Electroanalytical Chemistry for biological and environmental applications

being a thesis submitted for the degree of

Doctor of Philosophy

in

The University of Hull

by

Louise A Evans

2008

Table of Contents

Acknowledgements

This work was funded by the University of Hull and the EPSRC and for this opportunity I thank them.

I also thank my supervisor, Dr. Jay Wadhawan for the opportunity and his assistance throughout the course of my PhD, and colleagues past and present for their time and advice.

Particular thanks also go to Sal Peyman for her unwavering support, motivation and most of all keeping me going when things got too much over the past seven years. I thank her for the times when she just looked at me to know that a trip to the pub was required, and for the times when no excuse was needed. I think Sal was the first person to suggest doing a PhD, so I thank her for planting that seed in my mind. I would also like to thank Tom Dearing for his advice, support and kind words throughout the three years of my PhD. I would also like to thank him for always asking me to lunch in the first few weeks of my PhD when I only knew a few people, and for the Lou portions of lasagne, chilli and pizza, without which I may have wasted away.

Finally, but most importantly, my thanks go to my parents, Paul and Wendy. Without their love and support in all I have done, this would not have been possible and I would not have achieved all that I have without them.

Thank you all.

Glossary

Abbreviations

DMDNPD	N,N'-dimethyl-N,N'-dinitroso-*para*-phenylenediamine
EPS	Extracellular Polysaccharide
ESR	Electron Spin Resonance
HPLC	High Performance Liquid Chromatography
IHP	Inner Helmholtz Plane
LUMO	Lowest Unoccupied Molecular Orbital
MSAD	Mean Squared Absolute Deviation
NMR	Nuclear Magnetic Resonance
NO	Nitric Oxide
NOS	Nitric Oxide Synthase
OHP	Outer Helmholtz Plane
PEG	Polyethylene Glycol
SAM	Self Assembled Monolayer
SCE	Saturated Calomel Electrode
SECM	Scanning Electrochemical Microscopy
TBAP	Tetrabutylammonium Perchlorate

TMPD	Tetramethyl-*p*-phenylene diamine

Roman Symbols

C	Concentration
D	Diffusion Coefficient
E	Potential
F	Faraday's Constant (98485 C mol^{-1})
i	Current
k	Rate Constant
n	Number of Electrons
N	Number of Molecules
Q	Charge
R	Gas Constant (8.314 J mol^{-1})
r	Radius
T	Temperature
t	Time

Greek Symbols

α	Symmetry Factor
β	Symmetry Factor

η	Overpotential
μ	Ionic Mobility
ν	Scan Rate
ω	Rotation Speed of the Electrode

Abstract

Electroanalytical chemistry provides an elegant technique by which to explore, amongst others, various biological and environmental applications. To this end, four areas of electroanalytical chemistry are investigated in order to develop biologically- and environmentally-relevant sensors, together with exploring the electro-generation of a biologically important molecule and the diffusional factors that may affect this generation.

The first study involves the dynamics of the bond cleavage involved in the electro-generation of nitric oxide from a range of N-nitrosoamines. Adsorption phenomena is found to be of pivotal significance in the release of nitric oxide from two of the compounds explored, namely cupferron and N-nitrosodiphenylamine, whilst bis(nitroso)phenylenediamine released, as hoped, two moles of nitric oxide in a single step. The challenge is to isolate the product, and to determine which form of nitric oxide was generated, *i.e.* the cation, NO^+ or nitric oxide, NO. Isolation remains a challenge, however analysis of the reaction mechanism does allow a prediction of the product, be it NO^+ or NO. NO^+ is a highly oxidising species and hence is difficult to isolate, therefore it is far more preferable to electro-generate NO, which cupferron was the only compound investigated that achieved this.

The second study involved the investigation of axiosymmetric anisotropic diffusion to disc shaped microelectrodes, with theoretical expressions examined with experimental data in order to examine the factors. A ferrocene/PEG in acetonitrile system was examined in order to test this theory and to determine the effect of viscosity on the diffusion coefficients, and also if it was possible to investigate the anisotropy by effectively "blocking" either D_r or D_z. Excellent symmetry between theory and experiment was found, hence the focus turned to a ferricyanide in cæsium

pentadecafluorooctanoate/D_2O system where once again the calculated value of $\sqrt{D_z D_r}$ affords a theoretical waveshape with reasonable agreement between theory and experiment. Potential step chronoamperometry then determined separate values for D_r and D_z, with the resulting values affording an anisotropic ratio of 1.7, suggesting radial diffusion dominance over planar diffusion.

Third, the modification of electrodes is explored in order to develop biologically and environmentally relevant sensors. In a first strand, two liquid crystal ferrocene compounds are examined, immobilised on the surface of a glassy carbon electrode simply via solvent evaporation. Both compounds demonstrated typical ion transfer processes across the liquid|liquid interface, with both anion insertion and cation expulsion processes demonstrated. The differing voltammetry observed in the presence of different anions formed the basis of the anion sensor.

In a second avenue in this modified electrode work a cation sensor is developed, working on the basis of a biofilm, *i.e.* developing a modification of the electrode surface to mimic the action of a biofilm in chelating with cations. With this in mind, a basal plane graphite electrode was modified with a diazonium salt and polyphenol, and through the introduction of alginic acid into the polyphenol layer a degree of selectivity between the Group 2 cations was demonstrated, although quantitative properties eluded the work.

Last, an environmental sensor for cyanide was developed using an electrochemical probe, tetramethylphenylenediamine (TMPD). The reaction between the electro-generated $TMPD^{\bullet+}$ and cyanide is successfully followed colorimetrically, before product characterisation studies help to determine the reaction mechanism. Voltammetric studies form the basis of a sensor, with square wave voltammetry achieving a detection limit of 4.4 μM. The reaction between TMPD and cyanide allowed remediation studies to be

undertaken, with river freshwater samples from North Yorkshire (54^{o}15’19.19” N, 1^{o}46’13.49” W) and the Rodalquilar mine, Spain, (36^{o}50’52.9” N, 2^{o}02’36.87” W) demonstrating the removal of cyanide by an impressive three orders of magnitude.

1 Introduction

1.1 Dynamic Electrochemistry

1.1.1 Introduction

Dynamic electrochemistry is concerned with the transfer of electrons at an electrode/solution interface in a heterogeneous process. Electrochemistry is concerned with the electrode/solution interface in terms of the processes that occur there; the interface is perturbed by the application of a potential so as to encourage a current to flow. If a general electron transfer reaction is considered:

$$\boldsymbol{O}_{(aq)} + \boldsymbol{e}^{-}_{(aq)} \rightleftharpoons \boldsymbol{R}_{(aq)}$$

Equation 1-1

Where O represents the oxidised species, R represents the reduced species and n represents the number of electrons transferred. At equilibrium, Nernst showed that the potential established at the electrode surface is given by:

$$E = E^{\theta} + \frac{RT}{nF}\ln\left(\frac{a_o}{a_r}\right)$$

Equation 1-2

where E^{o} is the standard electrode potential of the electrochemical reaction when all species have unit activity, R is the gas constant (8.314 kJ mol^{-1}), T is the temperature, n is the number of electrons transferred, F is Faradays constant (98485 C mol^{-1}) and a_o and a_r are the activities of oxidised and reduced species. The Nernst equation is a thermodynamic attribute of the redox reaction, thus characterising the ease of electron transfer.

Figure 1 shows the process of electron transfer. At the Fermi level (E_f), the electrons are at their maximum energy and can be accepted or donated, and can be influenced by the application of a voltage. In a reduction process, as shown in the figure, the electrons must have a minimum energy in order to transfer from the electrode to the LUMO. In oxidation, the energy of the electrons in the donor species must be equal to or greater than the energy of the Fermi level of the metal. The energy of the electrons in the Fermi level correspond to the electrode potentials which are used to drive the process.[1]

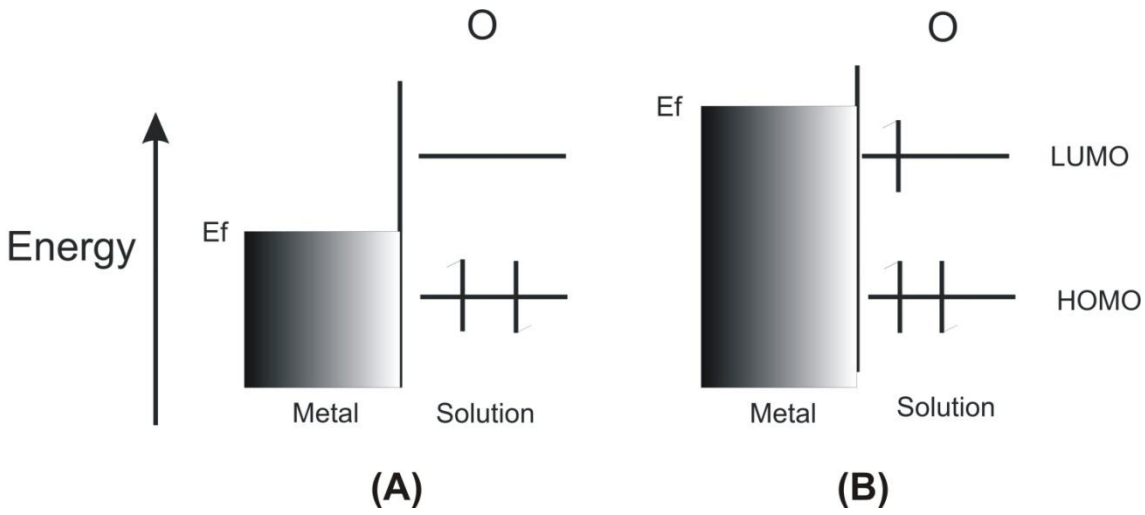

Figure 1: Transfer of an electron into the Fermi level. (A) The electrode potential is insufficient to drive the reduction of O, (B) the electrode is at a potential sufficient to drive the reduction and the process becomes thermodynamically favourable.

1.1.2 The Electrical Double Layer

The electrode/solution interface has critical importance when considering electron transfer reactions, and the processes which occur at the interface need to be understood. The electrode/solution behaves like a capacitor, a component of an electrical circuit made from two metal sheets separated by a dielectric material, and which stores energy.

In 1853 Helmholtz developed a simple model which describes the electrode/solution interface;[1] this is the electrical double layer. When a potential is applied to the electrode with respect to a reference electrode, a charge exists on the electrode, q_m, which arises

from an excess or deficiency of electrons.[1] For the interface as a whole to remain neutral, the solution must also have an equal but opposite charge, q_s, so that at all times:

$$q_m = -q_s$$

Equation 1-3

The charge in solution arises from the electrostatic rearrangement of electrolyte ions near to the surface of the electrode. It can also be caused by the reorientation of the dipole of solvent molecules. An excess of anion or cations is built up at the electrode surface, forming the electrical double layer, shown in figure 2.

The inner Helmholtz plane (IHP) consists of solvent molecules or ions that are specifically adsorbed to the electrode surface. The line drawn through the electrical centres of these adsorbed species is the IHP.[2] The outer Helmholtz plane (OHP) contains solvated ions which approach the electrode, but to a distance which is limited by the salvation shell of the ion. Again the line drawn through the centre of these solvated ions defines the OHP.[2] These ions are non-specifically adsorbed to the electrode surface, as only long distance electrostatic forces are involved and so the interaction is independent of the chemical properties of the ion. The region including the OHP and extending into the bulk solution is known as the diffuse layer, the thickness of which is dependent upon the concentration of ions in the solution; the thickness is less than ~ 100 Å for concentrations greater than 0.1 M.[2]

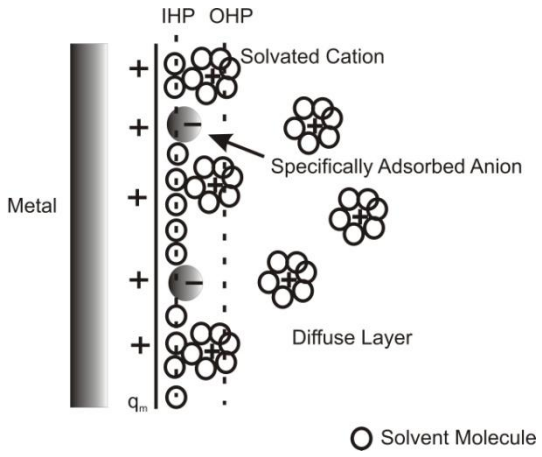

Figure 2: The Electrical Double Layer

1.1.3 Electrochemical Cells and Electrolysis

Electrochemical cells can be composed of two or three electrode systems. The two electrode system is the simplest approach to the study of current/voltage characteristics. The reaction occurs at the working electrode which provides the source of electrons. Considering again the general electron transfer reaction, equation 1-1, the reaction involves the transfer of an electron between an aqueous and a metallic phase. Due to this, a net charge separation must develop between the electrode and solution, which in turn must therefore create a potential difference at the electrode/surface, $\Delta\phi_{m/s}$ interface given by:

$$\Delta\phi_{m/s} = \phi_m - \phi_s$$

Equation 1-4

where ϕ_m is the potential at the electrode and ϕ_s is the potential of the solution. In order to measure this potential difference, a complete electrical circuit is required, hence the introduction of a second electrode, the reference electrode. This electrode maintains a constant potential drop at the electrode/solution interface, and hence the observed voltage, E, (the potential difference between the working electrode and the reference electrode) is given by:

$$E = \left(\phi_m - \phi_s\right) + C$$

Equation 1-5

In order to induce a current flow into the electrochemical cell, a potential is applied to the working electrode that is different to the equilibrium potential, E_e. This deviation of the potential, E, applied to the equilibrium potential is termed the overpotential, η:

$$\eta = E - E_e$$

Equation 1-6

The magnitude of the current flowing, i, is given by:

$$i = \oint nFj \, dA$$

Equation 1-7

Where n is the number of electrons transferred per mole of reactants, F is Faraday's Constant (96485 C mol^{-1}), A is the electrode area and j is the flux of electroactive species reaching the electrode surface in moles cm^{-2} s^{-1}. In kinetically limited processes:

$$j = k_0[O]_{surface}$$

Equation 1-8

where k_o is the heterogeneous rate constant of the electron transfer reaction. The flux of electroactive species to the surface is a very important parameter and will be explained further in section 1.1.4. So again considering the general electron transfer reaction, equation 1-1, with k_f representing the rate constant of the reductive process and k_b representing the rate constant of the oxidative process, the reductive current is given by:

$$i_{red} = -FAk_f[O]_{surface}$$

Equation 1-9

and the oxidative current is given by:

$$i_{oxd} = FAk_b[R]_{surface}$$

Equation 1-10

and hence the overall current, i, is given by:

$$i = FA\left(k_b[R]_{surface} - kf[O]_{surface}\right)$$

Equation 1-11

The measurement of current/voltage curves using a two electrode system is therefore the most simple approach, however it is limited to systems where only a tiny current flows, for example when using microelectrodes. When a current flow is induced between two electrodes, *i.e*. the working and reference electrodes, the solution experiences an ohmic drop, iR, and this has to be taken into account when considering the potential, E, applied to the working electrode:

$$E = \left(\phi_m - \phi_s\right) + iR + \left(\phi_s - \phi_{ref}\right)$$

Equation 1-12

When only very small currents flow between the working and reference electrodes, the ohmic drop in solution is negligible and the iR term can be disregarded, meaning potentials applied to the working electrode are directly related to the driving force term, $\left(\phi_m - \phi_s\right)$. When larger currents flow through the system, the iR term no longer becomes negligible and so changes to the potential applied to the working electrode are no longer limited to changing the $\left(\phi_m - \phi_s\right)$ term. A larger current flowing through the

system will increase the ohmic drop, iR, and also larger currents flowing through the reference electrode may cause changes in the chemical composition, and hence it may no longer be a constant value.[1]

To minimise this problem a third electrode is introduced creating the three electrode system which is more commonly used. This third electrode is the counter or auxiliary electrode, and in this system the current is passed between the working electrode and counter electrode hence halting any flow of current through the reference electrode, ensuring it remains at a stable, fixed potential. The counter electrode can be any electrode, although it is usually chosen as one that will not form electrolysis products that could reach the working electrode surface and cause interferences.

1.1.4 Mass Transport

An overall electrode reaction involves a series of steps as shown in figure 3.[2] The factors that affect the overall electrode reaction rate are:

- as just discussed, the mass transport of electroactive species from bulk solution to the electrode surface,
- the rate of electron transfer at the electrode surface,
- the rate of chemical reactions that may occur before or after the electron transfer and
- the effect of the adsorption or desorption of any material at the electrode surface.

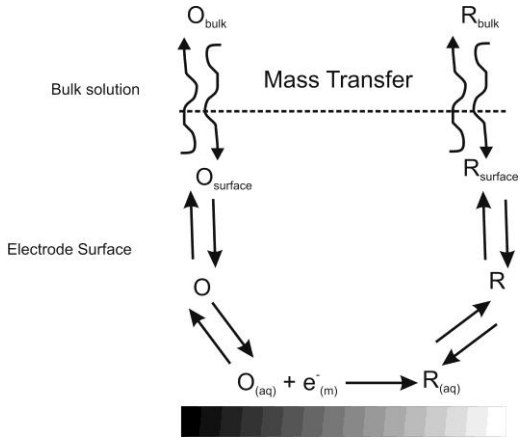

Figure 3: The steps involved in an electron transfer reaction

In order for electron transfer reactions to occur, the electroactive species must be transported from bulk solution to the electrode interface. The rate of reaction, that is the overall reaction, will depend on the slowest step and this may be the rate at which the electroactive species reaches the electrode interface. In electrochemistry there are three modes of mass transport that are significant:

- diffusion,
- migration and
- convection.

If all these modes of transport are in action in a system, the overall mass transfer in one dimension is given by the Nernst-Planck equation:

$$J_A(x) = -D_A \frac{\partial C_A(x)}{\partial x} - \frac{z_A F}{RT} D_A C_A \frac{\partial \phi(x)}{\partial x} + C_A \nu(x)$$

Equation 1-13

where $J_A(x)$ is the flux of species A at a distance x from the electrode,

D_A is the diffusion coefficient,

$\frac{\partial C_A(x)}{\partial x}$ is the concentration gradient at distance x,

$\frac{\partial \phi(x)}{\partial x}$ is the electric potential gradient,

z_A and C_A are the charge and concentration of species A respectively, and ν (x) is the velocity with which a volume element in solution moves along the axis.

Electrochemical experiments usually endeavour to have diffusion as the dominant mode of mass transport as diffusion only conditions allow well-defined behaviour to be accurately predicted. Therefore migration can be disregarded by adding excess supporting electrolyte and convection can be disregarded by stopping vibrations and stirring within the electrochemical cell. Natural convection is reduced by keeping electrochemical experiments down to a minimum time. The three forms of mass transport are now considered in more detail.

1.1.4.1 **Diffusion**

Diffusion is defined as the movement of a species under the influence of a concentration gradient, but more strictly speaking a chemical potential gradient. By considering this, it can be deduced that the rate of diffusion at a particular point in solution is dependent upon the concentration gradient. Fick's Laws[3] are used to describe and quantify diffusion. The first law shows the number of moles of material diffusing through a unit area in one second, j,

$$j = -D_A \frac{\partial [A]}{\partial x}$$

Equation 1-14

This defines the diffusional flux of material, D_A is the diffusion coefficient of species A and [A] is the concentration.

Fick's second law is concerned with how the concentration of a species at a point close to the electrode varies with time:

$$\frac{\partial}{\partial t}[A] = D_A\left(\frac{\partial^2[A]}{\partial x^2}\right)$$

Equation 1-15

This only considers movement in one direction, when more than one direction needs to be considered the equation is extended:

$$\frac{\partial[A]}{\partial t} = D_A\frac{\partial^2[A]}{\partial x^2} + D_A\frac{\partial^2[A]}{\partial y^2} + D_A\frac{\partial^2[A]}{\partial z^2}$$

Equation 1-16

1.1.4.2 **Migration**

Migration is defined as the movement of a charged species under the influence of an electric field. An electric field exists at the electrode/solution due to the Ohmic drop between the two phases. This electric field exerts an electrostatic force on any charged species in the diffuse layer, either attracting or repelling these species to or from the electrode surface.[1] This migratory flux is given by:

$$j_m\alpha - \mu[A]\frac{\partial\phi}{\partial x}$$

Equation 1-17

where [A] is the concentration of species A, $\frac{\partial \phi}{\partial x}$ is the electric field and μ is the ionic mobility:

$$\mu[A] = \frac{|z_A| F D_A}{RT}$$

Equation 1-18

where z_A is the charge and D_A is the diffusion coefficient.

1.1.4.3 **Convection**

Convection, of which there are two types, is transport of the bulk fluid via a collective velocity of particles in a fluid material. Natural convection is caused by density or thermal gradients and is the cause of general fluid flow. Forced convection follows some form of external mechanical force onto the solution. Natural convection arises in solution from exo- or endothermic reactions, or from electrolysis products forming near the electrode that are a different density to those in the bulk solution. An example of natural convection is the driving of hydrodynamic flows through surface tension gradients. Forced convection is caused by stirring, pumping the solution or bubbling gas through the solution. Convection is deliberately introduced into the solutions in a reproducible manner and with well-defined hydrodynamic behaviour in order to establish a quantitative description of the flow and hence predict the mass transport patterns. In a solution moving at a velocity v_x, concentration changes due to this velocity are given by:

$$\frac{\partial [A]}{\partial t} = -v_x \frac{\partial [A]}{\partial x}$$

Equation 1-19

1.1.5 Kinetics of Electron Transfer Reactions

If the simplest electrode reaction is considered, i.e. when the electron transfer is the rate determining step, then the net rate of the electrode reaction is controlled by the rate of mass transfer to the electrode and is given by:

$$v = \frac{i}{nFA}$$

Equation 1-20

If again the general electron transfer reaction is considered with rate constants:

$$O_{(aq)} + ne^-_{(m)} \xrightarrow{kf} R_{(aq)}$$

Equation 1-21

$$R \xrightarrow{kb} O + ne^-_{(m)}$$

Equation 1-22

Then the rate of the forward reaction, v_f, is:

$$v_f = k_f[O]$$

Equation 1-23

And the rate of the reverse reaction, v_b, is:

$$v_b = k_b[R]$$

Equation 1-24

then the overall net rate of conversion of O to R is:

$$v_{net} = k_f[O] - k_b[R]$$

Equation 1-25

When the reaction is at equilibrium, $v_{net} = 0$ and therefore the ratio of the rate constants, k_f/k_b is equal to the concentration ratio, [R]/[O].

Arrhenius was the first rationalise the thermal dependence of the rate constant in the following manner:

$$k = Ae^{-\frac{E_A}{RT}}$$

Equation 1-26

where E_A is the activation barrier. Modern interpretations of this empirical formula now understand this in terms of transition state theory.

For the case of electron transfer reactions, the following notions are employed:

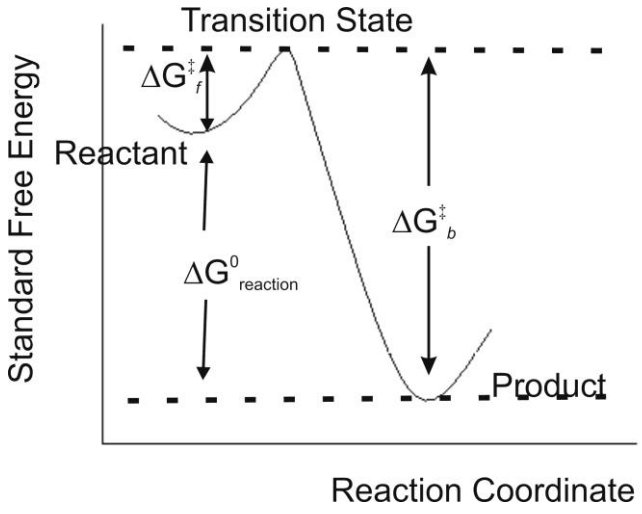

Figure 4: Standard free energy plot for a reaction

The reaction must overcome an energy barrier, E_A, in order to form the products. The peak of this energy barrier is known as the transition state. As the electron transfer is

considered as a function of the standard free energy in figure 4, the Arrhenius equation can be written as:

$$k = A\exp\left(\frac{-\Delta G^{\mp}}{RT}\right)$$

Equation 1-27

where $\Delta G^{\mp}$ is the standard free energy of activation.[4]

From previous discussion, (Section 1.1.3), it was shown that potential is an important factor in electrochemical reactions and therefore it needs to be considered when discussing kinetics. In order to do this, the product and reactant free energies, which are dependent upon potential, are considered. For any species:

$$molar\ free\ energy = C + zF\phi$$

Equation 1-28

Where C represents the chemical species as a function of temperature and pressure and zFϕ represents the electrical energy. So, if the following reaction is considered:

$$A^{z}_{(aq)} + e^{-}_{m} \rightarrow B^{z-1}_{(aq)}$$

Equation 1-29

Then the free energies of the reactants are:

$$G_{(react)} = C + zF\phi_{\ s} - F\phi_{\ m}$$
$$G_{(react)} = C + (z-1)F\phi - F(\phi_{\ m} - \phi_{\ s})$$

Equation 1-30

And the free energy of the products:

$$G_{(products)} = C' + (z-1)F\phi_s$$

Equation 1-31

It can be assumed that the transition state has a potential in between that of the reactants and the products, so the transition state free energy can be written as:

$$G^{\mp} = C'' + (z-1)F\phi_s - (1-\alpha)F(\delta_m - \delta_s)$$

Equation 1-32

α is the transfer coefficient ($0<\alpha<1$), and is a measure of the symmetry of the energy barrier. If α is closer to 0, then the transition state is reactant-like, if α is closer to 1 then the transition state is product like. Very often it is ½, suggesting that the transition state is half way between the reactants and products.[1]

1.1.5.1 Butler Volmer Kinetics

Referring back to figure 4, it can be seen that the cathodic activation energy is $\Delta G_{oc}^{\mp}$ and the anodic activation energy is $\Delta G_{oa}^{\mp}$. When the potential is applied to drive the reaction, *i.e.* the overpotential, the barrier for oxidation becomes less, $\Delta G_a^{\mp}$, hence:

$$\Delta G_a^{\mp} = \Delta G_{oa}^{\mp} - (1-\alpha)F(E - E^{\theta})$$

Equation 1-33

and;

$$\Delta G_c^{\mp} = \Delta G_{oc}^{\mp} + \alpha F(E - E^{\theta})$$

Equation 1-34

If the rate constants for the reduction, k_f, and the oxidation, k_b, are considered in Arrhenius form then:

$$k_f = A_f \exp\left(\frac{-\Delta G_c^{\mp}}{RT}\right)$$

Equation 1-35

$$k_b = A_b \exp\left(\frac{-\Delta G_a^{\mp}}{RT}\right)$$

Equation 1-36

If equations 1-35 and 1-36 are then inserted then:[2]

$$k_f = A_f \exp\left(\frac{-\Delta G_{oc}^{\mp}}{RT}\right)\exp\left[\frac{-\alpha F}{RT}\left(E - E^{\theta}\right)\right]$$

Equation 1-37

$$k_b = A_b \exp\left(\frac{-\Delta G_{oa}^{\mp}}{RT}\right)\exp\left[\frac{(1-\alpha)F}{RT}\left(E - E^{\theta}\right)\right]$$

Equation 1-38

At equilibrium, $k_f = k_b$ and so can be combined into a single value, k^0, enabling the rate constant at other potentials to be calculated:

$$k_f = k^o \exp\left[\frac{-\alpha F}{RT}\left(E - E^{\theta}\right)\right]$$

Equation 1-39

$$k_b = k^o \exp\left[\frac{(1-\alpha)F}{RT}\left(E - E^{\theta}\right)\right]$$

Equation 1-40

The Butler-Volmer Equation[5,6] is then formed by substituting these equations into equation 1-11:

$$i = i_0 \left(\frac{[R]_{surface}}{[R]_{bulk}} \exp\left\{ \frac{(1-\alpha)F\left(E - E^{\theta}\right)}{RT} \right\} - \frac{[O]_{surface}}{[O]_{bulk}} \exp\left\{ \frac{-\alpha F\left(E - E^{\theta}\right)}{RT} \right\} \right)$$

Equation 1-41

The surface concentrations will be equal to the bulk concentrations when the solution is efficiently stirred, and in this case the Butler-Volmer Equation is simplified to:

$$i = i_0 \left(\exp\left\{ \frac{(1-\alpha)F\left(E - E^{\theta}\right)}{RT} \right\} - \exp\left\{ \frac{-\alpha F\left(E - E^{\theta}\right)}{RT} \right\} \right)$$

Equation 1-42

1.1.5.2 **Tafel Analysis**

In order to investigate the kinetics of electrode reactions in a comprehensive manner, it is necessary to investigate the dependence of current on potential when it is not limited by mass transport of electroactive material to the electrode surface. In this case a low current flows, and Tafel showed that the current is exponentially related to the overpotential, η. The Tafel Equation shows this:

$$\eta = a + b \log_i$$

Equation 1-43

Considering equations 1-41 and 1-42, when i_0 is very small, a large overpotential is required to induce the flow of current. When the overpotential is applied at a value to drive the oxidative process the reductive current becomes negligible and the Butler-Volmer equation (equation 1-41) simplifies to:

$$\ln i = \ln i_0 + \frac{(1-\alpha)F}{RT}\eta$$

Equation 1-44

When the reductive process is driven by the overpotential the Butler-Volmer equation simplifies to:

$$\ln(-i) = \ln i_o - \frac{\alpha F}{RT}\eta$$

Equation 1-45

Tafel analysis allows α values to be calculated by plotting $\log_{10}$ i against E, with the slope = $\frac{-\alpha F}{2.3RT}$ for the oxidative process and $\frac{(1-\alpha)F}{2.3RT}$ for the reductive process.[7] By experimentally obtaining a value for α, which indicates the form of the transition state, the kinetics and mechanism of the electrode reaction can begin to be understood.

1.1.5.3 **Surface-Adsorbed Species Kinetics**

As outlined at the beginning of this section, one factor that affects the overall rate of reaction is the rate of adsorption or desorption of a species to the electrode surface. The rate of adsorption of a species onto an electrode surface is similar in behaviour to that of a general electrode reaction. When equilibrium is established between the bulk solution and the electrode surface, the amount of species adsorbed onto the surface is related to the concentration of the species at the electrode surface using an appropriate isotherm.

The adsorption isotherm describes the relationship between the amount of species, i, adsorbed on the surface (Γ_i), the activity of species i in bulk solution (a_i^b) and the electrical state of the system (E or q^m) all at a given temperature. The adsorption isotherm is obtained from considering the bulk (B) and adsorbed (A) species i at equilibrium when the electrochemical potentials are equal:

$$\overline{\mu}_i^{\,A} = \overline{\mu}_i^{\,B}$$

Equation 1-46

If $\overline{\mu}_i^{\,0}$ is the standard electrode potential, the standard free energy of adsorption, $\Delta\overline{G}_i^{\,0}$, is:

$$\Delta\overline{G}_i^{\,0} = \overline{\mu}_i^{\,0,A} - \overline{\mu}_i^{\,0,B}$$

Equation 1-47

If the Arrhenius equation is then used to describe the activity of the adsorbed species i, then:

$$a_i^{\,A} = a_i^{\,b} \exp\left(\frac{-\Delta\overline{G}_i^{\,0}}{RT}\right)$$

Equation 1-48

This equation forms the general adsorption isotherm.[2]

1.1.5.4 **Predicting Reaction Kinetics – Marcus Theory**

All the theories discussed above deal with the kinetics of electrode reactions in terms of rate constants and transfer coefficients. However, other factors such as molecular structure can affect the kinetics of the electron transfer process.

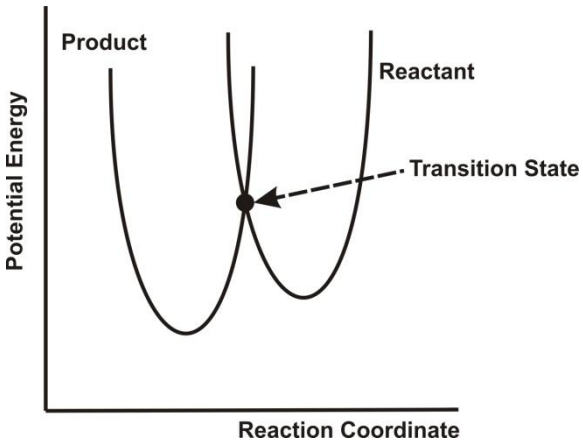

Figure 5: Potential energy plot with respect to reaction coordinate for an electron transfer

Marcus Theory of electron transfer reactions deals with the kinetics of the electron transfer in terms of the Franck-Condon Principle. Considering a general electron transfer reaction:

$$\boldsymbol{O_{(aq)} + e^{-}_{(aq)} \rightleftharpoons R_{(aq)}}$$

Equation 1-49

The electrons reach O by quantum mechanical tunnelling on a timescale of ~ 10^{-15} – 10^{-16} s.[1] The nuclear vibrations of R occur on a much larger time scale of 10^{-13} s. It therefore follows that the molecular shape of R, *i.e.* the bond angles and bond lengths, must be the same as that of O immediately before the electron transfer. A further consideration of Marcus theory recalls that there is no overall loss or gain of energy during electron transfer. Therefore the energy of the product R must be equal to the energies of the electron in the Fermi level of the metal and the energy of the reactant O. For an electron transfer to take place with both the constraint of the Franck-Condon principle and the energy restraints, both reactant O and product R must be in an excited state. The excited state of O represents the transition state, as this is when the geometries and O and R are the same. Hence; the transition state is seen as the activation of O into a geometry resembling O and R. Thus, the energy of the transition state will be higher if there is a large difference between the ground states of the reactants and the product. If the reactants and products are close in molecular geometry then the rate constant for the reaction, k_0, will be large corresponding to a low activation barrier for the reaction. Conversely, if the reactants and products are dissimilar in molecular geometry then k_0 is small and the activation energy of the reaction will be large.[7]

There are two types of reaction that can occur at an electrode: “outer-sphere” and “inner-sphere.” An inner-sphere reaction involves the specific adsorption of any of the

species involved in the overall electrode reaction to the electrode, *i.e.* there is a strong interaction with the electrode surface. In an outer-sphere reaction, the reactants and products remain a solvent layer distance from the electrode surface and no interaction is involved, with the reactant centre located in the outer Helmholtz plane.[1]

A further consideration in both understanding and predicting reaction kinetics lies in adiabatic and nonadiabatic effects, see figure 6.[7] When there is a strong interaction between the reactant, O, and the electrode there is a well-defined continuous curve connecting O with the product R. In this case there is strong coupling (compared with thermal energy) between the electrode and the reactant, leading to a high probability that the reaction system will progress into the valley corresponding to the products. This system is said to be adiabatic. If the interaction between the electrode and reactant is weak compared with thermal energy, the splitting between the energy curves at the point of intersection is small with respect to thermal energy in the system, and as the reaction reaches the transition state it has more of a tendency to remain on the reactant curve and the probability of crossover to reach R is small. This system is consequently nonadiabatic.[7]

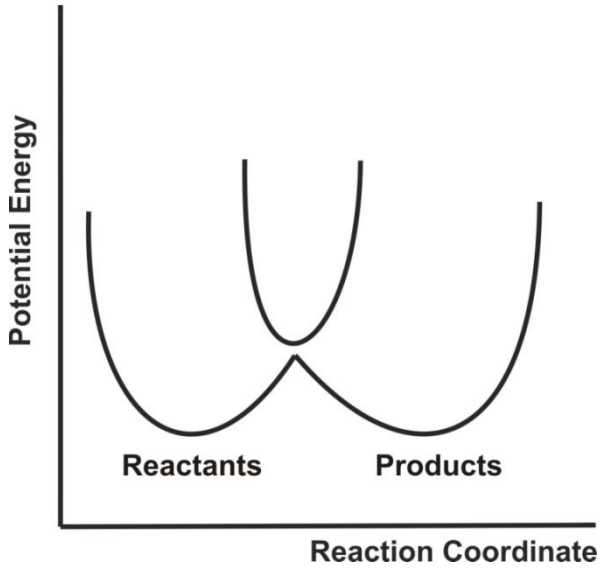

Figure 6: Adiabatic and non-adiabatic electron transfers

1.2 Voltammetric Techniques

Voltammetric techniques are used to investigate the mechanisms and kinetics of electron transfer reactions. The measurement of current flowing at a working electrode as a function of the potential applied to the cell provides a wealth of information which allows these kinetics and mechanism to be investigated.

1.2.1 Cyclic Voltammetry

Cyclic voltammetry is the more commonly used extension of linear sweep voltammetry, with both techniques belonging to a group of techniques called potential sweep methods. This is due to the general method of sweeping the potential from a value at which no electron transfer occurs to a value at which the electron transfer process is driven.[2] In the case of cyclic voltammetry, the potential is then swept back to the original potential driving the reverse process, shown in figure 7:

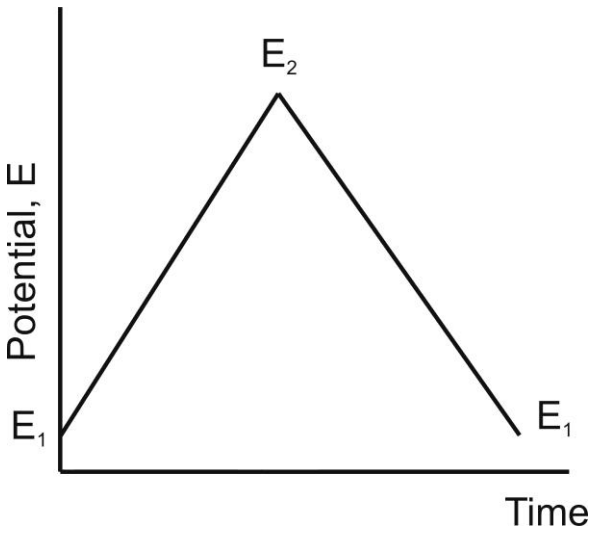

Figure 7: Potential sweeps in cyclic voltammetry

This then produces a current-potential plot, shown in figure 8:

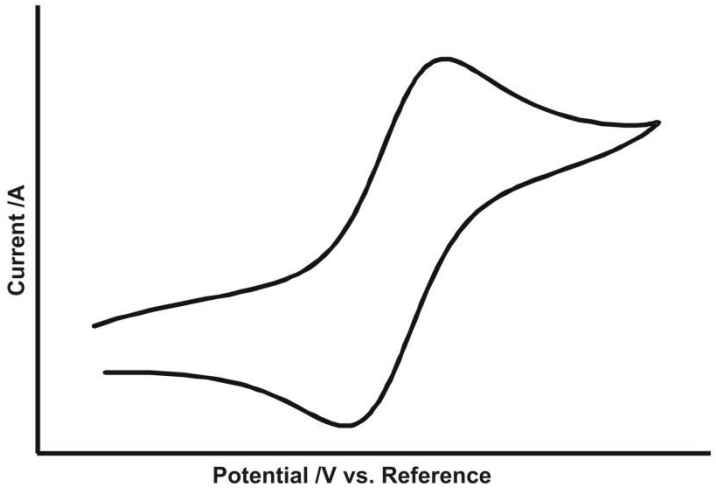

Figure 8: Example of a cyclic voltammogram

Considering a general electron transfer reaction:

$$O_{(aq)} + ne^-_{(m)} \underset{k_b}{\overset{k_f}{\rightleftharpoons}} R_{(aq)}$$

Equation 1-50

If the potential sweep starts at a value more positive than E^θ then only nonfaradaic currents flow until the potential starts to approach the E^θ value and the reduction process begins to be driven. At this point the current begins to flow and a peak begins to form. The voltammetry is conducted in stationary solution free from any stirring or vibrations and with the addition of excess supporting electrolyte, therefore the form of mass transport in use is diffusion. As the potential is swept to more negative values the concentration of O at the surface of the electrode begins to decrease as it is converted to R, hence the flux of O to the surface increases and the current flow increases. As the potential is driven past the E^θ value the concentration of O at the surface of the electrode decreases to almost zero, and the mass transfer, *i.e.* diffusion of O to the surface reaches a maximum rate. As the concentration of O at the electrode surface decreases, the flow of current decreases and hence a peak is formed.

If the potential scan is then reversed as is the case with cyclic voltammetry then the concentration of R at the surface of the electrode is very high. Therefore as the potential is swept back to more positive values and back towards the E^{θ} value, R is converted back to O in a similar manner to O being converted to R and the electron transfer is reversed. As the potential moves past the E^{θ} value all the R in the diffuse layer is reconverted back to O and the current drops back down to the background value.

The reversibility of the electron transfer affects the voltammogram. If the electron transfer is reversible then a certain amount of current flows prior to the E^{θ} value being approached, this is due to the thermodynamics of the reaction overtaking due to the rapid electron transfer kinetics associated with reversible reactions. In reversible systems the peak potential is found to be:

$$E_p = E_{1/2} - 1.109\frac{RT}{nF}$$

Equation 1-51

The peak current is given by (at 298 K):

$$i_p = \left(2.69\times10^5\right)n^{\frac{3}{2}}AD_O^{\frac{1}{2}}C_O\nu^{\frac{1}{2}}$$

Equation 1-52

where A is the area of the electrode, D_O is the diffusion coefficient, C_O is the concentration of O and ν is the scan rate. It is sometimes difficult to determine E_p if the peak itself is broad, therefore sometimes it is easier to determine $E_{p/2}$, which is also known as the half peak potential and is the potential at half the peak current, $i_{p/2}$. The half peak potential is given by:

$$E_{\frac{p}{2}} = E_{\frac{1}{2}} + 1.09\frac{RT}{nF}$$

Equation 1-53

Therefore:

$$\left| E_p - E_{\frac{p}{2}} \right| = 2.20\frac{RT}{nF}$$

Equation 1-54

So in reversible systems the peak potential is independent of the scan rate and the peak current is proportional to $\nu^{1/2}$, which in itself indicates that the electron process itself is under diffusional control.

If the electron transfer is irreversible then little or no current flows until the E^{θ} value is approached due to a much larger overpotential being required to drive the reduction and hence in irreversible systems the peak potential occurs at higher potentials, beyond the E^{θ} value. The peak potential is given by:

$$E_p = E^{\theta} - \frac{RT}{\alpha F}\left[0.780 + \ln\left(\frac{D_O^{\frac{1}{2}}}{k^0} \right) + \ln\left(\frac{\alpha F \nu}{RT} \right)^{\frac{1}{2}} \right]$$

Equation 1-55

The peak current is given by (at 298 K):

$$i_p = \left(2.99 \times 10^5\right) \alpha^{\frac{1}{2}} n\sqrt{n} A C_O D_O^{\frac{1}{2}} \nu^{\frac{1}{2}}$$

Equation 1-56

If $E_{p/2}$ is the potential at which the current is half the peak value, then:

$$\left| E_p - E_{\frac{p}{2}} \right| = \frac{1.857RT}{\alpha F}$$

Equation 1-57

Therefore for a completely irreversible system the peak potential is not independent of the scan rate as it is in the reversible systems, instead it is a function of the scan rate, shifting by 30 mV at 25^0C (or 1.15RT/αF) for each tenfold increase in the scan rate. It is also possible to obtain values for k^0 from the cyclic voltammetry of irreversible systems by expressing the peak current, i_p, in terms of the peak potential, E_p:

$$i_p = 0.227FAC_O k^0 \exp\left[\left(\frac{-\alpha F}{RT}\right)\left(E_p - E^\theta\right)\right]$$

Equation 1-58

And hence by plotting ln i_p against E_p - E^θ at different scan rates, the gradient of the slope should be equal to $\frac{-\alpha F}{RT}$ and the intercept should be proportional to k^0.

In both the reversible and irreversible systems the peak current, i_p, increases with increasing concentration of the reactant species and increasing scan rate. The increase in current with increasing scan rate is simple to rationalize by considering that the greater the concentration of O, the higher the concentration of O within the diffuse layer and hence the greater the conversion of O to R. The increase in i_p with increasing scan rate is explained by referring back to Fick's first law (see equation 1-14).

If it is considered that the i_p shows the flux of material reacting at the electrode surface and that near the peak potential this is controlled by the diffusion of the reactant species to the electrode. Fick's first law shows that the peak current represents the concentration gradient of O near to the electrode surface, which in turn is controlled by the diffusion layer thickness. At faster scan rates when the potential is swept from the initial potential

to the final potential more rapidly, less time is available for the electron transfer and the depletion of O at the electrode surface is reduced. This results in a thinner diffusion layer and therefore a steeper concentration gradient. As the concentration gradient increases, the flux of O to the electrode surface increases, hence a larger peak current.

In cyclic voltammetry the magnitude and peak potential of the reverse sweep can be used to determine the reversibility of the electron transfer process taking place. The separation of the peak potentials, $E_{pa} - E_{pc}$ is an important parameter in cyclic voltammetry and can be used to determine the reversibility of the reaction. For a reaction with reversible electron transfer kinetics the peak potential separation is given by:

$$E_{pa} - E_{pc} = 2.218\frac{RT}{nF}$$

Equation 1-59

At 25^{o}C this is approximately 56/n mV (where n is the number of electrons) and is independent of scan rate. A second important parameter in reversible systems is the ratio of the peak currents, i_{pa}/i_{pc}. In reversible systems this ratio is one, again independent of scan rate. Any deviation from unity for this ratio is indicative of homogenous kinetics or other complications in the electrode reaction process, for example adsorption of material onto the electrode surface.

In an irreversible system, the presence of a reverse peak is dependent on the scan rate, and again a large overpotential is required to drive the reverse electron transfer so the peak to peak separation ($E_{pa} - E_{pc}$) is dependent on how irreversible the system is. The i_{pa}/i_{pc} ratio is dependent on scan rate, and these differences with the reversible system can be diagnostic of the electrode kinetics occurring.

These two cases of reversible and irreversible electron transfer kinetics refer to the two extremes in electron transfer according to how fast the electrode kinetics are in relation to the mass transport conditions. There are of course systems which are neither extreme and have intermediate kinetics where the surface concentrations of O and R depend on both the scan rate and the mass transport of material to the surface. These cases are termed "quasi-reversible" and a peak is observed on the reverse potential sweep, however the peak to peak separation is dependent upon scan rate and the peak current is not proportional to the square root of the scan rate as is the case with the reversible systems. The magnitude of the peak on the reverse scan is however dependant on the scan rate, a small peak will be observed unless the potential is swept very quickly. A high potential is still required to drive the reverse electron transfer, if the scan rate is too slow nearly all of the product R formed in the forward scan will diffuse back into the bulk solution and none will remain at the electrode surface to carry out the reverse process, slower still will introduce natural convection.

The shape of the forward peak and the parameters of the peak were shown (Matsuda and Ayabe) to be functions of the transfer coefficient α and a further parameter, Λ which is defined as:

$$\Lambda = \frac{k^0}{\left(D_O^{1-\alpha} D_R^{\alpha} \nu \frac{F}{RT} \right)^{\frac{1}{2}}}$$

Equation 1-60

When the diffusion coefficients for O and R are equal ($D_O = D_R = D$), the equation is simplified to:

$$\Lambda = \frac{k^0}{\left(D\nu\frac{F}{RT}\right)^{\frac{1}{2}}}$$

Equation 1-61

The current is then given by:

$$i = nFAD_O^{\frac{1}{2}}C_O\left(\frac{F}{RT}\right)^{\frac{1}{2}}\nu^{\frac{1}{2}}\psi(E)$$

Equation 1-62

Where Ψ (E) is the quasi-reversible current function and varies with values of α and hence Λ.[2]

Cyclic voltammetry is a very useful technique, the main strength being the ability to attain and interpret qualitative and semi-quantitative behaviour. From this reaction mechanisms can begin to be understood.

1.2.2 Square Wave Voltammetry

Square wave voltammetry belongs to a group of voltammetric techniques termed pulse voltammetry which were developed from traditional polarographic methods. Square wave voltammetry combines the best aspects of a number of earlier pulse voltammetry techniques.

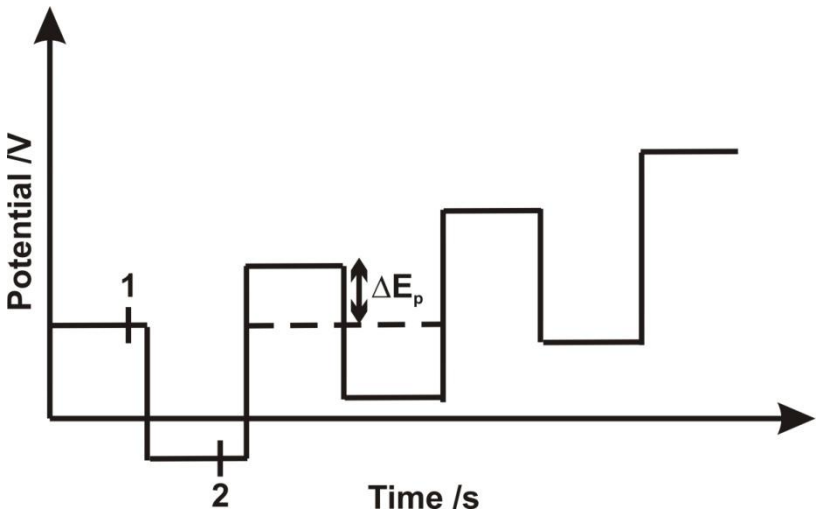

Figure 9: Waveshape of square wave voltammetry. Current is measured at positions 1 and 2.

Figure 9 shows the waveform and measurement scheme in square wave voltammetry. The waveform consists of a staircase scan superimposed by a symmetrical pulse both in the forward and reverse direction.[7]

There are a number of important parameters in square wave voltammetry, firstly the square wave itself is characterised by the pulse height, ΔE_p which itself is derived from the staircase tread and the peak width, t_p. The pulse width is also described in terms of a frequency, f:

$$f = \frac{1}{2} t_p$$

Equation 1-63

The staircase potential is stepped higher with each cycle (ΔEs) and this together with the frequency (f) is then used to define the scan rate, ν:

$$\nu = f \Delta E_s$$

Equation 1-64

Overall, t_p is the timescale for the experiment, while ΔE_s fixes the data points along the potential axis, therefore together they define the time required for the full scan to be completed.

The current is measured in two places in each cycle, once on the forward current , i_f, (position 1) and once in the reverse current, i_r, (position 2) as shown in figure 9. The forward current sample is taken at the end of the first pulse of each cycle and the reverse current is taken at the end of the second pulse for each cycle. The difference in current, Δi, is then determined as $i_f - i_r$. All three of these parameter are preserved and so the resulting voltammogram contains three voltammograms, the forward, reverse and difference currents plotted against the potential.[2] All three currents have useful properties, however the voltammogram usually presented is the difference current, shown in figure 10.

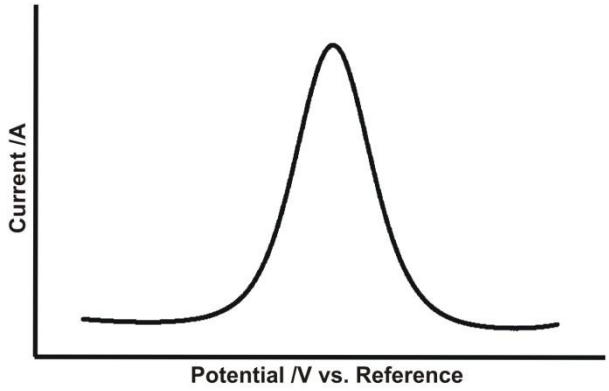

Figure 10: Example of square wave voltammetry

Due to the preservation of all three currents, square wave voltammetry has a very high information content and has the power to study electrode processes over a large potential range and in a reasonable time span. Square wave voltammetry has a number of advantages over cyclic voltammetry, the main strength being that it can analyse electrode processes at a much lower concentration than cyclic voltammetry due to its

ability to suppress the background. This suppression of the background arises from the lack of a charging current and hence there are no faradaic background processes contributing to the background current. Also, due to this suppression of the background signal, there is much less distortion of the signal due to the background.[2] There is also no need to remove oxygen through degassing since oxygen is not generally seen in square wave voltammetry.[8]

1.2.3 Potential Step Chronoamperometry

In potential step chronoamperometry, the potential is stepped from an initial value where no redox process occurs (E_1) to a value at which the reduction or oxidation is driven (E_2). The current flowing as a result of this potential step is monitored as a function of time.

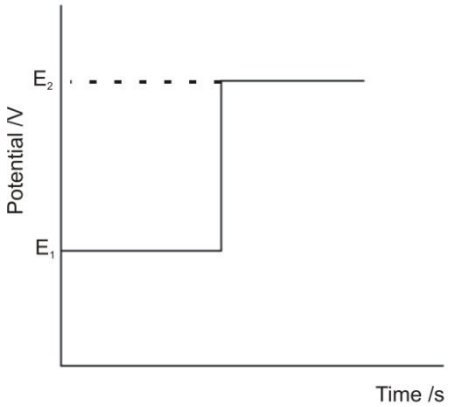

Figure 11: Figure showing potential waveform in potential step chronoamperometry

If a general redox reaction is considered:

$$\boldsymbol{O}_{(aq)} + \boldsymbol{e}^{-}_{(aq)} \rightleftharpoons \boldsymbol{R}_{(aq)}$$

Equation 1-65

Immediately following the step in potential, a large current flows due to the reduction of O to form R. As O is continually converted to R, the concentration gradient increases,

causing a flux of O to the electrode surface and hence a large current to flow. However, with a continuous flux of O to the surface, the thickness of the diffusion layer increases, decreasing the concentration gradient and therefore the current decreases steadily with time to a limiting point.

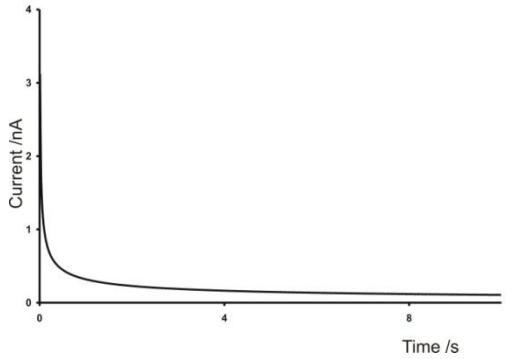

Figure 12: Current flow vs. time in potential step chronoamperometry

The current time response is given by the Cottrell equation:

$$i(t) = \frac{nFAD_O^{\frac{1}{2}}C_O}{\pi^{\frac{1}{2}}t^{\frac{1}{2}}}$$

Equation 1-66

As can be seen from the equation, potential step chronoamperometric experiments can be used to determine diffusion coefficients. The equation also shows that as the concentration of the electroactive species (C_O) at the electrode surface decreases, the $t^{1/2}$ function becomes an inverse function, and this is indicative that the rate at which the redox process occurs is under diffusion control.

1.2.4 Rotating Disc Electrode (RDE) Voltammetry

A rotating disc electrode is an example of a hydrodynamic electrode, which is defined as an electrode which introduces forced convection into the electrochemical system so that this is the dominant form of mass transport. Hydrodynamic methods achieve

steady-state conditions very quickly, which allows the capacitance measurement to be disregarded. The rate of mass transfer, which has previously been discussed as a very important parameter, is often larger in hydrodynamic methods. This is due to the rates of mass transfer at the electrode surface being larger than the rates of diffusion alone, which allows the kinetics of the overall electrode reaction to be further studied.

Rotating disc electrodes are a very common example of a hydrodynamic electrode which is easy to use and to prepare. The electrode is placed in solution and rotated at a constant speed in order to induce convective flow. This rotation spins the bulk solution out from the electrode surface and this in turn draws fresh solution up to the electrode surface hence a constant flow of electroactive material is supplied to the electrode surface.[8]

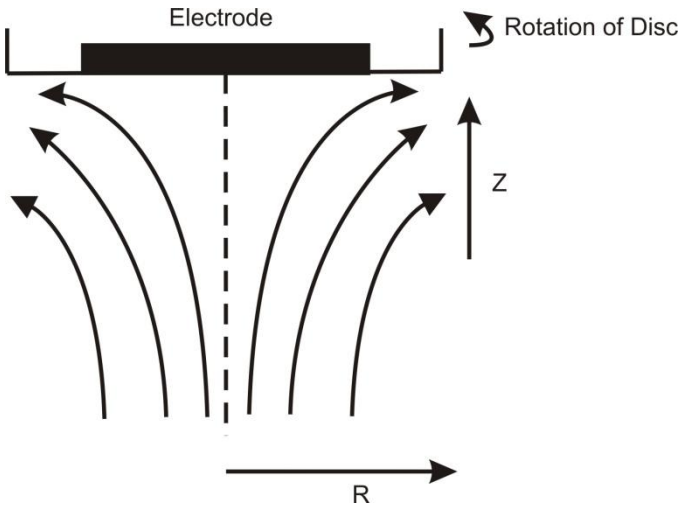

Figure 13: Laminar flow at a rotating disc

Flow regimes in fluidic systems are determined using a quantity known as the Reynolds number. This number is a ratio of the inertial forces to viscous forces and can therefore be used to determine the flow regime in a given system. In RDE experiments, the Reynolds number (Re) is given by:

$$R_e = \frac{\omega r_e^2}{\nu}$$

Equation 1-67

where ω is the rotation speed of the electrode (Hz), r_e is the electrode radius and ν is the viscosity of the solution. The flow to the electrode remains laminar as long as the Reynolds number does not exceed about 1 x 10^5 (depending on geometry).[1]

The flow of material normal to the electrode (z-direction) is quantified using the following equation:

$$\nu_z \approx -0.510\omega^{\frac{3}{2}}\nu^{\frac{1}{2}}D^{-\frac{1}{3}}z^2$$

Equation 1-68

where ω is the rotation speed (Hz), v is the viscosity, D is the diffusion coefficient and z is the distance from the electrode surface.

As the voltammetry is carried out at steady state, a sigmoidal curve is obtained, the limiting current of which is determined using the Levich equation,[9] which predicts the variation of the limiting current with changes in rotation speed:

$$i_{\lim} = 0.62nFA[B]_{bulk}D_B^{\frac{2}{3}}\nu^{-\frac{1}{6}}\omega^{\frac{1}{2}}$$

Equation 1-69

Using the Levich equation, it can be seen that a plot of i_{lim} vs. $\omega^{1/2}$ should yield a straight line through the origin, any deviation from this is indicative that there is a kinetic limitation at some point in the electron transfer reaction.

1.2.5 Voltammetry at Microelectrodes

Microelectrodes have by definition at least one dimension in the micrometre range, typically they possess dimensions of 25 µm or lower. The essential concept of microelectrodes is that the electrode itself is smaller than the scale of the diffusion layer of the experiment so that convergent diffusion ("edge effects") plays an important role.

The mass transport of electroactive material to the surface of microelectrodes is different to that of macroelectrodes, as shown in figure 14.

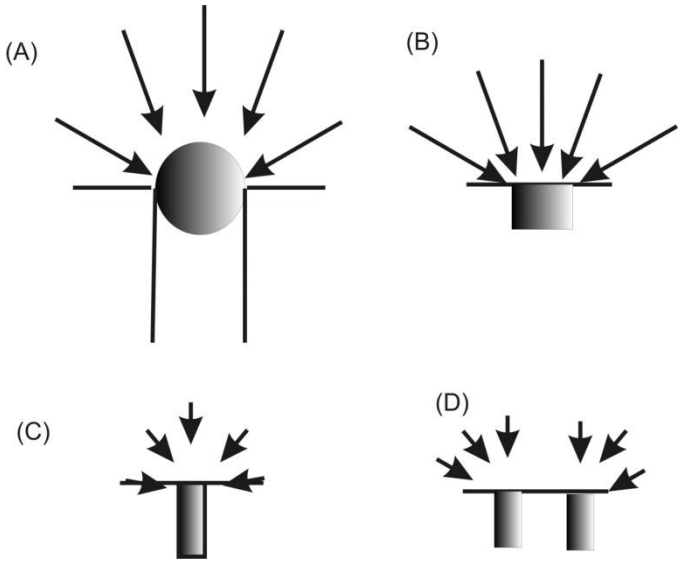

Figure 14: Diffusion at microelectrodes: (A) hemispherical, (B) disc, (C) band, (D) ring

As can be seen from the figure there are typically four different types of microelectrodes. The most common type is the disk microelectrode, the critical dimension of which is the radius of the electrode surface which should be less than 25 µm, with some having been made with a radius of 0.1 µm. The theory surrounding disk microelectrodes is significantly complicated by the diffusion of electroactive material to the electrode surface in two dimensions as shown in figure 14. Due to this, the current density is not consistent over the surface of the disk, with greater current density at the edge. Hemispherical microelectrodes behave in a similar manner to disk electrodes, with the critical dimension being the radius of the curvature, r_0. Band microelectrodes

differ from disk and hemispherical microelectrodes, with the critical dimension being the width. Band microelectrodes can produce a larger current as the geometric area of the band is varies with the width (the critical dimension) rather than the square of the critical dimension.

The current measured at an electrode is a function of the electrode area, as shown by equation 1-7, therefore the current induced at a microelectrode is much smaller than that at a macroelectrode. This in turn causes less electrolysis to be carried out and hence the diffusion layer thickness is much less than that involved with larger electrodes. Due to the smaller diffusion layer, the concentration gradient across the diffusion layer will be much higher and hence a there will be greater flux of electroactive material to the electrode surface. When the mass transport of material is slower than the actual electrochemical process then the voltammetry simply reflects the rate of diffusion in solution. When using microelectrodes this limitation is less likely due to the increased rate of mass transport, and hence rapid electron transfer reactions and fast chemical steps involved in the overall electron transfer reactions can be investigated using electrochemical methods. A further advantage of a smaller current flowing at microelectrodes arises from the charging current that follows changing the potential of the electrode. When this occurs it changes the ionic distribution of the electrolyte near to the electrode surface and this causes a charging current which can conceal or distort the signal of interest. As microelectrodes have a much smaller area this charging current is extensively decreased and hence the voltammetry suffers much less distortion and the potential can be swept at a much faster rate.[1,7]

Steady state currents can be obtained within a short time due to the advantages already described, with the limiting current given by:

$$i = 4nFDCr_o$$

Equation 1-70

The shape of the wave is given by:

$$E = E^0 + \frac{RT}{nF}\ln\frac{D_R}{D_O} + \frac{RT}{nF}\ln\left(\frac{i_d - i}{i}\right)$$

Equation 1-71

Where E^0 is the standard potential of the redox couple, $D_{R,O}$ the respective diffusion coefficients, i_d the diffusion limited current and i the overall current. The half-wave potential is then given by:

$$E_{\frac{1}{2}} = E^0 + \frac{RT}{nF}\ln\frac{D_R}{D_O}$$

Equation 1-72

1.2.5.1 **Reaction Mechanisms in Electron Transfer Reactions**

There are many variations of electron transfer reaction mechanisms possible, although they can be generally split into two groups: reactions with one electron transfer step and reactions with two or more electron transfer steps. Testa and Reinmuth[10] developed the notation for electrolysis mechanisms, with a heterogeneous electron transfer step designated as E and a homogeneous chemical reaction step designated as C.

1.2.5.2 **Reactions with one electron transfer step**

There are three types of electrochemical reactions that involve only one electron transfer step; EC reactions, CE reactions and catalytic EC' reactions.

(a) EC Reactions

These reactions involve an electron transfer reaction in which the product formed is not electroactive at the potential at which it was formed and undergoes some form of chemical reaction, for example the oxidation of octacyanomolybdate(IV).[11]

$$\boldsymbol{O + ne^{-} \rightleftharpoons R}$$

$$\boldsymbol{R \rightleftharpoons X}$$

Equation 1-73

This is quite a common reaction mechanism, as many electroactive species form a reactive substance once oxidised or reduced. The rate at which R is converted to X is lost and the rate at which this occurs affects the voltammetry observed. If the rate of conversion is very fast then as soon as R is formed it is converted to X which in terms of the voltammetry means that no reverse process can be carried out and the voltammogram appears irreversible. If the rate of conversion is slow however enough R is present at the electrode surface in order for the re-oxidation back to O and a reversible voltammogram is observed. This type of reaction mechanism is not limited to only one chemical reaction step, as a second reaction can follow, for example ECC reactions, or the chemical reaction product can rearrange due to bond weakening.

(b) CE Reactions

In this case a chemical reaction precedes the electron transfer, producing an electroactive product that then undergoes electrolysis at the electrode surface.

$$\boldsymbol{Y \rightleftharpoons O}$$

$$\boldsymbol{O + ne^{-} \rightleftharpoons R}$$

Equation 1-74

Due to the production of the electroactive species prior to the electron transfer, the kinetics of the overall reaction may in some cases govern the current induced during the electron transfer. An example of this type of reaction is the reduction of formaldehyde in aqueous solutions.[12]

(c) Catalytic EC' Reactions

These reactions involve the regeneration of the starting material, O, by reaction of the electrolysis product R with a non-electroactive species.

$$\boldsymbol{O + ne^{-} \rightleftharpoons R}$$

$$\boldsymbol{R + Z \rightleftharpoons O + X}$$

Equation 1-75

An example of an EC' reaction is the oxidation of thiols[2] mediated by $Fe(CN)_6^{3-}$.

1.2.5.3 Reactions with two or more electron transfer steps

There are a number of examples of multiple electron transfer reactions, the simplest of which is the EE reaction.

(a) EE Reactions

The EE reaction can occur in two ways, either in one single step involving a multi-electron transfer or in stepwise one electron oxidations or reductions.

$$A + e^- \rightleftharpoons B$$

$$B + e^- \rightleftharpoons C$$

Equation 1-76

When there is a significant structural change to form the final product following both electron transfers, then the process may become thermodynamically favourable and a multi-electron response is observed and only one peak is observed. However, if the electroactive species formed by the first electron transfer is harder to oxidise/reduce than the initial oxidation/reduction then the electron transfers will occur in a stepwise manner.

(b) ECE Reaction

The ECE reaction is simply an extension of the EC reaction.

$$A + e^- \rightleftharpoons B$$

$$B \rightarrow C$$

$$C + e^- \rightleftharpoons D$$

Equation 1-77

An example of this is the reduction of bromonitrobenzene.[13] The first two steps are identical to that of the EC reaction, however the product formed in the homogeneous chemical reaction is now electroactive and undergoes further electron transfer. This second electron transfer can either take place in bulk solution, which is then termed a DISP mechanism, or it can occur at the electrode surface, however it is difficult to ascertain between the two.

(c) $\vec{E}C\overleftarrow{E}$ Reaction

This is similar to the ECE reaction, however the product formed in the chemical reaction step is oxidised at the potential at which the initial reactant is reduced.

$$\boldsymbol{A + e^- \rightleftharpoons A^-}$$

$$\boldsymbol{A^- \longrightarrow B^-}$$

$$\boldsymbol{B^- - e^- \rightleftharpoons B}$$

Equation 1-78

For example, the reduction of $Cr(CN)_6^{3-}$ in sodium hydroxide.[2] The overall reaction involves no net transfer of electrons and the reaction is simply $A \rightarrow B$.

(d) Square Reaction Schemes

In these reactions all the substances involved are electroactive and an equilibrium exists between each component. An example of this kind of reaction is the redox chemistry of quinones.[14] This mechanism often occurs when there is a structural change following the electron transfer and can be complicated further by combining squares to form meshes.[2]

The reaction mechanisms outlined are the general electrode reactions that can occur. Each of them can be extended and varied further to fully describe electron transfer reactions taking place.

2 Experimental

2.1 Instrumentation

The electrochemical measurements were recorded using an Autolab PGSTAT30 potentiostat controlled by a Pentium IV processor computer. In all cases, unless otherwise stated, a three electrode system was employed, with a platinum wire wound into a spiral serving as the counter electrode, and a standard calomel electrode as the reference electrode in aqueous systems whereas in non-aqueous systems either a silver/silver chloride or a silver wire were utilised as the reference electrode (see individual chapters). The working electrodes (for specifics, see individual chapters) were polished prior to voltammetry being undertaken using decreasing grades of carburundum paper (400, 1200 2400 grade, Presi, France) followed by polishing on a cloth using 3 μm alumina paste (Presi, France).

2.1.1 Microelectrodes

All microelectrodes were polished prior to use using a fine grade of carborundum paper (2400) and finally alumina paste (0.3 μM). Each microelectrode was electrochemically calibrated prior to use in order to obtain an accurate measurement of the electrode radius. This was achieved using solutions of containing various concentrations of either ferricyanide or ferrocene depending on the system in use and using the following equation:

$$i = 4nFDCr_o$$

The diffusion coefficient, D, was taken to be 0.76 x 10^{-5} cm^2 s^{-1} for ferricyanide in aqueous 0.1 M KCl[15] and 2.3 x 10^{-5} cm^2 s^{-1} for ferrocene in 0.1 M tetra-*n*-butylammonium perchlorate (TBAP) and acetonitrile.[16]

2.1.2 Rotating Disc Electrode

Rotating disc analysis was undertaken using Metrohm rotating disc apparatus, (Metrohm 628-10) with rotation speeds of 170 rpm to 900 rpm, with a three electrode system employed as outlined earlier. Ferrocene in acetonitrile and TBAP (0.1 M) was used to calibrate the rotation speeds using the Levich equation (see equation 1-69).

2.1.3 UV-Visible Spectrometry

UV-visible spectrometry was undertaken using an Agilent 8453E UV-visible spectrometry system (Agilent Technologies, Germany), with a clear glass cuvette of path length 1 cm. The spectrometer was controlled using UV-vis chemstation software.

2.2 Reagents

All reagents were prepared using Analytical Grade chemicals, and all aqueous solutions were made up using deionised water from an Elgstat water system with a resistivity of not less than 18 MΩ cm. Any solvents used were of HPLC grade, and used without further purification. All solutions were purged with impurity free nitrogen prior to voltammetry, whilst the experiments themselves were conducted under a nitrogen atmosphere.

3 Nitric Oxide: Roles, Generation and Sensing

3.1 The Roles of Nitric Oxide

Nitric oxide is present both in the atmosphere and in biological systems, playing paradoxical roles in each. Within biological pathways the roles are many and diverse, with a plethora of research undertaken discovering these roles since the discovery of its biological relevance in 1987 by Palmer and his co-workers.[17] A further aspect of nitric oxide lies in its environmental impact, release into the atmosphere believing to have a negative effect on the ozone layer increasing the risk of global warming, an issue at the forefront of world politics at the present time.

$$NO + O_3 \rightarrow NO_2 + O_2 + light$$

Scheme 3-1

Nitric oxide is a colourless gas at room temperature, with a low boiling and melting point; -151.7 ^{o}C and -163.6^{o}C respectively.[18] It is a small molecule which is also a free radical, properties which lend themselves well to either its biological roles or its ability to pollute the atmosphere. As a free radical, released into the air via car exhausts, it is then partially oxidised in the air to form nitrogen dioxide which, together with other oxides of nitrogen, can cause photochemical smogs.[19] Further, nitric oxide reacts with the ozone layer causing depletion and therefore directly influencing global warming. Contrary to the toxic effects nitric oxide has outside of biological systems, within the body it is of critical importance in a number of the major systems and pathways, including the cardiovascular, immune and central nervous systems. It is in this area that the majority of research concerning the importance of nitric oxide is based.

In biological systems, nitric oxide can, in general, be seen as a physiological messenger. Independent of the role it is performing, it is certain to be acting as an emissary to initiate a further response. As previously mentioned, nitric oxide is influential in the cardiovascular, immune and central nervous systems. In 1987 it was discovered that the agent, commonly referred to as the endothelial-derived relaxation factor, released by endothelial cells to relax vascular smooth muscle was nitric oxide.[17] Nitric oxide is continuously released from endothelial cells in small amounts, producing a basal level of vascular smooth muscle relaxation.[20] The endothelial cells are surrounded by smooth muscle tissue, when nitric oxide is released it signals to this tissue to relax, thus dilating the blood vessel and increasing blood flow. Nitric oxide is therefore of critical importance in the mediation of vasorelaxation in blood cells, hence regulating vessel tone, haemostasis and blood pressure.[21]

Nitric oxide is toxic to a number of pathogens,[22-24] cytotoxic to tumours cells and may also inhibit viral replication.[20] It is this non-specificity that makes nitric oxide such a prolific agent within the immune system, and also the property that makes it so unique within the immune response with most other antibodies and lymphocytes specific to a particular antigen or pathogen. Despite this seemingly non-specificity, nitric oxide is believed to be of particular importance in the defence against intracellular pathogens.[25] However, nitric oxide produced during the immune response can cause complications due to the roles it also undertakes in the cardiovascular system. The massive presence of nitric oxide in the immune response can also lead to the dilation of the blood vessels, causing hypotension thereby leading to septic shock.

The physical properties of nitric oxide allow it to be of pivotal importance as a neurotransmitter within the central nervous system and also the peripheral nervous system.[19,20] Being a small molecule, nitric oxide can diffuse unrestricted throughout the

system. The majority of neurotransmitters can only transfer information from a pre-synaptic to a post-synaptic neuron; however nitric oxide can diffuse and act upon a number of nearby neurons, including those not connected by a synapse.

3.2 Biological Generation of Nitric Oxide

Nitric oxide is generated by a number of pathways within the human body. Following the discovery that nitric oxide was indeed the endothelium-derived relaxation factor, it was then shown in 1988[26] that nitric oxide is biosynthesised via the enzyme catalysed reaction of L-arginine with nicotine adenine dinucleotide phosphate (NADPH). The enzyme catalysing the reaction is nitric oxide synthase (NOS), of which there are three forms: neuronal NOS (also known as nNOS or NOS I), inducible NOS (iNOS or NOS II) and endothelial or constitutive NOS (eNOS or NOS III).[27] Each form is synthesised in a specific part of the body in order to execute a specific task. Neuronal NOS is located in neuronal tissue for use within the central nervous system, consequently generating nitric oxide as a neurotransmitter. This form of the NO synthase generates nitric oxide at low levels when stimulated. Inducible NOS is located within the immune system, generating nitric oxide as part of the human immune response. Endothelial NOS is located as expected within endothelial cells generating nitric oxide in response to a stimulus in order to regulate and mediate blood flow and blood pressure. Endothelial NOS generates nitric oxide in the largest quantity of all the enzymes, at a flux rate of 1.67 pmol cm^{-2} s^{-1}.[28] This is due to, as described before, the continuous, low level production of nitric oxide from endothelial cells. The stimulus in this case comes from every single heart beat, the pulsating action of the heart causing a pulsing flow of blood through vessels and hence stimulating the endothelial NOS.[29]

3.3 Chemical Generation of Nitric Oxide

Nitric oxide is produced on a large scale in industry *via* the production of ammonia by catalytic oxidation. In the laboratory nitric oxide can easily be afforded by the reduction of nitric or nitrous acid.[19] A great deal of research has also been undertaken into developing compounds which release nitric oxide, such compounds are referred to as NO donors and have further vital uses within medicinal chemistry and also advancing research into the uses and generation of nitric oxide within biological systems.

This is a large branch of nitric oxide research attracting an extensive amount of work. NO donors have been developed since the 1980s with fifteen classes and numerous compounds now recognised. Some compounds within each class are extremely sensitive to components such as light or heat and will spontaneously decompose under these conditions to release nitric oxide. N-nitrosamines are such an example; decomposing under physical conditions to release nitric oxide. A particular example within this class is cupferron, which is stable at room temperature; however nitric oxide release can simply be induced *via* thermal or photochemical decomposition.[30] A further example lies in the well-established and commercially available NOR-3, belonging to the class of NO-donors known as oximes.

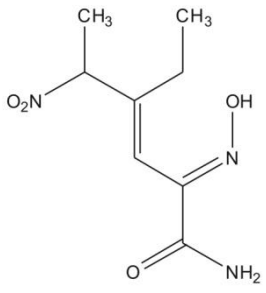

Figure 15: NOR-3

At room temperature and physiological pH, NOR-3 will decompose releasing nitric oxide with a half-life of approximately 45 minutes.[30] Other compounds require slightly more

vigorous conditions to initiate the release of nitric oxide, for example a chemical reaction, as in the case of organic nitrites which release nitric oxide via hydrolysis and trans-nitrosation.[30] Further, many classes of compound undergo chemical reaction with thiols which induce reduction or trans-nitrosation,[30] indeed thiols are an important component in a range of NO donors and are applicable to a range of classes of NO-donor, with thiols initiating nitric oxide release in a number of ways, see for example scheme 3-2.

$$Fe_2S_2(NO)_4^{2-} \xrightarrow{h\upsilon} Fe_2S_2(NO)_3^{2-} + NO$$

Scheme 3-2: Example of thiol initiated NO release

In most cases the thiol induces a reduction, for example in the case of organic nitrites the reaction with a thiol generates a one electron reduction yielding nitric oxide. In the case of furoxans, the reaction with a thiol leads to a ring-opening reaction with NO cleavage.[31] It can therefore be seen that thiols have a decisive role in NO-donor chemistry. Enzyme-catalyzed reactions also serve to release nitric oxide from a number of these compounds, the main enzyme employed being horse-radish peroxidase (HRP).[30,32] The popularity of HRP arises from the accessibility of the active site, allowing a number of different compounds to act as electron donors or acceptors.

Perhaps the simplest and cleanest method for nitric oxide generation, with minimal reagent requirements and the simple use of electrodes, involves electrochemical reaction using either oxidation or reduction depending on the compound involved. For example N-nitroso-N-oxybenzeneamine ammonium salts have been shown to release nitric oxide upon electrochemical oxidation, with Lawless and Hawley first demonstrating the release of nitric oxide from cupferron (N-nitroso-phenylhydroxyl-amine) in 1968.[33] In subsequent years and in 1999 this work was advanced further, investigating a range of N-nitroso-N-

oxybenzeneamine ammonium salts based on cupferron with *para*-substituted derivatives, exploring the effect of electron donating and electron withdrawing components.[34] The amount of nitric oxide generated by the donors was measured using a commercially available electrochemical sensor (WPI instruments) with fluxes of nitric oxide generated in the µM range, demonstrating the ease at which these nitric oxide donors can be developed using electrochemical methods. In contrast to this oxidative mechanism, S-nitrosothiols have been shown to release nitric oxide via electrochemical reduction, once again generating nitric oxide in the µM range using a simple three-electrode set-up.[35] In this mechanism, it is the nitric oxide radical that is formed, and this in itself forms the challenge presented with electrochemical nitric oxide donors: the formation of NO^+ or NO. N'-hydroxyguanidine derivatives have also been proven as electrochemical nitric oxide donor, albeit through a more complicated mechanism via two one electrode oxidations and deprotonation steps, yielding $^{\bullet}NO$.

Research has progressed to modified electrodes releasing nitric oxide in a quantitative manner. Self assembled monolayers (SAMs) have been utilised in the development of nitric oxide donors with Wang *et. al.*[36] employing SAM-modified gold electrodes to generate quantitative nitric oxide in the nano-molar range. This was achieved by attaching a thiol group in the *para* position of a cupferron ammonium salt and forming the SAM modified electrode, releasing the NO radical in a stepwise manner following a one electron oxidation.

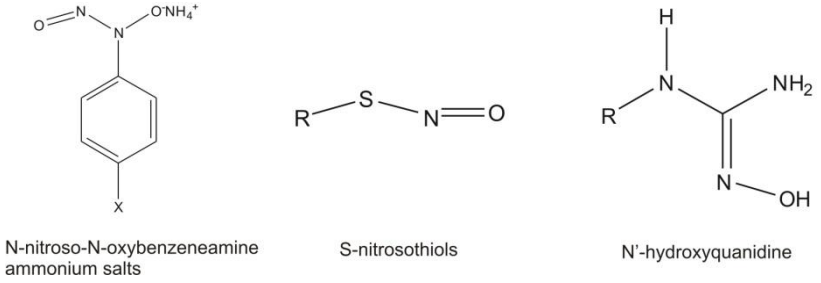

Scheme 3-3: Examples of electrochemical NO donors

Due to the seemingly ceaseless roles of nitric oxide and hence its presence expansively throughout the body, the challenge presented to further NO donor research lies in developing donors that can effect only one application within the body.

It has been shown that nitric oxide has been a major part of both biological and chemical research over the past two decades, with pivotal roles in vascular regulation, neuronal communication and as a cytotoxic agent in the immune system, together with the devastating effect it is having on the environment. When the pathways generating nitric oxide fail, or indeed over-produce nitric oxide, or atmospheric monitoring of nitric oxide is required, sensor systems need to be in place that are sufficiently sensitive to detect nitric oxide at the appropriate levels.

3.4 Nitric Oxide Sensors

Nitric oxide has a number of properties that impact the methodology employed to detect the substance in a variety of matrices. The molecule is extremely reactive, and in environments such as those provided in biological samples species such as oxygen are always present which will interfere and react with the free nitric oxide. Hence the lifetime of nitric oxide is very short, with a half-life of approximately 5 - 15 seconds[37], meaning the distance between the sensor and the source of the nitric oxide must be as small as possible. Other properties of an ideal sensor are those common to most types of analytical sensor; fast response time, reproducible, easy to use, suitable selectivity and sensitivity. Different forms of nitric oxide synthase generate nitric oxide in different concentration ranges and over varying time frames, for example constitutive NOS rapidly produces NO in the femto to nano molar range whereas inducible NOS slowly releases a constant flow of nitric oxide at higher concentrations.[38]

Aside from electrochemical techniques a number of analytical techniques have been employed namely chemiluminescence, colorimetry, electron spin resonance spectroscopy (ESR) and fluorometry. Each has advantages, however the main disadvantage of each lies in the inability of the techniques to be used *in vivo*, and they all detect nitric oxide indirectly via nitrite, nitrate or other secondary products. The chemiluminescence technique is based upon the reaction of nitric oxide with ozone, affording nitrogen dioxide in the excited state which subsequently emits light at wavelengths greater than 600 nm[39] when relaxing down to the ground state. The main disadvantage of using chemiluminescence in biological systems is the restriction of the analyte being in the gas phase, in these systems nitric oxide will be in liquid form thus removing the nitric oxide from solution into the gas phase compromises the sensitivity of the technique.

Nitric oxide reacts with amine groups to form triazoles, and it is this property that fluorometric methods exploit by using fluorescence agents with adjacent amine groups achieving detection limits in the nM range have been obtained using fluorometry.[40] UV-visible spectrometry has been used to colorimetrically monitor and detect nitric oxide, based on the reaction of nitric oxide with oxyhaemoglobin and the consequential shift in optical absorption spectra, affording a detection limit of 0.1 – 1.0 μM.[40] Nitric oxide is well known to react with haemoglobin, and was used in the initial work to show that nitric oxide was involved in a physiological role.[41] ESR spectroscopy allows real time measurements of nitric oxide with detection limits of 0.5 μM.[40] However, methods to trap the nitric oxide in order to detect it are complicated and difficult to achieve. This, together with the poor detection limit restricts the use of this technology.

Electrochemical techniques dominate the field of nitric oxide detection, particularly the use of microelectrodes allowing *in vivo* measurement, together with the other advantages

electrochemical methods offer: low cost, high sensitivity, high selectivity and the ability to be non-invasive and non-destructive to surrounding tissue at the origin of nitric oxide release. Furthermore, electroanalytical techniques are now recognised as the foremost methods for nitric oxide sensors as they allow real time detection of nitric oxide in biological systems, with continuous and accurate measurements possible.[42]

Reduction of nitric oxide is undesirable due to the similarities with O_2 and hence the possibility of severe interference. The oxidation of nitric oxide follows a simple EC mechanism to form nitrite (NO_2^-) which can then be further oxidised to nitrate; this process occurs at a potential very close to that at which the one electron oxidation of nitric oxide occurs. This poses a problem, as many biological systems have a high concentration of nitrite which will consequently interfere with the nitric oxide measurement. Other interferences arise from compounds found within biological matrices, such as l-arginine, glutathione and lipoproteins.[43] The possibility of all these interferences makes the detection of nitric oxide to a high precision challenging, determining that the only method to progress electrochemical methods was to use modified electrodes, either employing a nitric oxide permeable membrane or in further developments, surface modifications.

The first electrochemical methods applied to nitric oxide sensing were based upon the direct oxidation of nitric oxide on a variety of electrode surfaces, particularly platinum.[44,45] In 1990, Shibuki[44] developed the use of a platinum wire electrode using chloroprene as a rubber seal around the electrode surface and consequently serving as the nitric oxide permeable membrane. The design of this probe was based on the design of previously developed miniature oxygen electrodes[46,47] and achieved a sensitivity between 3.5 and 10.6 pA per 1 μM change in concentration. The sensor was based on the oxidation of nitric oxide and interferences from oxygen and nitrite/nitrate were avoided *via* the use of chloroprene (see

earlier). Following the development of this electrochemical nitric oxide probe, it was then used to further investigate the roles of nitric oxide within the cerebellum. In 1991, it was shown using this NO probe that within the cerebellum the release of endogenous nitric oxide is essential for the induction of synaptic plasticity.[48] In 1992, Shibuki further described the application of this electrochemical probe to detect endogenous nitric oxide release in rat cerebellar.[45] This initial development and application of an electrochemical nitric oxide sensor described a complicated construction of an NO probe requiring specialist expertise, however once fabricated produces a fast response time and respectable detection limits.

In 1994, Bedioui *et al.*[49] developed a similar electrochemical sensor using a gold microelectrode coated with a nickel porphyrin and Nafion®. This sensor achieved a limit of detection of 10 µM, however the work itself demonstrated the need to firstly determine the exact catalytic role of the porphyrin film and subsequently to optimise the coating of the both the porphyrin layer and the Nafion® layer.

Following these early successful developments with electrochemical nitric oxide sensors, attention turned to combining various layers to the electrode surface modification with the sole purpose of enhancing the performance of the sensor. As Nafion® had previously been successfully employed, it became a very popular choice of ion-exchange membrane used to eliminate interfering anions from the electrode surface, particularly the main interfering species in nitric oxide sensing; nitrite. However the main drawback of Nafion® was obviously the inability to block interferences from cations.

Work in 1993 combined a platinum/iridium working electrode with a three-layered membrane as the surface modification composed from potassium chloride, nitrocellulose and silicon,[50] affording a linear range from 0.2 nA to 1 µM of NO and a response time of 1.14 seconds. Subsequently in 1995 Lantoine *et. al.*[51] demonstrated the first example of a

calibration of a nickel porphyrin/Nafion® modified electrode. In a similar manner to Taha and Malinski[52] carbon microfiber electrodes were coated with nickel porphyrin layers and Nafion® layers and using differential pulse voltammetry produced a calibration in the range 1 nM to 50 μM. At this point, despite highlighting the need to determine the exact role of the porphyrin layer a year previously, the exact role of the porphyrin was still unknown, hence once again highlighting this need, together with the need to develop sensors that had the potential to be used in real time nitric oxide assays in biological systems.

The use of metalloporphyrins in the surface modification of electrochemical nitric oxide sensors then almost exploded, with a plethora of research undertaken. Metalloporphyrins had been used as electrocatalysts for a number of years, making the cross-over into electrode materials for chemical and biological sensors. In terms of nitric oxide sensing, following the work already mentioned, a number of studies were undertaken using a variety of metalloporphyrins including iron,[53] nickel[51,54,55] and manganese.[56-58] Indeed, the use of nickel porphyrins as electrocatalytic layers in electrochemical nitric oxide sensors has become one of the most commonly used.[59] Despite this, there are however a number of problems associated with porphyrinic sensors. Firstly the sensitivity and selectivity of the electrodes depend on a number of experimental variables, including the potential at which the nitric oxide is oxidised and the method and means to which the porphyrin is deposited onto the electrode surface. The porphyrin itself is also subject to a number of interferences which can affect the measurement, and perhaps the most influential problem lies in the irreproducibility of them, with the performance of each varying significantly between electrodes.[42]

Following the success of the porphyrin layers on the electrode surface, research began to advance onto using other materials as the electrocatalytic layer in order to overcome the limitations presented by the porphyrins. Work progressed utilising one of two approaches:

either employing conducting or non-conducting polymers. Obviously, the use of porphyrins as the electrocatalytic layer falls under the umbrella of a conducting polymer; however other materials such as metallophthalocyanines began to also be employed simultaneously. In 1997 Bedioui and co-workers[60] described for the first time the use of a nickel (II) tetrasulfonated phthalocyanine film as the electrocatalytic layer on a carbon microfiber. Metallophthalocyanines are very similar to metalloporphyrins, hence the reason for the work proceeding in this direction. In 1999, Jin *et al.*[61] described the use of electropolymerised films of metal tetraaminophthalocyanines as the conducting polymer layer, together with a Nafion® layer on a platinum microelectrode. Copper, nickel and cobalt tetraaminophthalocyanines were employed, affording a very reasonable detection limit of 10 ± 2 nM. The sensors had a long lifetime (twenty days), however no indication of a response time was provided. Further work with phthalocyanines was undertaken;[62] however they did not receive the attention that the metalloporphyrins did at that time and in subsequent years.

Non-conducting polymer layers on electrode form a permselective layer by limiting access of large molecules to the electrode surface.[63] In 1996, Friedemann *et al.*[64] described an *o*-phenylenediamine modified carbon fibre electrode, and compared it to a nickel (II) porphyrin modified electrode. The non-conducting polymer (*o*-phenylenediamine), in combination with Nafion®, gave a limit of detection twice as good as that achieved with the nickel (II) porphyrin electrode, 35 ± 6 and 76 ± 12 nM respectively. In addition, once optimised, the o-phenylenediamine/Nafion® electrode afforded rapid response times, excellent linearity at low nitric oxide concentrations and was selective against ascorbate, dopamine and nitrite.

3.5 Commercially Available Electrochemical Sensors

It was from the initial design by Shibuki in 1990[44] that the first commercially available nitric oxide sensor was developed by WPI instruments in 1993 (ISO-NO). Since then, WPI has continued to develop commercially available sensors, with a range of eight currently available. Each sensor is specifically suited to a particular application, including the smallest nitric oxide sensor (ISO-NOPF) with a maximum diameter of 200 μm and a detection limit of 0.2 nM.[65] Each sensor has a detection limit of 1 nM or less, and a response time of at least less than five seconds making them suitable for a range of biological applications. The electrodes used a based on a graphite electrode combined with a reference electrode, with a multi-layered nitric oxide selective membrane applied to the sensor which WPO claim will eliminate all interferences. The composition of this multi-layered membrane remains unknown.

3.6 Sensor Applications

In order to determine the viability, sensitivity and applicability of both the commercially available but perhaps more specifically the products of research groups, they need to be tested in real-life situations. This obviously involves applying the sensor to a system that requires nitric oxide detection, for example, and most commonly, biological systems. This allows the possibility of employing the technology on a wider scale to be assessed, together with testing the robustness, selectivity and sensitivity.

Polymer-modified electrodes have been coupled with scanning electrochemical microscopy (SECM) in order to position the sensor in very close proximity to cells in order to monitor nitric oxide release. In 2003, Schuhmann and his co workers[66] combined platinum electrodes modified with nickel tetrasulfonated phthalocyanine tetra-sodium salt with SECM and

applied this to observing nitric oxide release from human umbilical vein endothelial cells. This study outlined the importance of the distance of the sensor from the cell, as the intensity of the response to the nitric oxide significantly diminishes the further from the source the sensor is. Hence the use of technologies such as SECM to manoeuvre the sensor as close as possible to the source is pivotal in obtaining an accurate result. Further, a study in 2006[67] extended the use of SECM to applying it in the shear-force-dependant constant-distance mode, enabling a constant, reproducible distance between source and sensor and hence providing precise, reproducible results.

Following the preferred use of polymer-modified electrodes, in 2004, Bedoui and his co-workers developed a sensor for nitric oxide in its gaseous phase using a hydrogel-based amperometric device with the eventual aim being to develop a non-invasive biosensor.[68] Following this short communication outlining the principle, in 2006 the hydrogel-based device was applied to drug screening using adherently growing C6 gliome cells.[69] This study outlined a new compact biosensor, and also demonstrated an electrochemical device suitable for drug-screening tests towards NO production or inhibition.

Overall, the surface modified electrodes that have been developed have subsequently been shown to be perfectly suited to a wide range of biological applications, successfully monitoring nitric oxide release from a number of biological cells, including human umbilical vein endothelial cells (HUVEC),[55,70] C6 gliome cells,[54,69] endothelial cells,[55] rat brain cells[63] and the cells of tumour-bearing mice.[71]

Oxidative stress is a metabolic condition within the body in which nitric oxide is significantly involved. When aerobic cells are exposed to attack from a variety of local environment factors, for example viral or bacterial infection, they respond by releasing reactive oxygen and nitrogen species. Normally, the presence of these highly oxidising species is countered

by the occurrence of reducing substances such as vitamins or superoxide dismutase, however if this balance is perturbed, oxidative stress results. Hence, the ability to measure the quantity of nitric oxide produced during an oxidative stress episode and consequently the effects it then afflicts on the surrounding tissue is of significant interest to researchers. Electrochemical sensors provide an elegant detection method for this, and have been extensively used to investigate the oxidative stress phenomenon. Platinised carbon microelectrodes are commonly used for this application, with the set-up in concert with the living cell constituting an artificial synapse.[72-74] By applying these electrodes, researchers have been able to quantitatively establish the flux of nitric oxide and the reactive oxygen species during oxidative stress events, assisting in the advancement of understanding of these events and the role nitric oxide plays.

3.7 Conclusions

Nitric oxide is an extremely important molecule, both as an atmospheric pollutant believed to be enhancing global warming and within the body with a plethora of biological roles, finding applications in the cardiovascular system, the immune system and the central nervous system. Due to the abundance of tasks nitric oxide performs within the body, it is synthesised via a number of routes, each specific to the task it undertakes. Research has progressed to developing chemical mimics of the generation of nitric oxide, with compounds known as nitric oxide donors attracting a significant amount of research in the development of drugs that can be used to treat conditions in which pathways concerning nitric oxide generation within the body fail. A number of techniques are used in this chemical generation of nitric oxide, with electrochemical routes providing an elegant, clean and simple method through either oxidative or reductive mechanisms.

When biology fails in its task of generating nitric oxide, or indeed if it over-produces this potentially toxic molecule, sensor systems need to be in place that are sufficiently sensitive to detect nitric oxide at the appropriate levels. Also, in order to obtain further understanding and knowledge of the release of nitric oxide within biological systems, and the consequential effects of this, sensors need to be developed that can be used to detect the release of nitric oxide under various conditions. Electrochemical sensors lead the field in this area, as they are the only method by which nitric oxide can be detected in real time in biological systems, allowing continuous, quantitative and accurate measurements. Due to the wide range of interferences present in the detection of nitric oxide, surface-modified electrodes are principally used, achieving detection limits in the nano-molar range. They have also been successfully applied to a number of biological systems, providing an extensive amount of information as to the generation of nitric oxide, together with the pathways it undertakes once released.

4 Bond Cleavage Dynamics: N-N Bond Cleavage in N-Nitrosoarylamines

This section describes the electro-generation of nitric oxide from a range of N-nitrosoarylamines and has been published in the Journal of Physical Chemistry C.[75]

4.1 Aims and Scope

As described in Chapter 3, the chemical generation of nitric oxide in order to treat disease is an important area of research. This section is concerned with the electro-generation of nitric oxide resulting from the oxidative cleavage of N-N bonds in acetonitrile solution. Nitric oxide was chosen as it is a known protagonist in biology and biochemical pathways, with a vital role in chemotaxis and chemokinesis[76] together with pivotal roles in vascular regulation, neuronal communication and as an important agent within the immune system.[20,22,25] Accordingly, it is essential to describe systems that are able to release bio-signalling molecules at known rates. Electrolysis allows manipulation of the driving force so as to encourage a one-way reaction and promote bond cleavage through extensive solvation restructuring. This leads to the view that dissociative electron transfer - the cleavage of a σ-bond by virtue of electron transfer between a redox-active species (acceptor/donor) and an electrode (donor or acceptor) - is an elegant, chemically clean and mild method to achieve this goal. Moreover, the ability of the theory[77] to rationalise the kinetics of the electron transfer quantitatively in terms of highly simple concepts such as reorganisation energies, reaction driving force and the degree of electronic coupling between reactant and product states, together with electrochemical techniques such as voltammetry enables a dynamic and precise determination of the spatial and temporal coordinates of the electro-generated chemical stimulant.[7]

The choice of system studied for the electrochemical investigations reported herein, the N-nitrosoamines (see scheme 4-1) are well known as nitric oxide donors in aqueous systems,[30] albeit with very poorly understood reaction mechanisms and pathways. Indeed, for the exploitation of these systems as NO donors, it is crucial to ascertain whether electron-transfer initiated release follows a concerted or stepwise pathway.

Despite this, the main drawback with electrochemical generation of nitric oxide with the systems described herein lies in the concern with the electro-release of NO^+ rather than nitric oxide. This section addresses this concern, with the investigation of three compounds: cupferron (the ammonium salt of N-nitroso-phenylhydroxylamine), N-nitrosodiphenylamine and N,N'-dimethyl-N,N'-dinitroso-*para*-phenylenediamine (DMDNPD), shown in scheme 4-1.

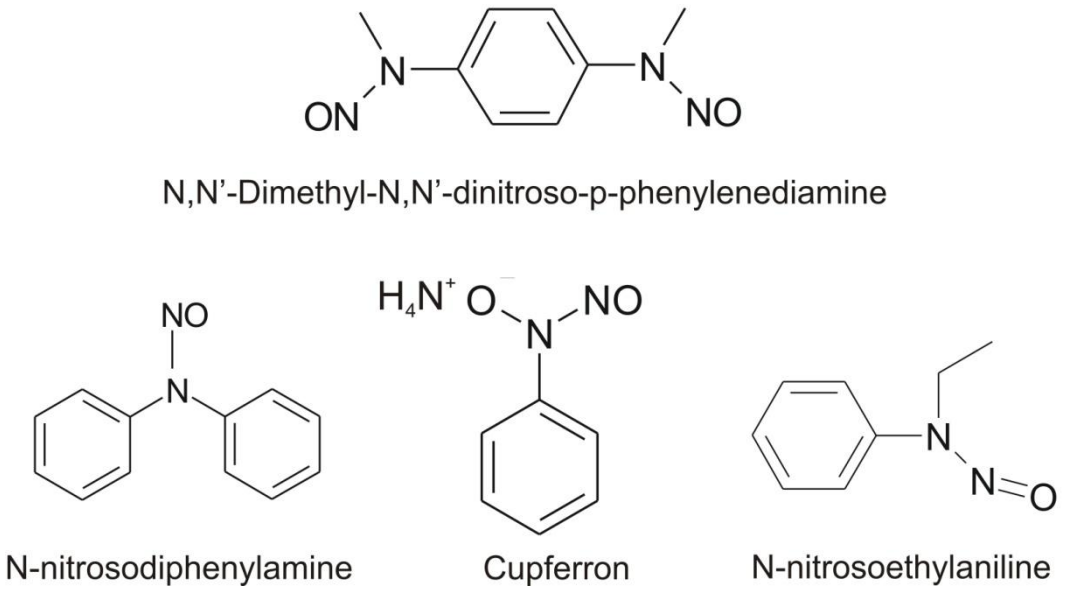

Scheme 4-1: N-nitrosoamines

4.2 Experimental

4.2.1 Instrumentation

Electrochemical measurements were undertaken as outlined in section 2.1. For all macroelectrode experiments excluding those with the N,N'-dimethyl-N,N'-dinitroso-*para*-phenylenediamine, a 3.0 mm diameter platinum electrode (Metrohm, Switzerland) was employed as the working electrode. For the N,N'-dimethyl-N,N'-dinitroso-*para*-phenylenediamine compound a 0.5 mm diameter platinum disc electrode was fabricated in house using standard procedures and used as the working electrode. The working electrode was polished prior to each experiment as described in section 2.1. Microdisc electrode voltammetry was undertaken using either a commercially available 25 μm platinum disc electrode or an in-house fabricated 25 μm platinum disc electrode which were polished prior to voltammetry as described in section 2.1.1 and calibrated as described in section 2.1.1. For the adsorption studies with N-nitrosodiphenylamine, several gold microdisc electrodes were used, fabricated in house and with a diameter of 0.5 mm. All experiments were carried out at a temperature (T) in the range $17 \leq T\ /^{o}C \leq 27$.

4.2.2 Reagents

The solvent used for all the 1 mM solutions of the N-nitrosoamines was acetonitrile (HPLC grade, Aldrich, UK), with tetra-*n*-butylammonium perchlorate (TBAP, 0.1 M, Fluka, UK) used as the supporting electrolyte in all cases. Cupferron (ACROS organics, UK), N-nitrosodiphenylamine (TCI Europe) and ferrocene (Aldrich, UK) were all purchased in the highest commercially available grade and used without further purification. Without rigorous purification of the acetonitrile, some water may have been present. Following the work of

Fujimori *et al* [78] and Pacheco *et al,*[79] N,N'-dimethyl-N,N'-dinitroso-*para*-phenylenediamine was synthesised by Dr. Charlotte Wiles as described below.

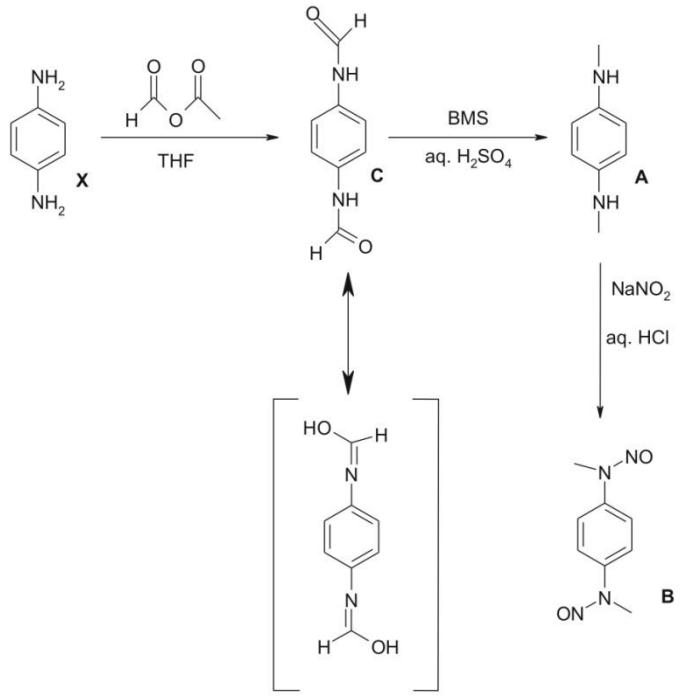

Scheme 4-2: Preparation of N,N'-dimethyl-N,N'-dinitroso-*para*-phenylenediamine

4.2.2.1 **Procedure for the synthesis of N,N-dimethylbenzene-1,4-diamine A:**

N-(4-formylaminophenyl)-formamide C (1.00 g) was dissolved in THF (20 mL) and the solution cooled to 0 °C, prior to the drop wise addition of borane:methyl sulphide (6.1 mL). After the initial vigorous reaction ceased, the resulting reaction mixture was heated to reflux for 3 hrs. The reaction mixture was subsequently cooled to 0 °C, methanol (20 mL) added and stirred for 1 hr. The reaction mixture was subsequently acidified (pH 1) using sulphuric acid and again refluxed for 1 hr. Upon cooling, methanol was added (100 mL) and the reaction mixture concentrated in vacuo to afford a purple oil which was washed with aqueous NaOH and extracted into DCM (3 x 50 mL). The combined organic extracts were dried over $MgSO_4$ and concentrated in vacuo to afforded a burgundy oil which was purified by column

chromatography (eluted 12 % ethyl acetate in hexane) to afford a burgundy oil (0.72 g, 87.2 % yield).

^{1}H NMR of A ($CDCl_3$): 2.79 (6H, s, 2 x CH_3), 3.75 (2H, br s, 2 x NH) and 6.65 (4H, s, 4 x ArH)

Carbon NMR of A ($CDCl_3$): 31.0 (2 x CH_3), 114.3 (4 x CH) and 140.5 (2 x CO)

ESI: m/z 137 (+H 138)

4.2.2.2 **Procedure for the synthesis of compound B:**

Sodium nitrite (4.06 g) was added to a solution of N,N-dimethylbenzene-1,4-diamine A (1.00 g) in deionised water (20 mL) and stirred at room temperature overnight. The reaction mixture was subsequently acidified using aqueous HCl and the reaction mixture diluted with deionised water (30 mL) and the product extracted into DCM (3 x 50 mL). The combined organic extracts were subsequently dried over $MgSO_4$ and concentrated in vacuo to afford a beige solid (1.28 g, 89.6 % yield).

^{1}H NMR of B ($CDCl_3$): 3.47 (6H, s, 2 x N(CH_3)NO) and 7.68 (4H, s, 4 x ArH)

Carbon NMR of B ($CDCl_3$): 31.2 (2 x NCH_3), 119.8 (4 x CH) and 141.1 (2 x CON)

ESI: m/z 194 (+H 195)

4.2.2.3 **Procedure for the synthesis of N-(4-formylaminophenyl)-formamide C:**

Acetic formic anhydride was formed via the dropwise addition of formic acid (11.16 mL) to acetic anhydride (22.73 mL) at 0 °C, followed by gentle heating (60 °C) for 3 hrs, prior to the addition of phenylenediamine (5.00 g) in THF (20 mL); the resulting purple reaction mixture was stirred at room temperature overnight. Removal of the reaction solvent in vacuo afforded a purple solid which was filtered under suction and washed with hexane (50 mL),

followed by DCM (50 mL), to afford N-(4-formylaminophenyl)-formamide C as a lilac solid (7.39 g, 96.9 % yield).

^{1}H NMR of C (50 % tautomer) (d-DMSO): 2.40 (0.25H, brs, OH), 3.29 (0.75H, s, NH), 7.06 (0.75H, d, J 8.6, ArH), 7.44 (0.5H, m, ArH), 8.14 (0.25H, s, C(OH)H), 8.62 0.75H, d, J 8.6, ArH), 10.05 (0.75H, s, COH).

Carbon NMR of C (d-DMSO): 118.3 (1.0 x CH), 119.6 (0.5 x CH), 120.2 (0.5 x CH), 133.9 (0.75 x CONH), 134.0 (0.25 x CON=COH), 159.3 (0.75 x CO) and 162.4 (0.25 x CN).

ESI: m/z 165 (+H 166).

N-nitrosoethylaniline was also synthesised by Dr. Charlotte Wiles following the work of D'Agostino *et al.*[80]

Scheme 4-3: Preparation of N-nitrosoethylaniline

N-Ethyl-*N*-nitrosoaniline was synthesised using the following procedure: Sodium nitrite (6.90 g) was added to a stirred solution of *N*-ethylaniline (12.60 mL) in deionized and doubly filtered water (20 mL) of resistivity not less than 18 MΩ cm, taken from an Elgastat machine (Vivendi, UK) and stirred at room temperature overnight. The reaction mixture was subsequently acidified using aqueous HCl to afford a yellow emulsion which was diluted with water (30 ml) and extracted using DCM (3 x 50 mL). The combined organic extracts were subsequently dried over $MgSO_4$, filtered and concentrated *in vacuo* to afford a pale yellow oil (15.04 g, 99 % yield); δ_H (400 MHz, $CDCl_3$/TMS) 1.16 (3H, t, J 7.4, CH_3), 4.07 (2H, q, J 7.4, CH_2), 7.35 (1H, m, ArH), 7.45 (2H, m, 2 x ArH) and 7.52 (2H, m, 2 x ArH); δ_C

(100 MHz, $CDCl_3$/TMS) 14.1 (CH_3), 42.6 (CH_2), 123.7 (2 x CH), 124.8 (2 x CH), 131.2 (CH) and 142.6 (C_0); ESI *m/z* 150 (+H 151).

4.2.3 Procedures

4.2.3.1 **Voltammetry of N-nitrosoamines**

Reproducibility of the experiments was ensured by rinsing the electrodes between scans with nitric acid (10% volume, Fisher Scientific, UK) so as to remove any adventitious adsorbates from the electrode surface. The diameters of the microdisc electrodes were electrochemically ascertained using ferrocene in acetonitrile and tetrabutylammonium perchlorate (TBAP, 0.1 M) and the diffusion coefficient[16] of 2.3 x 10^{-5} cm^2 s^{-1}.

4.2.3.2 **Voltammetry of adsorbed N-nitrosodiphenylamine**

The voltammetry of adsorbed N-nitrosodiphenylamine was achieved via soaking gold disc electrodes in a 1.0 mM solution of N-nitrosodiphenylamine in acetonitrile for a period of six hours, after which they were washed in fresh acetonitrile prior to undertaking voltammetry in acetonitrile/0.1 M TBAP.

4.3 Results and Discussion

Firstly the voltammetry of the archetypal N-nitrosoamine, cupferron, regarding its ability to engage in electrochemically induced nitric oxide release was investigated, before moving on to the voltammetry of other generic N-nitrosoamines.

4.3.1 The Oxidative Voltammetry of Cupferron

Figure 16 illustrates five consecutive voltammetric sweeps for the oxidation of 2.0 mM cupferron in acetonitrile in 0.1 M TBAP at a 3.0 mm diameter platinum electrode at 298 K at

a scan rate of 0.1 V s^{-1}. A single broad oxidation is observed at + 0.55 V vs. Ag/AgCl with no immediate reverse reduction signal obtained. Repetitive scanning causes a slight shift towards more positive potentials in the peak oxidative current, with a concomitant decrease in the magnitude of the peak current. These suggest that the oxidation is irreversible, a characteristic observed even at the fastest of scan rates employed (2.0 V s^{-1}), taken together with the absence of a reverse signal under these conditions. The reproduction of the voltammetry without extensive cleaning of the electrode using nitric acid was particularly difficult, suggesting the occurrence of adsorptive blocking of the electrode surface. Furthermore, the peculiar voltammogram obtained for the fifth scan as shown in figure 16 whereby the current on the reverse scan initially enhances before decreasing also suggests adsorption onto the electrode surface. Despite the absence of an immediate reverse signal corresponding to the oxidation peak, a reduction wave is observed when scanning to more negative potentials at - 0.35 V vs. Ag/AgCl, the wave is present whether or not the potential is driven first to oxidative potentials.

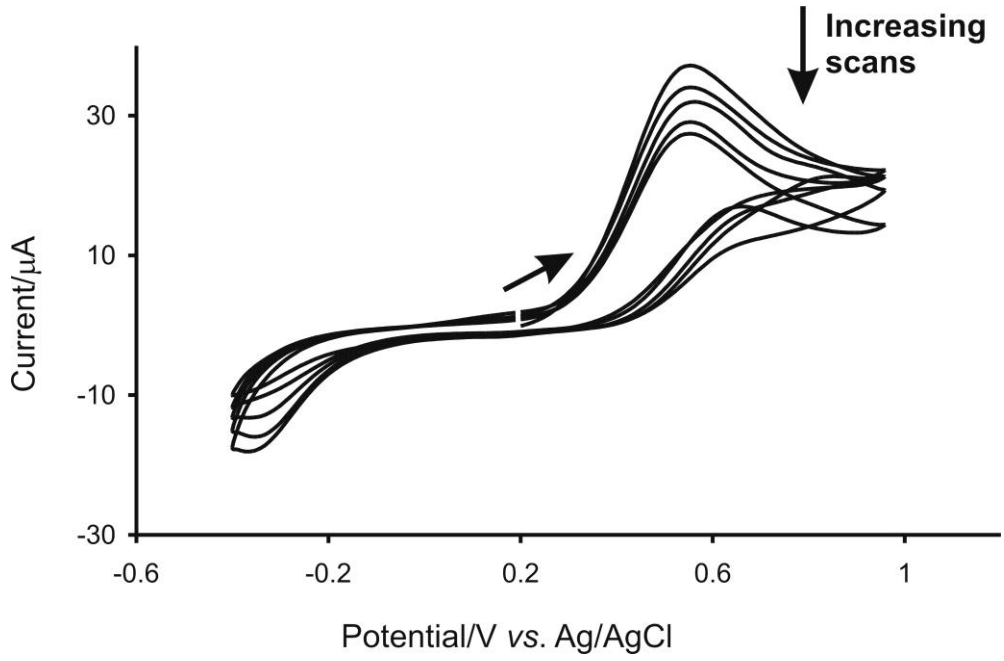

Figure 16: Cyclic voltammetry of 2 mM cupferron in acetonitrile in TBAP at a 3.0 mm diameter platinum electrode at 298 K at 0.1Vs^{-1}. Arrow indicates direction of scan.

Previous electrochemical work with cupferron in aqueous system[81,82] has suggested that the presence of a reduction wave is due to the electrochemical reduction of the hydroxylamine and nitroso moieties of cupferron. In this system, where the acetonitrile has not been purified, some water may have been present and thus the following mechanism is suggested for the reduction:[82]

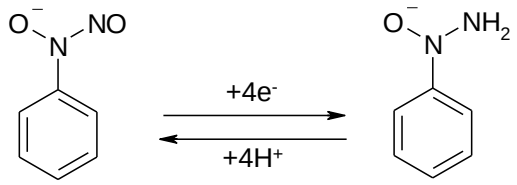

Scheme 4-4: Reduction of cupferron

The oxidation of cupferron has been extensively studied within aqueous systems,[83] and suggests upon oxidation of the cupferron, release of nitric oxide from the compound via cleavage of the N-N single bond following the electron transfer results. Although this work by Lawless and Hawley[33] was undertaken in an aqueous system, the similarities shown within this work using acetonitrile suggest that it is not unfeasible that the oxidation peak at + 0.55 V vs. Ag/AgCl is due to the release of nitric oxide. Further evidence of the release of nitric oxide was provided by Lawless and Hawley[33] by the presence of further oxidation waves at higher potentials due to the stepwise oxidation of the nitric oxide to firstly nitrite then nitrate. However, in the acetonitrile system these peaks were not present as the nitric oxide would appear to not be oxidised at the electrode at the potentials used in this experiment.

The suggestion of nitric oxide release from the compound upon oxidation invites the question: how does this release occur in non-aqueous systems? This mechanism could be an $E_{i/r}C_i$ in the Testa-Reinmuth notation[10] in a stepwise manner in which heterogeneous electron transfer between cupferron and the electrode occurs followed by N-N bond cleavage in the

resulting radical intermediate (see scheme 4-5). Alternatively, the concerted oxidation of cupferron may afford the products directly.

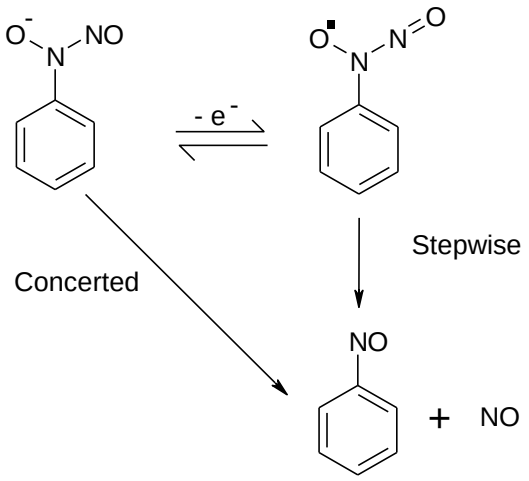

Scheme 4-5: Concerted and Stepwise mechanism for the oxidation of cupferron

In this concerted mechanism, it is not suggested that the radical intermediate does not exist, but rather its lifetime is less than the duration of one vibration. Further clarification of the mechanism is complicated via the apparent adsorption of some species during the overall electrode reaction to the electrode surface.

In order to elucidate this adsorption, experiments were undertaken in order to determine which species was adsorbing to the surface. Initially the reduction of potassium ferricyanide was used as a marker for the degree of blocking of the electrode due to adsorptive species. It was found that neither cupferron nor nitrosobenzene adsorbed to the surface, even after 90 minutes of soaking in an acetonitrile solution containing 1 mM cupferron or nitrosobenzene respectively. Following this, an experiment was undertaken to investigate whether the anionic cupferron was adsorbing to the positively charged electrode surface. The electrode was potentiostatted at a potential near to the foot of the oxidation wave whilst soaking the electrode for up to 20 minutes in acetonitrile containing 1 mM cupferron and 0.1 M TBAP.

This again showed negligible adsorption to the surface. However repeating this experiment, but subsequently performing the reduction of potassium ferricyanide caused a marked blocking of the voltammetry. This suggests that the cupferron does in fact adsorb to the electrode, however in a potential driven process, therefore simply soaking the electrode in a solution of cupferron does not provide the basis for any adsorption, however as the potential is driven, adsorption begins to occur.

Keeping in mind the presence of an adsorbate in the reaction pathway, the two pathways already described, *i.e*. concerted or stepwise, can be classified by using several distinguishing criteria. This is due to the intricate mixture of driving force and thermal effect factors that govern the dissociation electron transfer involved in the release of the nitric oxide. Firstly the behaviour of the voltammograms as a function of the timescale of the experiments is considered as an aid to distinguish between the two pathways. The timescale of the experiment is controlled by the potential sweep rate employed, hence a plot of the peak oxidative potential against the logarithm of the scan rate were constructed, showing a positive gradient. Reproducing these data however was very difficult, most likely owing to the presence of an adsorbed species together with the broadness of the peaks. Attention was therefore turned to Tafel analysis of the wave shapes in the upper and lower quartile potentials. These data are reported in table 4-1 as the gradient of the E *vs*. $\log_{10}$ i plots at each scan rate. It is clear from this data that the slope ($2.3RT/\beta F$) affords symmetry coefficients, β, of 0.3 with only slight variation over three orders of magnitude in timescale and indicative of an energetically uphill reaction pathway.

Scan Rate /Vs^{-1}	E vs. plot log_{10} i gradient	β
0.05	148.7	0.391
0.1	210.5	0.276
0.2	153	0.380
0.5	171.2	0.339
0.75	178.4	0.326
1	180.8	0.321
2	162.3	0.358

Table 4-1: Tafel analysis of cupferron

Such values of β, i.e. those less than 0.5, are indicative of a stepwise pathway, and if the rate constant of the electron transfer is considered with respect to the degree of adsorption, this can be further verified. Taking into account the potential driven adsorption of the cupferron, the rate constant will be altered as shown in equation 4-1:

$$k_{obs} = k_s(1-\theta))$$

Equation 4-1: The effect of adsorption on the rate constant

Where θ is the degree of blocking of the electrode. Taking this into account, it is possible to conclude that the overpotential required to drive the reaction will be much higher, and if the reaction profile of the reaction is considered (figure 17 (A)) it can be shown that the stepwise pathway does indeed require a higher starting potential.

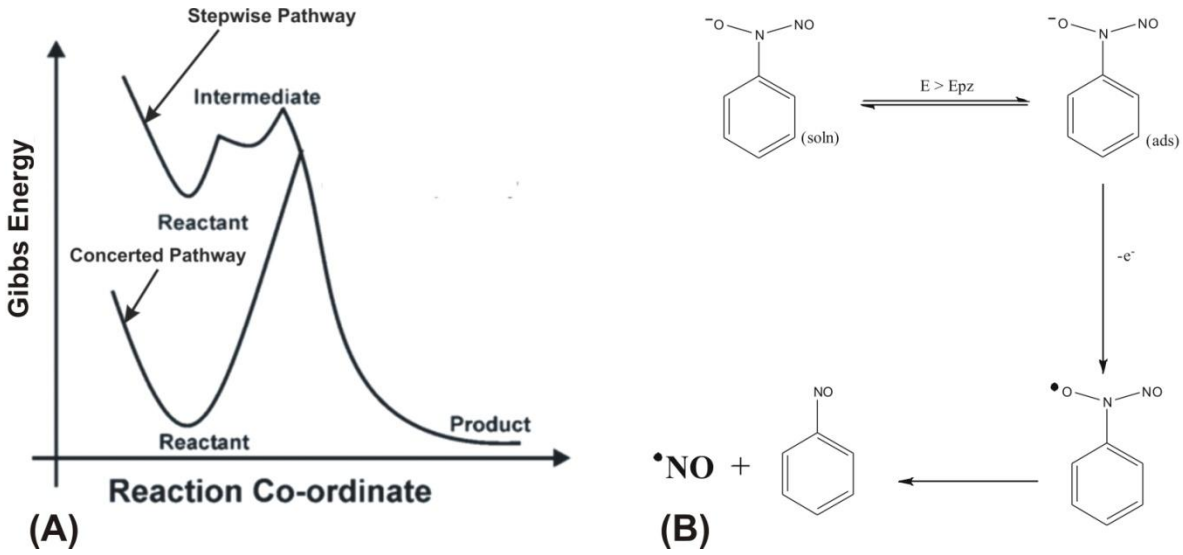

Figure 17: (A) Reaction profile for stepwise and concerted pathways, with the starting energy of the reactant in each case representing the standard energy of pathway. (B) Stepwise mechanism for the oxidation of cupferron

Steady-state voltammetry was then thought a useful tool to verify the following mechanism for the oxidation of cupferron by enhancing the mass transport of material to the electrode (figure 17 (B)). Hence rotating disc electrodes and microdisc electrodes were employed to further probe the oxidative voltammetry of cupferron. Rotating disc voltammograms, illustrated in figure 18, show a single electron oxidation occurring between $E_{1/2}$ = + 0.441 and + 0.407 V *vs*. Ag/AgCl, dependant on rotation speed.

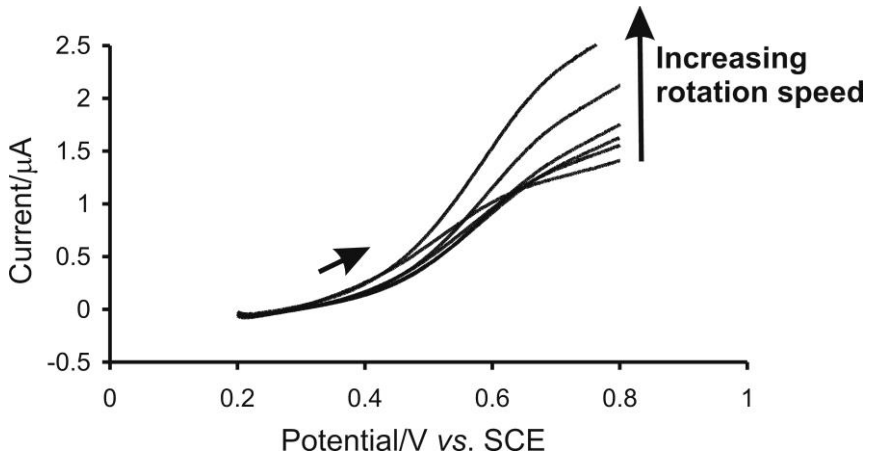

Figure 18: Rotating disc electrode voltammograms for 1 mM cupferron at a 3.0 mm platinum electrode at 298 K at 0.002 Vs^{-1}

This shift in $E_{1/2}$ is characteristic of a mechanism with unstable products, with the following reaction causing the potential to shift to more positive potentials and $E_{1/2}$ becoming a function of ω. The voltammetry was once again affected by the adsorption of some species within the mechanism, with difficulties in irreproducibility and also the apparent crossing of the voltammograms at different rotation speeds. The oxidation of 1.0 mM cupferron at both a 25 µm and 10 µm platinum disc electrode at 298 K is illustrated in figure 19.

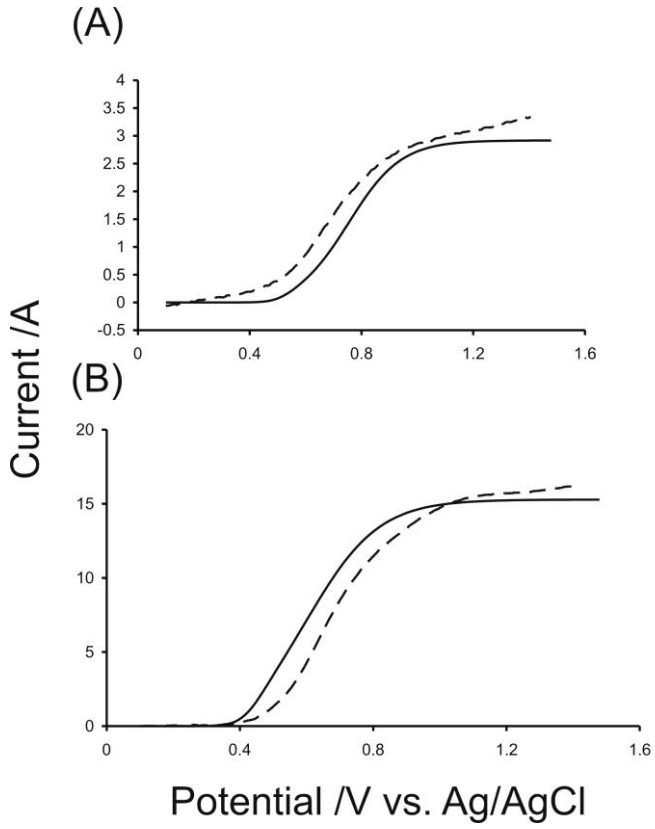

Figure 19: Microdisc voltammetry of cupferron at (A) 10 um platinum disc and (B) 25 um platinum disc. Dashed lines indicate experimental data; solid lines show theoretical data using a non-linear least squares algorithm.

Analysis of the potential parameters of the wave suggests initially slow kinetics followed by faster kinetics in the upper quartile of the wave. These data are entirely in agreement with the view that the oxidation of cupferron is self inhibiting, with significant adsorption affecting the initial kinetics of the mechanism. Once again, when attempting to model the steady-state

data at a microdisc electrode to a non-linear least squares algorithm based on the Butler-Volmer model,[84] no reasonable fit was obtained. Further, when applying the Bard and Mirkin method[85] to the data, the model once again failed to fit the experimental data providing further evidence of the self-inhibiting, adsorptive nature of the mechanism proposed.[86]

4.3.2 Voltammetry of Compounds Generic to Cupferron

It follows that the oxidation of other N-nitrosoamines could also follow a stepwise pathway that could also be controlled via adsorption. Accordingly, we next turn to the examination of other variations of this generic model.

The oxidation of 2.0 mM N-nitrosoethylaniline in acetonitrile/TBAP at 292 K at a 3.0 mm diameter platinum electrode at scan rates in the range $0.02 \leq \nu / V\ s^{-1} \leq 2$ is shown in figure 20:

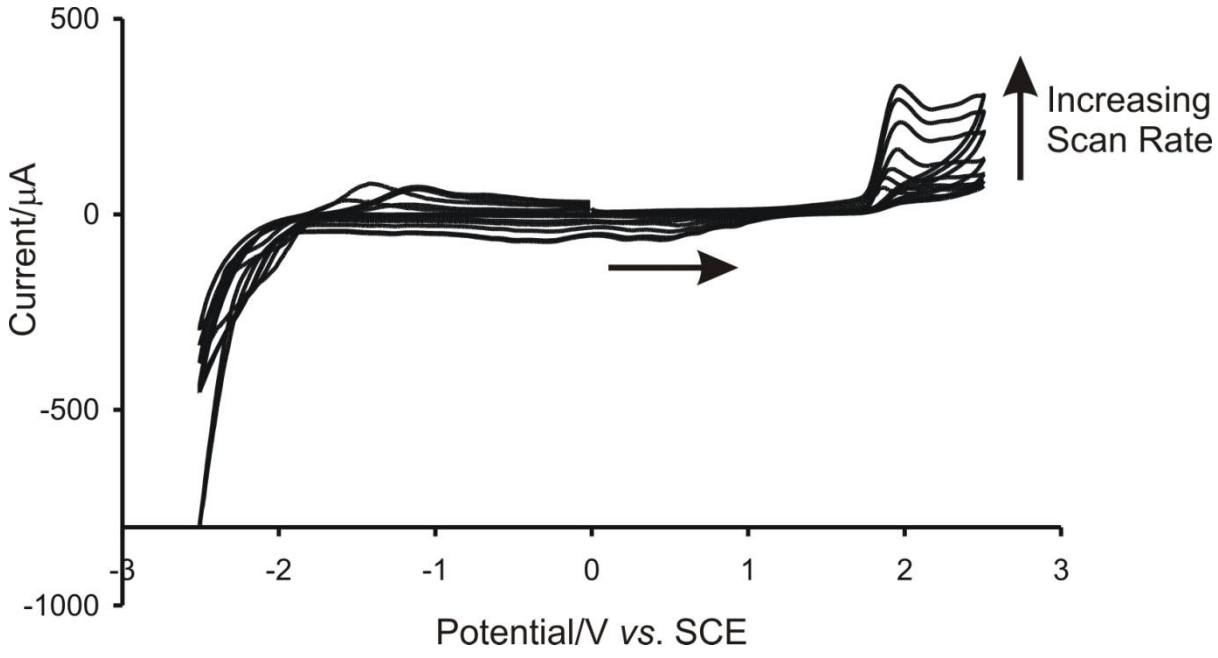

Figure 20: Cyclic voltammetry of 2 mM N-nitrosoethylaniline in acetonitrile/TBAP at a 3.0 mm diameter platinum electrode at 292 K.

A single oxidation is observed a + 1.98 V *vs*. SCE with no immediate reverse peak obtained. Repetitive scanning through the oxidative potentials causes a decrease in the magnitude of the peak current and a slight shift in peak potential to less positive values. Taken together, and with the absence of a reverse signal even at the fastest scan rates employed, (2.0 V s^{-1}), this suggests the oxidation is irreversible. The reverse sweep to more negative potentials encourages reduction waves firstly at + 1.0 V *vs*. SCE followed by a number of other reduction peaks. Considering the work outlined herein involving the oxidation of cupferron, it is viable to suggest that the oxidation of N-nitrosoethylaniline releases NO^+ leaving a radical product which then undergoes further reduction, hence the presence of many reduction peaks on the reverse sweep. Sweeping back to more positive potentials following the reductions encourages the presence of oxidation peaks at much lower potentials than those seen for the initial oxidation, i.e. - 1.44 V *vs*. SCE and + 0.86 V *vs*. SCE, suggesting a chemical reaction following the release of NO^+ and hence an $E_{i/r}C_i$ reaction mechanism similar to that presented for the cupferron.

Considering again which of the two pathways, stepwise or concerted, is the route involved, analysis of the voltammetric behaviour as a function of the timescale of the experiment, *i.e.* the scan rate, was undertaken. A plot of peak oxidative potential against the logarithm of the scan rate (see figure 21) afforded relatively linear data, with a gradient of 89 mV, with this dependency on of the peak oxidative potential on the scan rate confirms the irreversibility of the electron transfer. Analysis of the dependency of the peak oxidative current on the timescale of the experiments suggests the release of NO^+ is under diffusional control, with a plot of the peak current against the square root of the scan rate showing characteristic linearity.

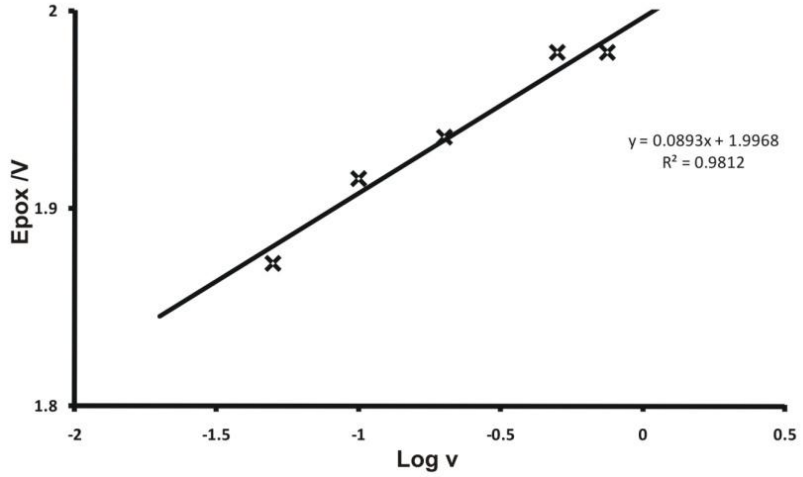

Figure 21: The dependence of E_{pox} on scan rate of N-nitrosoethylaniline

Tafel analysis of the oxidation wave in the upper and lower quartile potentials was undertaken, with the data reported in table 4-2 as the gradient of the potential against the logarithm of the current plots for each scan rate. Once again, the slope (2.3RT/βF) affords symmetry coefficients of 0.5 at slower scan rates, tending towards 0.3 at faster scan rates. Again the values are < 0.5, characterising the stepwise pathway. However, in this case the β values are dependent on the timescale of the experiment, with shorter timescales leading to a more definite stepwise pathway.

Scan Rate /Vs^{-1}	E vs. plot log i gradient	β
0.02	104.3	0.557
0.05	122.6	0.474
0.1	160.7	0.362
0.2	145.3	0.400
0.5	160.4	0.362
0.75	155.0	0.375
1	173.9	0.334
2	204.5	0.284

Table 4-2: Tafel Analysis of N-nitrosoethylaniline

Following this, attention turned to N-nitrosodiphenylamine, the voltammetric behaviour of which is shown in figure 22. Five consecutive scans are shown at 0.5 V s^{-1} at 294 K in acetonitrile/TBAP at a 3.0 mm diameter platinum electrode. One broad oxidation peak is observed at + 1.85 V *vs*. SCE, with no immediate reverse peak obtained, even at the fastest scan rates employed (2.0 V s^{-1}).

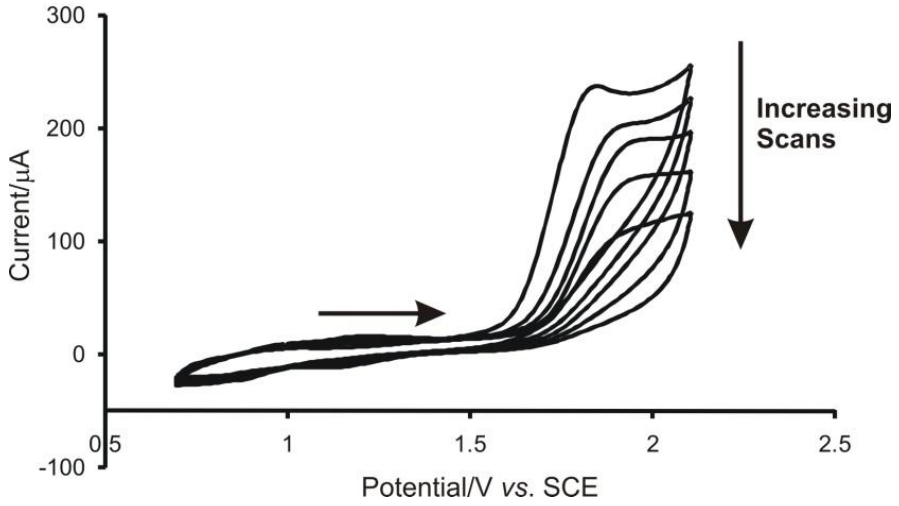

Figure 22: Oxidation of 1 mM N-nitrosodiphenylamine at a 3.0 mm diameter platinum electrode at 0.5 V s^{-1} at a temperature of 294 K

Immediately the broadness of the peaks indicates that once again an adsorptive process may be occurring. Repetitive scanning causes a slight shift in peak oxidation potential to more positive values, and a concurrent decrease in peak oxidative current. Also noteworthy is the progressive broadness of the peaks with consecutive scans. These data, taken together, suggest the oxidation is irreversible and that the voltammetry may be affected by adsorption. At faster scan rates (above 0.1 V s^{-1}) a reduction peak is induced at + 1.2 V *vs*. SCE. Consequently, sweeping the potential back to more positive values on consecutive scans encourages reverse oxidation peak to the reduction at + 1.2 V *vs*. SCE. This observation suggests a chemical reaction once again following the electron transfer. With the view that the nitric oxide is released upon oxidation in an $E_{i/r}C_i$ reaction via either a stepwise or

concerted pathway, in a similar manner to the cupferron, Tafel analysis was undertaken as a diagnostic tool to differentiate which reaction pathway occurs. The oxidation wave was analysed in the upper and lower quartile potentials; the data are reported in table 4-3 with the gradient from the plots of the potential against the logarithm of the current at each scan rate providing values for the transfer coefficient β. Once again the values for β were found to be dependent upon the timescale of the experiment, with a value of 0.4 afforded at longer timescales and 0.2 at more rapid timescales. Again the values are < 0.5, characteristic of the stepwise pathway.

Scan Rate /Vs^{-1}	**E vs. plot log i gradient**	**β**
0.02	138.8	0.419
0.05	150.0	0.387
0.1	172.3	0.337
0.2	178.1	0.326
0.5	182.7	0.318
0.75	211.7	0.274
1	214.9	0.270
2	273.8	0.238

Table 4-3: Tafel Analysis of N-nitrosodiphenylamine

Considering this pathway, steady-state voltammetry at a rotating disc electrode could once again be employed to verify the mechanism. Consequently, the voltammetric behaviour of 1 mM N-nitrosodiphenylamine at a 3.0 mm rotating disc platinum electrode at 298 K at 0.01 V s^{-1} is shown in figure 23:

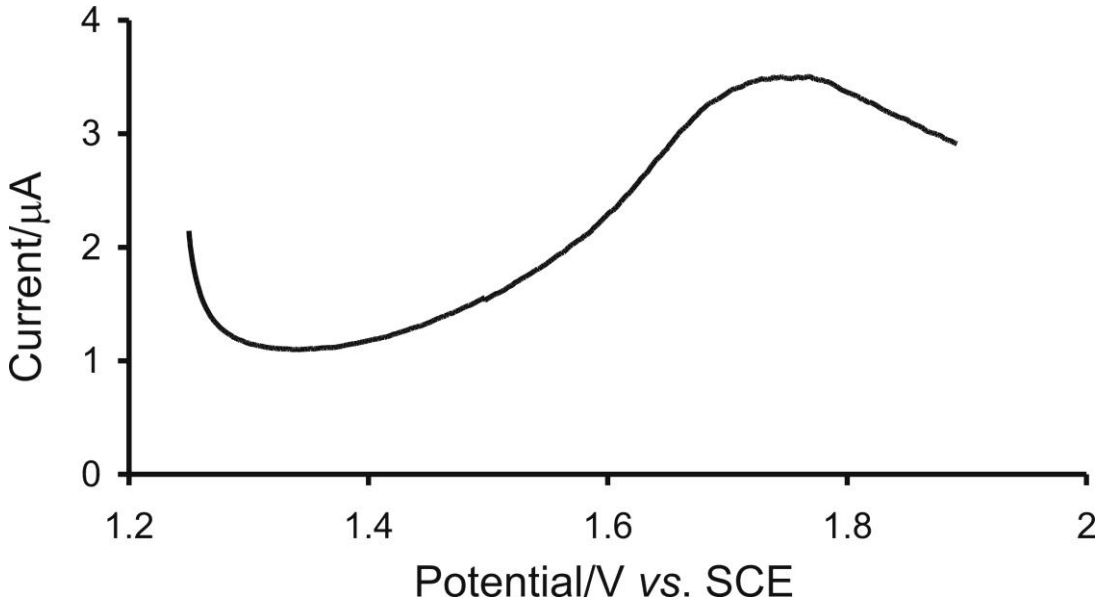

Figure 23: Voltammetry of N-nitrosodiphenylamine at a 3.0 mm rotating platinum electrode at 298 K

At steady state a sigmoidal curve is expected, interestingly here a peak is obtained at + 1.9 V *vs*. SCE, even at the slowest scan rates employed (0.002 V s^{-1}) suggesting that the N-nitrosodiphenylamine is adsorbing to the surface prior to the oxidation.

Accordingly the surface-confined kinetics of N-nitrosodiphenylamine were investigated in an adsorption study. Previous work has shown that nitrobenzenes in general have an affinity for gold surfaces and readily adsorb[87] and hence gold electrodes of different diameters (3.0 mm and 0.5 mm) were used in this study. The voltammetric behaviour of the 0.5 mm gold electrode in acetonitrile/TBAP solution with the N-nitrosodiphenylamine adsorbed to the surface at 1 V s^{-1} and at 298 K is shown in figure 24.

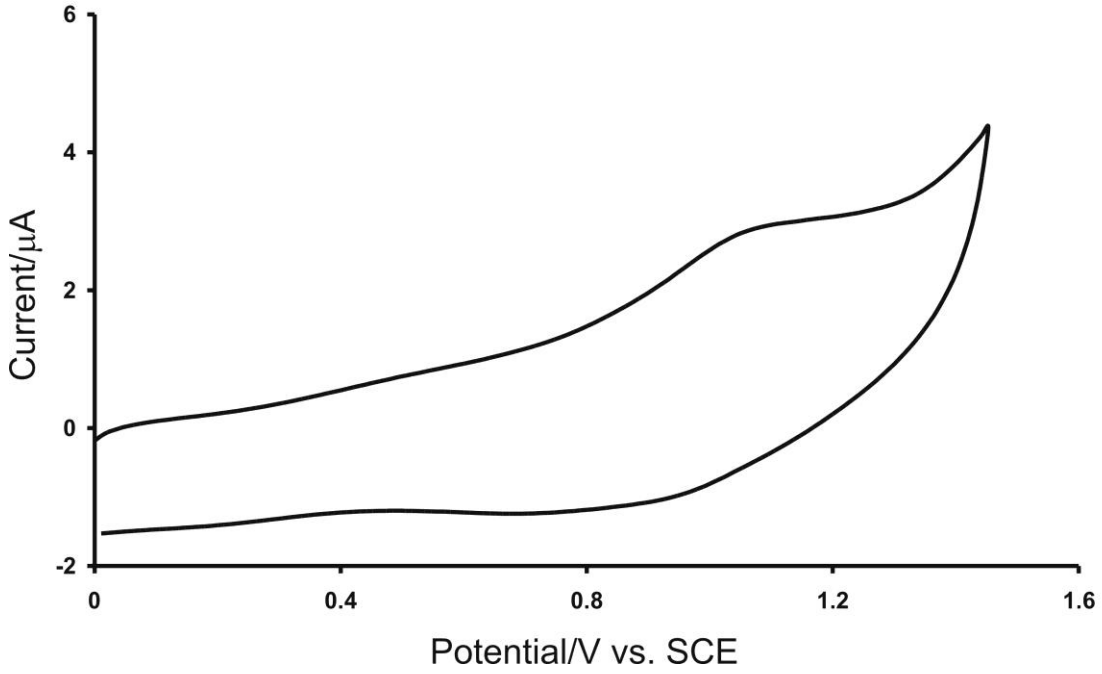

Figure 24: Voltammetry of 0.5 mm diameter gold electrode with the N-nitrosodiphenylamine adsorbed onto the surface at 1 Vs^{-1}.

A single broad oxidation peak is observed at +1.0 V - 1.1 V *vs*. SCE, with an immediate reduction peak also observed on the reverse sweep at + 1.0 V *vs*. SCE. These data, particularly the ~ 0 mV peak to peak splitting, is highly indicative of an adsorbed species. The symmetry observed in the voltammetry is due to the electrode reaction being exclusively controlled by the electron transfer kinetics as the issue of mass transport is no longer an issue with the N-nitrosodiphenylamine formerly confined to the electrode surface. Considering all these factors together, the following mechanism can be used to describe the release of nitric oxide from N-nitrosodiphenylamine.

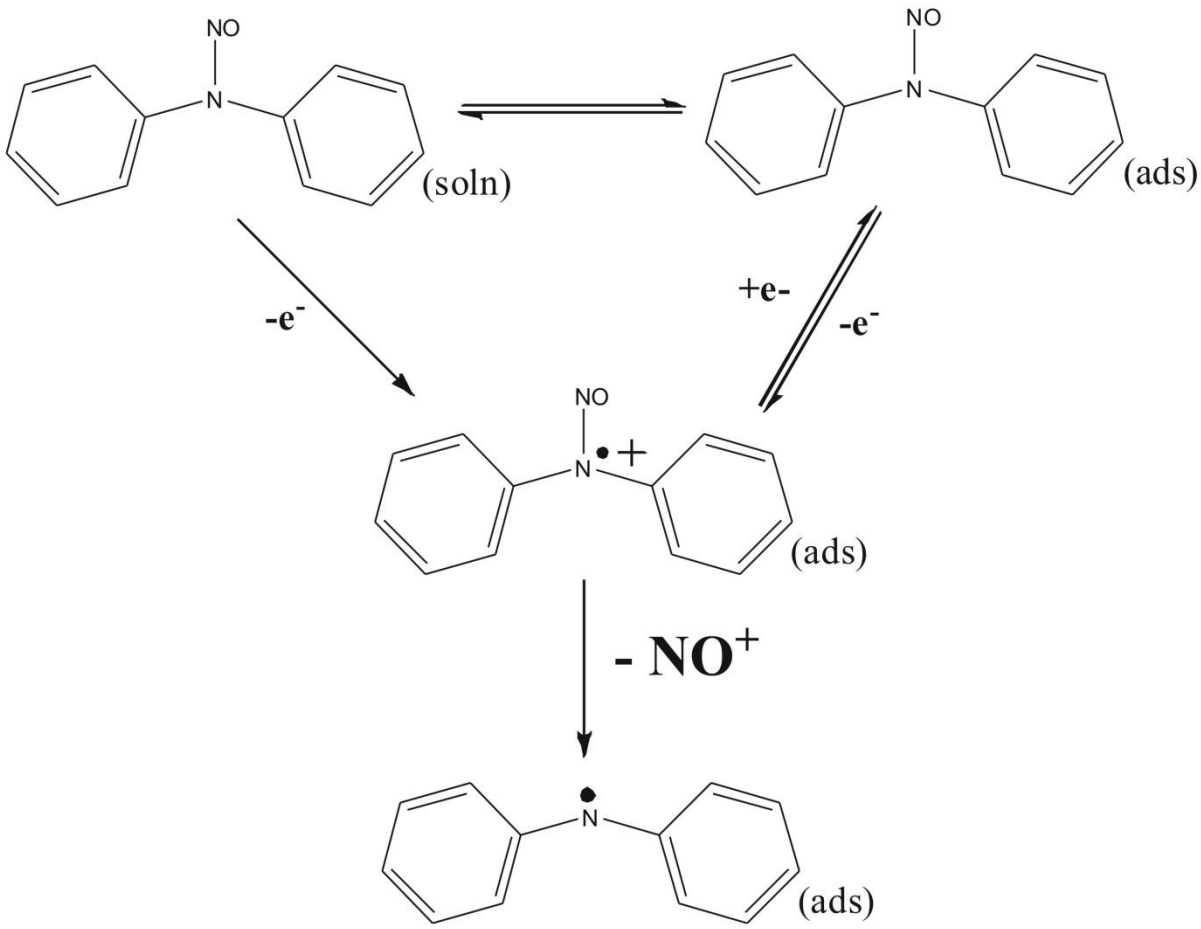

Figure 25: The mechanism of release of nitric oxide from N-nitrosodiphenylamine

The area underneath an oxidation (or reduction) peak in voltammetry represents the amount of charge required to perform the overall electrode reaction; for the case herein of the release of nitric oxide upon oxidation, the area beneath the oxidation peak represents the amount of charge required to release nitric oxide. Hence analysis of the integrated charge under the oxidation wave using the following equations will indicate the coverage density of the electrode with the N-nitrosodiphenylamine.

$$Q = nNF$$

where Q is the charge (C), n is the number of electrons transferred, N is the number of molecules and F is Faraday's Constant (96485 C mol^{-1}), then the number of molecules of N-nitrosodiphenylamine adsorbing to the surface of the electrode can be calculated. As

electrodes of different diameters have been used, charge densities were calculated and the number of molecules adsorbing (N) was calculated to be in the range $9x10^{-12} \leq N /cm^{-2} \leq 1x10^{-10}$, shown in table 4-4.

Electrode	**10^{10}N /cm^{-2} at 0.2 V s^{-1}**	**10^{12}N /cm^{-2} at 0.5 V s^{-1}**	**10^{10}N /cm^{-2} at 1 V s^{-1}**
1	1.77	156	1.07
2	2.11	153	1.79
3	0.845	0.581	1.43
4	0.845	9.50	1.27
5	-	137	0.686
6	-	0.528	0.686
7	1.00	0.792	-

Table 4-4: Number of molecules of N-nitrosodiphenylamine adsorbed to various electrodes at 0.2, 0.5 and 1 Vs^{-1}. Electrode 1 diameter = 3.0 mm, Electrodes 2-7 diameter = 0.5 mm.

An important property of a compound releasing nitric oxide is the rate at which it can do so, *i.e*. the flux of NO^+ released. Hence by further investigating the integrated charge underneath the oxidation peak on consecutive scans, the flux of nitric oxide can be calculated:

$$Q_1 = nN_1F$$
$$Q_2 = nN_2F$$

Then:

$$N_1 - N_2 = \frac{Q_1 - Q_2}{nF}$$

where $N_1 - N_2$ is equal to the number of moles of NO^+ produced. The timescale of the experiment must also be considered:

$$timescale = \frac{\Delta E \times 3}{\nu}$$

$$and\ hence\ the\ flux\ of\ NO^{+} = \frac{\nu}{\Delta E \times 3} \times \frac{(Q_1 - Q_2)}{nFA}$$

Using the above equation, the flux of NO from the surface adsorbed N-nitrosodiphenylamine was then calculated, the values for which are shown in table 4-5.

Electrode	Flux of NO^+ at 0.2 V s^{-1} /pmol $cm^{-2}s^{-1}$	Flux at of NO^+ 0.5 V s^{-1} /pmol cm^{-2} s^{-1}	Flux of NO^+ at 1 Vs^{-1} /pmol cm^{-2} s^{-1}
1	7.89	15.7	22.5
2	6.33	11.7	35.2
3	3.75		27.0
4	3.75	10.6	24.6
5	4.69	1.52	15.2
6		5.86	15.2
7	3.99	5.28	

Table 4-5: Flux of NO^+ at 0.2, 0.5 and 1 V s^{-1}. Electrode 1 diameter = 3.0 mm, Electrodes 2-7 diameter = 0.5 mm.

Endothelial cells within the body release nitric oxide at a flux of 1.67 pmol cm^{-2} s^{-1}.[28] The adsorbed N-nitrosodiphenylamine releases nitric oxide in this system at a flux in the range 4 $\leq$ pmol cm^{-2} $s^{-1} \leq$ 35, increasing with increasing scan rate.

4.3.3 Voltammetry of N,N'-dimethyl-N,N'-dinitroso-*p*-phenylenediamine (DMDNPD)

N,N'-dimethyl-N,N'-dinitroso-*para*-phenylenediamine (DMDNPD) is a compound that has the potential to release two moles of nitric oxide, with this in mind the voltammetric behaviour of this bisnitroso derivative of phenylenediamine at a 3.0 mm diameter platinum

electrode at 296 K and at a scan rate of 0.1 V s^{-1} was investigated and is illustrated in figure 26.

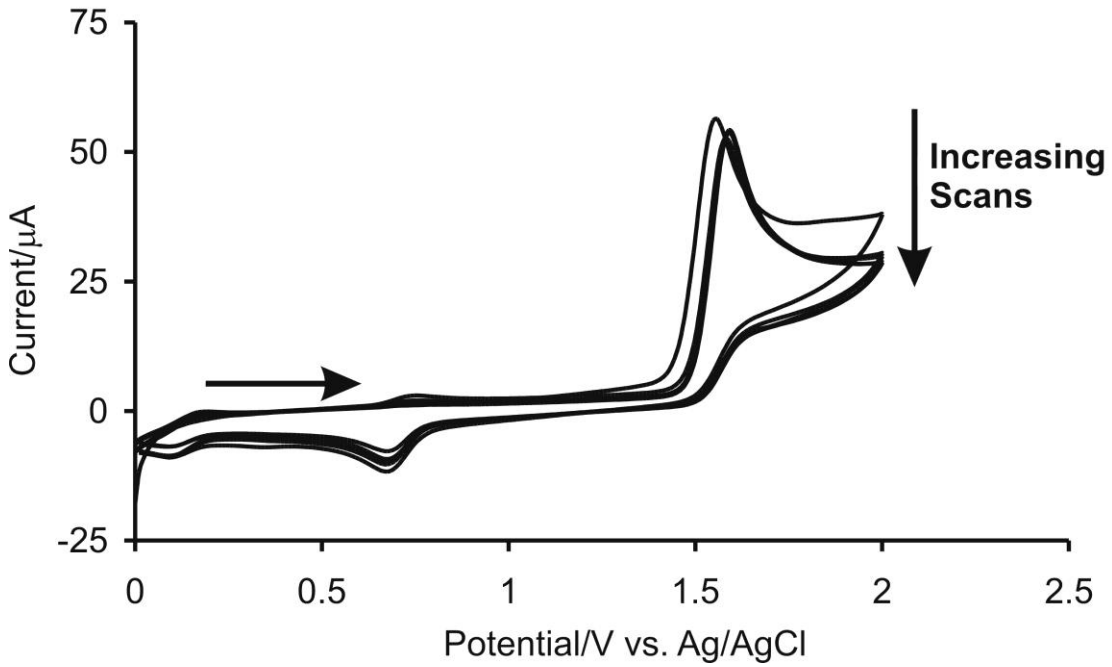

Figure 26: Oxidation of 1 mM of N,N'-dimethyl-N,N'-dinitroso-*para*-phenylenediamine at a 3.0 mm diameter platinum electrode at 296 K and a scan rate of 0.1 Vs^{-1}.Arrow indicates direction of initial scan.

One sharp oxidation peak is observed at +1.55 V *vs*. Ag/AgCl, with no immediate reverse peak obtained. Repetitive scanning cause a slight shift in peak oxidation potential to more positive values, with a concurrent slight decrease in peak oxidation current. This, together with the absence of a reverse peak even at the fastest timescales employed (2 V s^{-1}) suggests that the oxidation is irreversible. Reversing the potential back through less positive values encourages a reduction peak to be observed at all but the slowest scan rate (0.02 V s^{-1}) at +0.68 V *vs*. Ag/AgCl. This reduction then begins to obtain reversibility on consecutive scans, with an oxidation peak obtained at + 0.76 V *vs*. Ag/AgCl on subsequent scans, suggesting a follow-on reaction. It is in this potential region that the redox behaviour of tetra-N-substituted-*para*-phenylenediamines is normally observed, with two single reversible electron transfers usually seen. However, in the case herein, as previously mentioned only a single,

sharp oxidation is observed at a much higher potential suggesting a two-electron process. In order to confirm this, steady-state microelectrode chronoamperomograms were recorded at both a 10 µm and 25 µm platinum electrode, with the 25 µm data shown in figure 27.

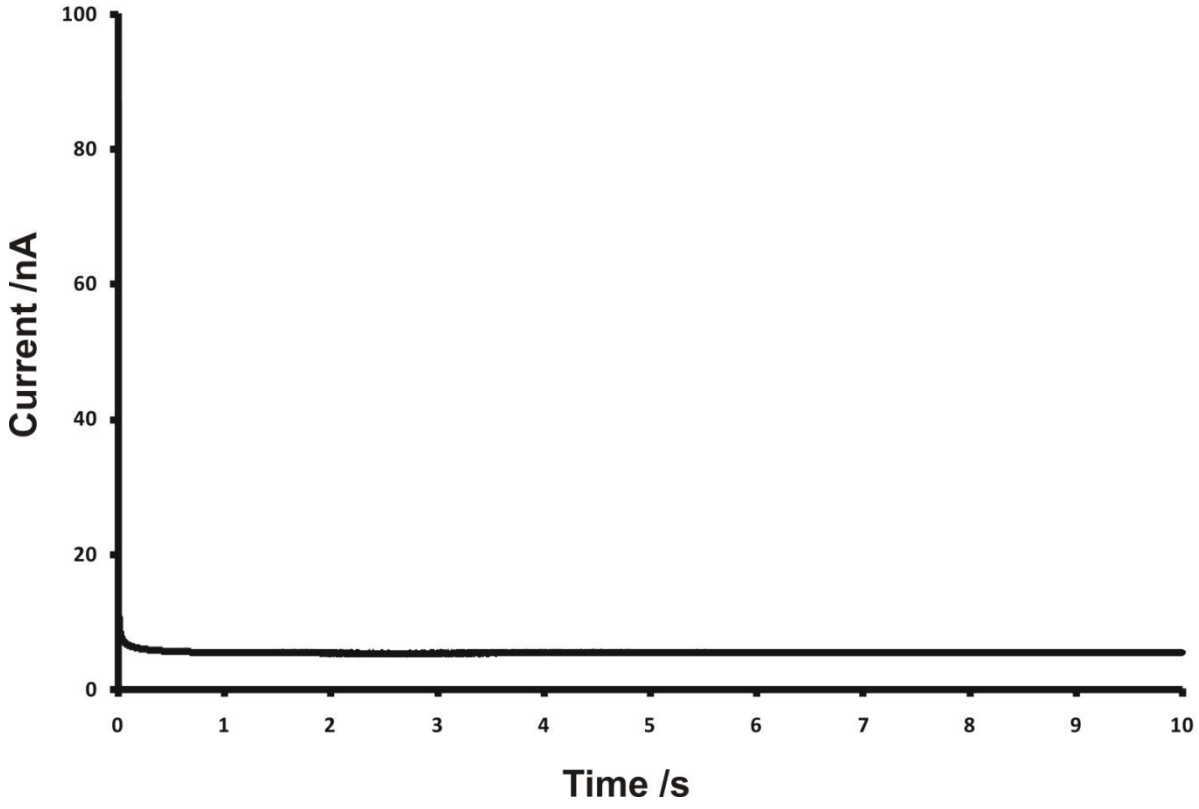

Figure 27: Transient data for 1 mM DMDNPD at a 25 µm platinum electrode.

The data was then analysed by comparison with a theoretical current as determined *via* the Shoup and Szabo expression:

$$i(t) = 4nFrDC\left[0.7854 + \sqrt{\frac{\pi r^2}{16Dt}} + 0.2146\exp\left(-0.3192\sqrt{\frac{r^2}{Dt}}\right)\right]$$

where n is the number of electrons transferred, F is Faraday's Constant, r is the radius of the electrode, D is the diffusion coefficient and C is the bulk concentration. Iterating through the number of electrons and diffusion coefficient values allowed an optimum fit to be found, by

observing a minimum in the mean-squared absolute deviation (MSAD) of the theoretical current:

$$MSAD = \frac{1}{\sum j}\sum_j \left(\frac{i_j^{expt} - i_j^{theory}}{i_j^{expt}} \right)^2$$

Equation 4-2: Determination of MSAD

where j is a dummy index representing the number of time points used. The process can be visualised by means of a flow chart, shown in figure 28, with the minima plots obtained shown in figure 29.

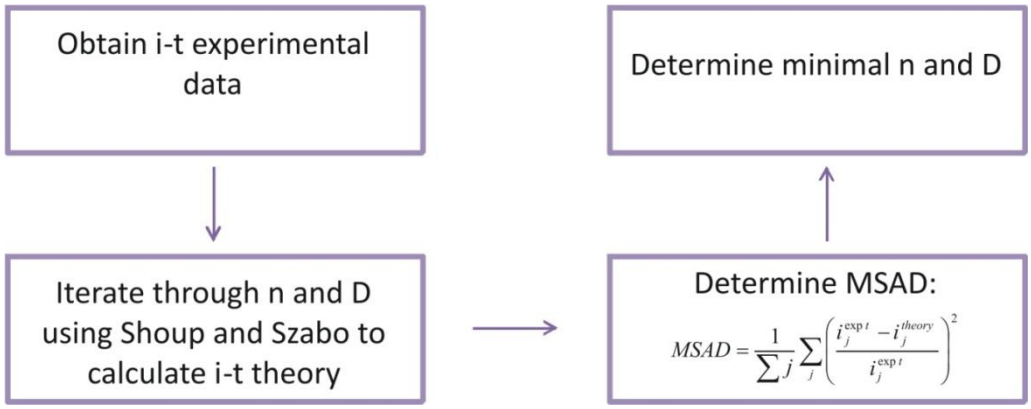

Figure 28: Flow chart demonstrating the process of determining n and D values

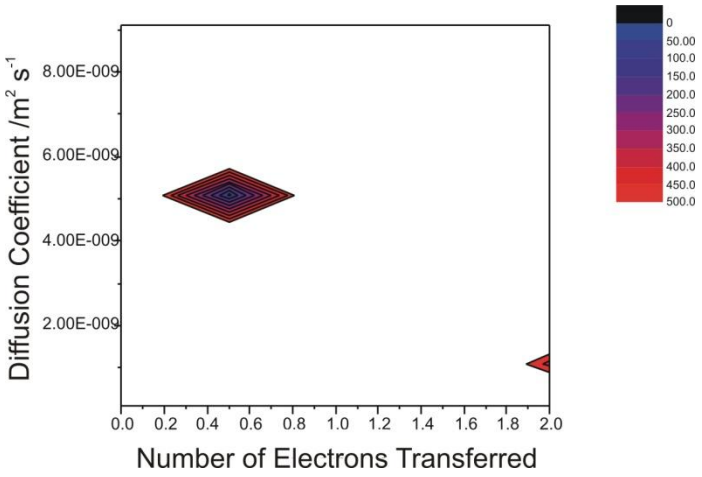

Figure 29: Minima plots

Figure 29 demonstrates two possible minima, hence a Wilke-Chang estimate of the diffusion coefficient was calculated, returning a diffusion coefficient of $1.6 \times 10^{-5} \pm 0.2 \times 10^{-5}$ cm^2 s^{-1}. This allows the first minima observed in figure 29 which suggests that 0.5 electrons are transferred with a diffusion coefficient of $5 \times 10^{-5} \pm 0.2 \times 10^{-5}$ cm^2 s^{-1} to be disregarded, and hence an n value of 2 and a diffusion coefficient of 1.5×10^{-5} cm^2 s^{-1} were determined through this method.

Analysis of the behaviour of the cyclic voltammograms as a function of the voltammetric timescale afforded a linear plot of the potential against the logarithm of the scan rate, with the peak oxidative potential shifting by 62.6 mV for each tenfold increase in scan rate, suggesting that the heterogeneous electron transfer kinetics are slow.

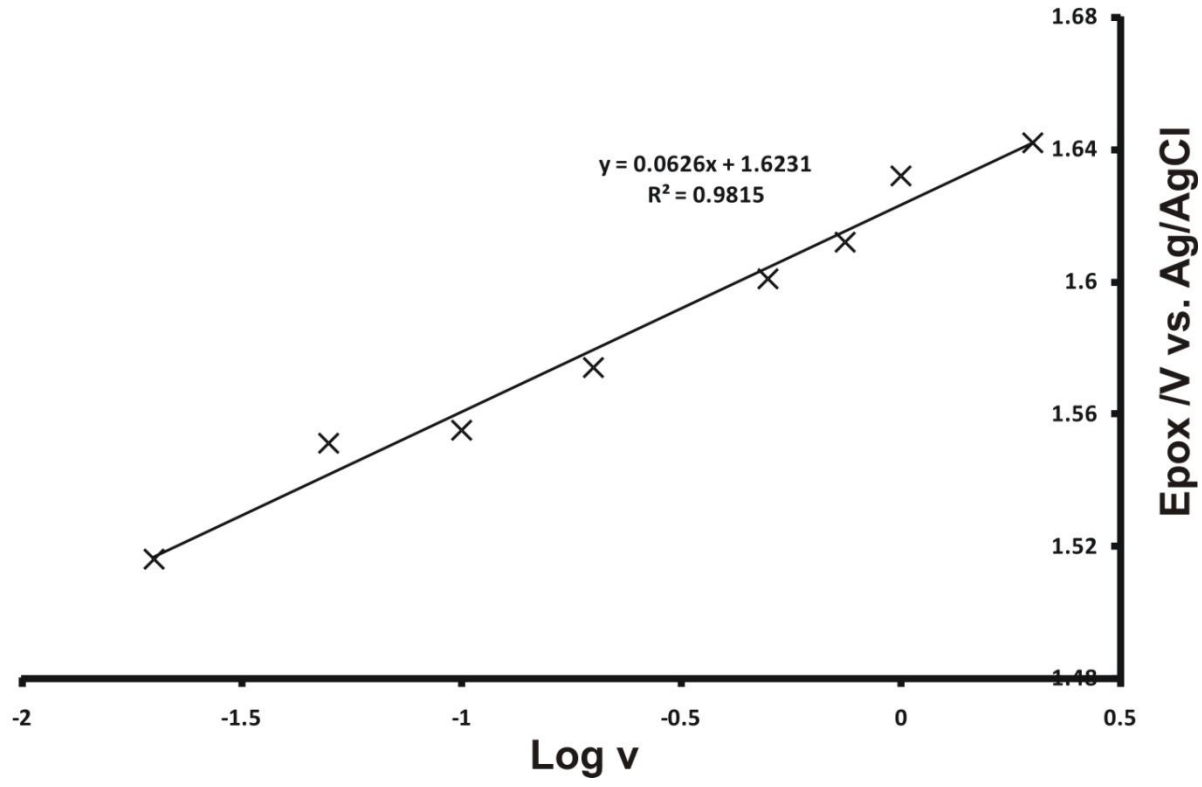

Figure 30: Dependence of E_{pox} on experimental timescale

Nernstian logic anticipates a value of 30 mV for this shift (taking into account an n value of 2), which is further confirmed with examination of the peak widths. These peak widths can

then be used to determine values for the symmetry coefficient, β, using the following relationship:

$$\beta = 1.857 \frac{RT}{nF\left(E_p - E_{p/2}\right)}$$

The calculated values are shown in table 4-6.

Scan Rate /Vs^{-1}	**$E_{pox} - E_{pox/2}$ /V**	**β**
.02	0.0452	0.527
0.05	0.0425	0.561
0.1	0.0491	0.486
0.2	0.0471	0.506
0.5	0.0544	0.438
0.75	0.0614	0.388
1	0.06	0.397
2	0.072	0.331

Table 4-6: Examination of peak widths and β values for DMDNPD

In order to attempt to clarify the mechanism by confirming the products of the electron transfer, bulk electrolysis was undertaken. Following the passage of two-Faradays-per-mole of DMDNPD, a marked colour change from the initial yellow solution to a dark brown was observed. NMR and mass spectrometry analysis failed to provide evidence of the expected product, however the colour change is not surprising and in the absence of oxygen as in this case is in itself indicative of the formation of the NO^+ cation, as this is known to form a number of intensely coloured charge-transfer complexes.[88] The experimental data and the subsequent analysis therefore suggest the release of the NO^+ cation in the mechanism as shown in scheme 4-6.

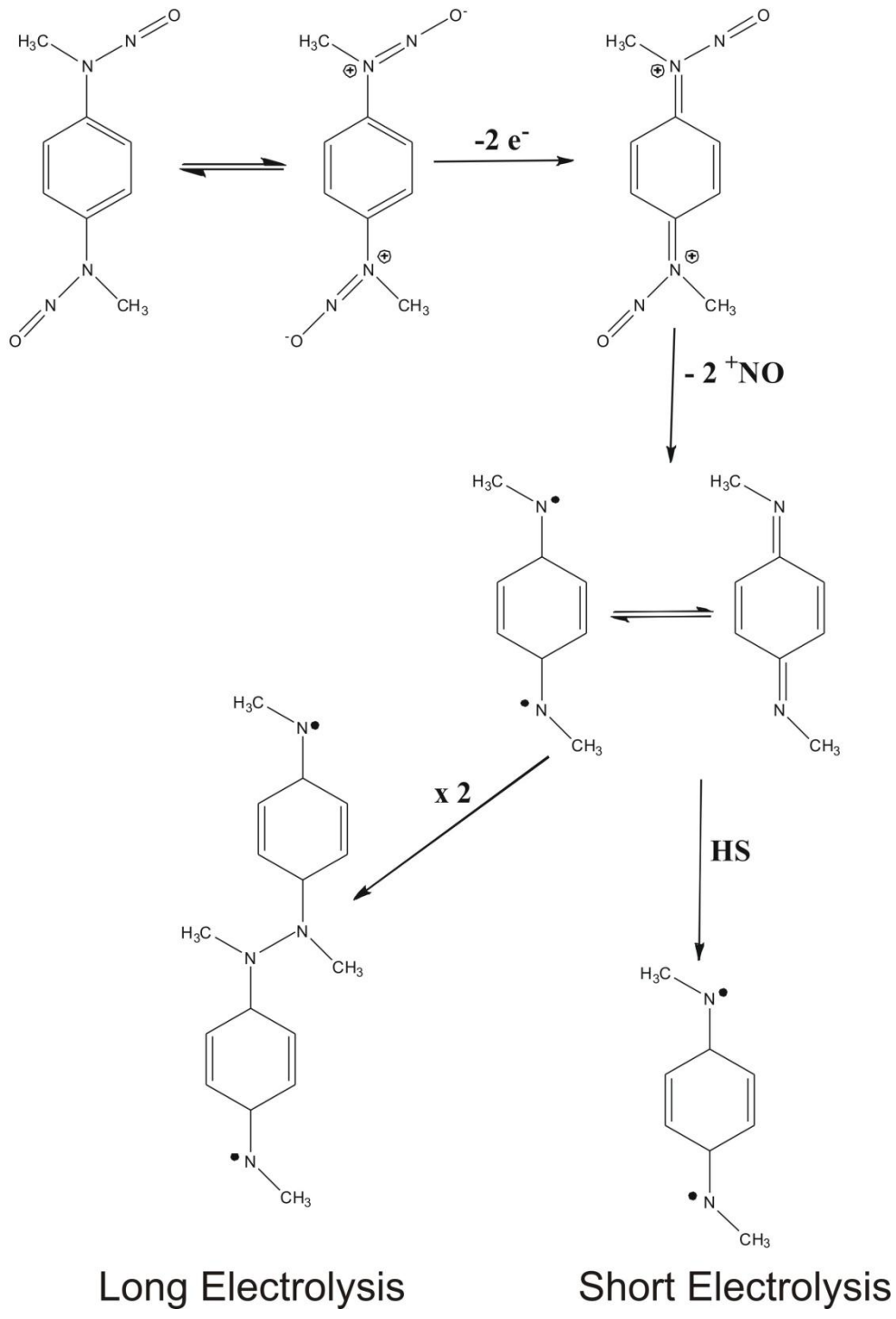

Scheme 4-6: Mechanism for the release of nitric oxide from DMDNPD (HS represents solvent molecules).

In order to determine whether the N-N bonds are cleaved in a concerted or sequential manner with the heterogeneous electron transfer, steady state microelectrode voltammograms were analysed by Dr. Jay Wadhawan, as described in appendix 1 so as to determine variations of

the heterogeneous rate constant (k_{het}) with applied potential and hence enable determination of the symmetry factor, β:

$$\beta = -\frac{\partial \Delta G^{\neq}}{\partial \Delta G^{0}} = 1 - \frac{RT}{nF}\frac{\partial \ln k_{het}}{\partial E} = \frac{1}{2}\left(1 - \frac{n\left(E - E^{0}\right)}{4\Delta G_{0}^{\neq}}\right)$$

Calculation of E^0 afforded a value of 1.3 ± 0.2 V vs. Ag | AgCl | Cl^-, consistent with the formation of NO^+. The experimental data are consistent with the formation of a dication with charge centred on the NO moieties, followed by fast NO^+ release or via an ECEC mechanism in which both chemical cleavages are fast and the second oxidation occurs faster than the first.

The electrochemical oxidation of a variety of N-nitrosoarylamines has been investigated, and the mechanisms of the consequent release of nitric oxide have been proposed. Cupferron does enable the electro-synthesis of nitric oxide, whereas N-nitrosoethylaniline, N-nitrosodiphenylamine and DMDNPD appear to produce NO^+, a highly oxidising species and consequently difficult to harness and utilise.

4.4 Conclusions

The aim of this section was to describe the electron-transfer initiated release of nitric oxide from a range of N-nitrosoarylamines in order to eventually describe the temporal and spatial properties of the electro-generated species. Firstly the voltammetry of cupferron, already established through pioneering work by Lawless and Hawley[33] and Kolthoff,[82] was investigated and the molecular mechanism probed. Reproducing the voltammetry was extremely difficult without extensive cleaning of the electrode using nitric acid, suggesting the occurrence of adsorptive blocking of the electrode surface. Indeed, experiments showed that cupferron adsorbs to the electrode surface in a potential driven process, thereby self-

inhibiting the reaction. Consideration of the adsorption phenomena and determination of symmetry coefficients indicated the release of nitric oxide in a stepwise manner.

Following this, the compounds generic to cupferron were investigated, beginning with N-nitrosoethylaniline. Contrary to cupferron, no adsorption phenomena was observed, with the compound releasing NO^+ in a stepwise manner, inferred via Tafel analysis.

N-nitrosodiphenylamine was investigated next, and was also found to adsorb to the surface of the electrode, and to release NO^+ in a stepwise mechanism. Studies into the adsorptive behaviour revealed typical bell shaped voltammograms with close to 0 mV peak-to-peak splitting. Analysis of the integrated charge underneath the oxidation waves indicated a coverage density in the range o 10^{-10} – 10^{-11} molecules cm^{-2} and a flux of NO^+ in the pmol range.

Finally the voltammetry of a bis(nitroso)phenylenediamine was probed. A single oxidation peak was observed, analysis of which using Shoup-Szabo theory and Wilke-Chang estimates indicated a two electron process. Potentiostatic electrolysis indicated that the NO^+ cation is formed upon oxidation, and β-values together with microdisc electrode data once again indicated the release of two moles of NO^+ in a stepwise manner.

The problem now lies in the design of compounds that release NO as opposed to NO^+ upon electrochemical perturbation. Cupferron was the only compound investigated here which was shown to electro-generate nitric oxide, with both N-nitrosodiphenylamine and N,N'-dimethyl-N,N'-dinitroso-*p*-phenylenediamine appearing to produce the cation. NO^+ is a highly oxidising species and hence is difficult to isolate, therefore it is far more preferable to electro-generate NO.

5 Electrochemical Determination of Diffusion Anisotropy in Molecularly-Structured Materials

Having established the bond-cleavage dynamics of the release of nitric oxide from a range of N-nitrosoamines it is pertinent to investigate the factors that affect the electro-generation of these compounds within systems, *i.e.* the local environment of the electrode surface. Accordingly, the anisotropic diffusion of *molecularly structured* materials is next explored. This work has been submitted for publication in the Journal of Physical Chemistry C. Theoretical considerations were derived by Dr. Jay Wadhawan.

5.1 Aims and Scope

There have been many recently developed substances which have a degree of molecular ordering, for example electrodes modified with elaborate architectures such as self assembled monolayers.[89] These materials have found a number of applications in technology, for example in gas sensors[90] or technology display devices,[91] and it is through the introduction of some anisotropy into these systems that enhances their operation. These artificially produced systems take their inspiration from naturally occurring systems, for example the bilayers in cellular membranes,[92] use anisotropic geometries in order to maximise their biological functioning.

In trying to utilise this technology and to better understand these biological systems, it is important to be able to characterise the degree of ordering of the structuring. Also, in the concept of this thesis, by understanding and being able to characterise the axiosymmetric anisotropic diffusion to an electrode, the use of electrochemical techniques to study the electro-generation of nitric oxide in real systems where structural ordering will be present can be more precisely understood. Also, further chapters will explore the modification of

electrode surfaces in electroanalysis, hence a greater understanding of the effect of these layers on the diffusion will improve the knowledge of those systems.

Previous work has pioneered electrochemical routes for measuring anisotropic diffusion, with Murray[93] employing perpendicular electrodes in order to measure diffusion in each direction. Subsequently, White *et al.*[94] determined the tortuosity of the diffusional flux in face-centred cubic opals using comparisons between voltammetry and simulations. The work in this section explores the theory of anisotropic diffusion before investigating the use of a single microdisc electrode to quantify anisotropic diffusion coefficients within model systems.

5.2 Theory

In an anisotropic system, in contrast to isotropic systems, mass transfer, such as diffusion, does not occur to an equal extent in all directions. Assuming that the principle diffusion axes in an anisotropic system are the same as the coordinates of a cylindrical system, *i.e.* axial (z), radial (r) and angular (φ), then the flux (j) of material to the electrode surface will follow Fick's first law as approximated by concentration (c):

$$j_z = -D_z \frac{\partial c}{\partial z} \quad j_r = -D_r \frac{\partial c}{\partial r} \quad j_\varphi = -D_\varphi \frac{\partial c}{\partial \varphi}$$

Equation 5-1

Therefore Fick's second law, which considers how the concentration at a point x varies with time, becomes:

$$\frac{\partial c}{\partial t} = D_r \left[\frac{\partial^2 c}{\partial^2 r} + \frac{1}{r} \frac{\partial c}{\partial r} \right] + \frac{D\varphi}{r^2} \frac{\partial^2 c}{\partial \varphi^2} + D_z \frac{\partial^2 c}{\partial z^2}$$

Equation 5-2

For a system that is axially symmetric, *i.e.* independent of φ, the φ terms can be neglected and equation 5-2 can reduce to:

$$\frac{\partial c}{\partial t} = D_r\left[\frac{\partial^2 c}{\partial^2 r} + \frac{1}{r}\frac{\partial c}{\partial r}\right] + D_z\frac{\partial^2 c}{\partial z^2}$$

Equation 5-3

This can then be reduced to the more familiar result obtained for isotropic media where the diffusion is identical in all directions, $D_r = D_z = D_{iso}$:

$$\frac{\partial c}{\partial t} = D_{iso}\left[\frac{\partial^2 c}{\partial^2 r} + \frac{1}{r}\frac{\partial c}{\partial r} + \frac{\partial^2 c}{\partial^2 z}\right]$$

Equation 5-4

For this case, under potential step conditions, the current flowing, i, is given by the Aoki and Osteryoung expression:

$$\psi = \frac{i}{4nFD_{iso}r_0c_o}$$

$$if\ \tau \geq 0.82:$$

$$\psi = 1 + \frac{0.71835}{\sqrt{\tau}} + \frac{0.05626}{\sqrt{\tau^3}} - \frac{0.0064}{\sqrt{\tau^5}}.....$$

$$if\ \tau \leq 1.44:$$

$$\psi = \sqrt{\frac{\pi}{4\tau}} + \frac{\pi}{4} + 0.094\sqrt{\tau}....$$

$$where\ \tau = \frac{4tD_{iso}}{r_0^2}$$

Equation 5-5

For isotropic systems, Shoup and Szabo generalised these results in isotropic systems using the following expression for the current flowing under potential step conditions at all times at a microelectrode to an accuracy greater than 0.6%:

$$\psi = \frac{i}{4nFD_{iso}r_0c_0} = 0.7854 + 0.8863\tau^{-\frac{1}{2}} + 0.2146\exp\left(-0.7823\tau^{-\frac{1}{2}}\right)$$

Equation 5-6

It is pertinent to consider two limiting cases of equation 5-3:

Firstly, if $D_z >> D_r$, the problem reverts to the case of planar diffusion, already well considered and solved. The spatial and temporal variation in the concentration of the electroactive species is given by:

$$c = c_0 erf\left(\frac{z}{2\sqrt{D_z t}}\right)$$

Equation 5-7

Where *erf* is the error function and is given by:

$$erf(z) = \frac{2}{\sqrt{\pi}}\int_0^z \exp\left(-t^2\right)dt$$

Equation 5-8

And the current flowing is given by the Cottrell equation:

$$i = nFSc_0\sqrt{\frac{D_z}{\pi t}}$$

Equation 5-9

Secondly, if $D_r >> D_z$ then radial diffusion dominates over normal, planar diffusion and it becomes the same case as that for a cylindrical electrode:

$$i = \frac{2nFD_r c_0}{\xi^2 r_0} \int_0^\infty \frac{\exp\left(\xi x^2\right)}{x\left\{J_0^2(x) + Y_0^2(x)\right\}} dx$$

Equation 5-10

$J_0(x)$ and $Y_0(x)$ are zeroth order Bessel functions of the first and second order respectively, x being the auxiliary variable. This expression has then been generalised by Aoki for $0 \leq \xi \leq 106$ to within 1% error and also by Szabo and co-workers giving:

$$\frac{ir_0}{nFD_r c_0} = \frac{\exp\left(-\sqrt{\frac{\pi\xi}{10}}\right)}{\sqrt{\pi\xi}} + \frac{1}{\ln\left[\sqrt{4\exp\left(-\gamma\xi\right)} + \exp\left(\frac{5}{3}\right)\right]}$$

Equation 5-11

As the diffusion regime is a function of the diffusion space at an electrode, it follows that the limiting cases of equation 5-3 above have particular implications for the case of electrodes immersed into isotropic media. When the diffusion coefficients in both the perpendicular (D_r) and peripheral (D_z) direction to the electrode, this characterises a non-modified electrode. For the case of an electrode with a type of architecture on the surface immersed into isotropic media, the following is understood. If $D_z > D_r$, *i.e.* planar diffusion dominates over radial diffusion, then the edge circumference of the electrode must be blocked off, for example the electrode surface is sunken into the surrounding insulation material. If $D_r > D_z$, *i.e.* radial diffusion dominates over planar diffusion, then this can be seen as a physical blocking of the normal mass transport (i.e. planar diffusion) by a large spherical object placed centrally on the disc electrode. Therefore through quantitative deconvolution of the diffusion rates in both

the planar and radial directions in isotropic media, the voltammetric sizing of any immobilised material on the electrode surface can be achieved, allowing the description of the structure of designer interfaces as shown by Amatore.[95]

Looking at two dimensional diffusion anisotropy at disk electrodes under steady state conditions, and considering only diffusion (no migration and no IR losses), the flux is defined as j_z and is given in equation 5-1. Given that the steady state current flowing, i_{lim}, is given as:

$$i_{\text{lim}} = nF \int j_z dS$$

Equation 5-12

where n is the number of electrons transferred, F is Faraday's constant and S is the electrode area, then in this case i_{lim} becomes:

$$i_{\text{lim}} = 2\pi nF \int_0^{r_0} r j_z dr$$
$$= 4nFc_0 \sqrt{D_z D_r} \int_0^{r_0} \frac{r dr}{\sqrt{r_0^2 - r^2}}$$

Equation 5-13

Therefore:

$$i_{\text{lim}} = 4nF \sqrt{D_z D_r}\, r_0 c_0$$

Equation 5-14

Equation 5-14 therefore demonstrates that diffusion coefficients in isotropic media can be expressed by the geometric mean of the individual diffusion coefficients in the axial and radial directions (D_z and D_r). This allows any analytical result obtained in isotropic media to be employed for the case of two dimensional anisotropy described here by using the

geometric mean of D_z and D_r as the average value. Equation 5-14 also indicates that the limiting current is a function of the diffusion coefficient in both directions, *i.e.* planar diffusion (D_z) and radial diffusion (D_r). It is this that then allows us to explore the axiosymmetric anisotropic diffusion to disk shaped electrodes.

5.3 Experimental

5.3.1 Instrumentation

Electrochemical measurements were undertaken as outlined in section 2.1. In all cases, a three electrode system was employed, with a 25 μm diameter platinum disk (fabricated in house) as the working electrode, with a nickel wire as the counter electrode and a silver wire was employed as the reference. Before and after each set of electrochemical experiments the working electrode surface was polished as outlined in section 2.1 and unless otherwise stated, all experiments were carried out at 22 ± 3 ^{o}C.

5.3.2 Reagents

All chemical reagents used were purchased from Fluka in the purest commercially available grade and used without further purification. Water was taken from an Elgastat system (Vivendi, Bucks, UK) with a resistivity of not less than 18 M Ω cm. Cæsium pentadecafluorooctanoate was prepared by Matthew Thomasson in house following the methods of Bowden *et. al.*[96] and Murray *et. al.*[93] via neutralisation in aqueous caesium hydroxide to a pH of 7.0.

5.3.3 Procedures

5.3.3.1 **Determination of D_z and D_r**

Steady state data of 1 mM ferrocene in acetonitrile was obtained at a 25 µ platinum disc electrode, and the effect of polyethylene glycol determined using equation 5-14 to estimate $\sqrt{D_z D_r}$.

Steady state data of 12.5 mM ferricyanide in cæsium pentadecafluorooctanoate/D_2O mixture was obtained, and using equation 5-14 an estimation of $\sqrt{D_z D_r}$ obtained. Using computational simulations and Shoup Szabo theory to obtain theoretical currents, the experimental data can then be compared with the theoretical data and a best fit found via a minimum mean-scaled absolute deviation (MSAD).

$$MSAD = \frac{1}{\sum s} \sum_s \frac{i^{theory} - i^{expt}}{i^{expt}}$$

Equation 5-15

This then allows the deduction of D_z and D_r from the experimental data.

5.4 Results and Discussion

5.4.1 The Effect of Viscosity on the Voltammetry of Ferrocene at Macroelectrodes

The oxidative voltammetry of 0.925 – 0.957 mM ferrocene in 0.1 M TBAP/acetonitrile and varying concentrations of polyethylene glycol (PEG) at a 3 mm platinum electrode is shown in figure 31. A reversible one electron oxidation is observed at approximately 0.5 V *vs.* Ag is observed, with a corresponding reduction wave at approximately 0.4 V *vs.* Ag.

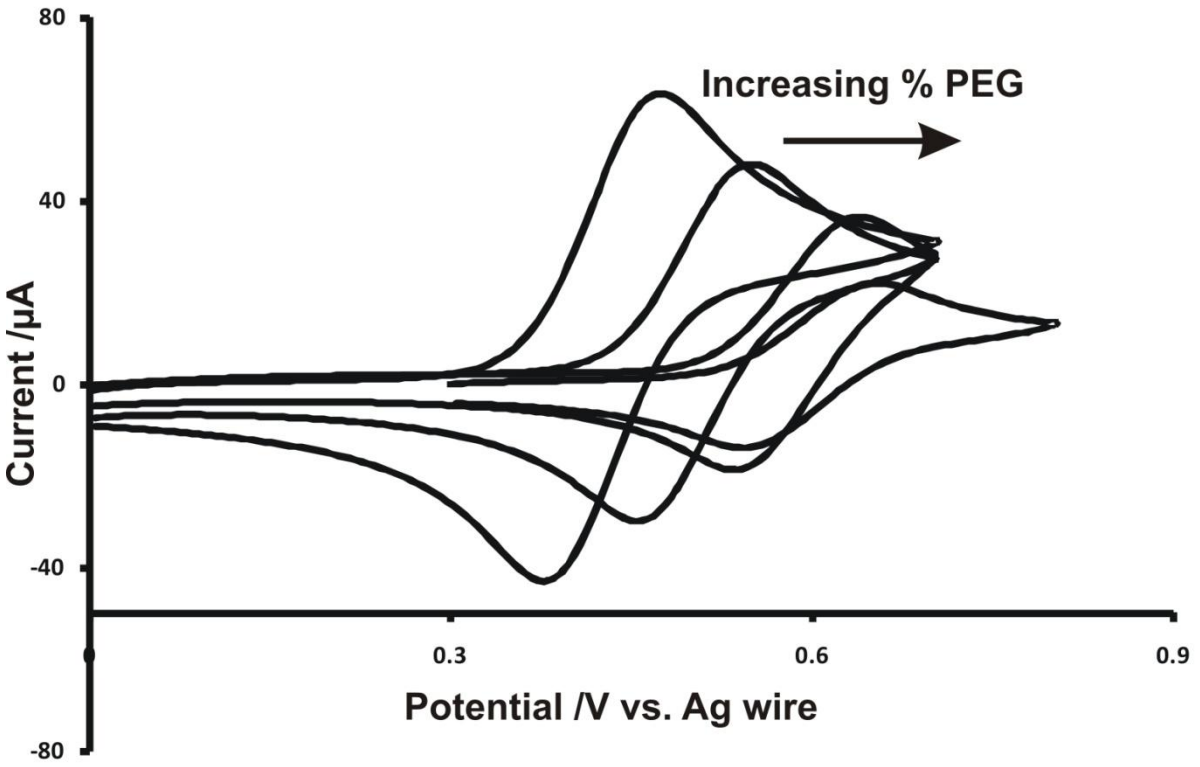

Figure 31: Cyclic voltammetry of ~ 1 mM ferrocene in 0.1 M TBAP/acetonitrile with increasing concentrations of PEG, scan rate = 0.5 V s^{-1}.

The voltammetry demonstrates a shift to more positive potentials with increasing PEG concentrations, indicating the oxidative process becomes more difficult to achieve. This makes intuitive sense, as with increasing PEG concentration the viscosity of the solution increases and considering the Stokes-Einstein equation:

$$D = \frac{k_B T}{6\pi\eta r}$$

Equation 5-16: Stokes-Einstein equation

where k_B is the Boltzmann constant (1.381 x 10^{-23} J K^{-1}), T is the temperature (K), η is the viscosity (P) and r is the radius of the electrode (m). The diffusion coefficient is inversely proportional to the viscosity of the solution and hence the diffusion coefficient should decrease with increasing viscosity, causing the oxidation to become more difficult to achieve

as diffusion to the electrode surface becomes inhibited. Table 5-1 demonstrates this trend, with D determined via a plot of $v^{1/2}$ *vs.* the peak current yielding a linear graph, and the calculation of D from the gradient as given by Randles-Sevick (see equation 1-56).

% PEG	Gradient	D /cm^2 s^{-1}
0	96.148	2.769×10^{-5}
10	71.538	1.641×10^{-5}
25	52.616	8.876×10^{-6}
50	32.819	3.453×10^{-6}

Table 5-1: Diffusion coefficients for the oxidation of ferrocene on 0.1 M TBAP/acetonitrile in the presence of varying concentrations of PEG.

Also demonstrated is a decreased oxidative and reductive current in concert with the shift in peak potentials, once again demonstrating that the diffusion of material to the electrode surface is impeded by the more viscous solutions. Also noteworthy is the effect of the increasing PEG concentration on the shape of the voltammogram, *i.e.* the reversibility of the process becomes less pronounced. As planar diffusion is dominant at macroelectrodes, these observations taken together would suggest that the viscosity of the solution severely affects planar diffusion in a negative manner. In order to further investigate the effect of viscosity on diffusion coefficients the voltammetry of ferrocene at microelectrodes with the presence of PEG was explored.

5.4.2 The Effect of Viscosity on the Voltammetry of Ferrocene at Microelectrodes

The electrochemical oxidation of 0.957 mM ferrocene in 0.1 M TBAP/acetonitrile at a 25 µm platinum disc electrode is shown in figure 32. A one electron wave is observed, with a half wave potential, $E_{1/2}$, at 0.456 V *vs.* Ag and a limiting current of 12.67 nA. Using the following equation:

$$i_{\lim} = 4nF\sqrt{D_z D_r}\, r_0 c_0$$

Equation 5-17

a $\sqrt{D_z D_r}$ value of 2.74 x 10^{-5} cm^2 s^{-1} is obtained, satisfyingly similar to the value of 2.3 x 10^{-5} cm^2 s^{-1} shown previously in literature.[16] Determination of the theoretical current anticipated was undertaken for this system using the following relationship:

$$i = 4nF\sqrt{D_z D_r}\, r_0 c_0 \frac{1}{1+\exp\left\{-\frac{F}{RT}\left(E - E_{1/2}\right)\right\}}$$

Equation 5-18

This is represented by the dashed line in figure 32, and as shown, it is clear that there is a pleasing match between experiment and theory.

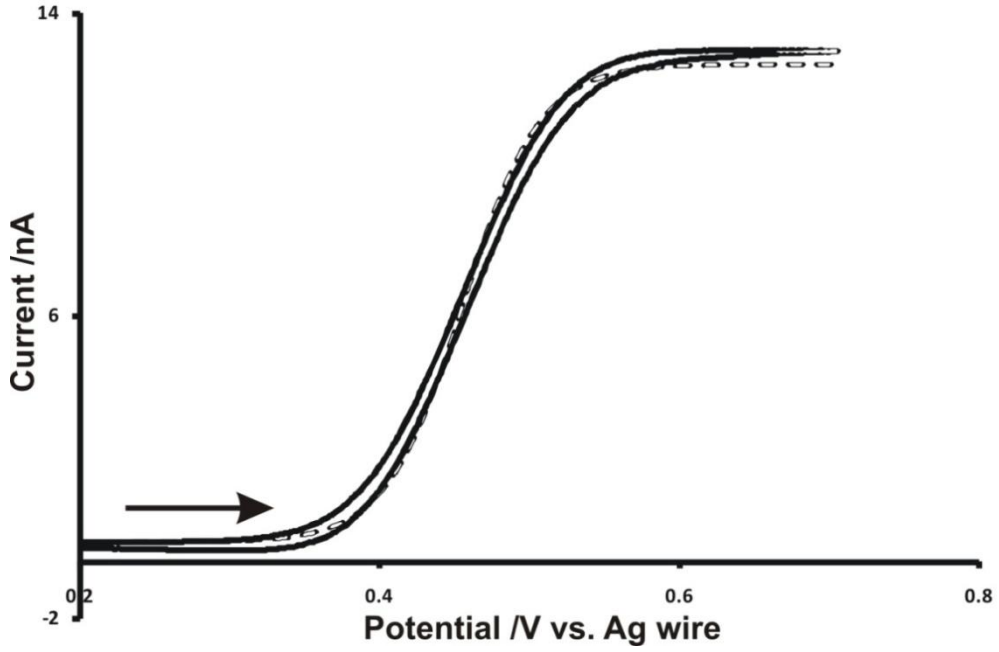

Figure 32: Steady state voltammogram of 0.957 mM ferrocene in 0.1 M TBAP/acetonitrile at a 25 µm platinum disc electrode, v = 0.02 v s^{-1} (solid line). The arrow indicates the direction of the scan. The dashed line represents the theoretical current anticipated for an electrochemically-reversible oxidation with $\sqrt{D_z D_r}$ = 2.74 x 10^{-5} cm^2 s^{-1} and a $E_{1/2}$ value of 0.456 V.

Having established this, attention turned to investigating the effect of viscosity on the value of $\sqrt{D_z D_r}$, and exploring the axiosymmetric anisotropic diffusion.

Table 5-2 illustrates the voltammetric data obtained under steady state conditions for 0.925 mM ferrocene in 0.1 M TBAP/acetonitrile with varying concentrations of polyethylene glycol (PEG). The addition of the PEG altered the viscosity of the solution and hence, as expected, had an immediate effect on the diffusion coefficients.

% PEG	**$E_{1/2}$ /V *vs.* Ag**	**i_{lim} /nA**	**$\sqrt{D_z D_r}$ /cm^2 s^{-1}**
0	0.456	12.67	2.74×10^{-5}
10	0.529	8.53	1.91×10^{-5}
25	0.616	5.38	1.21×10^{-5}
50	0.601	2.36	5.29×10^{-6}

Table 5-2: Experimental data for steady state voltammograms of 0.925 mM ferrocene in 0.1 M TBAP/acetonitrile and various concentrations of PEG

Obviously as the solution became more viscous, the diffusion coefficient decreases as would be logically expected from the Stokes-Einstein equation as described earlier.

Attention then turned to data obtained via potential step chronoamperometry, with the potential at the working electrode held at a potential corresponding to the transport-limited current in the potential sweep voltammetry. Using the Shoup and Szabo expression as outlined in section 5.2, a theoretical current was obtained and thus compared to that obtained experimentally in order to determine MSAD values.

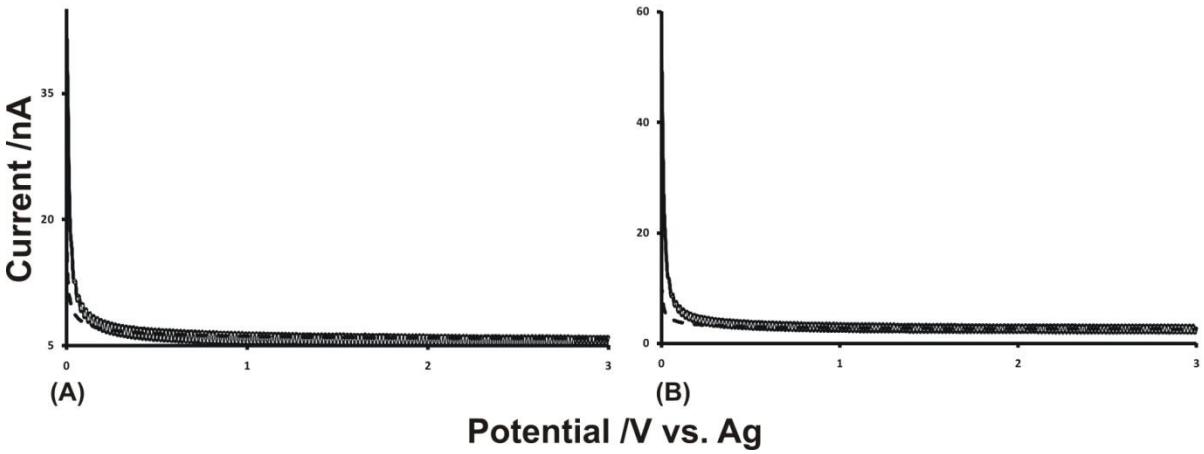

Figure 33: Chronoamperometric transients for (A) 0.925 mM ferrocene + 25% PEG, (B) 0.925 mM ferrocene + 50% PEG illustrated by the solid lines. Dashed lines represent the theoretical currents as determined by the Shoup and Szabo expression.

MSAD values were calculated using equation 5-15. Table 5-3 illustrates the MSAD values afforded from the data, with acceptable values obtained for each concentration of PEG.

% PEG	MSAD
0	0.0034
10	0.130
25	0.157
50	0.0492

Table 5-3: MSAD values from potential step chronoamperometry data

Following the successful application of this theory to this ferrocene/PEG system, attention was moved to the voltammetry of ferricyanide in cæsium pentdecafluorooctanoate/D_2O mixture. This system has been employed previously in the study of diffusion anisotropy,[93] however using two macroelectrodes positioned at right angles to each other to determine anisotropy ratios. By using microelectrode and applying the theory already established and proven using the ferrocene/PEG system, this ferricyanide in cæsium pentdecafluorooctanoate/D_2O system can be further investigated.

5.4.3 Voltammetry of Ferricyanide in Cæsium Pentadecafluorooctanoate and D_2O Mixture at a Microelectrode

The steady state voltammetry of the electrochemical reduction of 12.5 mM ferricyanide in a cæsium pentadecafluorooctanoate/D_2O mixture is shown in figure 34. A one electron wave is observed with a half wave potential ($E_{1/2}$) at 0.17 V *vs.* Ag and a limiting current of 11.8 nA. This allows a $\sqrt{D_z D_r}$ value of 2.1 x 10^{-6} cm^2 s^{-1} to be calculated, which in terms of the viscosity of this system is encouragingly smaller than the diffusion coefficient of ferricyanide in aqueous systems, given as 8.96 x 10^{-6} cm^2 s^{-1} at 298 K.[15] Also shown in figure 34 is a theoretical waveshape for the electrochemical reduction of ferricyanide, given the calculated value of $\sqrt{D_z D_r}$, and once again using equation 5-17 to determine the waveshape. It can be seen that there is reasonable agreement between theory and experiment.

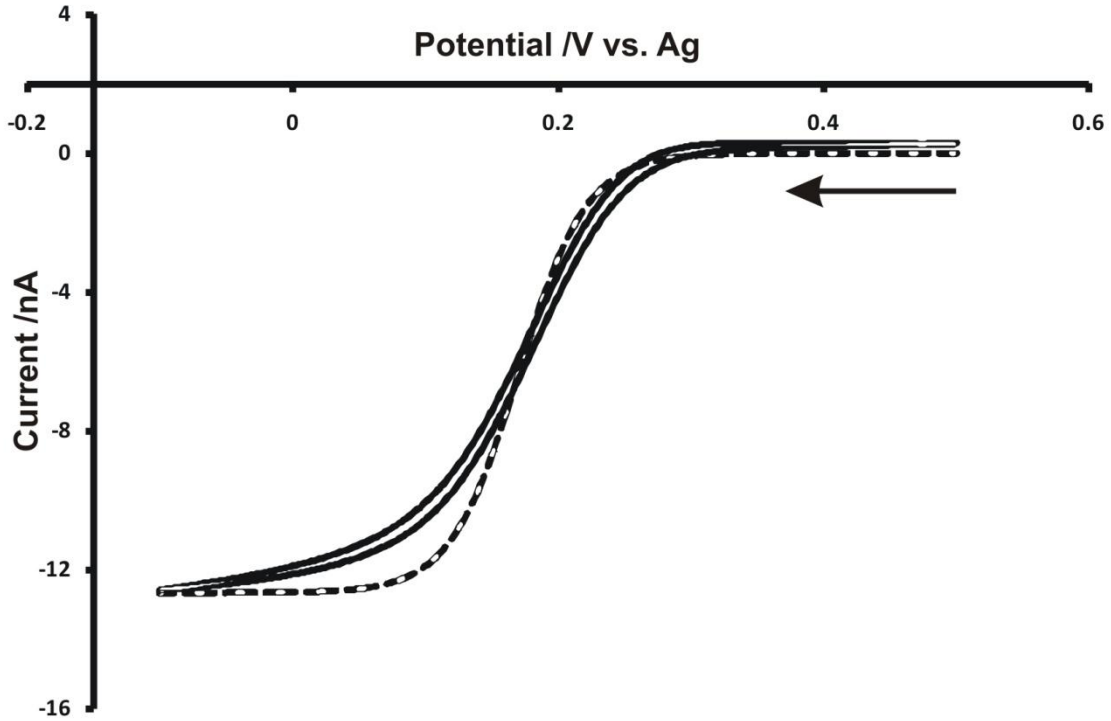

Figure 34: Steady state voltammogram for the reduction of 12.5 mM ferricyanide in cæsium pentadecafluorooctanoate/D_2O at a25 µm platinum disc microelectrode. The arrow indicates the direction of the scan and the dashed line represents the theoretical waveshape expected.

In order to better determine individual values for D_z and D_r, attention then turned to the data obtained via potential step chronoamperometry, shown in figure 35. The working electrode was held at a potential relating to the transport limited current as determined in the cyclic voltammetry, and analysis via iterative methods and computer simulations performed by Dr. Jay Wadhawan (see appendix 2) afforded transients with best fits when $D_z = 1.3 \pm 0.2 \times 10^{-6}$ cm^2 s^{-1} and $D_r = 2.2 \pm 0.2 \times 10^{-6}$ cm^2 s^{-1}. Hence, given that the $\sqrt{D_z D_r}$ value corresponds to the geometrical mean of D_z and D_r, $\sqrt{D_z D_r} = 1.7 \pm 0.2 \times 10^{-6}$ cm^2 s^{-1}, which is within the experimental error of the value obtained via the steady state data.

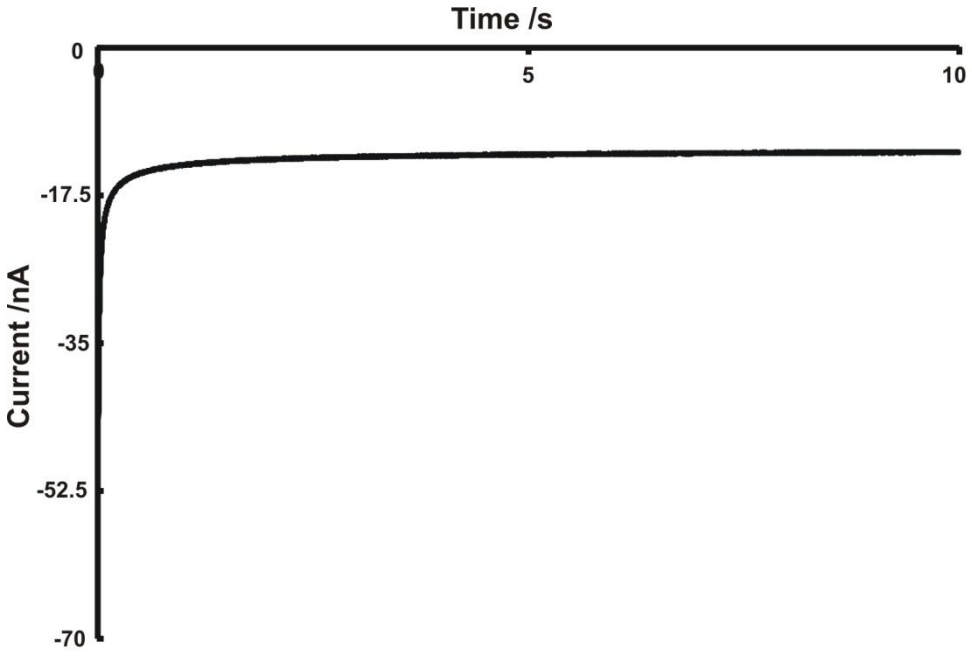

Figure 35: Chronoamperometric transients for 12.5 mM ferricyanide in cæsium pentadecafluorooctanoate/D_2O at a 25 µm platinum disc electrode.

The values afforded for D_z and D_r suggest an anisotropic ratio (D_r/D_z) of 1.7, suggesting that the radial diffusion is slightly dominant over the planar diffusion. If we consider the lamellae structure of the cæsium pentadecafluorooctanoate/D_2O mixture, shown in figure 36,[96] this suggests that the radial direction of the electrode is more closely aligned parallel to the lamellae, *i.e.* perpendicular to the macroscopic director.

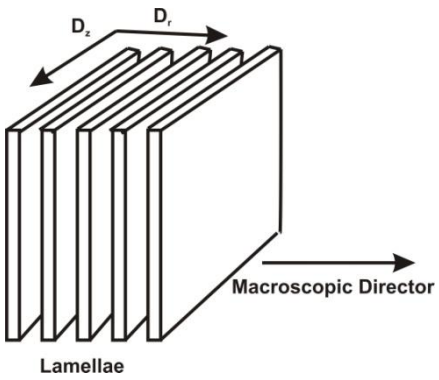

Figure 36: Cæsium pentadecafluorooctanoate/D_2O lamellae structure[96]

On the basis of this deduction, *i.e.* that the radial direction of the electrode is parallel with the lamellae, and assuming that the molecular ordering of the lamellae is not affected by the introduction of the electrode, then radial diffusion, D_z, characterises movement through the lamellae as described above and planar diffusion, D_r, represents aqueous diffusion of ferricyanide. Ferricyanide is a hydrophilic and highly charged ion; hence it is thought to exist mainly in the aqueous phase, allowing its movement through the aqueous layers between the lamellae.[96]

5.5 Conclusions

The aim of this study was to explore and present theory for the case of two-dimensional diffusion anisotropy in axiosymmetric systems. Following investigations into the theory of anisotropic diffusion, a ferrocene/PEG in acetonitrile system was examined in order to test this theory and to determine the effect of viscosity on the diffusion coefficients, and also if it was possible to investigate the anisotropy by effectively "blocking" either D_r or D_z. Voltammetry at macroelectrodes demonstrated the effect of the introduction of PEG into the system and consequently the effect of increasing viscosity, with planar diffusion to the electrode severely inhibited by the increase in viscosity. Microelectrode studies allowed a

value of $\sqrt{D_z D_r}$ to be calculated, and determination of a theoretical current utilising this value provided excellent symmetry between theory and experiment. The effect of viscosity on the steady state data was also investigated, with similar results to that of the macroelectrode, with decreasing $\sqrt{D_z D_r}$ values afforded with increasing viscosity, consistent with the Stokes-Einstein equation.

Following the successful application of the theory to the ferrocene/PEG case, attention was then focussed on a ferricyanide in cæsium pentadecafluorooctanoate/D_2O system. Previous studies with macroelectrodes had begun to establish the anisotropy ratios of this system, and through the use of microelectrodes the theory confirmed via the ferrocene/PEG system was applied in order to determine separate values for D_z and D_r and hence obtain a value for the anisotropic ratio. Once again the calculated value of $\sqrt{D_z D_r}$ afforded a theoretical waveshape with reasonable agreement between theory and experiment, and a value reassuringly smaller than the diffusion coefficient of ferricyanide in aqueous systems. Data obtained via potential step chronoamperometry allowed the determination of D_z and D_r separately through iterative methods, with $D_z = 1.3 \pm 0.2 \times 10^{-6}$ cm^2 s^{-1} and $D_r = 2.2 \pm 0.2 \times 10^{-6}$ cm^2 s^{-1}. These values afford an anisotropic ratio of 1.7, suggesting that radial diffusion (D_z) is slightly dominant over planar diffusion (D_r), and considering the lamellae structure of the cæsium pentadecafluorooctanoate/D_2O mixture, inferring that the radial direction of the electrode surface is more closely aligned parallel to the lamellae.

Overall, axiosymmetric anisotropic diffusion to disc shaped microelectrodes has been examined, with theoretical expressions accurate for the isotropic case found to be suitable for employment in this case providing that the isotropic diffusion coefficient is replaced by the geometrical mean of the diffusion coefficients for the planar and radial diffusion. Good

agreement was obtained between experiment and theory, and of the determined anisotropy ration with the literature.

6 Anion Sensing Using Electro-generated Ferrocene Surfactants

Continuing with the investigation of the local environment of an electrode surface, the triple phase boundary between the electrolyte surface, the organic redox liquid and an aqueous solution was investigated in terms of anion sensing. Of course, a liquid│liquid interface is itself a naturally anisotropic condensed phase system, linking with the previous chapter. This work has been accepted for publication in Electrochemistry Communications.

6.1 Aims and Scope

The use of chemically modified electrodes in electrochemistry has grown rapidly since 1976[97] finding applications in a number of fields including ionic liquids[98] and electroanalysis.[99,100] Redox liquids immobilised on an electrode surface allow the investigation of electrochemistry at a triple phase boundary between the electrolyte surface, the organic redox liquid and an aqueous solution. Particularly, ion transfer processes across liquid│liquid interfaces are of great interest in chemistry and biology, with living cells functioning through these kinds of interfaces.

As a consequence of electron transfer reactions at these liquid│liquid interfaces, electro-neutrality must be maintained within the immobilised liquid at the electrode surface, hence ion-transfer processes occur according to the Gibbs energy of transfer of the electrolyte anion. When this value is low, the anions transfer across the interface however when the value is high the anions do not transfer across, instead electro-generated ions are expulsed from the immobilised droplet into the aqueous solution. In general, the most hydrophobic anions will cross from the aqueous phase to the organic phase most readily.[99] Accordingly, the entire process is thought to exist under thermodynamic control. Assisted ion transfer in

this manner has attracted a plethora of research, with this type of chemistry at the liquid | liquid interface providing an elegant technique for sensing applications.[99-102]

To facilitate development of these sensing techniques, it is essential to ascertain and investigate suitable organic precursors so that the chemistry, kinetics and mechanisms are fully understood prior to sensing applications being sought. Generally, compounds which do not dissolve into the bulk aqueous even following electron transfer and consequently are unable to contribute to the signal via diffusion processes are desirable. Subsequently compounds with large, bulky, hydrophobic components are used, a range of which have already been explored.[99,103,104] These are predominantly compounds, or based on compounds, whose solution phase voltammetry is well established. Previous work has also shown that the structure of the organic pre-cursor has significant effects on the ion transfer processes at the liquid | liquid interface,[105] with the addition of simple chemical groups causing significant changes in the anion selectivity and the observed voltammetry.

This section is concerned with the redox chemistry of immobilised microdroplets of two liquid crystal ferrocene compounds (see figure 37) with different numbers of redox active moieties. Ferrocene electrochemistry is historically well known and well established, the large hydrophobic backbones of the two compounds here hoping to serve to decrease the potentiality of the compound dissolving into the bulk aqueous solution at any point through the electron transfer reaction. By deducing the electrochemistry and mechanisms of both compounds immobilised onto glassy carbon electrodes and immersed into various aqueous electrolyte solutions, the feasibility of then using these compounds as sensors/sensory mediators can be explored.

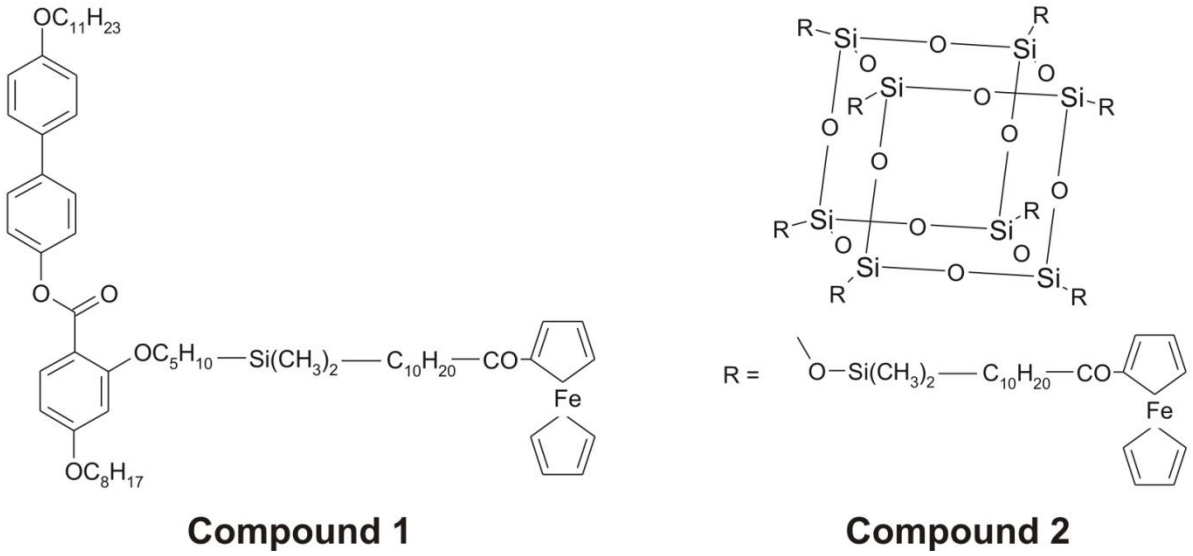

Compound 1 **Compound 2**

Figure 37: Structures of the Ferrocene Liquid Crystals

6.2 Experimental

6.2.1 Instrumentation

Electrochemical measurements were undertaken as outlined in section 2.1. In all cases, a three-electrode was employed, with a platinum wire counter electrode and a standard calomel electrode as the reference electrode. The working electrode in all cases was a 3 mm glassy carbon electrode (Metrohm, Switzerland). Before and after each set of electrochemical experiments the working electrode surface was polished as outlined in section 2.1 and unless otherwise stated, all experiments were carried out at 22 ± 3 ^{o}C.

6.2.2 Reagents

The solvent used for all solutions of the ferrocene liquid crystal compounds was dichloromethane (Fisher Scientific, UK), used without further purification. Aqueous solutions of perchloric acid, (Aldrich, UK) potassium dihydrogen orthophosphate, (Fisher Scientific, UK) potassium hexafluorophosphate, (Fluka, UK) potassium bromide, (BDH Laboratory

Supplies, UK) potassium chloride, (Fluka, UK) potassium fluoride, (BDH Laboratory Supplies, UK) sodium perchlorate (Sigma Aldrich, UK) and sodium sulphate (Fisher Scientific, UK) were prepared as described in section 2.2. All reagents were purchased at the purest commercially available grade.

6.2.3 Synthesis of the Ferrocene Liquid Crystals

The ferrocene liquid crystals were synthesised by Dr. Georg Mehl and Dr. Daniela Apreutesi using the following procedures.

6.2.3.1 **4-Octyloxy-2-{5-[1,1,3,3-tetramethyl-3-(11-oxo-11-ferrocenyl-undecyl)-disiloxanyl]-pentyloxy}**

6.2.3.2 **-benzoic acid 4'-undecyloxy-biphenyl-4-yl ester**

Ten to twenty drops of platinum (0)-1,1,3,3-tetramethyl-1,3-diviynldisiloxane (Karstedt catalyst) were added to a stirred solution containing one equivalent of 1-Ferrocenyl-undec-10-en-1-one and two equivalents of 4-Octyloxy-2-[5-(1,1,3,3-tetramethyl-disiloxanyl)-pentyloxy]-benzoic acid 4'-undecyloxy-biphenyl-4-yl ester dissolved in 15 mL of dry toluene. The solution was then dried with compressed air bubbled through the reaction mixture for one minute, followed by overnight stirring at room temperature. The solvent was then removed under reduced pressure and the residue purified by column chromatography with dichloromethane:hehanes in a ratio 2:1; this was followed by size exclusion chromatography on a sephadex column (LH20). The reaction yield was 51%.

6.2.3.3 **Octakis Ferrocene Liquid Crystal**

With dried compressed air bubbling through the reaction mixture for one minute, 25 drops of platinum (0)-1,1,3,3-tetramethyl-1,3-diviynldisiloxane (Karstedt catalyst) were added to a stirred solution containing one equivalent of Octakis(dimethylsilyloxy)silsesquioxane and

sixteen equivalents of 1-Ferrocenyl-undec-10-en-1-one (Fc1) dissolved in 15 mL of dry toluene. The reaction was allowed to stir overnight at room temperature before the solvent was removed under reduced pressure and the residue purified by column chromatography on silica gel with dichloromethane:ethyl acetate (10%). The reaction yield was 72%.

6.2.4 Procedures

6.2.4.1 **Immobilisation of the Ferrocene Liquid Crystals on the Electrode Surface**

The working electrode was modified with the redox active liquid microdroplet by solvent evaporation of a 10 μL aliquot of a 0.2 – 0.5 mM stock solution of the compound in dichloromethane.

6.3 Results and Discussion

The electrochemical characteristics of the mono-ferrocene liquid crystal (compound 1) were investigated first before moving on to the more complex and potentially exciting octakis ferrocene liquid crystal (compound 2), the structures of which are shown in figure 37.

6.3.1 Electrochemistry of immobilised mono ferrocene liquid crystal

Figure 38 illustrates the voltammetry of 0.28 mM of compound 1 immobilised on the surface of a glassy carbon electrode and immersed into 5 different solutions of aqueous perchloric acid in the concentration range $0.05 \leq [HClO_4]\ /M \leq 1$, at a scan rate of 0.005 Vs^{-1}. Three consecutive scans are shown. All voltammograms consist of a sharp oxidation and reduction, with splitting of the wave at higher scan rates in the lower concentrations (shown in figure 41). A broad, shallow peak is also observed at lower potentials, this will be discussed further later.

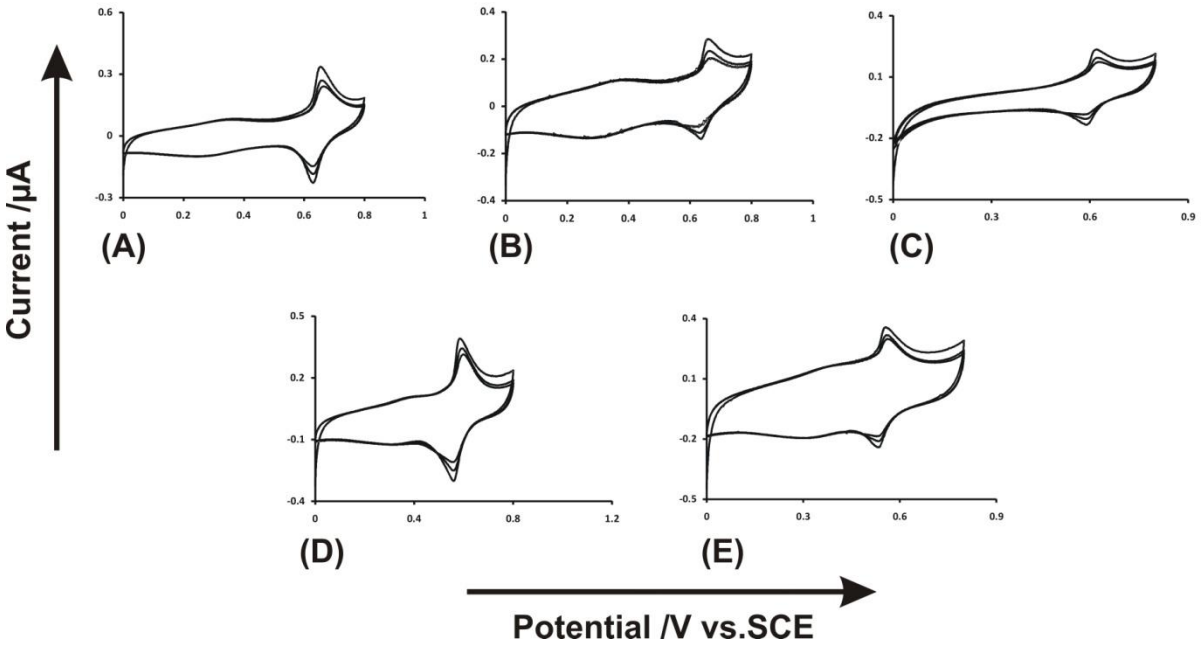

Figure 38: Current-Voltage plots for 0.28 mM of compound 1 immobilised on a 3mm glassy carbon electrode submerged in (A) 0.05 M (B) 0.1 M (C) 0.2 M (D) 0.5 M and (E) 1 M perchloric acid.

The timescale of the experiment is long (0.005 Vs^{-1}) and it is at these slow scan rates that we observe sharp oxidation and reduction peaks with minimal peak to peak separation. At faster scan rates, the peaks become slightly broader and the peak to peak separation increases, as demonstrated in figure 39 which illustrates the relationship of the peak potentials and the timescale of the experiments. This characteristic plot is observed at all concentrations of perchlorate and indicates that as the timescale of the experiment decreases, mass transport processes also becomes involved, most likely in the oil phase.

The voltammetry shown in figure 38 demonstrates a slight decrease in both oxidative and reductive currents at the peak observed at 0.5 – 0.65 V vs. SCE, indicating the loss of the oxidised species from the electrode surface in a similar manner to that previously reported for butyl-ferrocene:[103]

$$\boldsymbol{Fc_1SiM_{(l)} - e^- \rightleftharpoons Fc_1^+SiM_{(aq)}}$$

Considering the size of the molecule and the length of the hydrophobic chain, it is difficult to contemplate the entire molecule being expelled from the droplet. Therefore it is presumed that the oxidised species leaves the surface of the droplet in the micellar form, especially considering the surfactant properties of the compound.

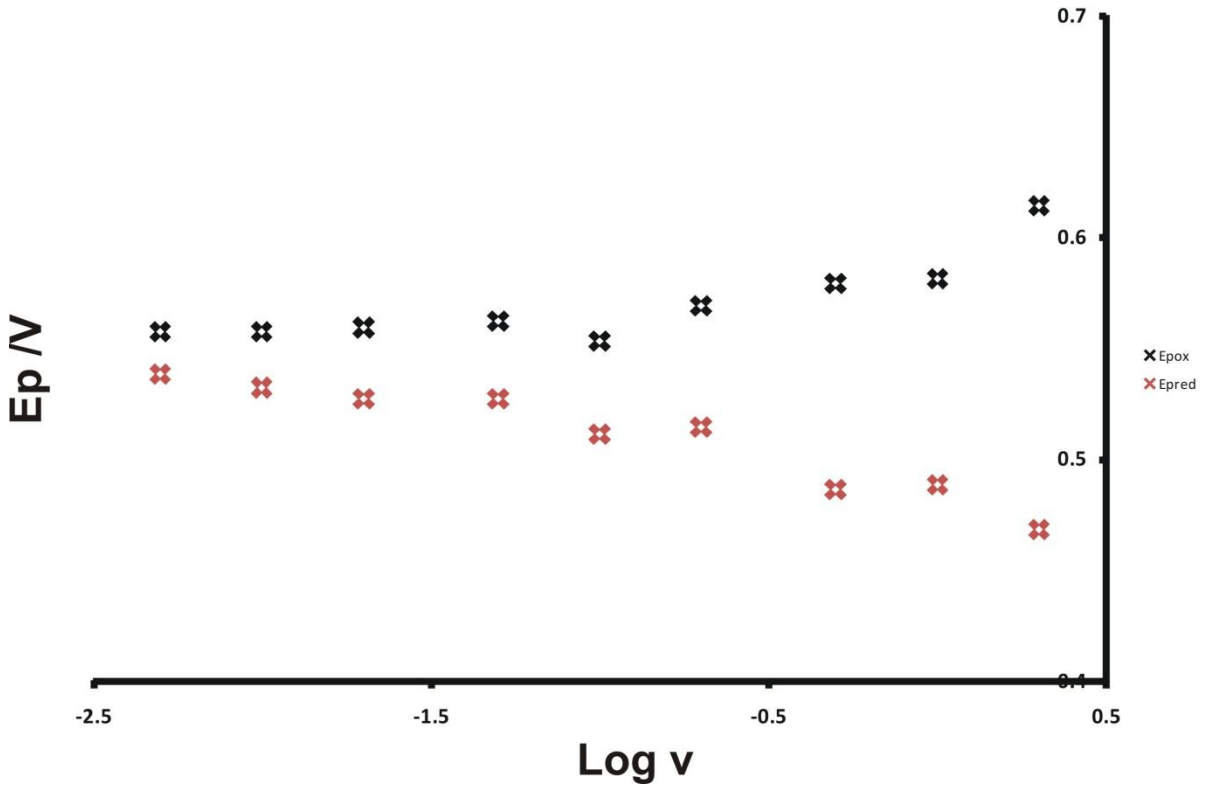

Figure 39: Plot showing the effect of scan rate on the peak potentials, 0.28 mM of compound 1 immobilised on a 3mm glassy carbon electrode submerged in 1 M perchloric acid

It can be seen from figure 39 and table 6-1, that as the concentration of perchlorate anions decreases, the oxidation becomes more difficult to achieve indicating that the process occurs, likely in concert with an ion-pairing process.

$[HClO_4]$ /M	E_{pox} /V	i_{pox} /µA
0.05	0.655	0.203
0.1	0.659	0.121
0.2	0.621	0.105
0.5	0.584	0.235
1	0.557	0.146

Table 6-1: Oxidation potentials of Compound 1 in Various Concentrations of Perchloric Acid

Further investigation of the voltammograms in figure 38 reveal a broad oxidation peak at approximately +0.3 V *vs.* SCE with a corresponding reduction peak on the reverse sweep. This is seen at all concentrations of perchloric acid to some extent, excluding 0.1 M, and the broadness of the peaks would suggest some adsorption phenomena. If this is considered further and together with the sharp oxidation peak at higher potentials, this would suggest that there is a degree of adsorption of the liquid crystal producing the broad peak at approximately +0.3 V *vs.* SCE, whilst the sharp peak at 0.5 – 0.8 V *vs.* SCE (dependant on perchloric acid concentration) is attributed to the bulk of the droplet film on the electrode surface. If this is all taken together, a "breathing mode" of the droplet may be considered. Upon oxidation of the liquid crystal, the film expands as the anion adsorbs on to the surface of the immobilised droplet at the three-phase boundary countering the charge on the ferrocenium cation and forming a gel-like surface adsorbed state. This electrochemistry occurs at the surface of the droplet and accounts for the broad oxidation and reduction peaks. The sharp peak can then be attributed to the formation of the ferrocenium cation within the droplet in an ion-pairing process as previously described.

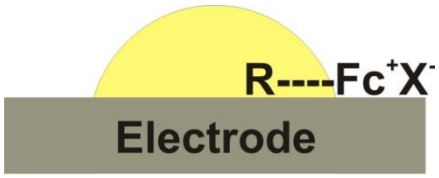

Figure 40: Surface adsorption of the anion

In contrast to the slower scan rates, rather than observing two separate peaks, splitting of the oxidation wave at 0.5 – 0.65 V *vs*. SCE occurs with lower concentrations of perchlorate when the timescale of the experiment is small (shown in figure 41). Also, the current magnitude is maintained over consecutive scans in both the oxidation and reduction peak, suggesting some anion insertion into the droplet, again in an ion-pairing process. The splitting of the waves becomes more pronounced at lower concentrations of perchlorate, *i.e.* when the concentration of water is highest suggesting that water co-inserts with the anion with the higher water concentration accentuating the splitting of the wave. This is in contrast to the findings of Evans *et. al*.,[103] who found that increasing the concentration of perchlorate anions enhanced the splitting of the wave. The splitting of the wave in this case was attributed to the ferrocene adsorbing to the electrode surface, with one signal from the adsorbed compound and the second from the solution phase compound; however the fulfilment of the electroneutrality pseuodo-condition was achieved via ion expulsion in contrast to the anion insertion case described in the work herein.

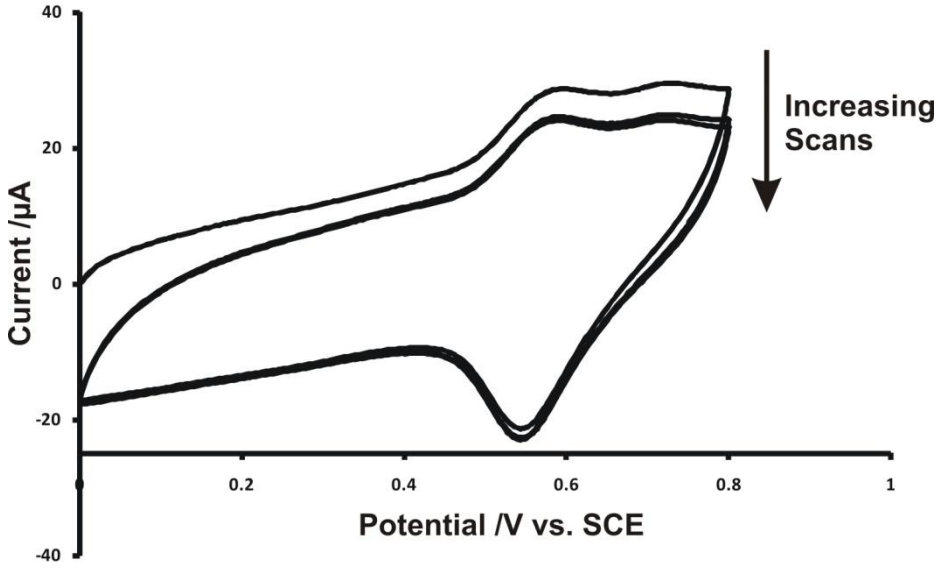

Figure 41: Current-Voltage plots for 0.28 mm of compound 1 immobilised on a 3 mm glassy carbon electrode submerged in 0.05 M perchloric acid, 2 Vs^{-1}.

The current/voltage characteristics of a glassy carbon electrode modified with compound 1 and soaked in a 0.1 M solution of compound 1 for 16 hours varied significantly from those observed in figure 38, shown in figure 42, providing further evidence that the anion is inserting into the oil phase. If the voltammetry had been similar, this would have suggested that the cation formed upon oxidation was dissolving into the aqueous phase.[103]

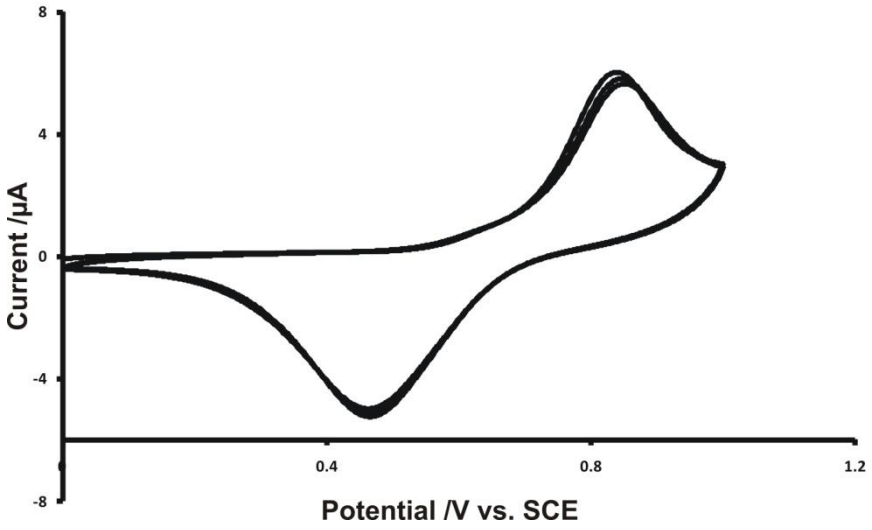

Figure 42: Glassy carbon electrode modified with compound 1, and soaked in 0.1 M of compound 1 overnight, voltammetry in 0.1 M perchloric acid

In order to further investigate the biphasic voltammetry of compound 1, a number of different 0.1 M aqueous anion solutions were used as the supporting electrolyte, the voltammograms of which are illustrated in figure 43. Sodium perchlorate and potassium hexafluorophosphate demonstrate similar voltammetric behaviour to that shown by the perchloric acid, therefore the oxidation of compound 1 at the electrode surface is accompanied by the micellar loss of the oxidised form lost from the electrode surface.

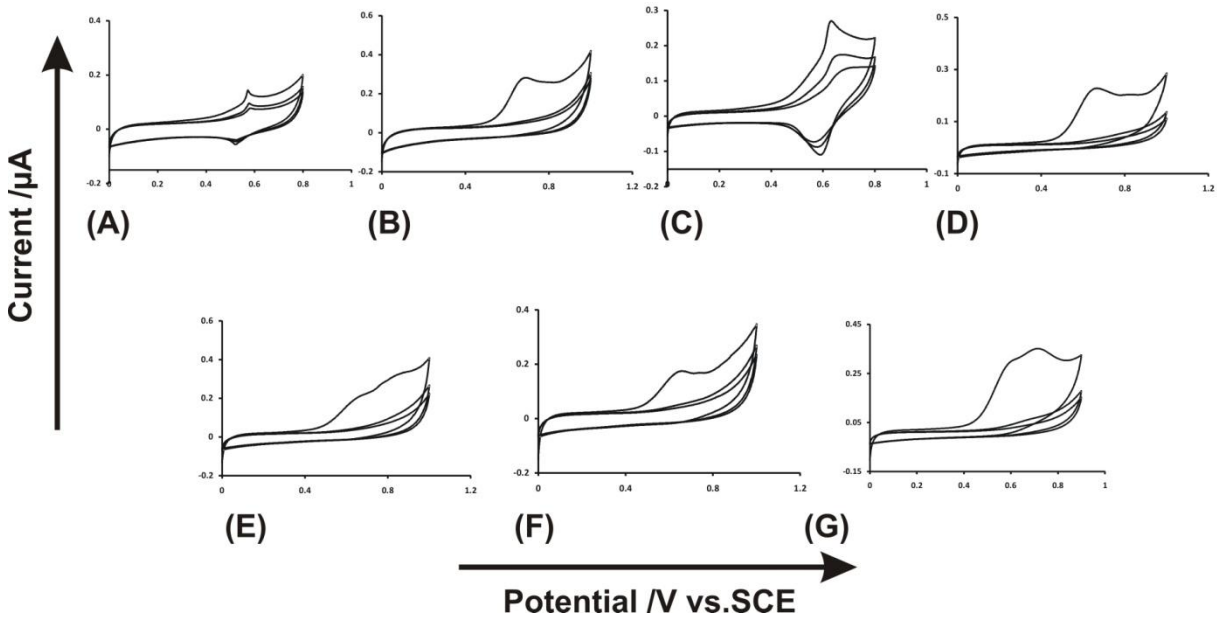

Figure 43: Current-Voltage plots for 0.28 mM of compound 1 immobilised on a 3 mm glassy carbon electrode submerged in 0.1 M (A) KPF_6 (B) KH_2PO_4 (C) $NaClO_4$ (D) Na_2SO_4 (E) KNO_3 (F) KCl (G) KF. Scan rate = 0.005 Vs^{-1}

As shown in table 6-2, there is very little effect on the peak potentials when changing the cation present to sodium, a feature also observed in previous work.[103]

Anion	E_{pox} /V	i_{pox} /µA
PO_4^-	0.691	0.257
PF_6^-	0.573	0.048
Cl^-	0.656	0.148
F^-	0.716	0.048
NO_3^-	0.663	0.174
$NaClO_4$	0.629	0.128
SO_4^{2-}	0.670	0.028

Table 6-2: Oxidation potentials of compound 1 in different anion solutions

Voltammetry of compound 1 in the presence of potassium hexafluorophosphate shows an oxidation peak at a potential more negative than those shown for both sodium perchlorate and perchloric acid at the same concentration. Hexafluorophosphate is the most hydrophobic of the three anions, and it has been shown previously that the more hydrophobic anions will pair

with cations in the organic phase more readily,[99] hence making the oxidation easier and shifting the oxidation potential to a more negative value.

The remaining anions considered differed in their voltammetry quite significantly, as illustrated in figure 43. The voltammetry of compound 1 in phosphate, chloride, fluoride and sulphate shows a more dramatic loss of signal after the first redox cycle at slower scan rates. With the exception of potassium chloride, no reduction peak corresponding to the oxidation is observed on the first cycle until the higher scan rates, *i.e.* ≥ 0.5 Vs^{-1}, at which point the loss of current signal also begins to decrease. Once again, the loss of current signal can be attributed to the loss of the redox species at the electrode surface; again in the micellar form as seen with the perchlorate ions. This also explains the lack of a reduction peak, as the electro-generated cation diffuses into the aqueous solution and away from the electrode surface, thus rendering the electron transfer irreversible, which is more pronounced at the slower scan rates where there is sufficient experimental time prior to the reductive potentials being attained for the electro-generated cation to diffuse away from the electrode surface. At the faster scan rates the timescale of the experiment is less and hence some electro-generated cation may remain within the diffuse layer allowing the re-reduction to take place. This also explains the lack of unity in the ratio of oxidative and reductive current where it is present, with some cation having already diffused into the aqueous layer before the potential is swept back to reductive potentials.

Both the phosphate and the chloride anion cause a splitting of the oxidative wave at higher scan rates; in this case this is more comparable to the butylferrocene case[103] with the cation expulsion. Consequently the splitting here can be explained by a degree of adsorption of the compound to the electrode surface resulting in a signal from the adsorbed component and a

signal from the bulk component of the droplet at slightly different potentials and hence a splitting of the wave.

6.3.2 Electrochemistry of Solution Phase Compound 2

Compound 2 contains eight ferrocene moieties, one on each corner of the cubic shaped molecule, hence the possibility of the transfer of eight electrons, either in multiple steps or a single step. Solution phase voltammetry, as shown in figure 44, was used as a preliminary diagnostic tool in order to determine if the loss of eight electrons in one step was in fact occurring. The voltammetry showed a single oxidation peak at 0.7 – 0.8 V *vs.* silver wire with an immediate reduction peak also observed at 0.5 – 0.6 V *vs.* silver wire. No further peaks were observed, even within a wider potential window. This suggests that eight electrons are indeed transferring in the one step. The peak-to-peak splitting (> 0.1 V at slower scan rates and > 0.2 V at scan rates of 1 V s^{-1} and greater), and slanted peaks shown in the voltammetry suggest that the kinetics of the electron transfer are slow.

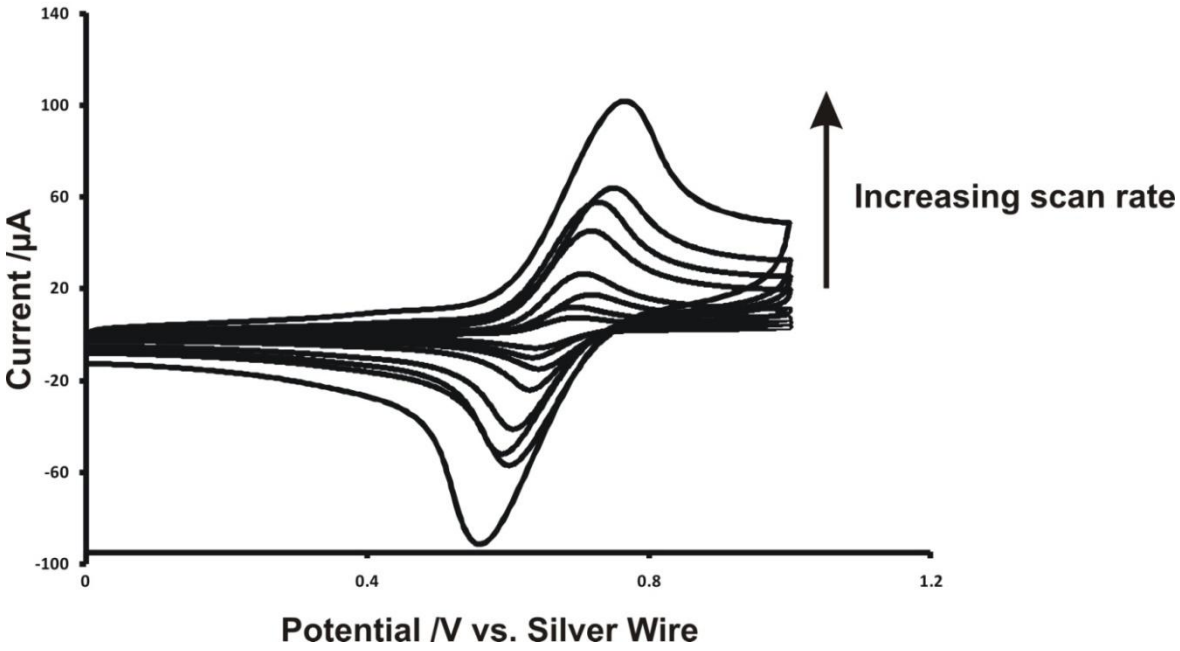

Figure 44: 0.29 mM Octakis ferrocene liquid crystal in DCM with 1 M TBAP, solution phase voltammetry, 3 mm glassy carbon electrode

In order to further investigate this, the voltammetry of the compound immobilised onto an electrode surface and submerged in various anion solutions was undertaken.

6.3.3 Electrochemistry of Immobilised Compound 2

Figure 45 illustrates the voltammetry of 0.44 mM of compound 2 immobilised onto the surface of a glassy carbon electrode and immersed into 5 different solutions of perchloric acid in the concentration range $0 \leq M \leq 1$, at a scan rate of 0.005 Vs^{-1}. Three consecutive scans are shown once again, consisting of a single oxidation and one or two reductions. Compound 2 oxidises at more negative potentials than compound 1, hence it is easier to oxidise although the shift is relatively small.

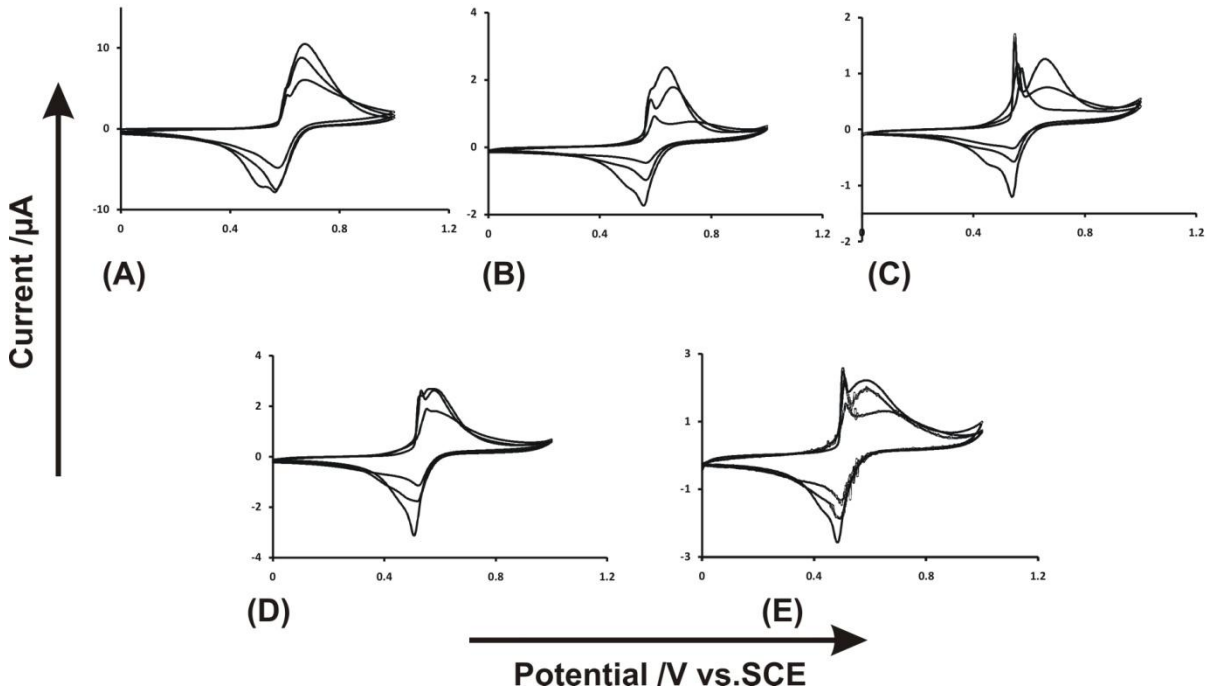

Figure 45: Current-voltage plots for 0.44 mM of compound 2 immobilised on a 3mm glassy carbon electrode submerged in (A) 0.05 M (B) 0.1 M (C) 0.2 M (D) 0.5 M and (E) 1 M perchloric acid.

Other voltammetric characteristics are similar, with splitting of the oxidation peak, and the lower the perchloric acid concentration, the harder the oxidation as shown in table 6-3 and providing evidence of an anion facilitated process.

$[HClO_4]$ /M	E_{pox} /V	i_{pox} /µA
0.05	0.673	9.99
0.1	0.636	2.16
0.2	0.549	1.15
0.5	0.561	2.47
1	0.502	1.70

Table 6-3: Oxidation potentials of compound 2 in various concentrations of perchloric acid

However trends in the splitting relating to scan rate and perchloric acid concentration are not apparent, for example, with 1 M and 0.1 M perchloric acid the peak splitting becomes more pronounced with increasing scan rate, whilst with 0.5 M and 0.05 M the splitting decreases with increasing scan rate. In contrast to compound 1, considering the oxidative and reductive potentials as functions of the timescale of the experiment does not lead to the expected characteristic plot, indeed the reductive peak is independent of the experimental timescale, with erratic values obtained with the oxidation peak.

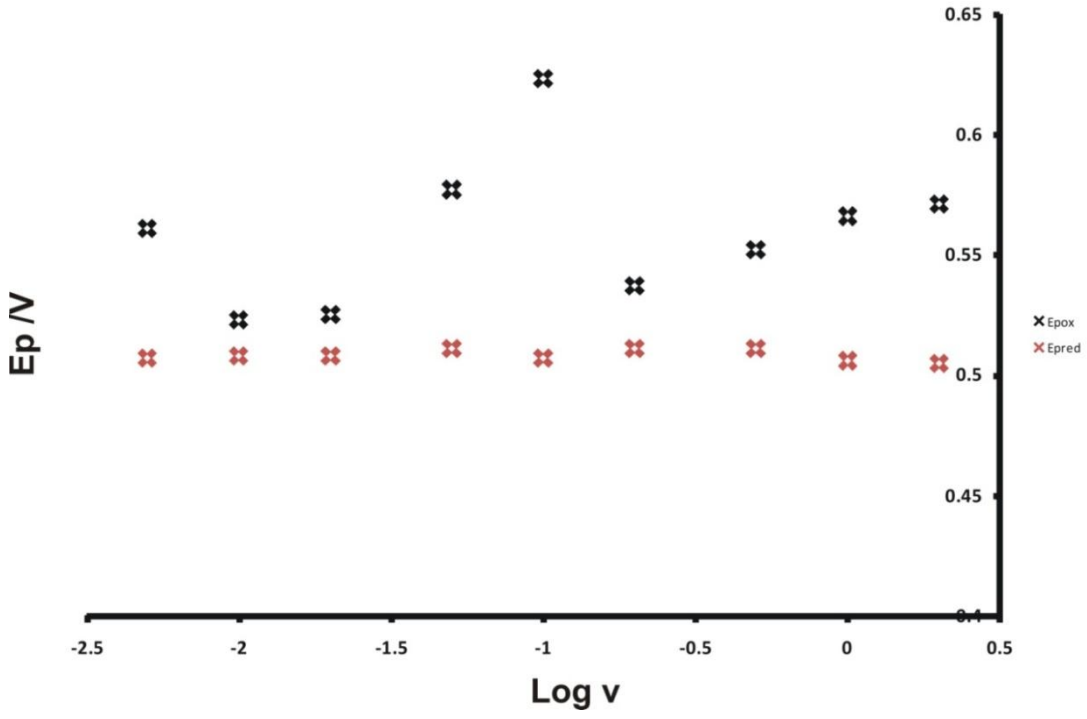

Figure 46: Plot showing the effect of scan rate on the peak potentials, 0.44 mM of compound 2 immobilised on a 3mm glassy carbon electrode submerged in 0.5 M perchloric acid

This could indicate that either (1) the oxidative product may be adsorbing to the surface of the electrode, or (2) the oxidative product remains immobilised at the electrode surface, either of which would also begin to explain the slightly unpredictable redox response on consecutive scans. At scan rates greater than 0.05 or 0.01 Vs^{-1} the magnitude of the current augments slightly with consecutive scans, together with the splitting of the peak which could be expected with the adsorption element. Any adsorption would also account for the lack of trends when considering the varying concentrations, as reproducibility would become difficult. The current signal is not decreasing to any significant degree, and as mentioned in fact increases on occasions. Therefore in a similar manner to compound 1, the oxidation of immobilised compound 2 is accompanied by the insertion of the perchlorate anion forming an ion pair. The result of this oxidation affords a product which adsorbs to the electrode surface; the overall reaction is given in scheme 6-1.

$$R(Fc)_{8(oil)} - e^- \rightleftharpoons R(Fc)^+_{8(oil)}$$

$$R(Fc)^+_{8(oil)} + X^- \rightleftharpoons R(Fc)^+_8 \cdots X^-_{(ads)}$$

Scheme 6-1

The reduction peak is also split at all perchloric acid concentrations, indeed two peaks may be present, particularly at higher scan rates.

Through analysis of the integrated charge under the sharp pre-wave and also that of the main wave, the amount of charge attributed to the pre-wave can be determined and this can then begin to explain the splitting of the peak and the process causing it. Such analysis (see appendix 3) demonstrated that on average the very sharp pre-wave accounted for 20% of the overall charge, representing the dominance of surface chemistry due to the restrictions imposed on the molecule in the oil phase. As a cube, the ferrocene moieties lie on each

vortex, consequently when considering the redox process at the droplet surface, not all the ferrocenium cations formed upon oxidation will be at the surface. Therefore in order to form an ion pair with the anion the molecule will rotate in order to bring the ferrocenium cation to the surface, creating a torque on the molecule as it rotates. This would explain the sharp splitting of the wave, as the molecule rotates allowing further ferrocene moieties to the surface of the droplet, promoting the anion-driven process. Full dissolution of the molecule (*i.e.* the solution phase voltammetry) allows full rotation so that ion-pairing of all the ferrocene moieties becomes possible, hence only one oxidation wave observed in the solution phase voltammetry.

In a similar manner to compound 1, the electrochemistry of the immobilised compound was further investigated by using a number of different 0.1 M aqueous anion solutions as the supporting electrolyte, the voltammograms of which are illustrated in figure 47.

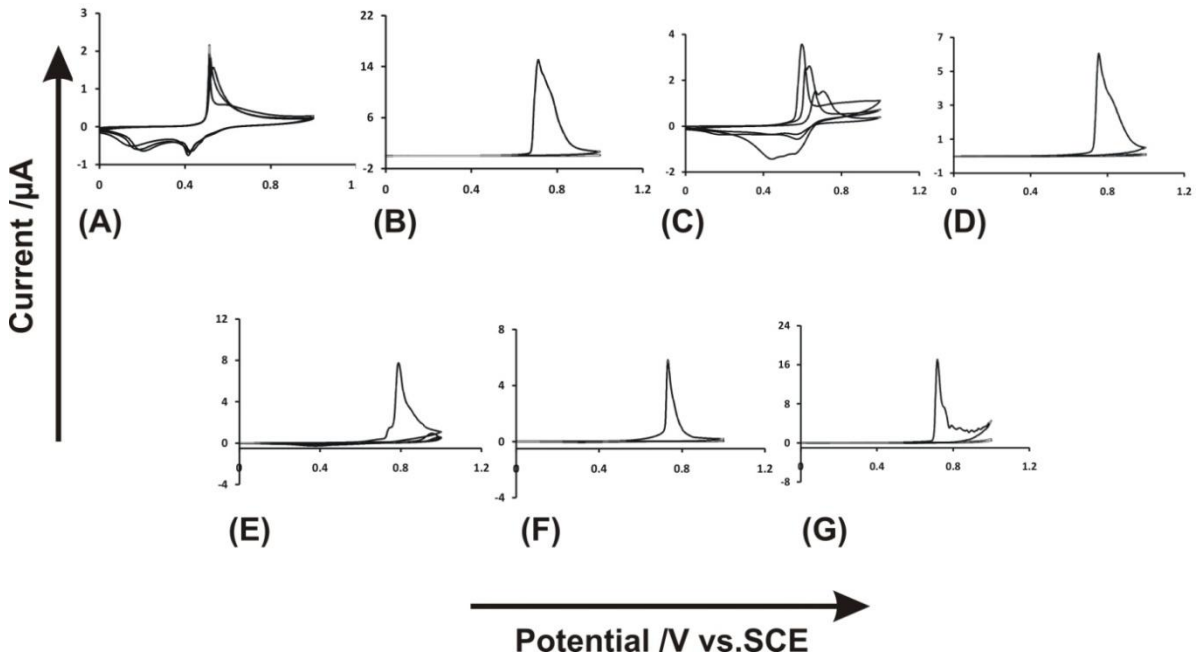

Figure 47: Current-Voltage plots for 0.44 mM of compound 2 immobilised on a 3mm glassy carbon electrode submerged in 0.1 M (A) KPF_6 (B) KNO_3 (C) $NaClO_4$ (D) Na_2SO_4 (E)KF (F) KCl (G) KBr. Scan rate = 0.005 Vs^{-1}

The voltammetry of compound 2 in potassium hexafluorophosphate (figure 47 (A)) shows similar characteristics to that of the perchloric acid, with minimal change in oxidative current with consecutive scans; once again indicating anion insertion behaviour. A shoulder peak is observed in the oxidative voltammetry at faster scan rates, together with a corresponding shoulder on the reduction peak. This reduction peak also becomes broader with increasing scan rate; while plots of the oxidative and reductive peak potentials varying with the scan rate reveal scattered data. However in general, as the oxidative potential becomes more positive with increasing scan rate, the reduction potential becomes more negative and hence the peak to peak separation increases.

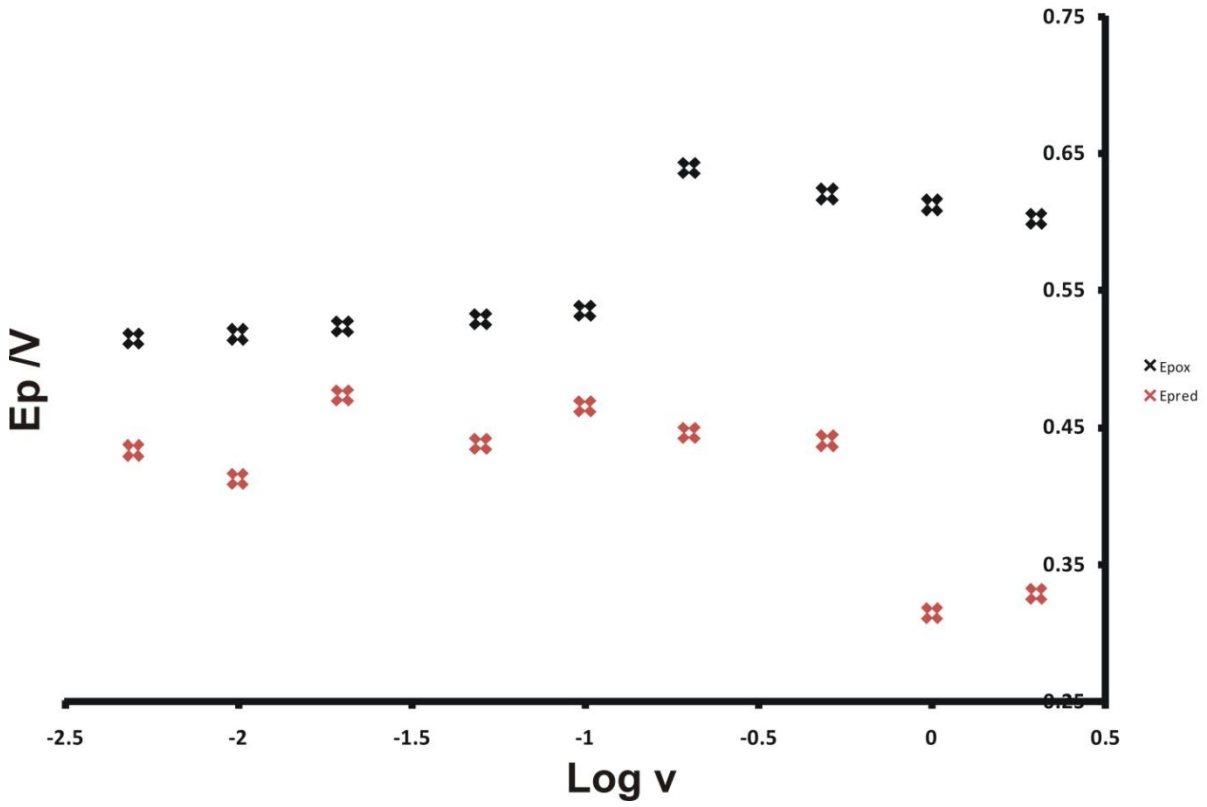

Figure 48: Plot showing the effect of scan rate on the peak potentials, 0.44 mM of compound 2 immobilised on a 3mm glassy carbon electrode submerged in 0.1 M KPF_6

Similar to compound 1, the oxidation of compound 2 occurs at more negative potentials in the presence of potassium hexafluorophosphate than in the presence of perchloric acid, again this can be explained by the more hydrophobic nature of the hexafluorophosphate anion.

Also similar to compound 1, in the presence of the remaining more hydrophilic anions compound 2 demonstrated differing behaviour consistent with the full oxidative release of the redox oil deposits into the aqueous phase in the micellar form. The halide anions demonstrate similar behaviour, with the bromide causing oxidation at the most negative potential and fluoride the least negative of the three. The voltammetry of all three is also very similar demonstrating comparable characteristics with sharp, bell-shaped oxidation peaks at longer experimental timescales with no corresponding reduction peak. The oxidation becomes broader from 0.05 Vs^{-1} and greater together with a corresponding reduction peak, until at 2 Vs^{-1} the oxidation is lost, however the reduction is still present. In contrast to compound 1, some voltammetry was observed in the presence of bromide anions; however this was limited to a narrow range of scan rates. The voltammetry of compound 2 in the presence of the halide anions results in the same mechanism as compound 1, *i.e.* oxidation accompanied by the expulsion of micelles of the redox droplet, however the voltammetry itself is far more spectacular, with total loss of signal at longer timescales and large, sharp bell-shaped peaks.

Therefore compound 2 demonstrates some similar behaviour to compound 1, with both anion insertion and cation expulsion characteristics demonstrated, particularly the oxidative release of the redox oil droplets into the aqueous phase, depending upon the anion present. However, the novelty arises from the compound itself, and in the explanations formed for the voltammetric behaviour observed, *i.e.* the rotation of the molecule upon oxidation.

6.4 Conclusions

The voltammetric behaviour of two ferrocene liquid crystal compounds immobilised onto the surface of a glassy carbon electrode has been investigated. Both compounds demonstrated typical ion transfer processes across the liquid | liquid interface, with both anion insertion and cation expulsion processes demonstrated. As described, these ion transfer processes occur as a consequence of the electron transfer reactions at the liquid | liquid interface, with ions transferring across the interface in order to maintain electro-neutrality within the immobilised droplet.

Compound 1, the mono ferrocene liquid crystal, was found to demonstrate a "breathing mode" upon oxidation, particularly in the presence of perchloric acid. Upon oxidation, the anion adsorbs on to the surface of the immobilised droplet at the three-phase boundary countering the charge on the ferrocenium cation and forming a gel-like surface adsorbed state, the droplet expands. As described, the voltammetry exhibits two peaks, and it is the first, broad peak that can be described by this breathing mode. The second, sharp more obvious peak observed can be accredited to the formation of the ferrocenium cation within the droplet in an anion-facilitated process.

Compound 2, a liquid crystal compound with eight ferrocene moieties, one on each corner of the cube-shaped molecule had the potential to increase the analytical signal eight-fold, hence significantly increasing the analytical sensitivity. Solution-phase voltammetry demonstrated a single oxidation peak with a corresponding reduction peak, suggesting the transfer of eight electrons in a single step. Further investigation with the immobilised compound found that in fact Compound 2 demonstrates some rotation upon oxidation, as the charged species moves closer to the surface of the droplet in order to form an ion pair with the corresponding anion.

Cation expulsion characteristics were also demonstrated in some of the supporting electrolytes for both compounds, this would appear a little improbable due to the size and hydrophobic nature of the anchoring fragment of the molecule. It is therefore suggested that the entire charged molecule is not expelled from the droplet; rather the charged portion of the molecule, i.e. the ferrocenium cation is expelled from the surface and the liquid | liquid interface, as shown in figure 40.

By exploring the electrochemistry of these ferrocene liquid crystals and beginning to understand the mechanisms and kinetics that are occurring, it is then possible to apply this knowledge to sensing techniques. It has been shown herein that the liquid crystal compounds behave in differing manners in the presence of different anions, and it is this concept that could be taken further and applied to the sensing of anions.

7 Cation Sensing Using "Intelligent" Environment Design

The local environment of the electrode surface has proved to be an important consideration of the electrode dynamics, through further exploration of the modification of electrodes via more intelligent consideration of biological processes occurring naturally and attempting to mimic these, smarter sensors may be developed. This work follows preliminary studies by Issah Alhassan, and forms part of a manuscript to be submitted to Physical Chemistry Chemical Physics.

7.1 Aims and Scope

Modified electrodes are widely used in the electro-analytical field in the development of robust and efficient sensors for numerous applications.[99,100] Modification of the electrochemical probe allows the overall sensitivity and selectivity of the sensor to be enhanced due to the altered heterogeneous kinetics compared with those in solution and the altered specificity gained through the modification.[97,106] It is in the design of this local environment of the sensor that the performance of the device can be improved, leading to more novel and efficient sensors to be developed.

In the design of a cation sensor, biofilms were considered due to the inherent ability to chelate with divalent cations through the secretions of the extracellular polysaccharide layer (see figure 49) in an ion sequestration process.[107] It was with this process in mind that the design of the modification of a basal plane electrode for use as a cation sensor was established.

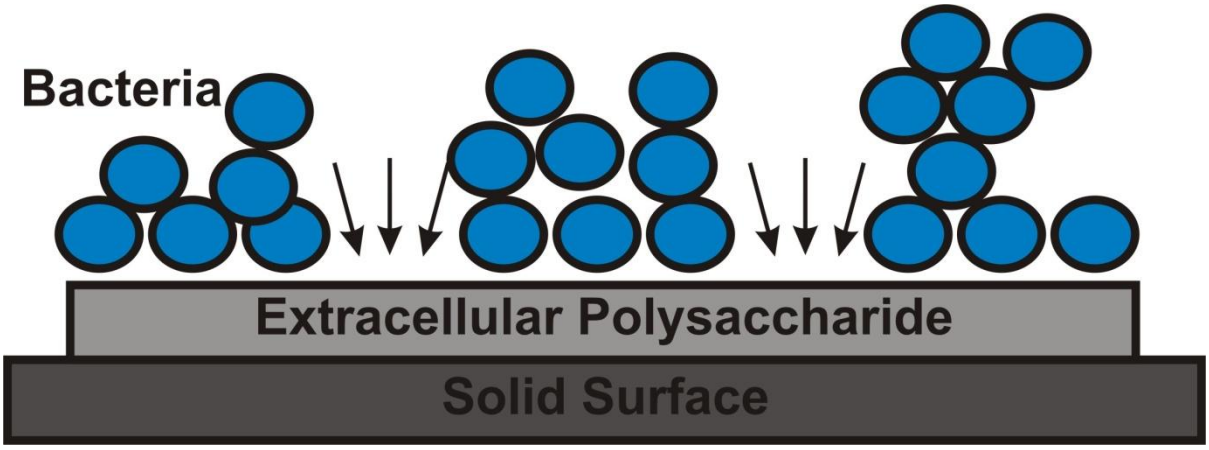

Figure 49: Structure of a biofilm

A schematic of a biofilm is shown in figure 49, with individual bacteria swarming in clusters and excreting an extracellular polysaccharide (EPS) layer. Further consideration of the structure a biofilm allows us to envisage the similarities it can be seen to have with a microelectrode array. The gaps between the bacterial colonies on the surface of the EPS layers can be seen to be analogous to a randomly-sprinkled microelectrode array, with convergent diffusion through those gaps (as indicated by the arrows in figure 49) in a similar manner to that seen with conventional microelectrode arrays.

EPS sequesters divalent cations from solution, and this is the first step in the formation of $CaCO_3$.[108] The aim here is to mimic the EPS whilst also being able to monitor a redox signal; this is achieved in the following way.[108] Upon reduction, diazonium salts form aryl radicals which readily covalently bond to carbon surfaces.[109] Poly-(phenol) layers can then be employed forming a second generation modified electrode, and it is this polymerisation of the phenol that forms a conducting polymer layer, hydrogen bonding to the electro-grafted diazonium salt and acting as the model substance as a basis for the chelation of the cation, *i.e.* the mimicking of biofilm activity.

Alginic acid is thought to readily bind with divalent cations[110] for example Ca^{2+}. It is a linear co-polymer of β-D-mannuronic acid and α-L-glululronic acid; the structure is shown in figure 50.

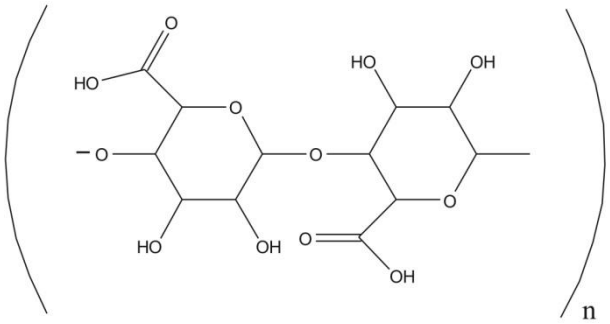

Figure 50: Alginic Acid

By incorporating alginic acid into the poly-(phenol) layer, it was thought that the selectivity of the film towards different cations could be improved due to the inherent affinity the substance possesses for divalent cations.

7.2 Experimental

7.2.1 Instrumentation

Electrochemical measurements were undertaken as outlined in section 2.1. A basal plane electrode (Le Carbone Lorraine, Ltd, constructed in house), diameter 5 mm, was used in all cases, except in the quantitative studies in which a basal plane electrode constructed in house was used, of area 149.5 mm^2. The surface of the electrode was renewed following each experiment by removing basal plane layers from the surface with a scalpel, followed by manual polishing on carburundum paper, grade P4000 (Presi, France).

7.2.2 Reagents

Aqueous solutions of 1 mM phenol (Fisher Scientific, UK) were prepared in 1 M potassium hydroxide (VWR International, UK). 1 mM solutions of Fast Red AL salt (ACROS Organics, Belgium) were prepared in acetonitrile (Fisher Scientific, HPLC Grade, UK) and 0.1 M tetrabutylammonium perchlorate (TBAP, Fluka, UK). The acetonitrile was used as purchased, with no further purification or drying processes employed. Solutions of magnesium chloride (BDH Laboratory Supplies, UK), calcium chloride (BDH Laboratory Supplies, UK), strontium chloride (BDH Laboratory Supplies, UK) and barium chloride (Fluka, UK) were prepared in 1 M hydrochloric acid (Fisher Chemicals, UK).

7.2.3 Procedures

7.2.3.1 **Electro-grafting of Fast Red Al Salt**

1 mM Fast Red AL salt was electro-grafted onto the surface of the electrode *via* the reduction of the compound using cyclic voltammetry in a three electrode system, with a nickel wire serving as the counter electrode and a silver wire providing the reference electrode. The structure of Fast Red AL salt is shown in figure 51.

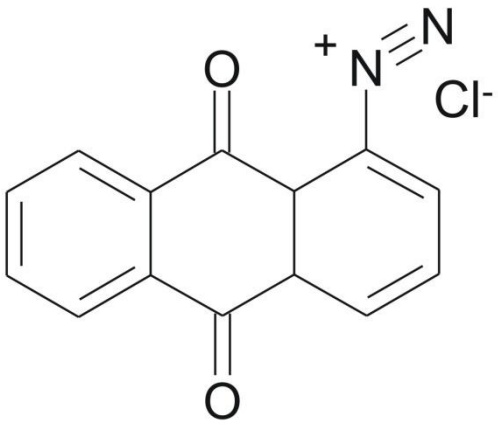

Figure 51: Structure of Fast Red AL salt

The solution was degassed with impurity-free nitrogen prior to voltammetry, and twenty cycles at a scan rate of 0.1 V s^{-1} of the reduction were employed to ensure a sufficient layer on the electrode surface, determined via observing the voltammetry of the modified electrode in aqueous 1 M HCl.

7.2.3.2 **Polymerisation of Phenol**

1 mM phenol was polymerised onto the surface of the electrode via the oxidation of the compound, once again using cyclic voltammetry in a three electrode system as described above, however a saturated calomel electrode was used as the reference electrode. The solution was degassed with impurity-free nitrogen prior to voltammetry, and twenty cycles of the oxidation at a scan rate of 0.1 V s^{-1} were undertaken, once again to ensure that a sufficient layer of the polymer was deposited onto the electrode surface, again determined via voltammetry of the electrode in aqueous 1 M HCl. When the polymerisation of the phenol was preceded by the electro-grafting of the Fast Red AL salt, the electrode was rinsed thoroughly prior to voltammetry to ensure the removal of any excess Fast Red AL salt. When alginic acid was introduced into the system, 5 mM was added to the phenol solution and the polymerisation undertaken.

7.2.3.3 **Voltammetry of the Modified Electrode**

Prior to the voltammetry of the modified electrode in aqueous 1 M HCl and the Group 2 chloride solutions, the electrode was rinsed thoroughly with 1 M HCl. The electrode was submerged in the solution for two minutes prior to the voltammetry whilst impurity-free nitrogen was used to degas both the solution and the polymer film on the electrode surface. The reductive behaviour of the modified electrode was then investigated in Group 2 chloride solutions, with 1 M HCl used as the blank comparative solution.

7.3 Results and Discussion

The sensing capabilities of a basal plane graphite electrode modified with both Fast Red AL salt and phenol were investigated in various solutions of the Group 2 chlorides, before progressing to polymerising the phenol onto the diazonium salt modified electrode in the presence of alginic acid and exploring the effect of the alginic acid on the selectivity of the multi-layer film.

7.3.1 Modification of the Electrode

7.3.1.1 Electro-grafting Fast Red AL Salt onto the Surface of a Basal Plane Graphite Electrode

Diazonium salts are well known to graft to electrode surfaces upon their reduction.[109] Following the procedure as outlined by Allongue *et al.*[109], 1 mM Fast Red AL salt was electro-grafted onto the surface of a 5mm diameter basal plane graphite electrode, the voltammetry of which is shown in figure 52. Twenty consecutive scans were performed in order to ensure a sufficient layer of the diazonium salt was deposited onto the electrode surface.

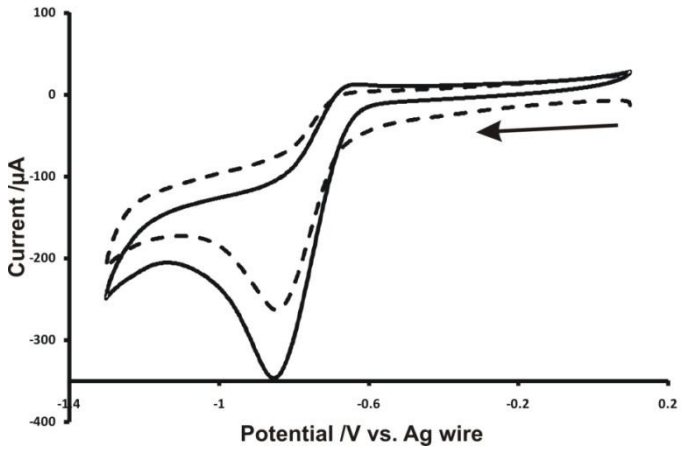

Figure 52: Voltammogram demonstrating the electro-grafting process of the Fast Red AL salt. Scan rate = 0.1 Vs^{-1}, dashed line represents scan 1, black line represents scan 20.

The voltammetry shows a reduction peak at -0.9 V *vs.* SCE silver wire which increases in reductive current with consecutive scans, with a simultaneous slight negative shift in potential. This is explained by the grafted film tending towards saturation, but still allowing constrained diffusion of the cations towards the small gaps between the grafted radicals and subsequently allowing their reduction.[109] In general, aryl radicals covalently attach to a carbon electrode surface in a concerted pathway as shown in figure 53 (A), and consequently, the fast red AL salt upon reduction will graft to the basal plane surface in similar manner, as shown in figure 53 (B).[109]

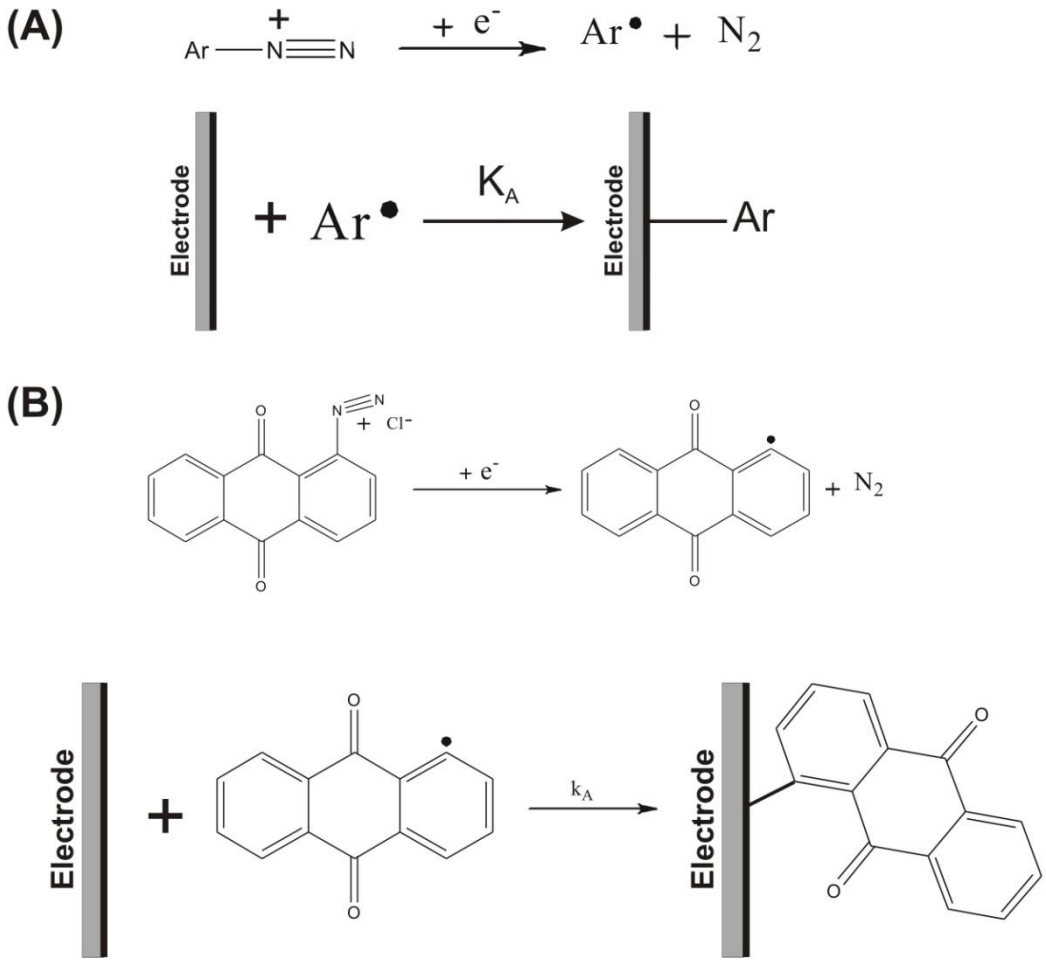

Figure 53: (A) General grafting of aryl radicals to a carbon surface, (B) Electro-grafting of the Fast Red AL salt

The voltammetry of this modified electrode was then investigated in aqueous 1 M HCl, as it is this redox process that forms the basis of the cation sensor. The voltammetry is shown in figure 54 with a reduction peak observed at -0.12 V *vs.* Ag and a corresponding oxidation peak at -0.11 V *vs.* Ag, with the very small peak-to-peak separation (ca. 10 mV) indicative of the adsorbed material and of an electrochemically reversible process.

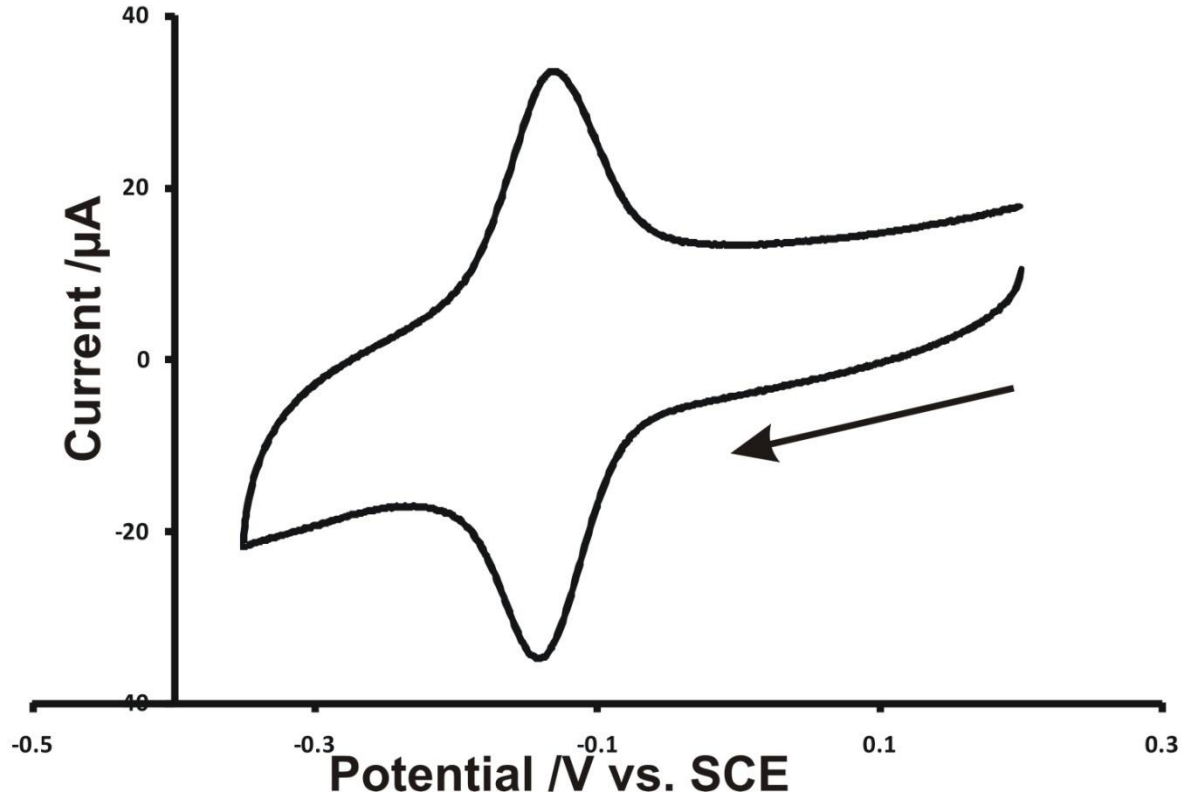

Figure 54: Voltammetry of a basal plane graphite electrode modified with Fast Red AL salt in 1 M HCl

7.3.1.2 **Polymerisation of Phenol onto the Surface of a Basal Plane Graphite Electrode**

In the construction of the modification layers on the electrode surface, phenol was then polymerised on top of the diazonium salt forming a conducting polymer layer and hydrogen-bonding to the grafted diazonium salt. Poly-(phenol) will form on the surface of an electrode upon oxidation;[111] figure 55 demonstrates this process, with the phenol radical formed upon oxidation and consequently polymerising.

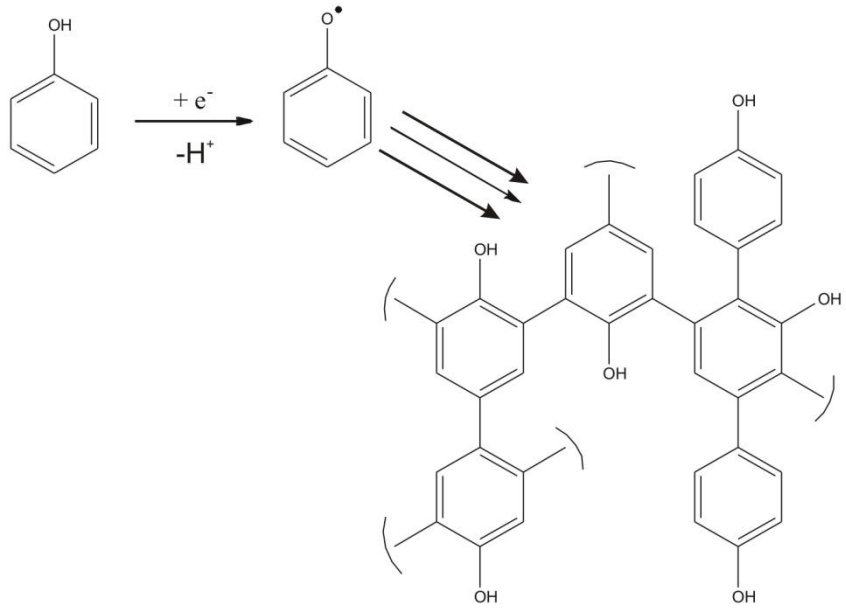

Figure 55: Polymerisation of phenol

The voltammetry of this process is shown in figure 56, with twenty scans performed and the gradual coverage of the electrode surface demonstrated with the consecutive scans and the loss of Faradaic current.

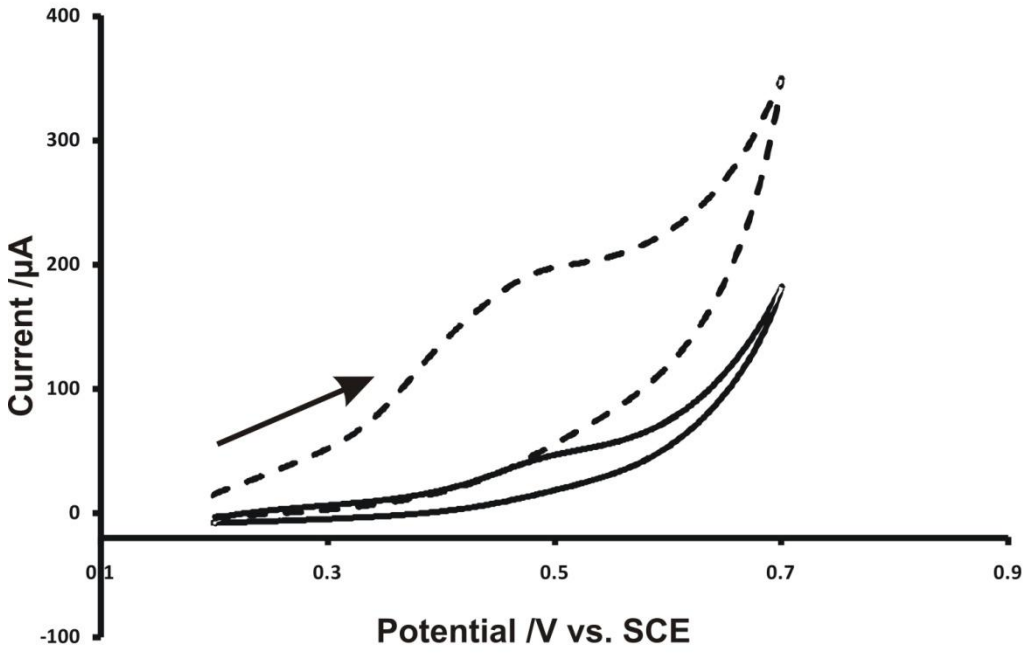

Figure 56: Voltammetry demonstrating the polymerisation of the phenol. Scan rate = 0.1 Vs^{-1}, dashed line represents scan 1, black line represents scan 20.

The voltammetry of the polymerised phenol layer in the absence of the diazonium salt was explored, so as to determine any features due to this layer. This is shown in aqueous 1 M HCl in figure 57.

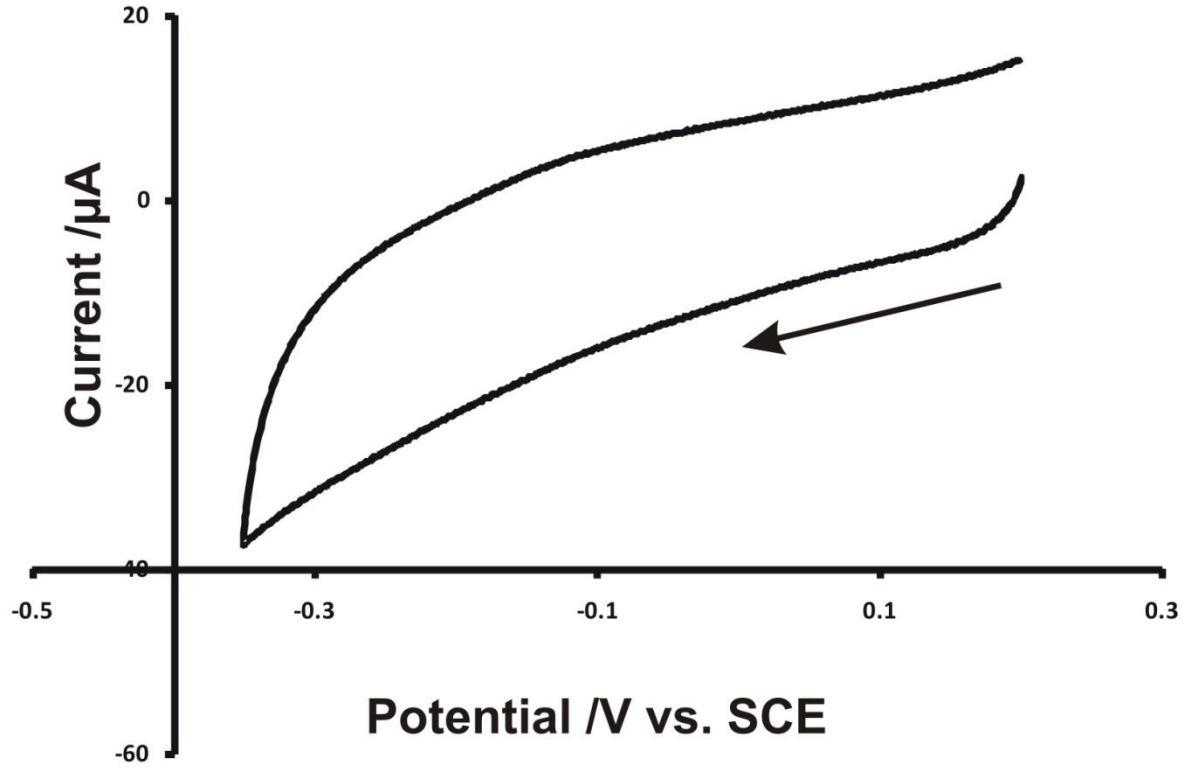

Figure 57: Voltammetry of a basal plane electrode modified with a poly-(phenol) layer in 1 M HCl, scan rate = 0.1 V s^{-1}.

No redox chemistry is observed, as expected when considering the structure of the poly-(phenol) layer.

7.3.2 Voltammetry of the Basal Plane Graphite Electrode Modified with both the Fast Red AL Salt and Poly-(phenol)

The voltammetry of the basal plane electrode modified with both the diazonium salt and the poly-(phenol) was then investigated in aqueous 1 M HCl, illustrated in figure 58.

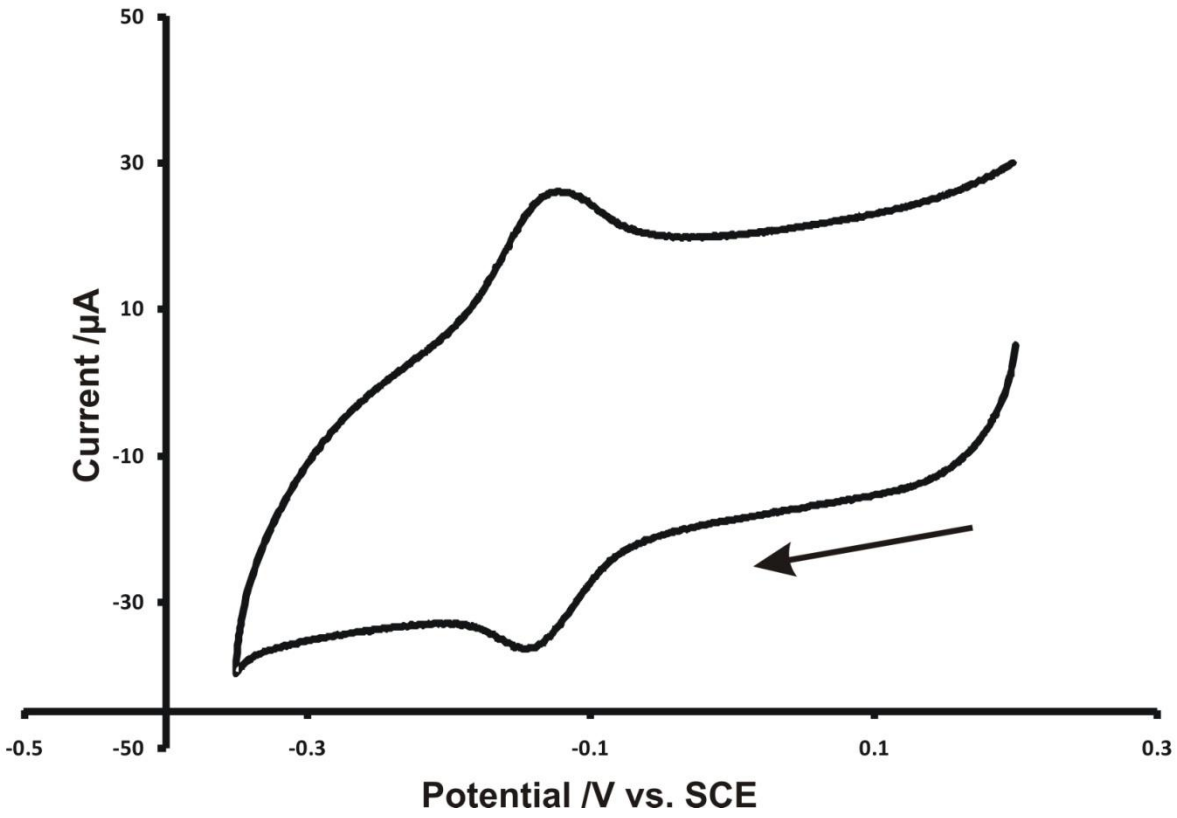

Figure 58: Voltammetry of a basal plane graphite electrode modified with a diazonium salt and poly-(phenol) in aqueous 1 M HCl. Scan rate = 0.1 V s^{-1}.

A reduction peak is observed at -0.15 V vs. SCE, with a corresponding oxidation peak at -0.1 V *vs.* SCE, suggesting electrochemical reversibility and attributed to the reduction of the anthraquinone moiety of the electro-grafted diazonium salt in a two-electron, two proton process, as shown in scheme 7-1. The process is shown as both a single, two electron process and as two one electron reductions, as either mechanism could be followed. As only one peak is observed in the voltammetry it is thought that the single two electron pathway is followed herein.

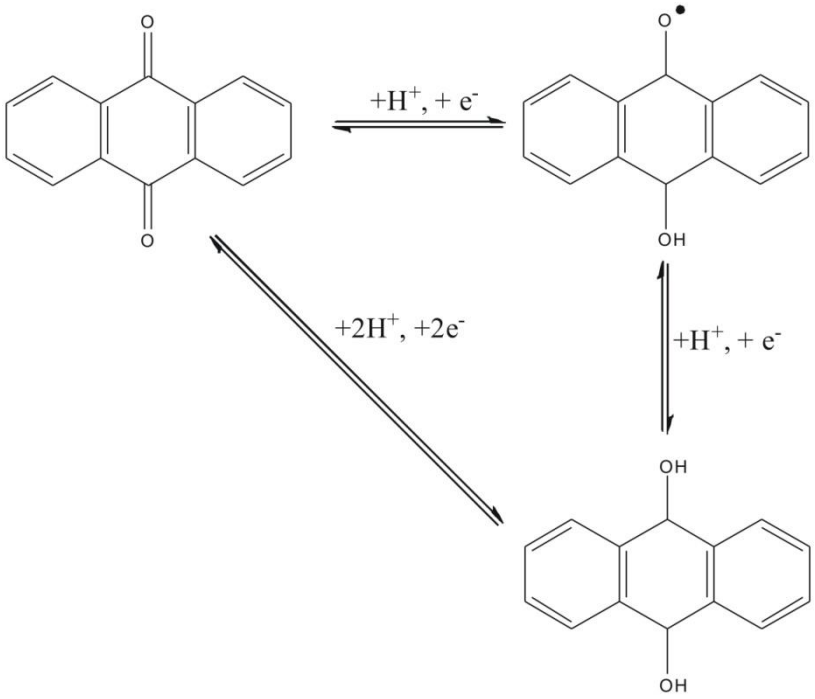

Scheme 7-1: Scheme illustrating the two electron, two hydrogen reduction of the anthraquinone

7.3.3 Voltammetry of the Basal Plane Graphite Electrode Modified with Fast Red AL Salt and Poly-(phenol) in the Presence of Cations

The response of a basal plane graphite electrode modified with a layer of Fast Red AL salt and a layer of poly-phenol submerged in 1 M HCl doped with 1 x 10^{-4} M MCl_2 (where M^{2+} is Ca^{2+}, Mg^{2+}, Sr^{2+}, Ba^{2+}). Each voltammogram was obtained using a fresh modification of the electrode as previously described, and is shown with its corresponding blank (1 M HCl in the absence of M^{2+}).

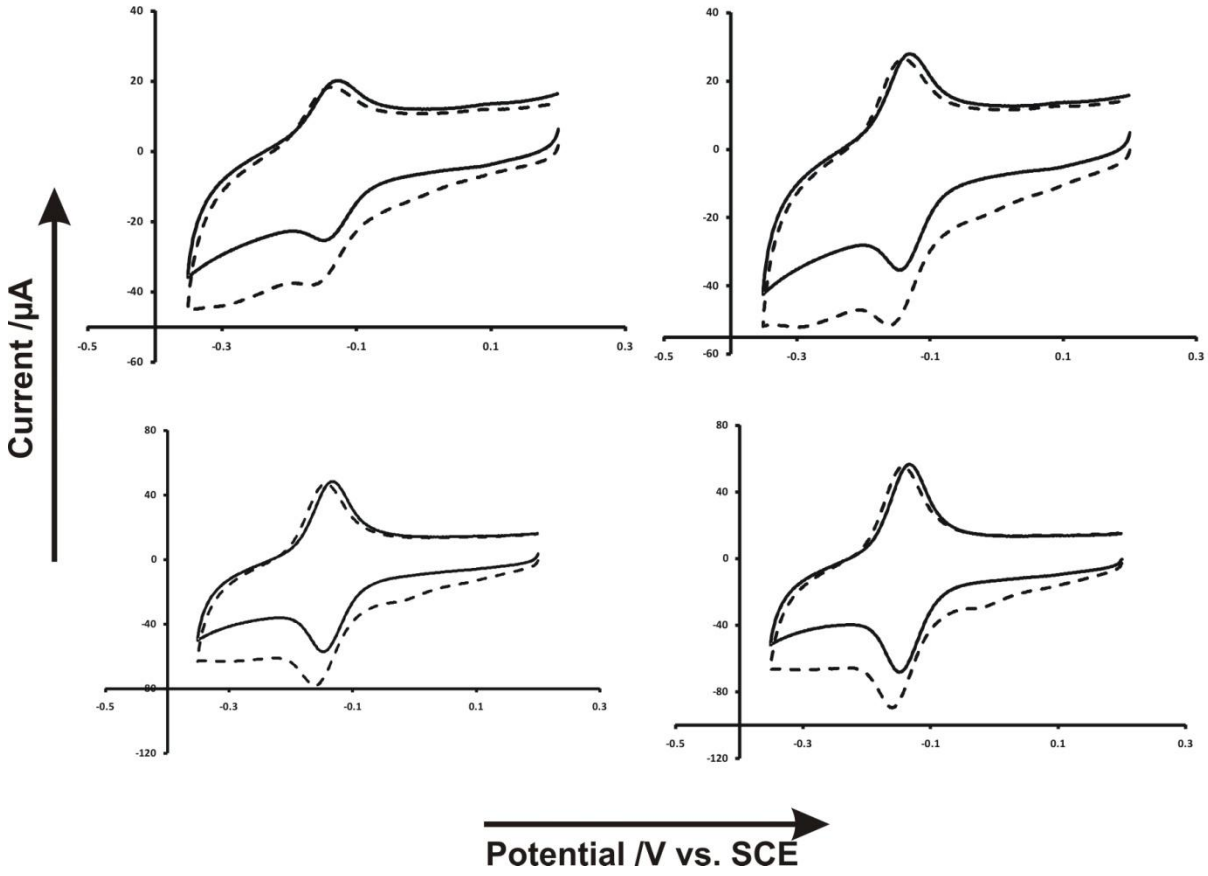

Figure 59: Fast red AL salt and poly-(phenol) modified electrode, voltammetry in (A) 1 M HCl + [$MgCl_2$], (B) 1 M HCl + [$CaCl_2$], (C) 1 M HCl + [$SrCl_2$], (D) 1 M HCl + [$BaCl_2$], at 0.1 V s^{-1}. Dashed line represents the voltammetry in 1 M HCl in the absence of MCl_2.

Once again a reduction peak is observed at -0.15 V vs. SCE with a corresponding oxidation peak at -0.1 V vs. SCE due to the reduction and subsequent oxidation of the anthraquinone moiety as described previously. Upon addition of the cation, the capacitative current is reduced; however this characteristic is also noted upon consecutive scans in a blank solution and is simply due to the stabilisation of the semi-quinone, *viz.* "breaking in" of the film. As the voltammetry shows, a significant shift in both reductive and oxidative peak potentials to less negative values is observed with the addition of a Group 2 metal cation to the solution, a characteristic not observed in blank solutions on consecutive scans, suggesting that the reduction of the anthraquinone becomes easier in the presence of the cation. As previously explained, the poly-(phenol) layer interacts with the electro-grafted anthraquinone layer

through hydrogen bonding. The introduction of the cation into the solution perturbs this interaction, as the poly-(phenol) layer preferentially chelates with the cation instead of hydrogen bonding with the anthraquinone. This causes the polymer film to constrict, "opening out" the surface grafted anthraquinone species, enabling more facile proton transfer and hence allowing the reduction to take place more easily in comparison with the absence of the cation.

Cation	Potential Shift /mV
Barium	+14.5 ± 7.8
Calcium	+12.5 ± 10.6
Magnesium	+12 ± 2.83
Strontium	+14 ± 1.41

Table 7-1: Potential shifts with the presence of |Group 2 cations

A significant potential shift is seen with all the hydrated Group 2 cations investigated (values shown are an average of two repeats), with increasing ionic radius causing an increasing potential shift; however this correlation is very weak and there is very little selectivity between each.

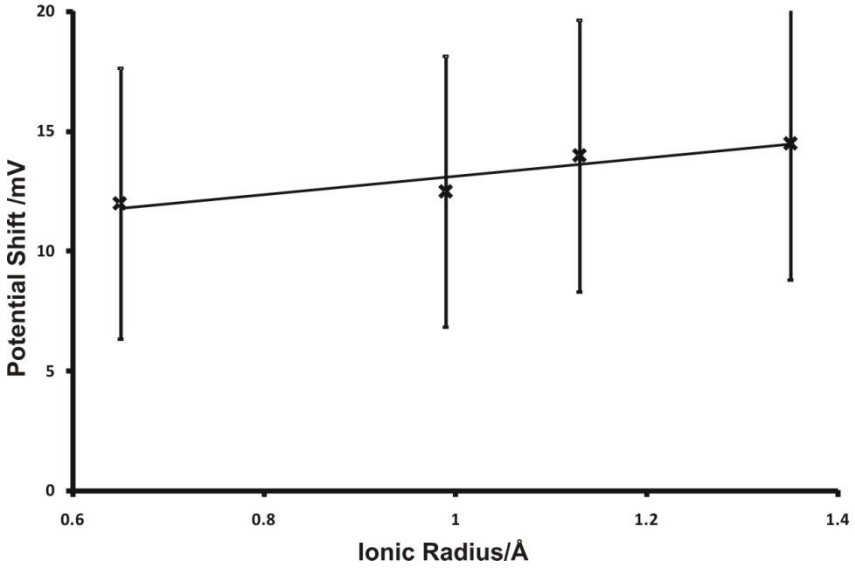

Figure 60: Relationship between ionic radii and potential shift observed

When considering the hydrated ionic radius, as cations exist in the hydrated form, as the radius decreases the potential shift increases, however once again there is very little selectivity between the cations. In an attempt to enhance the selectivity of the modified electrode towards the Group 2 cations, alginic acid was incorporated into the polymer layer.

7.3.4 Voltammetry of the Basal Plane Graphite Electrode Modified with Fast Red AL Salt and Poly-(phenol) in the Presence of Alginic Acid

As explained in section 7.2.3.2 alginic acid was incorporated into the poly-(phenol) layer, due to the inherent affinity the substance possesses for divalent cations[110] and its presence in the EPS of biofilms. Figure 61 illustrates the voltammetry of the basal plane graphite electrode modified with the diazonium salt and poly-(phenol)/alginic acid in 1 M HCl and 1 M HCl with $1x10^{-4}$ M MCl_2.

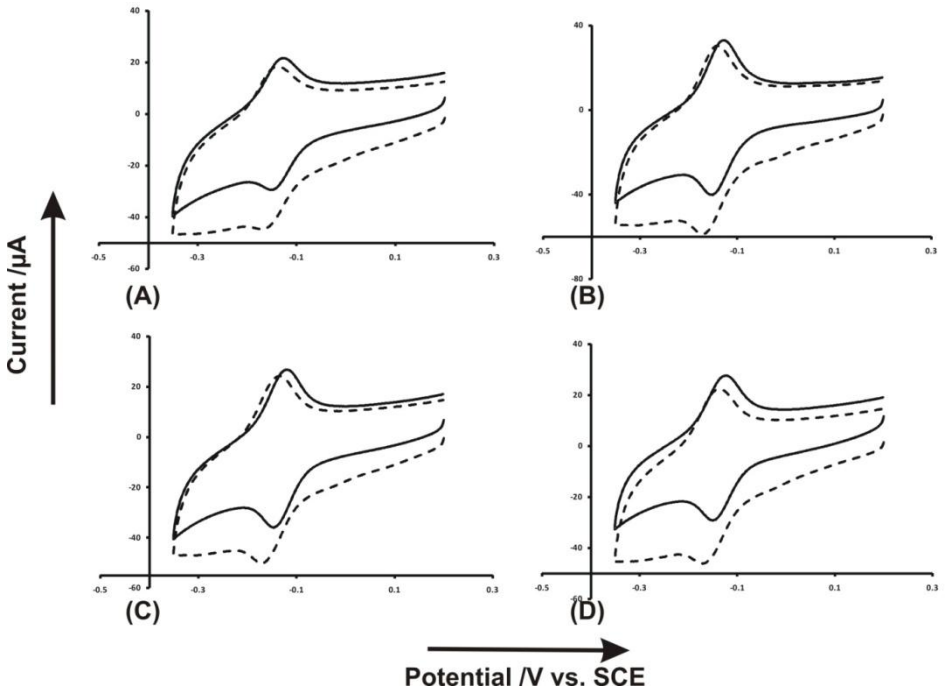

Figure 61: Fast Red AL salt and phenol in the presence of alginic acid modified electrode, voltammetry in (A) 1 M HCl + $1x10^{-4}$ M $MgCl_2$, (B) 1 M HCl + $1x10^{-4}$ M $CaCl_2$, (C) 1 M HCl + $1x10^{-4}$ M $SrCl_2$, (D) 1 M HCl + $1x10^{-4}$ M $BaCl_2$, at 0.1 V s^{-1}. Dashed line represents the voltammetry in 1 M HCl in the absence of MCl_2.

Similar voltammetry was observed, with the typical redox process of the surface grafted anthraquinone demonstrated. Also, similar to previously, there is a shift in peak potential to less negative values upon the addition of the metal cation in comparison with the voltammetry in the absence of the cation, however with the addition of the alginic acid the shifts are greater and are slightly more selective. The data is summarised in table 7-2 (n = number of repeats).

Cation	Potential Shift /mV	n
Barium	+18.5 ± 6.03	4
Calcium	+14.75 ± 3.77	4
Magnesium	+16.75 ± 4.5	4
Strontium	+21.75 ± 3.40	4

Table 7-2: Potential shifts with the presence of Group 2 cations, with alginic acid incorporated into the film on the electrode surface.

Values shown within table 7-2 are an average of four repeats, and as can be seen the presence of the alginic acid increases the degree of shift in reduction potential hence increasing the sensitivity of the sensor (*i.e.* the response of the modified electrode to the presence of a cation), and also exhibits slightly more selectivity between the cations (*i.e.* demonstrating differing potential shifts for different cations), showing the largest shift for strontium, with calcium demonstrating the least response in a similar manner to previous experiments. This trend differs to that exhibited in the absence of the alginic acid, with charge densities and ionic radii providing no rationalisation for the observed behaviour. However, if we consider that the cation is being removed from the aqueous system as it chelates with the poly-(phenol) layer, the energy required to do this, combined with the size of the ion will determine the ease at which the chelation occurs and hence the potential at which the reduction takes place.

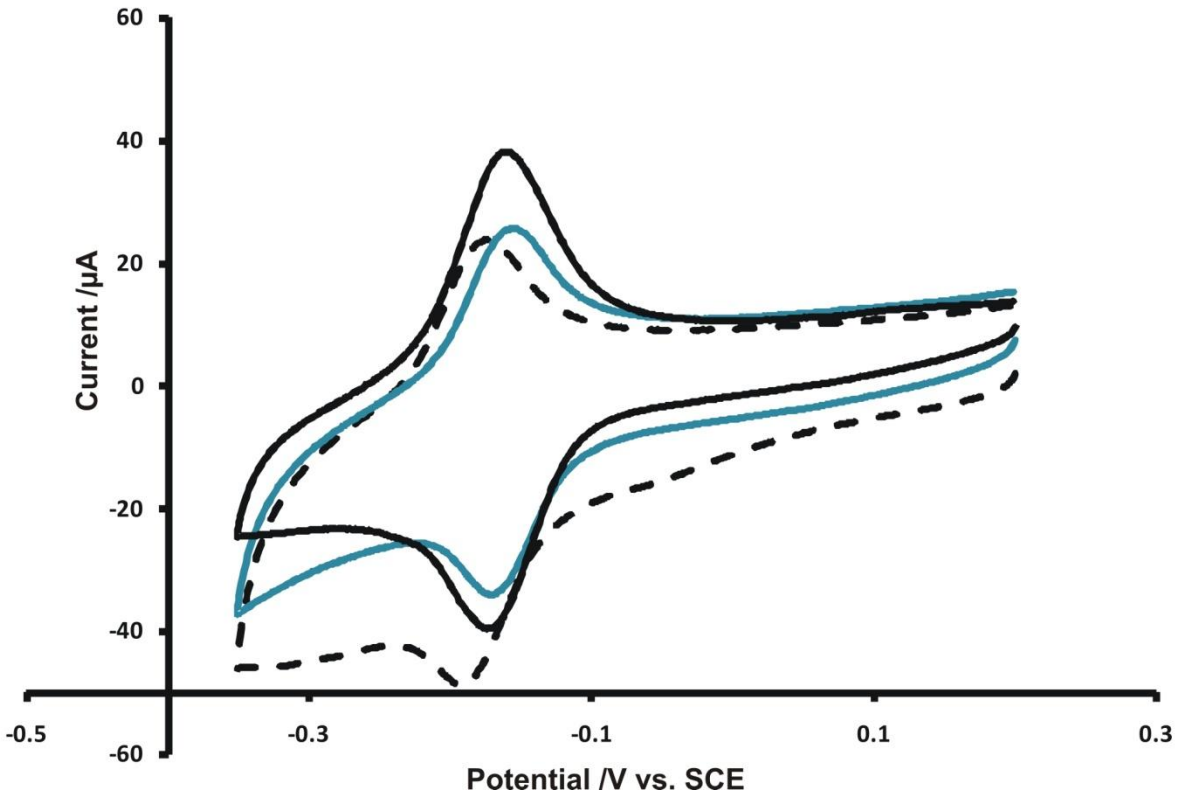

Figure 62: Summary of the cation sensor. Black line represents the voltammetry of a Fast Red AL salt modified electrode in 1 M HCl, dashed line represents the voltammetry of a Fast Red AL salt and poly-(phenol) modified electrode in 1 M HCl and the blue line represents the voltammetry of a Fast Red AL salt and poly-(phenol) modified electrode in 1 M HCl + 1 x 10^{-4} M MCl_2.

Figure 62 summarises the action of the cation sensor, demonstrating the shift in potential both to more negative values with the addition of the poly-(phenol) layer due to the inhibiting effect it has on the proton transfer, and to less negative values with the addition of cations due to the preferential chelation of the cations by the poly-(phenol) layer.

These data show that the multi-layer modified electrode is indeed mimicking a biofilm, as observed by up-take of the metal cation into the film via the shift in potential in the voltammetry. Following the establishment of this qualitative response of the modified electrode with the alginic acid incorporated towards the hydrated Group 2 cations, it was pertinent to investigate any possible quantitative aspects.

7.3.5 Quantitative Studies

The experimental procedure was followed as in previous experiments and as outlined in section 7.2.3.3 for the Group 2 cations in the concentration range $1 \times 10^{-7} \leq [MCl_2] /M \leq 1 \times 10^{-4}$, the results are summarised in table 7-3 (n = 4).

Barium	**Potential Shift /mV**
1×10^{-4}	3 ± 7.7
1×10^{-5}	16.5 ± 3.5
1×10^{-6}	13.5 ± 10.6
1×10^{-7}	11 ± 0
Calcium	**Potential Shift /mV**
1×10^{-4}	11.5 ± 0.71
1×10^{-5}	14.5 ± 0.71
1×10^{-6}	15 ± 4.2
1×10^{-7}	15 ± 1.4
Magnesium	**Potential Shift /mV**
1×10^{-4}	13.5 ± 6.4
1×10^{-5}	12 ± 2.8
1×10^{-6}	9.5 ± 4.9
1×10^{-7}	23 ± 0
Strontium	**Potential Shift /mV**
1×10^{-4}	6.5 ± 0.71
1×10^{-5}	15.5 ± 6.4
1×10^{-6}	10.5 ± 4.9
1×10^{-7}	17.5 ± 7.8

Table 7-3: Potential shifts for different concentrations of each cation.

The data shows no quantitative response, with all cations demonstrating erratic shifts in potential with different concentrations, demonstrating no general trend. Perhaps the most obvious explanation for this is the reproducibility of the formation of the layers in the process of modifying the electrode. As a new sensing surface is produced each time, *i.e.* for each

separate sensing measurement, it is very difficult to reproduce the modification repetitively, hence the reproducibility in the data sets (large ± values). Quantitative experiments using an electrode that was modified a single time and repeatedly used to sense for various concentrations of the Group 2 cations also proved unsuccessful, with no quantitative response achieved. The voltammetry of the basal plane graphite electrode modified with the diazonium salt and poly-(phenol) in aqueous 1 M HCl solutions doped with calcium chloride in the concentration range $1x10^{-4} \leq [CaCl_2]\ /M \leq 0.1$, beginning with 1 M HCl and working from low concentrations to high, is shown in figure 63.

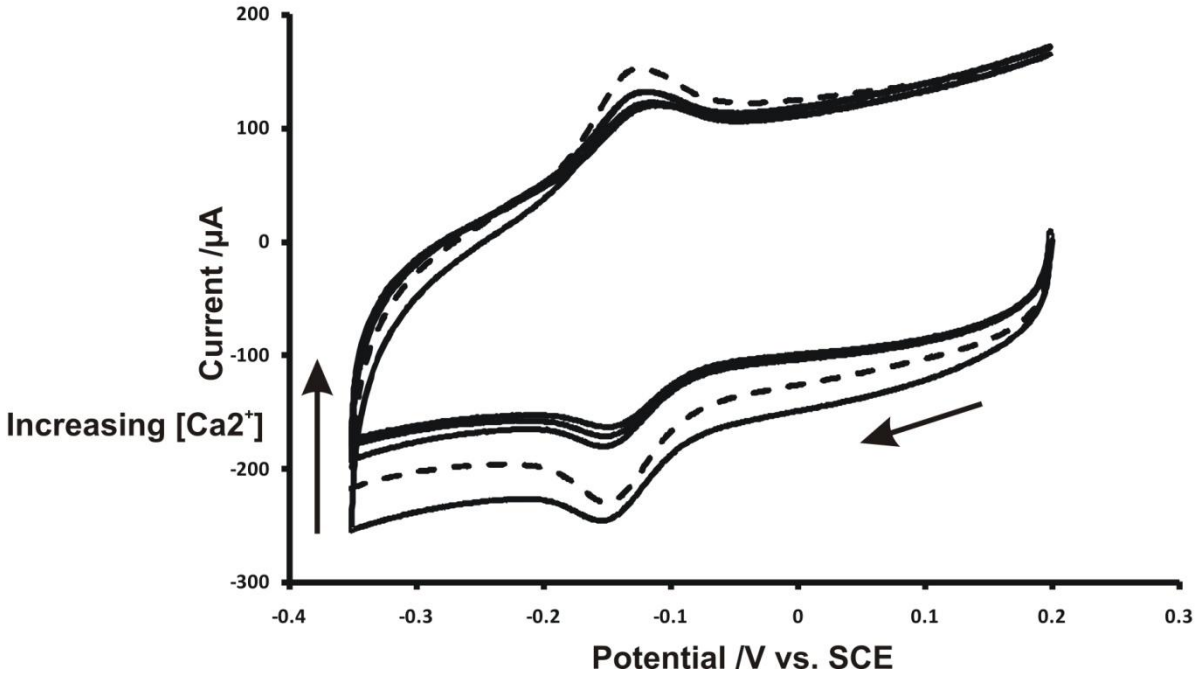

Figure 63: Fast Red AL salt and poly-(phenol) modified electrode, voltammetry in 1 M HCl + $[CaCl_2]$ in the range $1x10^{-4} \leq [CaCl_2]\ /M \leq 0.1$ at 0.5 V s^{-1}. Dashed line represents the voltammetry in 1 M HCl in the absence of $CaCl_2$. Horizontal line indicates the direction of the scan.

The lack of a quantitative response here was thought to be due to electrode history interferences, with the modified layer becoming saturated with the cation with repeated immersion into the cation solutions, hence affecting the voltammetric response.

7.4 Conclusions

The main aim of this study was to develop a sensor for cations based upon the principle of a biofilm, *i.e*. taking-up the cation into the film and monitoring this via the altered voltammetry. The surface of a basal plane graphite electrode was modified by electro-grafting a diazonium salt (Fast Red AL salt) to the surface initially, followed by the polymerisation of phenol forming a poly-(phenol) layer on top of the diazonium salt layer. This formed the basis of the sensor, with the modification mimicking the action of a biofilm.

Analysis of the data demonstrated that the modified electrode was indeed affected by the presence of the Group 2 cations analysed, however it lacked selectivity. In order to improve this, alginic acid was introduced into the layers on the electrode surface as it is well known to readily bind with divalent cations.[110]

The introduction of alginic acid did indeed improve the selectivity of the film, with calcium demonstrating the least response and strontium illustrating the greatest response. This promising result allowed the quantitative aspects of the sensor to be investigated. Unfortunately, no quantitative properties were evident. A primary reason for this is that the modification of the electrode surface was to be refreshed prior to each sensing measurement, thereby introducing intrinsic reproducibility issues affecting the kinetics of the cation up-take into the sensing layers.

8 Electrochemical Bond Formation: The Use of an Electrochemical Probe to Develop a Cyanide Sensor

In a continuation of developing an environmentally relevant sensor, and in contrary to the bond cleavage dynamics explored with the generation of nitric oxide, this section describes the development of a cyanide sensor through reaction between an electrochemical probe and the analyte, cyanide in collaboration with Dr. Graham Ferrier in the Department of Geography. Hence a bond formation process is explored, and the reaction mechanisms established.

8.1 Aims and Scope

Cyanide is a very toxic compound, acting as a exceptionally rapid poison to both humans and mammals.[112] Despite this apparent toxicity, cyanide is continually used in many industries such as gold mining, metal plating and in the manufacture of plastics.[113] Together with this, a number of natural sources also release cyanide, particularly plants.[114] A number of electrochemical methods, including polarography,[115,116] ion selective electrodes,[117,118] potentiometry,[119] amperometry,[120,121] stripping voltammetry[122,123] and cyclic voltammetry[124] have previously been developed to detect cyanide, with limits of detection ranging from milli-molar to nano-molar. Sulphide is considered to be a major interference in cyanide detection, together with being a significant environmental hazard itself. Hence, an abundance of research has also been undertaken into the detection of sulphide,[125] and it is investigated here in order to determine the interfering effect it has on the cyanide sensor.

The aim of this work therefore was to develop and optimize a methodology for the detection of cyanide using electrochemical techniques, developing a sensor that is selective and sufficiently sensitive to meet the requirements of the World Health Organisation, who set the

limit of cyanide to be found in drinking water at 0.07 mg L^{-1}. Hence, using a variety of electrochemical techniques, this section outlines the development and optimization of methodology for the detection of cyanide using the voltammetry of N,N,N,N'-tetramethyl-*p*-phenylenediamine, (TMPD).

8.2 Experimental

8.2.1 Instrumentation

Electrochemical measurements were undertaken as outlined in section 2.1. A glassy carbon electrode of 3 mm diameter was used as the working electrode in all cases (Metrohm, Switzerland) and was polished prior to each experiment as described in section 2.1.

8.2.2 Reagents

Solutions of N,N,N,N'-tetramethyl-*p*-phenylenediamine (TMPD, Fluka, UK) were prepared in either Britton Robinson buffer (an equimolar mixture (0.04 M) of orthophosphoric acid, boric acid and glacial acetic acid) or a 0.1 M solution of potassium chloride, with the pH then adjusted to approximately pH 10 using a 1 M solution of sodium hydroxide in both cases. All solutions were kept above pH 10 in order to maintain the potassium cyanide above the pK_a value (9.2) and hence prevent the release of hydrogen cyanide, a requirement of working in the laboratory, a mandatory safety condition imposed.

8.2.3 Procedures

8.2.3.1 **Product Characterisation**

Product characterisation studies were performed using both chemical synthesis and bulk electrolysis.

8.2.3.1.1 Chemical synthesis

100 mM of potassium hexacyanoferrate was reacted with 10 mM TMPD in Britton Robinson buffer in order to form the radical cation, followed by reaction with an excess of potassium cyanide. This procedure was repeated using 0.1 M potassium chloride as the medium as opposed to Britton Robinson buffer, and finally in both cases the products were extracted into chloroform in preparation for further analysis. These experiments were repeated with the oxidation in the presence of cyanide, blank syntheses were also undertaken as reference points.

8.2.3.1.2 Bulk Electrolysis

Using the following equation to calculate the amount of charge required:

$$Q = nNF$$

Where Q is the amount of charge (C), n is the number of electrons, N is the number of moles and F is Faraday's Constant (96485 C mol^{-1}), bulk electrolysis was undertaken using a three electrode system. The working electrode comprised two graphite rods connected via an insulated platinum wire, three graphite rods were used in a similar manner as the counter electrode and a standard calomel electrode was employed as the reference electrode. Subsequent to the calculated quantity of charge passing an excess of potassium cyanide was added to the 1 mM solution of TMPD and left stirring for thirty minutes. This electrolysis was performed using both Britton-Robinson buffer and potassium chloride solutions, pH 11, with the latter employing an experimental set-up comprising a salt bridge separating the counter electrode from the remaining two electrodes so as to prevent the deactivation of oxidised material at the cathode.

8.2.3.2 **Construction of a Silver/Silver Cyanide Electrode**

A silver/silver cyanide electrode was constructed by passing current through a 10 cm length of silver wire wound into a coil and a graphite rod connected by a 9V battery and submerged into a 0.1 M potassium cyanide solution (pH ~11, Britton Robinson buffer). The electrode was stored in the dark and calibrated using a Fluke 77 multimeter on a daily basis with a standard calomel electrode used as the reference.

8.2.3.3 **Remediation of Cyanide from River Water Samples**

River water samples were collected in a sterile, plastic bottle from the mid-part of the flow of the River Swale, North Yorkshire ($54^{o}15'19.19''$ N, $1^{o}46'13.49''$ W) and stored in the refrigerator at 4^{o}C. Dr. Graham Ferrier collected samples from Rodalquilar former gold mine, Spain ($36^{o}50'52.9''$ N, $2^{o}02'36.87''$ W) and they were treated in the same manner. They were then spiked with a known amount of cyanide and TMPD and the potential was measured using a Fluke 77 multimeter, the calibrated Ag/AgCN electrode and a SCE as the reference. Bulk electrolysis was then undertaken using a three electrode system, with graphite rods as the working and counter electrodes and a SCE as the reference, followed by a further measurement of the potential using the Fluke 77 multimeter, the calibrated Ag/AgCN electrode and a SCE as the reference.

8.3 Results and Discussion

The reaction between the electrochemical probe, TMPD, and cyanide was initially monitored in a colorimetric manner, utilising UV-visible spectrometry, before experiments exploring the character of the product and the possible reaction mechanism were undertaken. Following this, TMPD was then used as an electrochemical probe in order to develop a cyanide sensor, with cyclic voltammetry and square wave voltammetry employed. Finally, a potentiometric

sensor was developed, with the possibility of applying the reaction between TMPD and cyanide in remediation studies.

8.3.1 N,N,N,N'-tetramethyl-*p*-phenylenediamine (TMPD) as an Electrochemical Probe in the Development of a Cyanide Sensor

8.3.1.1 Investigations with UV-absorption spectrophotometry

Aqueous TMPD in solution forms a very light purple colour, however upon formation of the radical cation, $TMPD^{+\bullet}$, a blue colour is observed. This colorimetric difference was used to follow the reaction of TMPD with cyanide spectrophotometrically using a UV-absorption spectrometer to monitor the oxidation of TMPD by potassium hexacyanoferrate.[126]

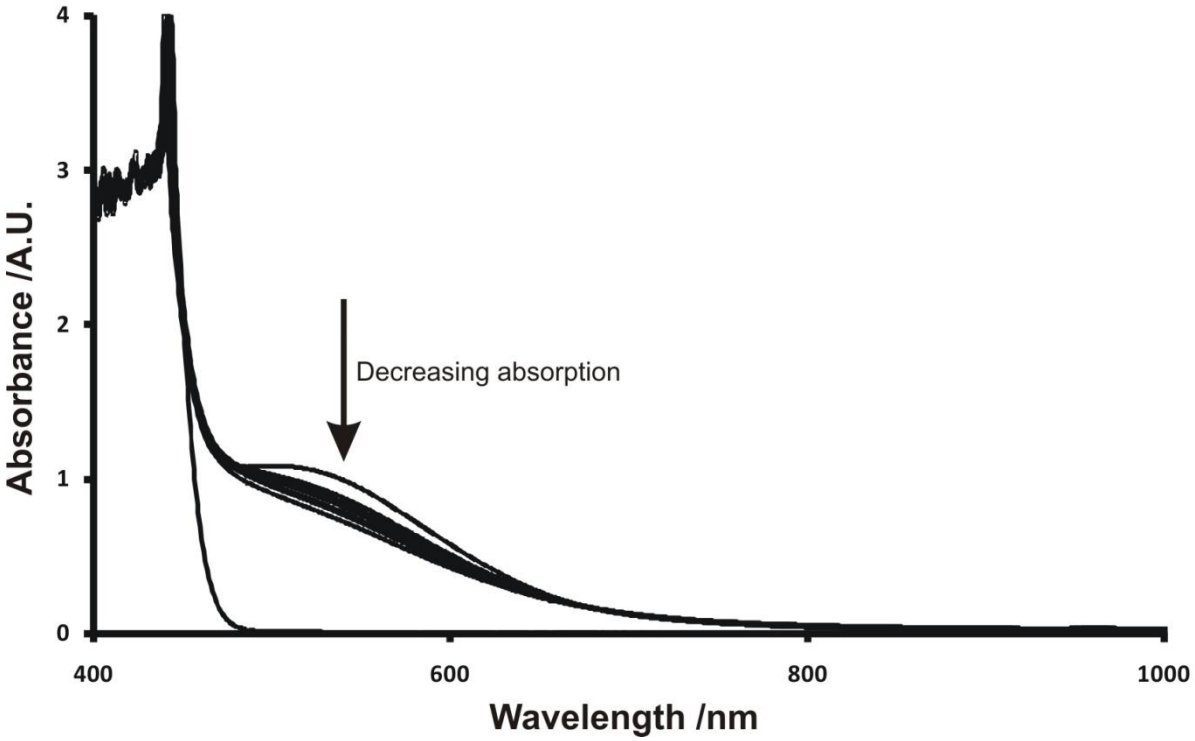

Figure 64: UV-visible Spectrum for TMPD in the Presence of Various [KCN]

A variety of peaks were observed within the spectrum in the region 400 – 1000 nm however the peak observed at ca. 530 nm is of specific interest as the absorption intensity decreases with increasing potassium cyanide concentration in a linear fashion as shown in figure 65.

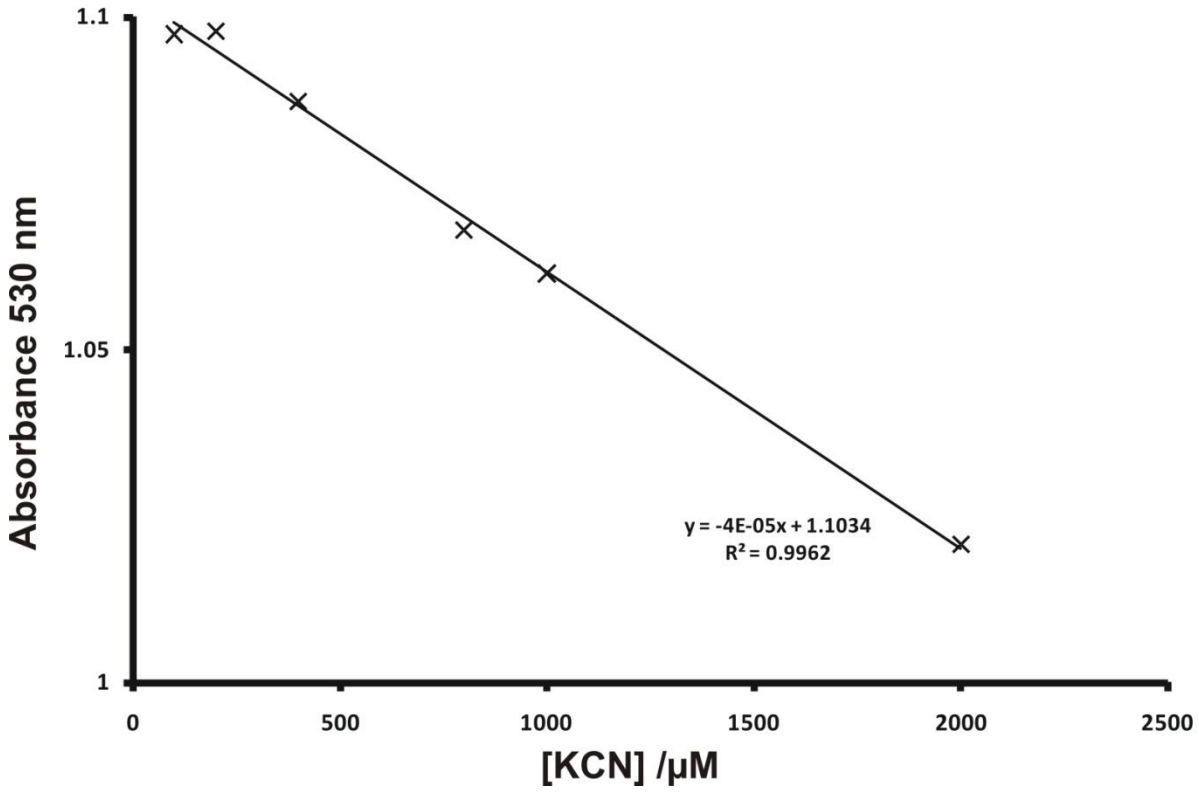

Figure 65: Graph demonstrating the linear response of UV-vis absorption with increasing [KCN]

The presence of this peak and the subsequent decrease in response to the presence of the cyanide confirms that the reaction between TMPD and cyanide can be monitored spectrophotometrically. If we consider this further, the TMPD radical cation is the coloured product being observed, therefore the absorption measured is proportional to the concentration of $TMPD^{+\bullet}$ present. As the absorbance is affected with increasing potassium cyanide concentration, this indicates that the cyanide reacts with the radical cation and decreasing the concentration of this $TMPD^{+\bullet}$ present. In reaction with the cyanide anion, the concentration of the radical cation is diminished, therefore resulting in the decreased absorbance being observed and confirming the incidence of a reaction between the TMPD and the cyanide.

In order to confirm these results obtained through UV-absorption experiments, to determine the reaction mechanism and to develop a robust and sensitive sensor, it was pertinent to

further investigate the reaction between the radical cation and the cyanide by undertaking some product characterisation studies.

8.3.1.2 **Product characterisation**

Two methods of synthesis were undertaken, chemical and bulk electrolysis, as described in section 8.2.3.1. With a number of analysis methods utilised in order to qualitatively describe the products formed. If the possible products are first considered, qualitative analysis becomes easier by using direct references.

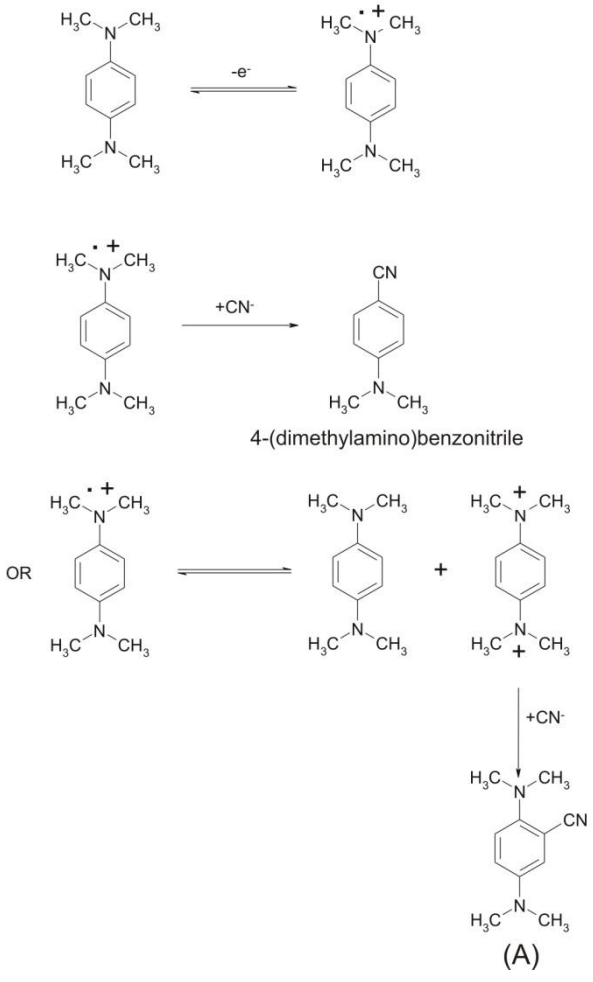

Scheme 8-1: Reaction of TMPD with cyanide

8.3.1.3 **Chemical Synthesis of the Electrochemical Products**

Conducting the synthesis in both Britton-Robinson buffer and potassium chloride solution revealed similar products present following thin layer chromatography analysis. A portion of starting material remained in the final product, together with an amount of 4-(dimethylamino)benzonitrile and a number of different compounds differentiated by the colours they demonstrated.

Gas chromatography-mass spectrometry analysis gave inconclusive qualitative results, with no definitive product identified. NMR analysis gave a very complex spectrum, with an array of products demonstrated, however no 4-(dimethylamino)benzonitrile was found to be present.

8.3.1.4 **Bulk Electrolysis**

Thin layer chromatography analysis of the bulk electrolysis products revealed a large amount of starting material still remaining, together with three other products, none of which were consistent with 4-(dimethylamino)benzonitrile. Gas chromatography-mass spectrometry did however reveal a more encouraging product with an m/z value of 189, corresponding to compound A in scheme 8-1. NMR analysis of products from the bulk electrolysis process in Britton-Robinson buffer revealed an asymmetrical product confirming the reaction between TMPD and cyanide. However, a reference spectrum for 4-(dimethylamino)benzonitrile was not consistent with that obtained from the bulk electrolysis.

8.3.1.5 **Product Characterisation Summary**

Analysis of the chemical synthesis products using thin layer chromatography consistently demonstrated the presence of 4-(dimethylamino)benzonitrile in the product, however gas-chromatography-mass spectrometry and NMR analysis failed to confirm this. Bulk electrolysis did not reveal the presence of any 4-(dimethylamino)benzonitrile, however gas

chromatography-mass spectrometry demonstrated the presence of compound A as shown in scheme 8-1. This product is the result of a 1,4–Michael Addition, with the nucleophilic cyanide attacking in the 1,4 position on the ring following the disproportionation of the radical cation.

Having established the possible products of the reaction between TMPD and cyanide and determining a possible reaction mechanism, it was then pertinent to begin to develop an electrochemical sensor for the cyanide, beginning with explorations using cyclic voltammetry.

8.3.1.6 **Investigations using cyclic voltammetry**

The electrochemistry of TMPD is well established, with two reversible one electron oxidations observed in the region $-0.2 \leq E\ /V\ vs.\ SCE \leq 1.2$. The cyclic voltammetry experiments herein were undertaken with a variety of scan rates were investigated, with the optimal scan rate found to be 0.1 V s^{-1}, giving the best quantitative response to the presence of the cyanide. Figure 66 illustrates the cyclic voltammetry of 1 mM TMPD in the presence of increasing concentrations of potassium cyanide in the range $0 \leq [KCN]\ /M \leq 100$ μM in six increments of 20 μM.

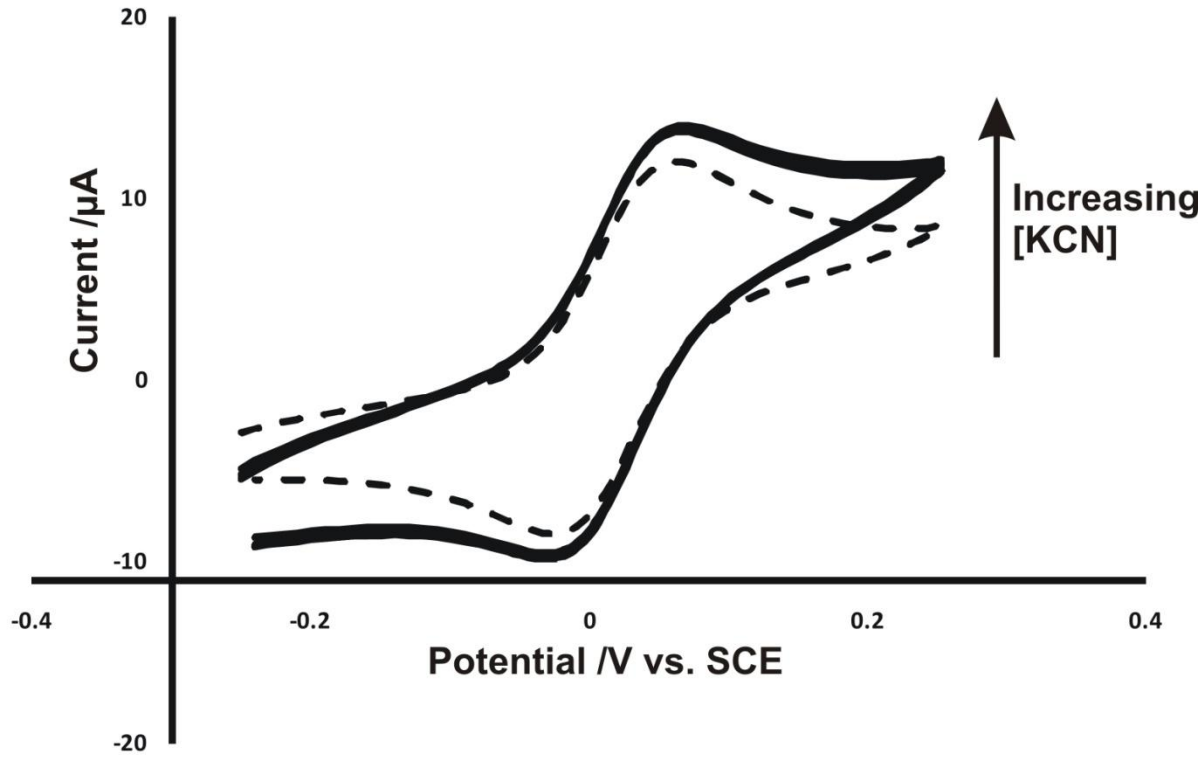

Figure 66: Cyclic voltammetry of TMPD in the presence of increasing [KCN]. Dashed line represents the voltammetry of TMPD in the absence of cyanide, with the solid lines representing the voltammetry in the presence of the cyanide, scan rate = 0.1 V s^{-1}.

As demonstrated in figure 66 a one electron oxidation is observed at 0.06 V *vs*. SCE with a corresponding reduction peak at -0.03 V *vs*. SCE. The electrochemistry was focussed on the single oxidation as this demonstrated the best response, together with only requiring a cation as opposed to the dication in reaction with the cyanide. With the addition of cyanide, the oxidative current is seen to increase, together with a very slight simultaneous positive shift in oxidation potential from approximately 0.06 V *vs*. SCE to 0.07 V *vs*. SCE. This increase was not a major response, however considering the increase in oxidation current as a function of the concentration of potassium cyanide present revealed a promising linear response, with further repeats allowing the standard error to be calculated and hence a limit of detection to be determined:

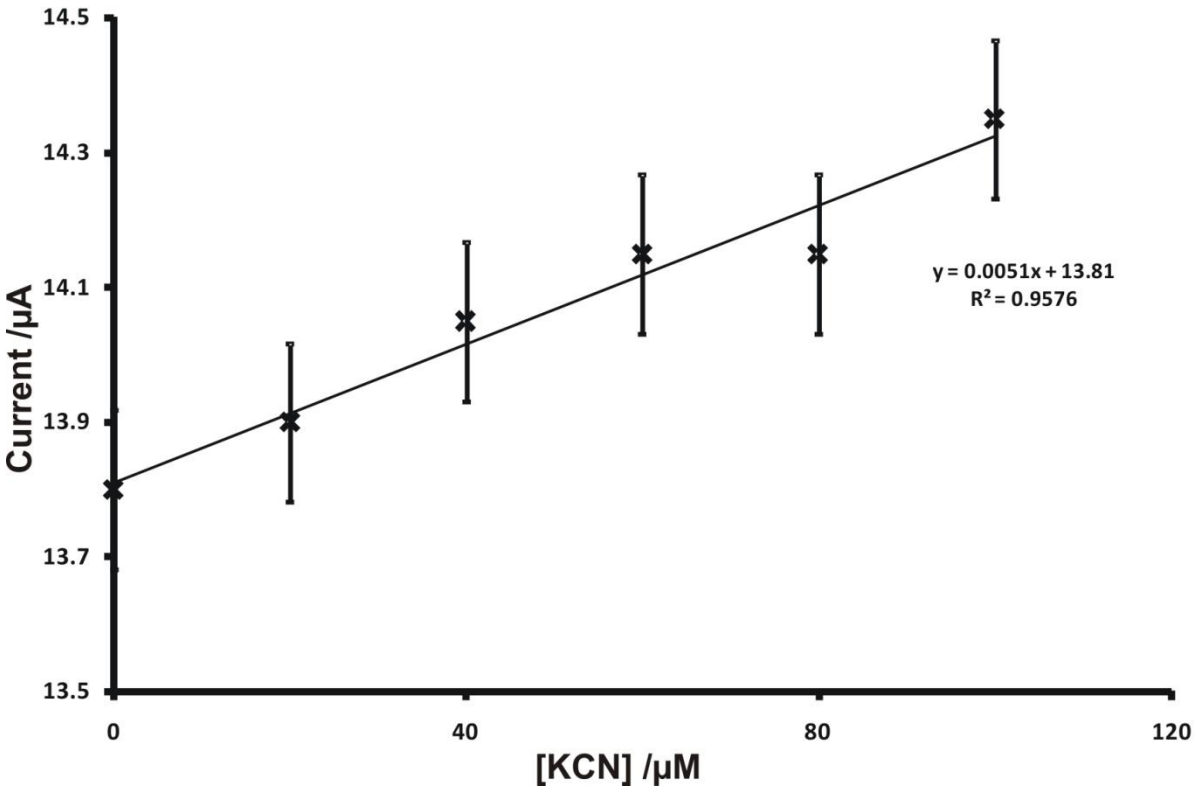

Figure 67: Average oxidative current at various [KCN]

$$Limit\ of\ \ Detection = \frac{(3 \times SE)}{gradient}$$

$$SE = \frac{\sigma}{\sqrt{n}}$$

Where SE is the standard error, σ is the standard deviation and n is the number of samples. The limit of detection was determined as 48 µM, which is insufficient by an order of magnitude for the World Health Organisation, however it showed the quantitative response of the TMPD towards cyanide and formed the beginnings of a sensor which could be further improved. Square wave voltammetry is intrinsically more sensitive than cyclic voltammetry due to the very high information content it achieves and the ability to suppress the background signal, allowing lower concentrations of analyte to be investigated; hence attention was then focussed on the development of the sensor via square wave voltammetry.

8.3.1.7 **Investigations with square wave voltammetry**

The square wave voltammetry of 1 mM TMPD in the presence of increasing concentrations of potassium cyanide is shown in figure 68. As demonstrated, the oxidation potential is unaffected by the addition cyanide, remaining constant at 0.1 V *vs.* SCE. However, the oxidative current is indeed influenced by the addition of potassium cyanide, decreasing with increasing cyanide concentration.

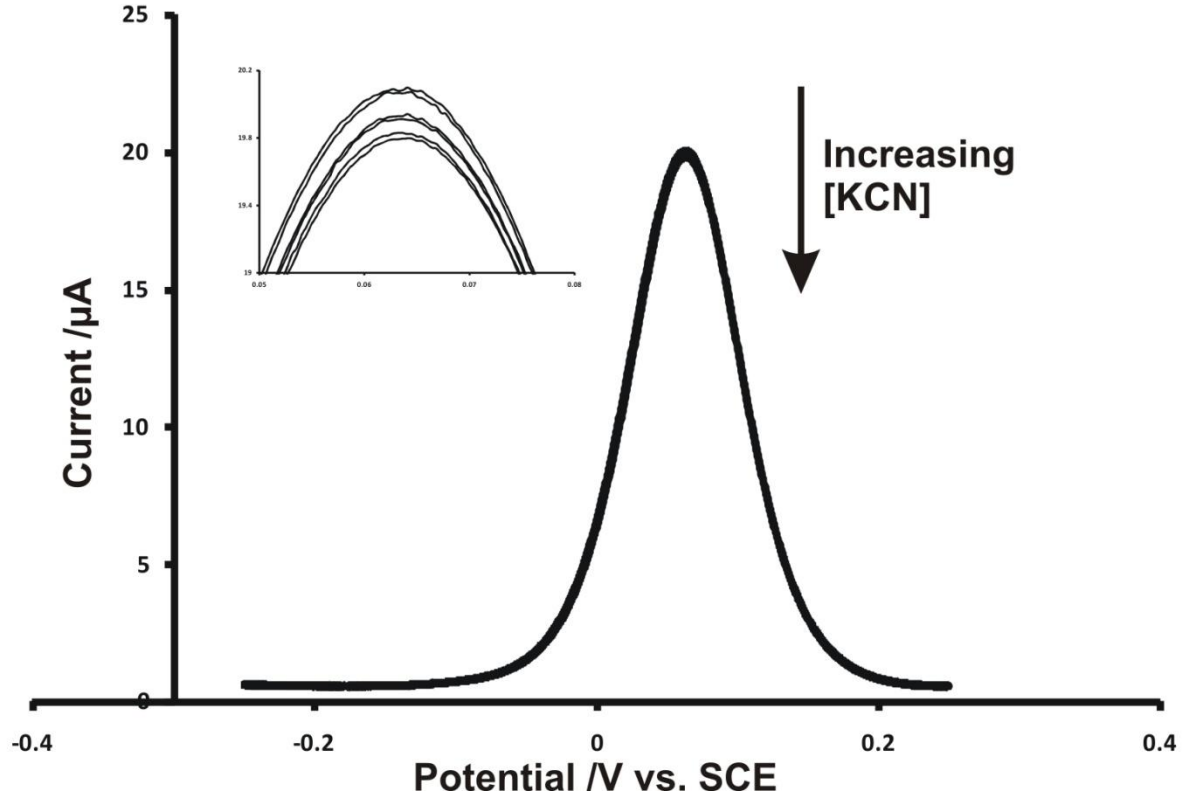

Figure 68: Square wave voltammetry of TMPD in the presence of various [KCN]. Step potential = 0.0025 V, amplitude = 0.01 Hz, scan rate = 0.1 Vs^{-1}. Inset shows the peak currents.

Optimisation of the square wave voltammetric parameters by lowering the step potential and hence increasing the timescale of the perturbation, allowing more time for the reaction between the TMPD and cyanide to occur, allowed a linear response to be obtained and hence a limit of detection to be calculated, giving a value of 4.4 µM. This limit of detection is a full

order of magnitude more sensitive than the cyclic voltammetry, and despite not quite meeting the requirements of the World Health Organisation it forms a good basis for a cyanide sensor.

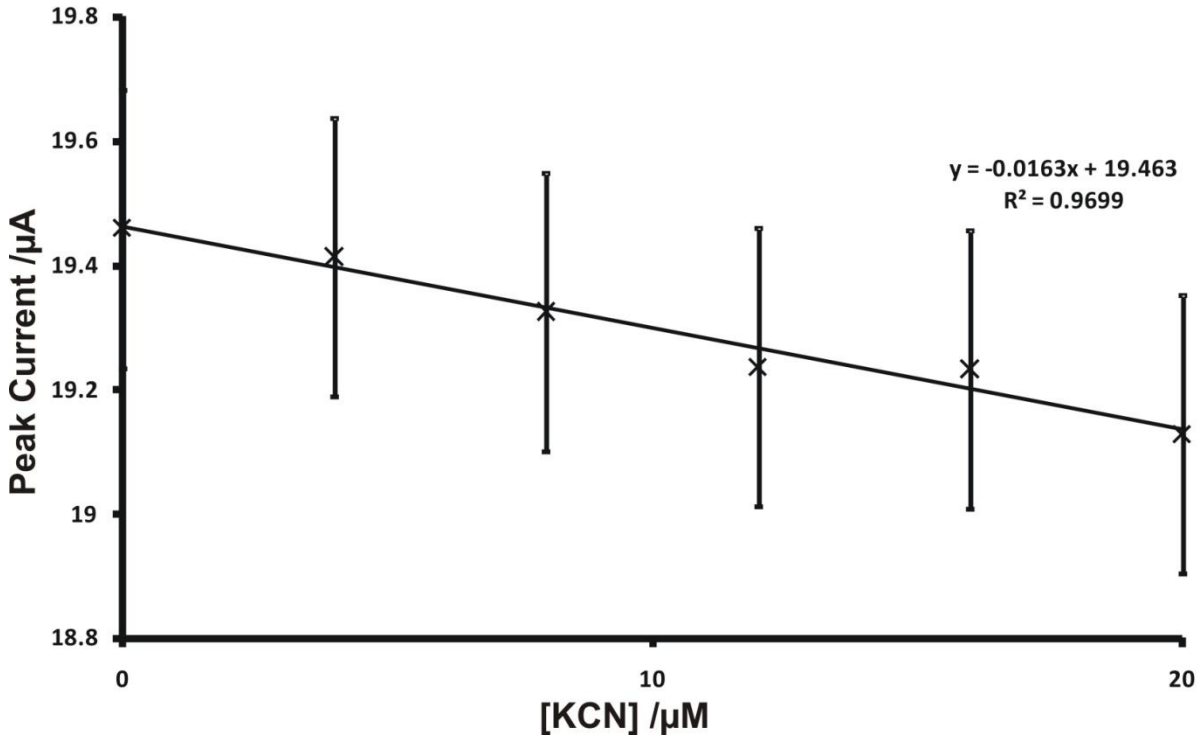

Figure 69: Graph showing the variation of peak current with [KCN] using square wave voltammetry

As illustrated in figure 69, the peak current decreases with increasing cyanide concentration, similar to the response observed in the UV-visible absorption spectrophotometry, hence suggesting that the reaction between the TMPD and the cyanide forms an intermediate, consuming the TMPD available and thereby reducing the voltammetric response due to TMPD. In contrast, the cyclic voltammetry demonstrated an increasing peak current with increasing cyanide concentration. This is likely due to the conflicting timescales, with the cyclic voltammetry showing reversible characteristics, oxidising then reducing in an EC mechanism, whereas the square wave quickly switches between oxidation and reduction potentials.

8.3.2 Potentiometric Cyanide Sensor and the Application of the Sensors to River Water Samples

Following the success of the amperometric response obtained through both cyclic voltammetry and square wave voltammetry, the possibility of a simple potentiometric sensor was explored. An Ag/AgCN reference electrode was fabricated as described in section 8.2.3.2, and calibrated over a period of three weeks using a set of six calibration solutions of potassium cyanide and hence forming the basis of the potentiometric sensor. Figure 70 demonstrates this calibration, showing a linear response in the range $1 \times 10^{-5} \leq [KCN] /M \leq 1 \times 10^{-3}$ with a gradient of -86.1 mV.

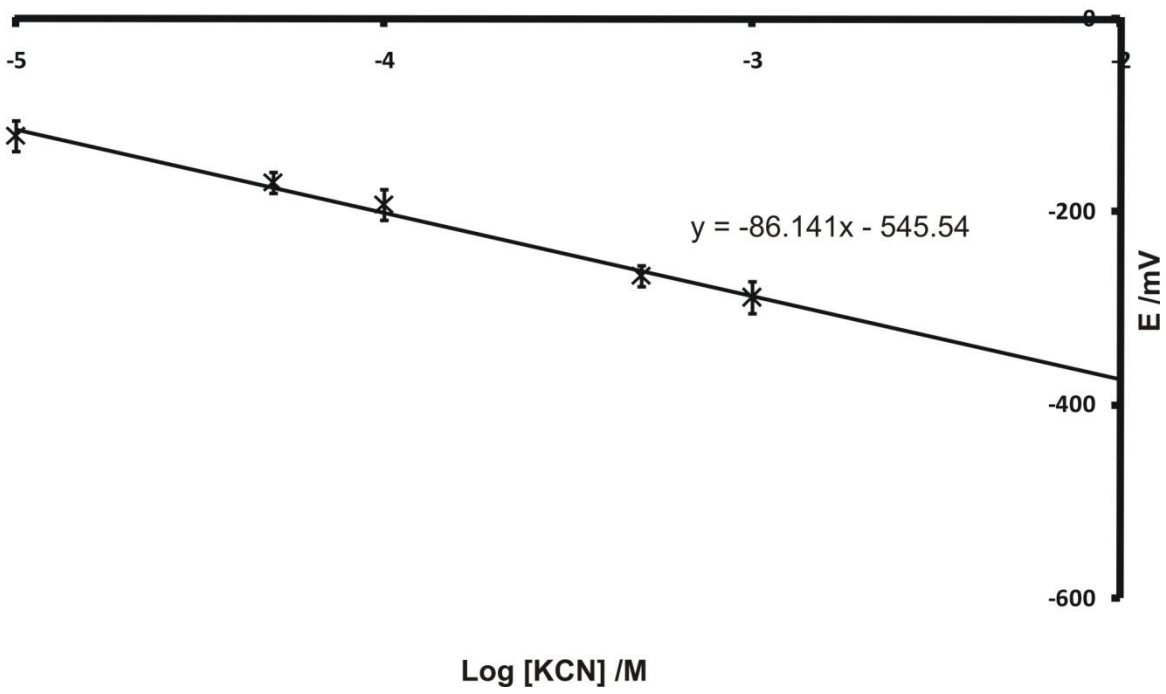

Figure 70: Calibration of Ag/AgCN electrode over a period of three weeks

In order to test the robustness of this calibration, river water samples were spiked with potassium cyanide and the potential measured. River water samples were obtained from the River Swale in Richmond, North Yorkshire (54°15'19.19" N, 1°46'13.49" W), stored in the

dark, and the experiments conducted as explained in section 8.2.3.3. Following the calibration, 1.84 x 10^{-4} M potassium cyanide was added to the river water sample and the potential measured, providing a value of 1.24 x 10^{-4} M for the concentration of cyanide present in the sample.

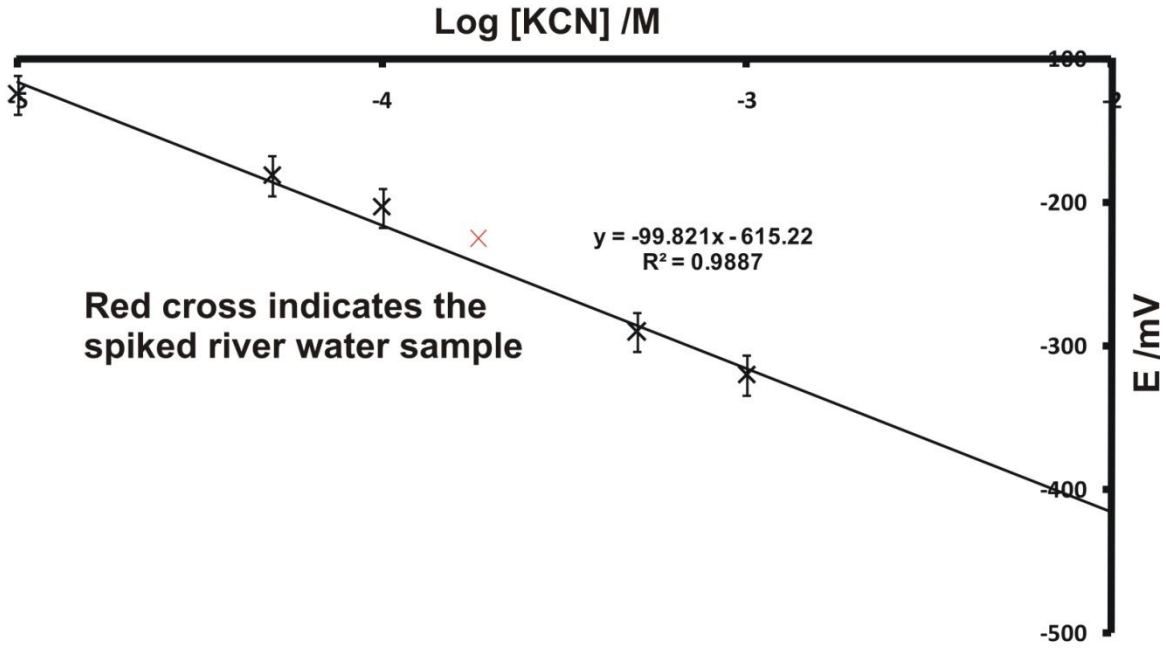

Figure 71: Calibration of potentiometric sensor and testing of river water sample

This provided good evidence that the Ag/AgCN electrode demonstrates a reliable calibration, and that it can perform as a reliable sensor for the cyanide. Possible reasons for obtaining a lower concentration reading than the amount added to the sample include possible interferences as the matrix would be complex, also perhaps the timescale of the experiments, *i.e.* insufficient time was available for all the cyanide present to react with the TMPD.

Due to the linear response with a much improved limit of detection achieved with square wave voltammetry it was applied to real samples. Mine water samples were taken from the Rodalquilar former gold mine, Spain (36°50'52.9" N, 2°02'36.87" W), again stored in the dark, and the amount of cyanide already present in the sample calculated using square wave

voltammetry and verified potentiometrically using an Ag/AgCN electrode. The linear response was maintained within the real system, with reasonable agreement between the potentiometric measurements and amperometric (square wave voltammetry) measurements.

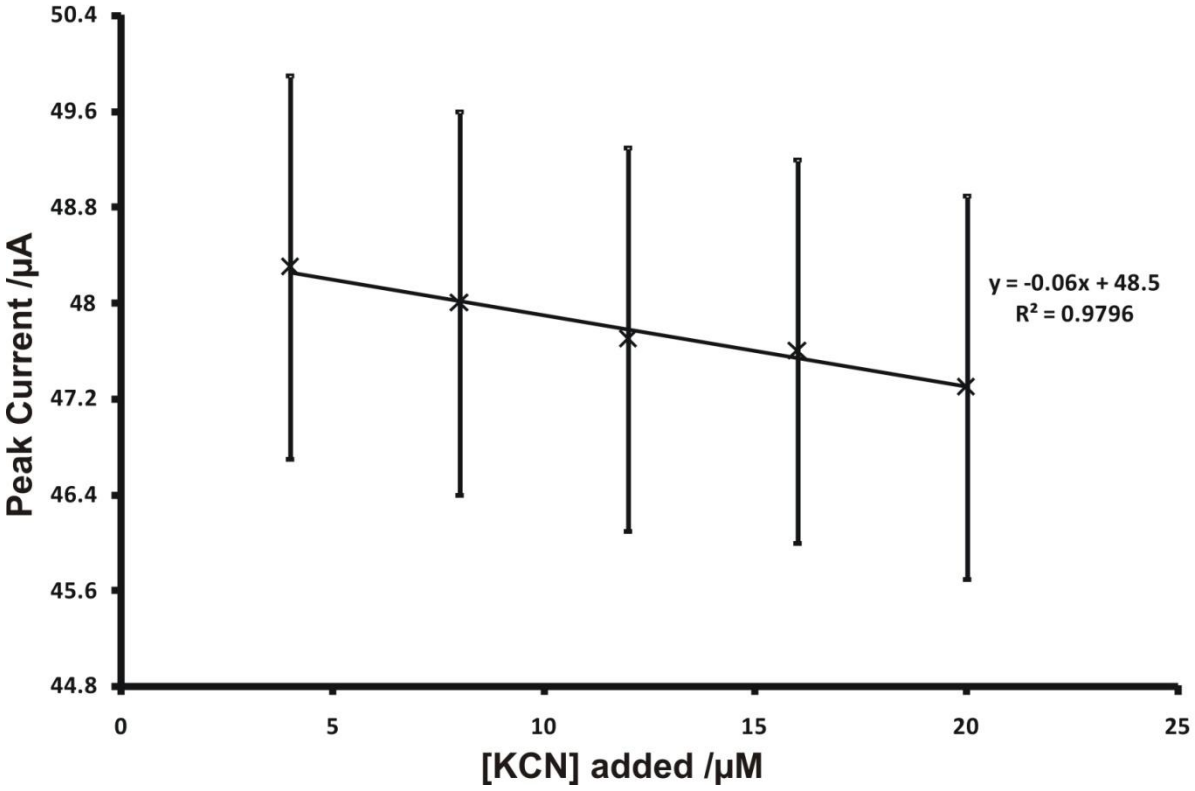

Figure 72: Square wave voltammetry response in a mine water sample

Using the equation of the line, the amount of cyanide already present in the sample was determined to be 6.67 µM, whilst potentiometric measurements returned a value of 1.96 µM, hence a very good agreement and demonstrating the reliability and robustness of both the amperometric and potentiometric sensors.

8.3.3 Remediation of Cyanide

The addition of cyanide to TMPD causes a bimolecular reaction to occur, as demonstrated by both the product characterisation studies and the square wave voltammetry with the decreasing oxidative current corresponding to increasing cyanide concentration. If the

reaction mechanisms suggested herein are further considered (see scheme 8-1), it can be seen that the mechanism removes free cyanide from the solutions, therefore it was imperative to investigate the possibility of cyanide remediation from aqueous samples. In order to explore this, remediation experiments were undertaken as outlined in section 8.2.3.3. Figure 70 has already demonstrated the calibration of the Ag/AgCN electrode over a period of three weeks, showing excellent reproducibility and a good linear response in the concentration range 1 x $10^{-5} \leq$ [KCN] /M $\leq$ 1 x 10^{-3}. Using this calibrated Ag/AgCN electrode, an initial river water cyanide concentration of 0.265 ± 0.118 mM was observed and following the remediation process, *i.e.* the bulk electrolysis, a cyanide concentration of 0.638 ± 0.306 μM was obtained. This is a decrease in cyanide concentration corresponding to three orders of magnitude, an excellent result and demonstrating both further evidence for the bimolecular reaction between the TMPD and the cyanide, together with a very successful method for the remediation of cyanide from real river water samples in a simple, robust and reproducible manner.

8.3.4 Interferences

In order to develop a smart environmental sensor, possible matrix interferences are an important consideration. Sulphide has often been found to respond in a similar manner to cyanide in a number of techniques, and consequently cyanide and sulphide are often simultaneously detected as part of water and environmental control procedures.[115,127,128] This presents major problems in the development of a cyanide sensor, with sulphide causing a significant interference and therefore often requiring a separation method prior to detection. With this in mind, the effect of sulphide on the square wave voltammetry sensing and the potentiometric measurements was investigated.

Initially, the effect of sulphide on the square wave voltammetry was investigated, with standard additions of sodium sulphide in the range 0 $\leq$ [Na_2S] /μM $\leq$ 50 to a solution of

TMPD in a similar manner to the cyanide experiments. The voltammogram is shown in figure 73, with the first facet to notice being the very different oxidative potential observed compared to the voltammetry in the presence of cyanide.

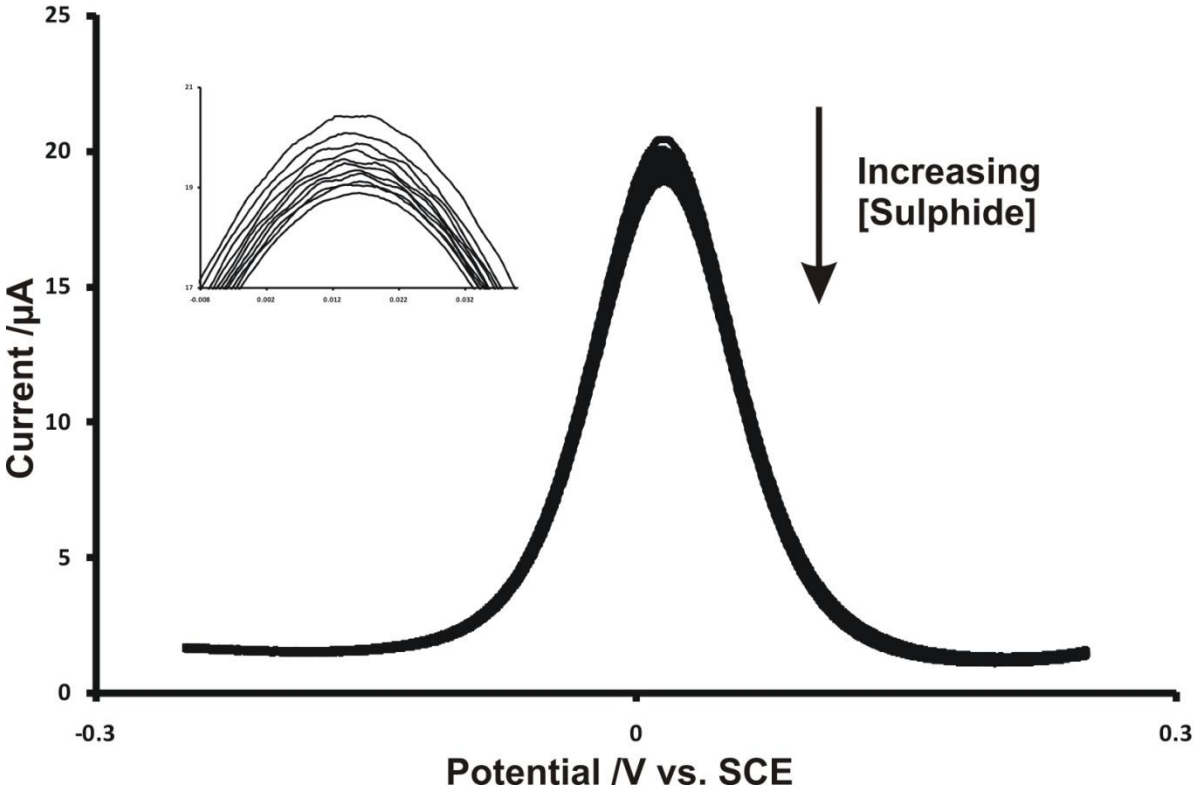

Figure 73: Square wave voltammetry of TMPD in the presence of increasing concentrations of sodium sulphide

In the presence of cyanide, the oxidative potential was close to 0.1 V *vs.* SCE, whereas in the presence of sulphide the oxidative potential is shifted closer to 0 V at 0.02 V *vs.* SCE which in itself is promising, as it suggests that the response to cyanide and the response to sulphide can be monitored separately. Also noteworthy was the complete loss of colour observed within the solution upon addition of ≥ 30 µM of sulphide; as previously described TMPD forms a slight purple colour in aqueous solution, therefore this complete loss of colour suggests the presence of a reaction between the TMPD and sulphide. The oxidative current decreases with increasing sulphide concentration in a similar manner to the cyanide

voltammetry, hence with this in mind the voltammetry of TMPD in the presence of a fixed, known amount of sulphide and increasing amounts of cyanide was then explored. Once again, the oxidative potential was shifted to values closer to 0 V compared to those observed in the absence of the sulphide, and the characteristic negative linear response observed with the square wave voltammetry was less reproducible and less distinct, suggesting some interference with the senor. Despite this, as previously shown the sensor performed well in real samples, *i.e.* both the river water samples and the mine water samples, maintaining a linear response to the presence of cyanide, with good agreement between the amperometric and potentiometric responses. This would indicate that despite the possibility of sulphide interference, the sensor can still perform in complex matrices to a high level.

8.4 Conclusions

The aim of this study was to develop a sensor for cyanide using an electrochemical probe, with detection limits sufficient to meet the requirements of the World Health Organisation (0.07 mg L^{-1}). Initially, UV-visible spectrometry was successfully used to follow the reaction between the electrochemical probe, TMPD, and cyanide, confirming the presence of the reaction. Product characterisation studies then explored the possible products of the reaction, with a chemical synthesis producing 4-(dimethylamino)benzonitrile, however this was only confirmed by thin layer chromatography. Bulk electrolysis afforded a product whereby the cyanide attacked the TMPD in the *ortho*-position on the ring. Following the establishment of the reaction, attention was then focussed on the electrochemical sensor, with cyclic voltammetric studies affording a limit of detection of 48 µM, and square wave voltammetry improving this detection limit to 4.4 µM. This is still outside World Health Organisation requirements; however forms the basis of a promising sensor.

Perhaps the most exciting part of the work was found in the application of the reaction between TMPD and cyanide in remediation studies, with a potentiometric system developed through the use of a Ag/AgCN electrode and subsequently utilised to remove cyanide from aqueous systems, including water samples both from a North Yorkshire river and a Spanish mine stream. A decrease in cyanide concentration by three orders of magnitude was observed, an excellent result and demonstrating both further evidence for the bimolecular reaction between the TMPD and the cyanide, together with a very successful method for the remediation of cyanide from real river water samples in a simple, robust and reproducible manner.

Possible matrix interferences are an important consideration when developing a sensor; hence the effect of sulphide was investigated. Despite the fact that the presence of sulphide did have a slight negative effect on the performance of the sensor in the presence of cyanide, the sensor performed well in real samples, *i.e.* both the river water samples and the mine water samples, maintaining a linear response to the presence of cyanide, with good agreement between the amperometric and potentiometric responses.

9 Conclusions

The range of electrochemical studies presented has shown that electroanalytical chemistry is a useful tool in biological and environmental applications, allowing mechanistic studies, bond cleavage and bond forming dynamics together with mass transport theory to be investigated. The study on the electro-generation of nitric oxide allowed complex mechanistic studies to be undertaken, with the determination of the form of the nitric oxide generated arising from ascertaining the reaction mechanism. As NO^+ is a highly oxidising species and hence is difficult to isolate, the next step for this work would be to further develop designs of compounds that release NO as opposed to NO^+ upon electrochemical perturbation, and to confirm the reactant products.

The diffusion anisotropy study allowed theory to be tested and compared with experimental results in order to produce theory for the axiosymmetric anisotropic diffusion. This was achieved, and in doing so provided some evidence for the factors that affect the generation of molecules such as nitric oxide and also the diffusion of material to the electrode surface, perhaps when considering an electroanalytical sensor. Further work in this area could perhaps investigate the rate of electron transfer in the two dimensions.

The study investigating anion sensing using electro-generated ferrocene surfactants formed the beginning of using electroanalytical chemistry to develop biological sensors by utilising modified electrode redox chemistry. Two exciting ferrocene liquid crystal compounds were investigated, with both compounds exhibiting typical ion transfer processes across the liquid│liquid interface, with both anion insertion and cation expulsion processes demonstrated. The differing voltammetry observed in the presence of different anions formed the basis of the anion sensor. The next step for this work would be to focus on the anion sensing and investigate limits of detection and any interference that may be present.

The development of a cation sensor was the next part of the modified electrode work, however this time the modification involved mimicking a naturally occurring phenomenon: a biofilm. The modification proved successful, up-taking cations into the film and forming the basis of a sensor. Once again, further work in this area would involve focussing on the sensor and determining detection limits and applications.

The final study involved the development of an environmental sensor for cyanide. A limit of detection of 4.4 μM was achieved using square wave voltammetry following product characterisation studies. Remediation work formed the most exciting part of the study, with a reduction in cyanide concentration of river water samples and mine water samples of three orders of magnitude.

Overall, this work has shown that electro-analytical methods can be applied to a number of biological and environmental situations and by intelligent analysis of the data, mechanistic properties can be understood. By developing smart modifications to electrode surfaces, elegant sensors can be developed, together with describing the precise processes occurring in complex natural systems.

10 References

(1) Fisher, A. C. *Electrode Dynamics*; Oxford University Press: Oxford, 1998.
(2) Bard, A. J.; Faulkner, L. R. *Electrochemical Methods: Fundamentals and Applications*; Second ed.; John Wiley and Sons, 2001.
(3) Fick, A. *J. Sci.* **1855**, *30*.
(4) Crow, D. R. *Principles and Applications of Electrochemistry*; Third ed.; Blackie Academic and Professional: Glasgow, 1994.
(5) Butler, J. A. V. *Trans. Faraday Soc.* **1924**, *19*, 729.
(6) Butler, J. A. V. *Trans. Faraday Soc.* **1924**, *19*, 734.
(7) Compton, R. G.; Banks, C. E. *Understanding Voltammetry*; World Scientific Publishing: London, 2007.
(8) Brett, C. M. A.; Brett, A. M. O. *Electroanalysis*; Oxford University Primers: Oxford, 1998.
(9) Levich, V. G. *Physicochemical Hydrodynamics*; Prentice-Hall: Englewood Cliffs, New Jersey, 1962.
(10) Testa, A. C.; Reinmuth, W. H. *Anal. Chem.* **1961**, *33*, 1320.
(11) Nekrassova, O.; Kershaw, J.; Wadhawan, J. D.; Lawrence, N. S.; Compton, R. G. *Phys. Chem. Chem. Phys.* **2004**, *6*, 1316-1320.
(12) Balazs, G. B.; Glass, R. S.; Summers, L. J. *Analyst* **1995**, *120*, 523-527.
(13) Compton, R. G.; Dryfe, R. A. W.; Fisher, A. C. *J. Chem. Soc., Perkin Trans. 2* **1994**, 1581-1587.
(14) Bailey, S. I.; Ritchie, I. M. *Electrochim. Acta* **1985**, *30*, 3-12.
(15) Lide, D. R. *CRC Handbook of Chemistry and Physics*; 76 ed.; CRC Press: Boca Raton, 1995.
(16) Jacob, S. R.; Hong, Q.; Coles, B. A.; Compton, R. G. *J. Phys. Chem. B* **1999**, *103*, 2963-2969.
(17) Palmer, R. M. J.; Ferrige, A. G.; Moncada, S. *Nature* **1987**, *327*, 524-526.
(18) Greenwood, N. N.; Earnshaw, A. *Chemistry of the Elements*; Butterworth-Heinemann: Oxford, 1995.
(19) Butler, A. R.; Williams, D. L. H. *Chem. Soc. Rev.* **1993**, *22*, 233-241.
(20) Lowenstein, C. J.; Dinerman, J. L.; Snyder, S. H. *Ann. Int. Med.* **1994**, *120*, 227-237.
(21) Naseem, K. M. *Mol. Asp. Med.* **2005**, *26*, 33-65.
(22) Croen, K. D. *J. Clin. Invest.* **1993**, *91*, 2446-2452.
(23) Liew, F. Y.; Li, Y.; Milliott, S. *Immunolgy* **1990**, *71*, 556-559.
(24) Fortier, A. H.; Polsinelli, T.; Green, S. J.; Nacy, C. A. *Inf.and Imm.* **1992**, *60*, 817-825.
(25) Fang, F. C. *J. Clin. Invest.* **1997**, *100*, S43-S50.
(26) Palmer, R. M. J.; Ashton, D. S.; Moncada, S. *Nature* **1988**, *333*, 664-666.
(27) Papapetropoulos, A.; Rudic, R. D.; Sessa, W. C. *Cardiovas. Res.* **1999**, *43*, 509-520.
(28) Hetrick, E. M.; Schoenfisch, M. H. *Chem. Soc. Rev.* **2006**, *35*, 780-789.
(29) Bruckdorfer, R. *Mol. Asp. Med.* **2005**, *26*, 3-31.
(30) Wang, P. G.; Xian, M.; Tang, X. P.; Wu, X. J.; Wen, Z.; Cai, T. W.; Janczuk, A. J. *Chem. Rev.* **2002**, *102*, 1091-1134.
(31) Feelisch, M.; Schonafinger, K.; Noack, E. *Biochem. Pharmacol.* **1992**, *44*, 1149-1157.
(32) Cai, T. W.; Xian, M.; Wang, P. G. *Bioorg. Med. Chem. Letts.* **2002**, *12*, 1507-1510.
(33) Lawless, J. G.; Hawley, M. D. *Anal. Chem.* **1968**, *40*, 948-951.

(34) McGill, A. D.; Yang, Y. F.; Wang, J. Q.; Echegoyen, L.; Wang, P. G. In *Nitric Oxide, Pt C*, 1999; Vol. 301.
(35) Hou, Y. C.; Wang, J. Q.; Arias, F.; Echegoyen, L.; Wang, P. G. *Bioorg. Med. Chem. Letts.* **1998**, *8*, 3065-3070.
(36) Hou, Y. C.; Chen, Y. S.; Amro, N. A.; Wadu-Mesthrige, K.; Andreana, P. R.; Liu, G.; Wang, P. G. *Chem. Comm.* **2000**, 1831-1832.
(37) Palmerini, C. A.; Arienti, G.; Palombari, R. *Talanta* **2003**, *61*, 37-41.
(38) Bedioui, F.; Villeneuve, N. *Electroanalysis* **2003**, *15*, 5-18.
(39) Fontijn, A.; Sabadell, A. J.; Ronco, R. J. *Anal. Chem.* **1970**, *42*, 575-&.
(40) Taha, Z. H. *Talanta* **2003**, *61*, 3-10.
(41) Ignarro, L. J.; Buga, G.; Wood, K.; Byrns, R.; Chaudhuri, G. *Proc. Nat. Acad. Sci.* **1987**, *84*, 9265-9269.
(42) Zhang, X. *Front. Biosci.* **2004**, *9*, 3434-3446.
(43) Brunet, A.; Pailleret, A.; Devynck, M. A.; Devynck, J.; Bedioui, F. *Talanta* **2003**, *61*, 53-59.
(44) Shibuki, K. *Neurosci. Res.* **1990**, *9*, 69-76.
(45) Shibuki, K. *Neuroprotocols* **1992**, *1*, 151-157.
(46) Shibuki, K. *J. Physio.* **1990**, *422*, 321-331.
(47) Shibuki, K. *Brain Res.* **1989**, *487*, 96-104.
(48) Shibuki, K.; Okada, D. *Nature* **1991**, *349*, 326-328.
(49) Bedioui, F.; Trevin, S.; Devynck, J. *J. Electroanal. Chem.* **1994**, *377*, 295-298.
(50) Ichimori, K.; Ishida, H.; Fukahori, M.; Nakazawa, H.; Murakami, E. *Rev. Sci. Inst.* **1994**, *65*, 2714-2718.
(51) Lantoine, F.; Trevin, S.; Bedioui, F.; Devynck, J. *J. Electroanal. Chem.* **1995**, *392*, 85-89.
(52) Malinski, T.; Taha, Z. *Nature* **1992**, *358*, 676-678.
(53) Bedioui, F.; Trevin, S.; Albin, V.; Villegas, M. G. G.; Devynck, J. *Anal. Chim. Acta* **1997**, *341*, 177-185.
(54) Castillo, J.; Isik, S.; Blochl, A.; Pereira-Rodrigues, N.; Bedioui, F.; Csoregi, E.; Schuhmann, W.; Oni, J. *Biosens. Bioelectro.* **2005**, *20*, 1559-1565.
(55) Oni, J.; Pailleret, A.; Isik, S.; Diab, N.; Radtke, I.; Blochl, A.; Jackson, M.; Bedioui, F.; Schuhmann, W. *Anal. Bioanal. Chem.* **2004**, *378*, 1594-1600.
(56) Oni, J.; Diab, N.; Radtke, I.; Schuhmann, W. *Electrochim. Acta* **2003**, *48*, 3349-3354.
(57) Diab, N.; Oni, J.; Schulte, A.; Radtke, I.; Blochl, A.; Schuhmann, W. *Talanta* **2003**, *61*, 43-51.
(58) Diab, N.; Schuhmann, W. *Electrochim. Acta* **2001**, *47*, 265-273.
(59) Ciszewski, A.; Milczarek, G. *Talanta* **2003**, *61*, 11-26.
(60) Bedioui, F.; Trevin, S.; Devynck, J.; Lantoine, F.; Brunet, A.; Devynck, M. A. *Biosens. Bioelectro.* **1997**, *12*, 205-212.
(61) Jin, J. Y.; Miwa, T.; Mao, L. Q.; Tu, H. P.; Jin, L. T. *Talanta* **1999**, *48*, 1005-1011.
(62) Vilakazi, S. L.; Nyokong, T. *J. Electroanal. Chem.* **2001**, *512*, 56-63.
(63) Park, J. K.; Tran, P. H.; Chao, J. K. T.; Ghodadra, R.; Rangarajan, R.; Thakor, N. V. *Biosens. Bioelectro.* **1998**, *13*, 1187-1195.
(64) Friedemann, M. N.; Robinson, S. W.; Gerhardt, G. A. *Anal. Chem.* **1996**, *68*, 2621-2628.
(65) www.wpiinc.com; Vol. 2008.
(66) Pailleret, A.; Oni, J.; Reiter, S.; Isik, S.; Etienne, M.; Bedioui, F.; Schuhmann, W. *Electrochem. Comm.* **2003**, *5*, 847-852.
(67) Isik, S.; Schuhmann, W. *Angew. Chem. Int. Ed.* **2006**, *45*, 7451-7454.
(68) Wartelle, C.; Bedioui, F. *Chem. Comm.* **2004**, 1302-1303.

(69) Wartelle, C.; Schuhmann, W.; Blochl, A.; Bedioui, F. *Electrochim. Acta* **2005**, *50*, 4988-4994.
(70) Isik, S.; Berdondini, L.; Oni, J.; Blochl, A.; Koudelka-Hep, M.; Schuhmann, W. *Biosens. Bioelectro.* **2005**, *20*, 1566-1572.
(71) Griveau, S.; Dumezy, C.; Seguin, J.; Chabot, G. G.; Scherman, D.; Bedioui, F. *Anal. Chem.* **2007**, *79*, 1030-1033.
(72) Amatore, C.; Arbault, S.; Bruce, D.; de Oliveira, P.; Erard, M.; Vuillaume, M. *Faraday Discus.* **2000**, 319-333.
(73) Amatore, C.; Arbault, S.; Bruce, D.; de Oliveira, P.; Erard, M.; Vuillaume, M. *Chem. Eur. J.* **2001**, *7*, 4171-4179.
(74) Arbault, S.; Sojic, N.; Bruce, D.; Amatore, C.; Sarasin, A.; Vuillaume, M. *Carcinogenesis* **2004**, *25*, 509-515.
(75) Evans, L. A.; Petrovic, M.; Antonijevic, M.; Wiles, C.; Watts, P.; Wadhawan, J. *J. Phys. Chem. C* **2008**, *112*, 12928-12935.
(76) Murad, F. *Angew. Chem. Int. Ed.* **1999**, *38*, 1856-1868.
(77) Nitzan, A. *Chemical Dynamics in Condensed Phases*; Oxford University Press: Oxford, 2006.
(78) Namiki, S.; Arai, T.; Fujimori, K. *J. Am. Chem. Soc.* **1997**, *119*, 3840-3841.
(79) Cabail, M. Z.; Lace, P. J.; Mooren, P. E.; Patel, N. K.; ver Haag, M. P.; Pacheco, A. A. *J. Photochem. Photobiol. A* **2002**, *152*, 109.
(80) Dagostin.Jt; Jaffe, H. H. *J. Am. Chem. Soc.* **1970**, *92*, 5160-&.
(81) Chuang, L.; Fried, I.; Elving, P. J. *Anal. Chem.* **1964**, *36*, 2426-2431.
(82) Kolthoff, I. M.; Liberti, A. *J. Am. Chem. Soc.* **1978**, *70*, 1885.
(83) Hou, Y. C.; Janczuk, A.; Wang, P. G. *Curr. Pharmaceut. Des.* **1999**, *5*, 417-441.
(84) Bond, A. M.; Oldham, K. B.; Zoski, C. G. *J. Electroanal. Chem.* **1988**, *245*, 71.
(85) Mirkin, M. V.; Bard, A. J. *Anal. Chem.* **1992**, *64*, 2293-2302.
(86) Wadhawan, J. D.; Welford, P. J.; Maisonhaute, E.; Climent, V.; Lawrence, N. S.; Compton, R. G.; McPeak, H. B.; Hahn, C. E. W. *J. Phys. Chem. B* **2001**, *105*, 10659-10668.
(87) Wadhawan, J. D.; Davies, T. J.; Clegg, A. D.; Lawrence, N. S.; Ball, J. C.; Klymenko, O. V.; Rees, N. V.; Bethell, D.; Woolfall, M. P.; France, R. R.; Compton, R. G. *J. Electroanal. Chem.* **2002**, *533*, 33-70.
(88) Amatore, C.; Kochi, J. K. *Adv. Elect. Trans. Chem.* **1991**, *1*, 55.
(89) Amatore, C.; Maisonhaute, E.; Schollhorn, B.; Wadhawan, J. *Chemphyschem* **2007**, *8*, 1321-1329.
(90) Buzzeo, M. C.; Hardacre, C.; Compton, R. G. *Anal. Chem.* **2004**, *76*, 4583 - 4588.
(91) Tsoi, W. C.; O'Neill, M.; Aldred, M. P.; Kitney, S. P.; Vlachos, P.; Kelly, S. M. *Chem. Mat.* **2007**, *19*, 5475-5484.
(92) Jiang, F. Y.; Bouret, Y.; Kindt, J. T. *Biophys. J.* **2004**, *87*, 182-192.
(93) Postlethwaite, T. A.; Samulski, E. T.; Murray, R. W. *Langmuir* **1994**, *10*, 2064-2067.
(94) Newton, M. R.; Morey, K. A.; Zhang, Y. H.; Snow, R. J.; Diwekar, M.; Shi, J.; White, H. S. *Nano Letts.* **2004**, *4*, 875-880.
(95) Amatore, C.; Bouret, Y.; Maisonhaute, E.; Goldsmith, J. I.; Abruna, H. D. *Chem. Eur. J.* **2001**, *7*, 2206-2226.
(96) Boden, N.; Corne, S. A.; Jolley, K. W. *J. Phys. Chem.* **1987**, *91*, 4092-4105.
(97) Moses, P. R.; Murray, R. W. *J. Am. Chem. Soc.* **1976**, *98*, 7435 - 7436.
(98) Schroder, U.; Compton, R. G.; Marken, F.; Bull, S. D.; Davies, S. G.; Gilmour, S. *J. Phys. Chem. B* **2001**, *105*, 1344-1350.
(99) Marken, F.; Blythe, A.; Compton, R. G.; Bull, S. D.; Davies, S. G. *Chem. Comm.* **1999**, 1823-1824.

(100) Evans, R. G.; Banks, C. E.; Compton, R. G. *Analyst* **2004**, *129*, 428-431.
(101) Hoshino, T.; Oyama, M.; Okazaki, S. *Electroanalysis* **2000**, *12*, 1373-1378.
(102) Ghica, M. E.; Brett, C. M. A. *Anal. Letts.* **2005**, *38*, 907-920.
(103) Wadhawan, J. D.; Evans, R. G.; Compton, R. G. *J. Electroanal. Chem.* **2002**, *533*, 71-84.
(104) Wadhawan, J. D.; Evans, R. G.; Banks, C. E.; Wilkins, S. J.; France, R. R.; Oldham, N. J.; Fairbanks, A. J.; Wood, B.; Walton, D. J.; Schroder, U.; Compton, R. G. *J. Phys. Chem. B* **2002**, *106*, 9619-9632.
(105) Marken, F.; Blythe, A. N.; Wadhawan, J. D.; Compton, R. G.; Bull, S. D.; Aplin, R. T.; Davies, S. G. *J. Solid State Electrochem.* **2001**, *5*, 17-22.
(106) Marken, F.; Webster, R. D.; Bull, S. D.; Davies, S. G. *J. Electroanal. Chem.* **1997**, *437*, 209-218.
(107) Haack, E. A.; Warren, L. A. *Environ. Sci. Technol.* **2003**, *37*, 4138-4147.
(108) Rogersona, M.; Pedleya, H. M.; Wadhawan, J. D.; R., M. *Geochim. Cosmochim. Acta* **2008**, *In Print*.
(109) Allongue, P.; Delamar, M.; Desbat, B.; Fagebaume, O.; Hitmi, R.; Pinson, J.; Saveant, J. M. *J. Am. Chem. Soc.* **1997**, *119*, 201-207.
(110) Davis, T. A.; Volesky, B.; Mucci, A. *Water Res.* **2003**, *37*, 4311-4330.
(111) Mengoli, G.; Musiani, M. M. *Prog. Org. Coat.* **1994**, *24*, 237-251.
(112) Lindsay, A. E.; Greenbaum, A. R.; O'Hare, D. *Anal. Chim. Acta* **2004**, *511*, 185-195.
(113) Manahan, S. E. *Toxicological chemistry and biochemistry.*; Third ed.; CRC: Boca Raton, 2003.
(114) Keusgen, M.; Kloock, J. P.; Knobbe, D. T.; Junger, M.; Krest, I.; Goldbach, M.; Klein, W.; Schoning, M. J. *Sens. Act. B* **2004**, *103*, 380-385.
(115) Canterford, D. R. *Anal. Chem.* **1975**, *47*, 88-92.
(116) doNascimento, P. C.; Bohrer, D.; Tramontina, J. *Analyst* **1997**, *122*, 835-838.
(117) Jovanovic, V. M.; Sakbosnar, M.; Jovanovic, M. S. *Anal. Chim. Acta* **1987**, *196*, 221-227.
(118) McCloskey, J. A. *Anal. Chem.* **1961**, *33*, 1842-1843.
(119) Tuhtar, D. *Anal. Chem.* **1983**, *55*, 2205-2208.
(120) Pihlar, B.; Kosta, L. *Anal. Chim. Acta* **1980**, *114*, 275-281.
(121) Nagy, A.; Nagy, G. *Anal. Chim. Acta* **1993**, *283*, 795-802.
(122) Anh, N. B. H.; Sharp, M. *Anal. Chim. Acta* **2000**, *405*, 145-152.
(123) Safavi, A.; Maleki, N.; Shahbaazi, H. R. *Anal. Chim. Acta* **2004**, *503*, 213-221.
(124) Lindsay, A. E.; O'Hare, D. *Anal. Chim. Acta* **2006**, *558*, 158-163.
(125) Lawrence, N. S.; Davis, J.; Compton, R. G. *Talanta* **2000**, *52*, 771-784.
(126) Wadhawan, J. D.; Schroder, U.; Neudeck, A.; Wilkins, S. J.; Compton, R. G.; Marken, F.; Consorti, C. S.; de Souza, R. F.; Dupont, J. *J. Electroanal. Chem.* **2000**, *493*, 75-83.
(127) Bond, A. M.; Heritage, I. D.; Wallace, G. G.; McCormick, M. J. *Anal. Chem.* **1982**, *54*, 582-585.
(128) Leung, L. K.; Bartak, D. E. *Anal. Chim. Acta* **1981**, *131*, 167-174.

11 Appendix 1

A general procedure for the determination of heterogeneous electron transfer kinetics at microdisc electrodes using Marcus-Hush theory or Savéant concerted dissociation theory.

The oxidation of a species at microdisc electrodes is considered under arbitrary, slow heterogeneous electron transfer kinetics, k_{het}, merely assuming adiabatic electron transfer, *viz.*

$$k_{het} = Z_{el} \exp\left(-\frac{\Delta G^{\neq}}{RT}\right)$$

Equation 11-1

where Z_{el} is the electrochemical collision frequency:

$$Z_{el} = \sqrt{\frac{RT}{2\pi M}}$$

Equation 11-2

where M is the molar mass of the reactant and $\Delta G^{\neq}$ is the activation free energy. Although, *stricto sensu*, non-adiabatic reactions should be recognised, especially given the use of platinum electrodes in the experimental cases, this is not considered herein (except that equation 11-3 can be used in this case if the intrinsic barrier is multiplied by 1.07). The global approach adopted herein is then valid for any relationship between the activation free energy and the free energy change, ΔG^{0} in electron transfer reactions, such as the following.

(i) Marcus-Hush electron transfer theory

$$\Delta G^{\neq} = \Delta G_0^{\neq}\left(1+\frac{\Delta G^0}{4\Delta G_0^{\neq}}\right)^2$$

Equation 11-3

where

$$\Delta G_0^{\neq} = \frac{\lambda_i + \lambda_o}{4}$$

Equation 11-4

is the intrinsic activation energy and λ_j is the solvent reorganisation parameter for inner (i) or outer (o) shells.

(ii) Marcus-Levine-Agmon theory

$$\Delta G^{\neq} = \Delta G^0 + \frac{\Delta G_0^{\neq}}{\ln 2}\left\{1+\exp\left[-\frac{\Delta G^0 \ln 2}{\Delta G_0^{\neq}}\right]\right\}$$

Equation 11-5

where $\Delta G_0^{\neq}$ is as defined above. Amatore and Kochi have demonstrated that it is very difficult to distinguish between the expression given above, the Rehm-Weller theory and that in equation 11-3 experimentally, especially in the endergonic region.

(iii) Savéant concerted electron transfer and bond dissociation theory, for which equation 11-3 still upholds, with the intrinsic barrier given as $\Delta G_0^{\neq} = \frac{D_R + \lambda_o}{4}$ where D_R is the bond dissociation free energy of the reactants.

(iii) Savéant theory pertinent for "sticky" dissociative electron transfer theory:

$$\Delta G^{\neq} \approx \Delta G_0^{\neq}\left(1+\frac{\Delta G^0-\Delta G_{sp}^0}{4\Delta G_0^{\neq}}\right)^2$$

Equation 11-6

where the intrinsic barrier is:

$$\Delta G_0^{\neq}=\frac{\left(\sqrt{D_R}-\sqrt{D_P}\right)^2+\lambda_o}{4}$$

Equation 11-7

in which D_P is the bond dissociation energy of the ion-paired cluster, and $\Delta G_{sp}^0 = D_P - T\Delta S_{sp}^0$ is the difference between the standard free energies of the separated and caged fragments respectively.

The diffusion-only mass transport of reactant A to a microdisc electrode in cylindrical polar co-ordinates is (r,z co-ordinates where z is the co-ordinate normal to the electrode, r is that tangential to the electrode surface):

$$\frac{\partial a}{\partial t}=D\left[\frac{\partial^2 a}{\partial z^2}+\frac{1}{r}\frac{\partial a}{\partial r}+\frac{\partial^2 a}{\partial r^2}\right]$$

Equation 11-8

where D is the isotropic diffusion coefficient of species A in solution, and adimensional concentrations, $a=\frac{c_A}{c_0}$, c_i representing concentration of species *i*, with 0 pertaining to bulk solution, are employed. Using dimensionless spatial co-ordinates, *viz.* $R=\frac{r}{r_0};\ Z=\frac{z}{r_0}$ where r_0 is the disc electrode radius, equation 11-8 becomes, at steady-state:

$$\frac{\partial^2 a}{\partial R^2} + \frac{1}{R}\frac{\partial a}{\partial R} + \frac{\partial^2 a}{\partial Z^2} = 0$$

Equation 11-9

The boundary conditions for solution of 14-9 pertinent for the slow heterogeneous electron transfer are:

$\frac{\partial a}{\partial Z} = k_{eff}\left[a\right]_{Z=0}$	R ≤ 1, Z = 0	(Electrode reaction)
$\frac{\partial a}{\partial R} = 0$	R = 0, ∀ Z	(Symmetry axis)
$\frac{\partial a}{\partial Z} = 0$	R> 1 Z = 0	(Insulation plane)
a = 1	$R \rightarrow \infty$, $Z \rightarrow \infty$	(Bulk solution)

The first boundary condition above relates to the electron transfer kinetics, equation 11-1 via:

$$k_{eff} = \frac{k_{het} r_0}{D}$$

Equation 11-10

To determine the current (i) flowing between the working and the counter electrodes as a result of electrolysis, the following normalised equation needs to be evaluated, F is the Faraday constant.

$$\psi = \frac{i}{4nFDr_0c_0} = \frac{\pi}{2}\int_0^1 \left(\frac{\partial a}{\partial Z}\right)_{Z=0} RdR$$

Equation 11-11

Amatore and Fosset demonstrated an elegant and efficient method to solve equation 11-9 using a quasi-conformal map, which requires the following change of variable to [Γ,Θ] space:

$$Z = \Theta \tan\left(\frac{\pi}{2}\Gamma\right)$$
$$R = \sqrt{1-\Theta^2}\sec\left(\frac{\pi}{2}\Gamma\right)$$

Equation 11-12

This transformation maps the semi-infinite (R,Z) space into closed [Γ,Θ] space(Γ is the transformed radial distance) with each new co-ordinate spanning the range $0 \le \Gamma,\Theta \le 1$, so that equal intervals in the quasi-conformal space produce Θ lines with varying angular spacing in (R,Z) being more widely spaced near the symmetry axis. Although this can introduce inefficiencies in the simulation, this can be corrected by redefining Θ as $\cos\left(\frac{\pi}{2}\Theta\right)$, to afford highly efficient numerical simulation. Nevertheless, in the transformed space defined by equation 11-12 and equation 11-8 becomes:

$$\frac{1}{\left[\Theta^2 + \tan^2\left(\frac{\pi}{2}\Gamma\right)\right]}\left\{\frac{4}{\pi^2}\cos^2\left(\frac{\pi}{2}\Gamma\right)\frac{\partial^2 a}{\partial\Gamma^2} + \left(1-\Theta^2\right)\frac{\partial^2 a}{\partial\Theta^2} - 2\Theta\frac{\partial a}{\partial\Theta}\right\} = 0$$

Equation 11-13

with the following relevant boundary conditions applicable.

a = 1	$0 \le \Theta \le 1$	Γ = 1
$\frac{\partial a}{\partial\Theta} = 0$	Θ = 0	$0 \le \Gamma \le 1$

$$\frac{\partial a}{\partial \Theta} = 0 \qquad \Theta = 1 \qquad 0 \le \Gamma \le 1$$

$$\frac{2}{\pi\Theta}\left(\frac{\partial a}{\partial \Gamma}\right) = k_{eff}\left[a\right]_{\Gamma=0} \qquad 0 \le \Theta \le 1 \qquad \Gamma = 0$$

The normalised current is also transformed:

$$\psi = \int_0^1 \left(\frac{\partial a}{\partial \Gamma}\right)_{\Gamma=0} d\Theta$$

Equation 11-14

Equation 11-13 can be solved numerically employing finite differences. Briefly, the true solution, a, is approximated at location Θ_k,Γ_j by the unknown concentration vector **a**, with the location being described as follows.

$$\Theta_k = k\Delta\Theta \qquad 1 \le k < NK$$
$$\Gamma_j = j\Delta\Gamma \qquad 1 \le j < NJ$$
$$\Delta\Theta = \frac{1}{NK}; \quad \Delta\Gamma = \frac{1}{NJ}$$

Equation 11-15

For the calculations employed herein, NK = NJ =100, which is sufficient for convergence to better than 0.5%. Discretising equation 11-13 and solving using the finite difference method keeping equation 11-13 in pentadiagonal form and employing pre-conditioned Krylov sub-space (NAG Library F11) methods as previously described, using trapezoid quadrature for the evaluation of the current:

$$\psi \approx \frac{\Delta\Theta}{\Delta\Gamma}\left[\frac{3}{2}a_{1,1} + \frac{3}{2}a_{1,NK-1} + \sum_{k=2}^{NK-2} a_{1,k}\right]$$

Equation 11-16

This enables the construction of a semi-logarithmic working curve illustrating the dependence of the adimensional current on the magnitude of the kinetic parameter, k_{eff}, see figure 74. This smooth transition of the steady-state limiting current between zero (at low values of k_{eff}) and unity (at high values of k_{eff}) is sufficient to model the heterogeneous electron transfer kinetics of any reaction, provided r_0 and D are known.

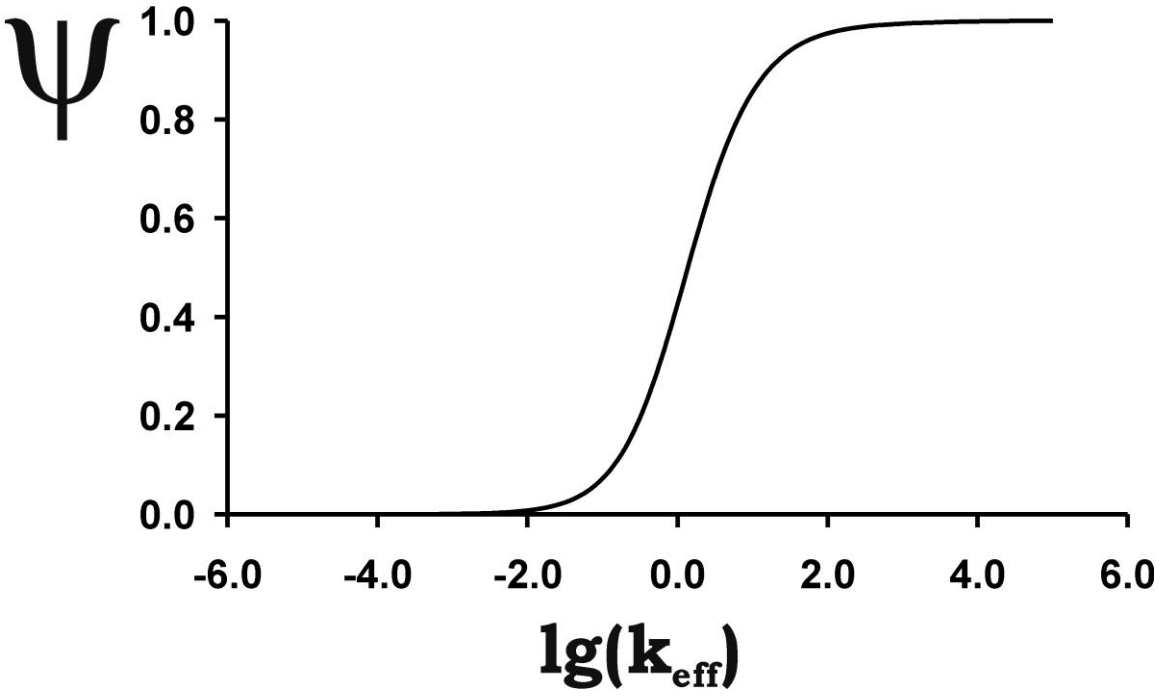

Figure 74

12 Appendix 2

Two-dimensional diffusion anisotropy at disk electrodes under steady-state

Under steady-state conditions, and, assuming D_r is finite, equation 5-2 transforms to:

$$\frac{\partial^2 c}{\partial r^2} + \frac{1}{r}\frac{\partial c}{\partial r} + \left(\frac{D_z}{D_r}\right)\frac{\partial^2 c}{\partial z^2} = 0$$

Equation 12-1

The pertinent boundary conditions are as follows.

Initial conditions: $t \leq 0$

$c = c_0$ $\quad \forall$ r,z (Bulk solution)

At steady-state: $t \rightarrow \infty$

$c = 0$ $\quad r \leq r_0, z = 0$ (Transport-limited electrolysis)

$\frac{\partial c}{\partial z} = 0$ $\quad r > r_0, z = 0$ (Insulation boundary)

$c = c_0$ $\quad r \rightarrow \infty, z \rightarrow \infty$ (Bulk solution)

Suppose equation 12-1 is separable, and with a solution of the form $c(r,z) = F(r)G(z)$, where $G(z)$ takes the form $G(z) = \exp\left[-\sqrt{\frac{D_r}{D_z}}qz\right]$, in which q is a constant. Then, equation 12-1 transforms into the following Bessel form.

$$\frac{\partial^2 F(r)}{\partial r^2} + \frac{1}{r}\frac{\partial F(r)}{\partial r} + q^2 F(r) = 0$$

Equation 12-2

A solution of equation 12-2 is:

$$F(r) = AJ_0(qr) + BY_0(qr)$$

Equation 12-3

where J0(qr), variable s, is the zeroth order Bessel function of the first kind, *viz.* $J_0(qr) = \sum_{s=0}^{\infty} \frac{(-1)^s}{s!\Gamma(s+1)}\left(\frac{qr}{2}\right)^{2s}$ in which $\Gamma(s+1)$ is the gamma function, Y_0(qr) is the Bessel function of the second kind, order zero, A and B are integration constants. Since the problem is for axial symmetry, for F(r) to be finite everywhere, B = 0. Thus, a general solution of equation 12-1 is the superposition of solutions of the form:

$$c_0 - c = J_0(qr)\exp\left[-\sqrt{\frac{D_r}{D_z}}qz\right]$$

Equation 12-4

viz.

$$c_0 - c = \sum_{n=1}^{\infty} A_n J_0(q_n r)\exp\left[-\sqrt{\frac{D_r}{D_z}}q_n z\right]$$

Equation 12-5

Exploiting the orthogonality of the Bessel functions under the boundary conditions of z = 0, enables the deduction of the coefficients A_n so that the general solution of equation 12-1 becomes:

$$c_0 - c = \frac{2c_0}{\pi}\int_0^{\infty} \sin(qr_0)\exp\left[-\sqrt{\frac{D_r}{D_z}}qz\right] J_0(qr)\frac{dq}{q}$$

Equation 12-6

Considering the result deduced by Saito for the isotropic case, it is seen that equation 12-6 differs only by the presence of the square root of the diffusion coefficient ratio in the exponential term. Whilst equation 12-6 satisfies equation 12-1, it is further demonstrated below, using standard results that equation 12-6 is of the correct form when z = 0, *viz.* it reduces to a real constant (equal to c0 for r ≤ r0, and so that $\frac{\partial c}{\partial z} = 0$ for r > r_0).

$$\left(c_0 - c\right)_{z=0} = \frac{2c_o}{\pi}\int_0^{\infty} \sin\left(r_0 q\right) J_0\left(qr\right)\frac{dq}{q} = \left\{\begin{array}{l} c_0 \quad \text{if } 0 < r < r_0 \\ \frac{2c_0}{\pi}\arcsin\left(\frac{r_0}{r}\right) \quad \text{if } r_0 < r < \infty \end{array}\right\}$$

Equation 12-7

$$\left(\frac{\partial c}{\partial z}\right)_{z=0} = \frac{2c_0}{\pi}\sqrt{\frac{D_r}{D_z}}\int_0^{\infty} \sin\left(qr_0\right) J_0\left(qr\right) dq = \left\{\begin{array}{l} 0 \quad \text{if } r^2 > r_0^2 \\ \frac{2c_0}{\pi}\sqrt{\frac{D_r}{D_z}}\frac{1}{\sqrt{r_0^2 - r^2}} \quad \text{if } r_0^2 > r^2 \end{array}\right\}$$

Equation 12-8

Last, in order to derive appropriate mapping tools for the numerical solution of the particular problem in hand, equation 12-6 is solved, *ex cathedra*, using standard integral results ∀ r,z:

$$\frac{c}{c_0} = 1 - \frac{2}{\pi}\arcsin\left\{\frac{2}{\sqrt{\left(\frac{D_r}{D_z}\right)Z^2 + (1+R)^2} + \sqrt{\left(\frac{D_r}{D_z}\right)Z^2 + (1-R)^2}}\right\} \quad Z > 0$$

Equation 12-9

where Z and R are dimensionless variables characterising mass transfer in the normal and radial directions respectively, *viz.* $Z = \frac{z}{r_0} \qquad R = \frac{r}{r_0}$. Using this notation, the solutions provided in equation 12-7 for the concentrations at the electrode surface (z = 0) become:

$$\frac{c}{c_0} = \left\{\begin{array}{l} 0 \quad \text{if } 0 \le R \le 1 \\ 1 - \frac{2}{\pi}\arcsin\left(\frac{1}{R}\right) \quad \text{if } 1 < R < \infty \end{array}\right\} \quad Z = 0$$

Equation 12-10

Simulation of the temporal dependence of the current using conformal mapping techniques

As previously mentioned, the employment of potential-step chronoamperometry enables the characterisation of the temporal dependence of the anisotropic diffusion regime, since the electrode can be held at a driving force, potential (E), sufficiently greater than the formal redox potential, allowing the observed variable, the current (i) to not reflect the effects of the heterogeneous electron transfer process. The axiosymmetric nature of the problem allows for simplification via simulation of only half the disc surface, thereby introducing a new boundary condition due to the presence of the symmetry axis, *viz.*, $\left(\frac{\partial c}{\partial r}\right)_{r=0} = 0 \quad \forall\, z$.

Accordingly, first, an appropriate co-ordinate transform is sought.

Derivation of a quasi-conformal map for the simulation of axially-symmetric diffusion anisotropy

One useful aspect of using conformal mapping techniques is that one of the conformal variables, Γ, takes the solution of equation 12-1, *viz.* equation 12-9. For ease, equation 12-9 is converted into the following form.

$$\frac{c}{c_0}=\frac{2\beta}{\pi}\arctan\left\{\frac{Z\sqrt{\frac{D_r}{D_z}}}{\sqrt{\frac{1}{2}\left[1-\frac{D_r}{D_z}Z^2-R^2+\sqrt{\left(R^2+\frac{D_r}{D_z}Z^2-1\right)^2+4\frac{D_r}{D_z}Z^2}\right]}}\right\}$$

Equation 12-11

Thus, the conversion of equation 12-11 into a closed-grid form, *viz*. [0,1], is achieved by splitting equation 12-11 into the following form:

$$\Theta=\sqrt{\frac{1}{2}\left[1-\frac{D_r}{D_z}Z^2-R^2+\sqrt{\left(R^2+\frac{D_r}{D_z}Z^2-1\right)^2+4\frac{D_r}{D_z}Z^2}\right]}$$

$$\Gamma=\frac{2\beta}{\pi}\arctan\left\{\Theta^{-1}\sqrt{\frac{D_r}{D_z}}Z\right\}$$

Equation 12-12

Hence, rearranging the expressions in equation 12-12 enables the formation of the following co-ordinate transform.

$$R = \left(1 - \Theta^2\right)^{1/2} \sec\left(\frac{\pi}{2\beta}\Gamma\right)$$
$$Z = \Theta\sqrt{\frac{D_z}{D_r}} \tan\left(\frac{\pi}{2\beta}\Gamma\right)$$

Equation 12-13

This is an adapted form of the familiar conformal mapping transform pioneered by Amatore and Fosset, and allows the curved iso-concentration lines observed at steady-state to become straight, parallel and equidistant lines ($\beta = 1$) in the [Γ,Θ] space. It is constructive to note that application of $\Theta = \cos\left(\frac{\pi}{2\beta}\Xi\right)$, where Ξ is a normalised co-ordinate that replaces Θ, to the relations in equation 12-13 (and those proceeding equation 12-13) results in the formulation of the currently most-efficient quasi-conformal transform, and merely improves the angular resolution of the mapped space, thereby leading to a more efficient simulation. Attention is next focused on the meaning of β.

The constant parameter β in conformal space

Since the mappings exploit the steady-state concentration profile, the accuracy of the transform under non-steady-state conditions for isotropic systems tends to diminish, in particular at short electrolytic timescales or when the diffusion coefficients of Ox and Red are sufficiently different, so that it often becomes more efficient to undertake computations based on the real space co-ordinates since that space enabled the development of geometrically-expanding, adaptive simulation grids which contain a very large number of nodes around the singularities and an increasingly fewer number of nodes towards the semi-infinite limits, allowing for the rapid and accurate simulation of the problem compared with very fine meshes required for the conformal problem. For the anisotropic problem, this also becomes a

problem whenever diffusion in one-dimension becomes dominant (*viz.* $\frac{D_z}{D_r} \neq 1$, where Cottrellian effects at short time electrolyses are implicit). One method to bypass this is to introduce an adjustable parameter, β, defined as follows, into the conformal map.

$$\beta = 1 + \frac{r_0}{\alpha\sqrt{\left(\theta\sqrt{D_z D_r}\right)}} = 1 + \frac{2}{\alpha\sqrt{\tau_{\max}}\sqrt[4]{D_z / D_r}}$$

Equation 12-14

In the above expression, θ is the maximal duration of the simulated experiment (in real time, units seconds, expressed in adimensional form, τ_{max}), so that $\beta \to 1$ as $\theta \to \infty$ (*viz.* steady-state conditions). Note that $\tau_{\max} = \frac{4\theta D_r}{r_0^2}$. Thus, for short-time electrolyses, $\theta \to 0$, the fractional part of equation 12-14 plays a more dominant role, so that $\frac{\pi}{2\beta} \to 0$. Likewise, as $D_z \to \infty$, $\beta \to 1$. Hence, the introduction of this variable accounts for the smaller diffusion layer in the Z-direction that is obtained when small timescales are employed, and acts in an adaptive sense, in that it adjusts the distance between the nodes in the Γ-direction. Similar arguments apply for variation in D_r. The final term in equation 12-14, α, an integer, merely signifies that further accuracy is achievable by allowing it to take a arbitrary value in this work, the value of α is taken to be 20.

The use of the above conformal mapping techniques in simulating chronoamperometry at microdisk electrodes immersed in a two-dimensionally anisotropic medium is next considered.

The form of Fick's second law for the simulation of chronoamperometry in quasi-conformal map conditions

Equation 5-2 is first re-written in the following reduced form.

$$4\frac{\partial a}{\partial \tau} = \frac{\partial^2 a}{\partial R^2} + \frac{1}{R}\frac{\partial a}{\partial R} + \frac{D_z}{D_r}\frac{\partial^2 a}{\partial Z^2}$$

Equation 12-15

where $a = \frac{c}{c_0}$ is the normalised concentration of species Ox and $\tau = \frac{4D_r t}{r_0^2}$ is the reduced time variable, and exploits the radial diffusion coefficient. Changing the variables as indicated in equation 12-13 transforms equation 12-15 to the following form:

$$\frac{\partial a}{\partial \tau} = \frac{1}{4\left[\Theta^2 + \tan^2\left(\frac{\pi}{2\beta}\Gamma\right)\right]}\left\{\frac{4\beta^2}{\pi^2}\cos^2\left(\frac{\pi}{2\beta}\Gamma\right)\frac{\partial^2 a}{\partial \Gamma^2} + \left(1-\Theta^2\right)\frac{\partial^2 a}{\partial \Theta^2} - 2\Theta\frac{\partial a}{\partial \Theta}\right\}$$

Equation 12-16

The subtle change of the dimensionless variables as indicated transposes the anisotropic problem to the identical form observed for isotropic diffusion. The transformed boundary conditions for this axially-symmetric case for chronoamperometry are also identical to the isotropic system, *viz.*,

Initial conditions: $\tau \leq 0$

$a = 1$ $\quad \forall\ \Gamma,\Theta$ (Bulk solution)

During electrolysis: $\tau > 0$

$a = 0$ $\quad 0 \leq \Theta \leq 1,\ \Gamma = 0$ (Transport-limited electrolysis)

$\frac{\partial a}{\partial \Theta} = 0$ $\Theta = 0, 0 \le \Gamma \le 1$ (Insulation plane)

$\frac{\partial a}{\partial \Theta} = 0$ $\Theta = 1, 0 \le \Gamma \le 1$ (Symmetry axis)

$a = 1$ $0 \le \Theta \le 1, \Gamma = 1$ (Bulk solution)

It is evident that $a = \Gamma$ satisfies equation 12-16 and all other boundary conditions.

The expression for the observed current flowing through the disk electrode is:

$$i = 2\pi nFD_z c_0 r_0 \int_0^1 \left(\frac{\partial a}{\partial Z}\right)_{Z=0} RdR = 4\beta nF\sqrt{D_z D_r}\, r_0 c_0 \int_{\Theta=0}^{\Theta=1} \left(\frac{\partial a}{\partial \Gamma}\right)_{\Gamma=0} d\Theta$$

Equation 12-17

Hence, the steady-state normalised form of the current, Ψ, is deduced as:

$$\psi = \beta \int_{\Theta=0}^{\Theta=1} \left(\frac{\partial a}{\partial \Gamma}\right)_{\Gamma=0} d\Theta$$

Equation 12-18

This succinct representation of the current demonstrates that $\Psi \to 1$ as the experiment approaches steady-state. Simulation of the problem using the ADI method is now detailed.

Simulation of chronoamperometry in transformed space

For simulation of chronoamperometric traces, equation 12-16 was converted into finite difference form for a uniformly spaced Γ,Θ grid ($d\Gamma = d\Theta = h$) and solved using the alternating direction implicit (ADI) method. Briefly, equation 12-16 transforms into the following form.

$$\frac{\partial a}{\partial \tau} = \lambda_{zz}\frac{\partial^2 a}{\partial \Gamma^2} + \lambda_{rr}\frac{\partial^2 a}{\partial \Theta^2} + \lambda_r \frac{\partial a}{\partial \Theta}$$

Equation 12-19

where,

$$\lambda_{zz} = \frac{\beta^2 \cos^2\left(\frac{\pi}{2\beta}\Gamma\right)}{\pi^2\left[\Theta^2 + \tan^2\left(\frac{\pi}{2\beta}\Gamma\right)\right]}$$

$$\lambda_{rr} = \frac{1-\Theta^2}{4\left[\Theta^2 + \tan^2\left(\frac{\pi}{2\beta}\Gamma\right)\right]}$$

$$\lambda_r = -\frac{\Theta}{2\left[\Theta^2 + \tan^2\left(\frac{\pi}{2\beta}\Gamma\right)\right]}$$

Equation 12-20

In the (semi-implicit) ADI method, the full time step, Δt, is split into two. The first half time-step allows for a "bottom-to-top" grid march, that is, the calculation occurs implicitly with respect to the Θ variable, indexed using k, but explicitly with respect to the Γ variable, indexed by j. *Mutatis mutandis* for the second half time-step, corresponding to a grid-march that goes "left-to-right". Hence, for the first half time-step (*viz.* τ = n to τ = n+½ corresponding to a time step of Δt/2), equation 12-19 becomes:

$$-\frac{\Delta t}{2h}\left(\frac{\lambda_{rr}}{h} + \frac{\lambda_r}{2}\right)a_{j,k+1}^{n+1/2} + \left(1 + \frac{\lambda_{rr}\Delta t}{h^2}\right)a_{j,k}^{n+1/2} - \frac{\Delta t}{2h}\left(\frac{\lambda_{rr}}{h} - \frac{\lambda_r}{2}\right)a_{j,k-1}^{n+1/2}$$
$$= \frac{\lambda_{zz}\Delta t}{2h^2}\left(a_{j+1,k}^{n} + a_{j-1,k}^{n}\right) + \left(1 - \frac{\lambda_{zz}\Delta t}{h^2}\right)a_{j,k}^{n}$$

Equation 12-21

The second half time-step (*viz.* $\tau = n+½$ to $\tau = n+1$, again corresponding to a time step of $\Delta t/2$) transforms to the following.

$$\frac{\Delta t}{2h}\left(\frac{\lambda_{rr}}{h}+\frac{\lambda_r}{2}\right)a_{j,k+1}^{n+½}+\left(1-\frac{\lambda_{rr}\Delta t}{h^2}\right)a_{j,k}^{n+½}+\frac{\Delta t}{2h}\left(\frac{\lambda_{rr}}{h}-\frac{\lambda_r}{2}\right)a_{j,k-1}^{n+½}$$
$$=-\frac{\lambda_{zz}\Delta t}{2h^2}\left(a_{j+1,k}^{n+1}+a_{j-1,k}^{n+1}\right)+\left(1+\frac{\lambda_{zz}\Delta t}{h^2}\right)a_{j,k}^{n+1}$$

Equation 12-22

The boundary conditions in conformal space can likewise be appropriately transformed, *viz.* $a_{0,k} = 0$, $a_{j,0} = a_{j,1}$, $a_{j,N\Theta} = a_{j,N\Theta-1}$, and $a_{N\Theta,k} = 1$. Hence, since equations 12-21 and 12-22 enables representation of the concentrations at the individual conformal space grid nodes in matrix form, with the matrix of known coefficients taking the familiar tridiagonal form, solution at each half-time step is readily afforded by application of the Thomas Algorithm.

Accordingly, simulations were undertaken, via program encoding using FORTRAN, using a grid size $N\Gamma$ x $N\Theta$ of 100 x 100, resulting in a value of h = 0.01, and 500000 time points for a transient of $\tau_{max} = 4.11$ (*viz.* $\Delta t = 8.22$ x 10-6). These sizes are sufficiently small for convergent simulations, and were chosen so that the ADI method furnished stable solutions at all time points considered, *viz.* $\chi = \frac{\Delta t}{4h^2} < 1$, resulting in smooth logarithmic plots of Ψ versus τ.

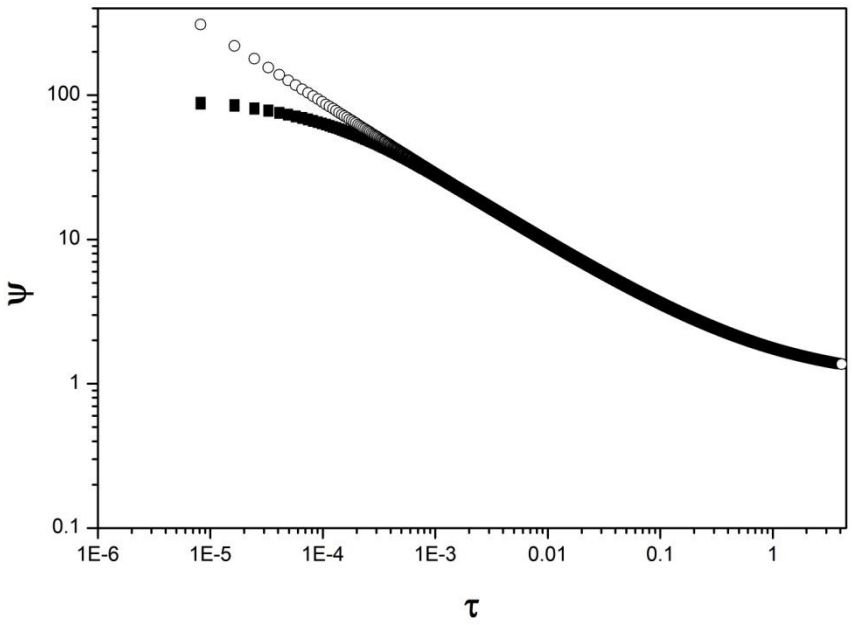

Figure 75: Reduced variable transients (over four million points are plotted) simulated using the quasi-conformal map and via the Shoup-Szabo microdisc approximation (○).All simulations were undertaken using adimensional variables using c_0 = 2.0 mM, r_0 = 10.0 μm, n = 1, -10 ≤ lg(D_r/m² s^{-1}) ≤ -8 and -10 ≤ lg(D_z/m² s^{-1}) ≤ -8. Note the deviation between the two plots at $\tau < 4 \times 10^{-4}$ stems from convergence errors in the simulations (smaller normalised time steps removes these deviations), and are shown here so as to indicate that two types of data are present.

13 Appendix 3

0.05 M Perchloric Acid

v /Vs^{-1}	10^{6} Pre-Wave Charge /C	10^{5} Overall Charge /C	10^{-1} Ratio	%
0.0005				
0.01	7.04	8.56	0.822	8.224299
0.02				
0.05	8.33	3.88	2.15	21.46907
0.1	11.5	2.01	5.72	57.21393
0.2				
0.5	4.53	1.80	2.52	25.16667
1				
2	3.96	0.878	4.51	45.10251

0.1M Perchloric Acid

v /Vs^{-1}	10^{6} Pre-Wave Charge /C	10^{5} Overall Charge /C	10^{-1} Ratio	%
0.0005	6.18	5.74	1.08	10.76655
0.01	7.56	4.05	1.87	18.66667
0.02	7.33	3.60	2.04	20.36111
0.05				
0.1	2.66	1.43	1.86	18.6014
0.2	3.66	1.0	3.49	34.85714
0.5				
1				
2	5.87	1.25	4.70	46.96

0.2 M Perchloric Acid

v /Vs^{-1}	10^{6} Pre-Wave Charge /C	10^{5} Overall Charge /C	10^{-1} Ratio	%
0.0005	5.69	3.74	1.52	15.2139
0.01	7.68	6.91	1.11	11.11433
0.02	9.22	6.49	1.42	14.20647
0.05	1.52	4.96	0.306	3.064516
0.1				
0.2	4.97	1.41	3.52	35.24823
0.5				
1	5.21	1.10	4.74	47.36364
2	2.16	1.19	1.82	18.15126

0.5 M Perchloric Acid

v /Vs^{-1}	10^{6} Pre-Wave Charge /C	10^{5} Overall Charge /C	10^{-1} Ratio	%
0.0005	5.79	7.58	0.764	7.638522
0.01	5.08	5.76	0.882	8.819444
0.02	4.91	3.19	1.54	15.39185
0.05				
0.1	1.20	4.11	0.292	2.919708
0.2	3.10	1.88	1.65	16.48936
0.5	5.44			
1	5.63	1.26	4.47	44.68254
2	5.79	7.58	0.764	7.638522

1 M Perchloric Acid

v /Vs^{-1}	10^{6} Pre-Wave Charge /C	10^{5} Overall Charge /C	10^{-1} Ratio	%
0.0005	8.02	8.17	0.982	9.816401
0.01	6.38	5.79	1.10	11.019
0.02	4.74	3.47	1.37	13.65994
0.05	7.23	4.97	1.45	14.54728
0.1				
0.2	1.82	1.43	1.27	12.72727
0.5	3.47	1.60	2.17	21.6875
1	3.35	1.38	2.43	24.27536
2	1.90	1.38	1.38	13.76812